

Innovative low-mass cooling systems for the ALICE ITS Upgrade detector at CERN

THÈSE N° 6993 (2016)

PRÉSENTÉE LE 11 MAI 2016

À LA FACULTÉ DES SCIENCES ET TECHNIQUES DE L'INGÉNIEUR
LABORATOIRE DE TRANSFERT DE CHALEUR ET DE MASSE
PROGRAMME DOCTORAL EN ENERGIE

ÉCOLE POLYTECHNIQUE FÉDÉRALE DE LAUSANNE

POUR L'OBTENTION DU GRADE DE DOCTEUR ÈS SCIENCES

PAR

Manuel GÓMEZ MARZOA

acceptée sur proposition du jury:

Prof. S. Haussener, présidente du jury
Prof. J. R. Thome, directeur de thèse
Prof. T. Karayiannis, rapporteur
Prof. R. Revellin, rapporteur
Prof. J. Schiffmann, rapporteur



ÉCOLE POLYTECHNIQUE
FÉDÉRALE DE LAUSANNE

Suisse
2016

Acknowledgements

I would like to first thank Prof. John R. Thome for his supervision, advice, and careful reading of this thesis. I would like to express my gratitude to Michele Battistin for thinking of me for a doctoral studentship at CERN and to Luciano Musa for welcoming me in the ALICE ITS Upgrade project. As part of this work was carried out at the Heat Transfer Research Lab at the USP São Carlos in Brazil, I would like to thank Prof. Gherhardt Ribatski for his guidance and encouragement during the 9 months I spent in his lab. This collaboration was possible thanks to the support of a Doctoral Mobility fellowship awarded by Swiss National Science Foundation (SNSF), which I hereby warmly acknowledge.

I would like to thank the committee members, Prof. Sophia Haussener, Prof. Tassos Karayiannis Prof. Rémi Revellin, and Prof. Jürg Schiffmann for their time evaluating and helping improve this thesis.

I wish to thank all the colleagues at CERN, especially José Botelho Direito; Elisa Laudi and Corrado Gargiulo from the ITS Upgrade project, for their trust and knowledge; Sergey Igolkin, for his skills with carbon fibre; and Pieter Izjermanns, Andrea Francescon and Martin Doubek for their help at the lab. It is a pleasure to sincerely thank Prof. Enrico Da Riva for his great support, patience, and all he taught me during the almost 3 years we shared an office at CERN. I would like to thank my colleagues at the CFD-Team for their friendship: Vinod Rao, Gennaro Bozza, Sylwia Wojnarska, Gianluca Camplone, Piotr Pacholek, and Aniko Rakai. A very big thanks to Michael Plagge for his generous help. Thanks to my friends in Geneva, especially the crew from the house in Meyrin, the CinéClub pals, and the members from the CERN Vélo Club and the Ski Touring Club, for sharing unforgettable times and showing me incredible places in this beautiful region. Also, my most sincere gratitude goes to my friends from Spain and elsewhere for their encouragement, and the great times and trips together.

My best thoughts go to the colleagues and friends in São Carlos. I want to thank Hélio Donizete Trebi and José Bogni for his invaluable help putting together the experimental facility. Thanks to Fábio Kanizawa, Hugo Leão, Chicão Nascimento, Daniel Sempértegui and Cristiano Tibiriçá for their support during the experiments. I wish to thank the rest of the lab students, as well as my housemates and my cycling friends, for their big smiles and true friendship. You will always be in my heart.

I would like to extend my gratitude to the colleagues of the LTCM lab at EPFL, which helped me in many occasions and shared coursework, dinner and ski times. A big thanks to Cécile Taverney and Nathalie Matthey-de-l'Endroit for their prompt help with the administrative work.

My deepest thanks go to Lucía, who has faithfully put up with me for all these years. This work would not have been possible without your encouragement and your love, rain or shine.

Last, but not least, many, many thanks to my family for their unconditional love and support.

Lausanne, 4th April 2016

Manuel Gómez Marzoa

Abstract

The Phase-1 upgrade of the LHC to full design luminosity, planned for 2019 at CERN, requires the modernisation of the experiments around the accelerator. The Inner Tracking System (ITS), the innermost detector at the ALICE experiment, will be upgraded by replacing the current apparatus by new silicon pixels arranged in 7 cylindrical layers. Each layer is composed by multiple independent modules, named *staves*, which provide mechanical support and cooling to the chips. This thesis aims to develop and validate experimentally an ultra-lightweight stave cooling system for the ITS Upgrade. The moderate thermal requirements, with a nominal power density of 0.15 W cm^{-2} and a maximum chip temperature of 30°C , are counterweighted by extreme low-mass restrictions, obliging to resort to lightweight, non-metallic materials, such as carbon fibre-reinforced polymers and plastics.

Novel lightweight stave concepts were developed and experimentally validated, meeting the thermal requirements with minimal material inventory. The proposed staves are made of thin, layered, composite high thermal conductivity carbon fibre plates, with dimensions up to $1502 \times 30 \text{ mm}$, and innovative polyimide cooling channels, with inner diameters (IDs) ranging from 1.024 mm to 2.667 mm and thin walls. Six different stave layouts were tested with water at sub-atmospheric pressure (leak-less cooling), showing excellent cooling performances: the temperature differences between the heated surfaces and the coolant are below 7 K at 0.15 W cm^{-2} , with low surface temperature gradients.

Cooling tests with evaporative C_4F_{10} refrigerant were performed on the baseline stave prototypes, yielding similar thermal performance as with water. This indicates that the thermal resistance of conduction in the stave dominates over the convective one between the channel wall and the coolant. A two-phase coolant would display low material inventory thanks to the presence of the vapour phase, lighter than liquid. An experimental study on the two-phase coolant inventory was carried out in one stave. The results are compared with void fraction prediction methods integrated along the cooling channel length, to find the best one for calculating the material budget of the two-phase coolant.

An experimental study on the two-phase pressure drop and flow boiling heat transfer in a 2.689 mm ID water-heated polyimide channel was performed, using R245fa as operating fluid. Mass fluxes ranging from 100 to $500 \text{ kg m}^{-2} \text{ s}^{-1}$, heat fluxes from 15 to 55 kW m^{-2} , vapour qualities between 0.05 and 0.80 , and saturation temperatures of 35 , 41 and 47°C were considered in the 300-point experimental database. The influence of the two-phase flow parameters on the mean heat transfer coefficient was analysed parametrically, being its lack of dependence on the heat flux the major finding. Finally, the results were compared with other experimental data and with prediction methods in the literature.

Keywords: high-conductivity materials, CFRP, polyimide, lightweight cooling, material budget, two-phase flow, flow boiling, pressure drop, microscale, refrigerants.

Version abrégée

L'amélioration du LHC au CERN vers sa luminosité maximale en 2019 implique la modernisation des expériences dans l'accélérateur. Le détecteur Inner Tracking System (ITS) dans l'expérience ALICE sera remplacé par un nouveau détecteur constitué de puces en silicium groupées en 7 couches cylindriques. Chaque couche est composée de plusieurs modules indépendants, qu'on appelle *staves*, et qui assurent le support mécanique et le refroidissement des puces. Cette thèse vise à développer et valider expérimentalement un système de refroidissement ultraléger pour le ITS Upgrade. Les contraintes thermiques modérées (la température des puces ne doit pas dépasser 30°C pour une densité de puissance de 0.15 W cm⁻²) sont contrastées par des exigences de légèreté extrême du système, ce qui oblige à utiliser des matériaux légers et non métalliques, comme les fibres de carbone ou les plastiques.

Des nouveaux modules ultralégers ont été développés et validés expérimentalement, en respectant les limites du matériel et les exigences thermiques. Les modules proposés sont composés de plaques fines construites à partir de couches en fibre de carbone superposées, avec des dimensions jusqu'à 1502 × 30 mm, et des tuyaux de polyimide innovants intégrés pour le réfrigérant, avec des diamètres internes mesurant de 1.024 mm jusqu'à 2.667 mm. 6 modules de différentes conceptions ont été évalués expérimentalement avec de l'eau en pression sous-atmosphérique. Tous les modules ont montré de bonnes capacités de refroidissement, avec des différences de température entre la surface chauffée et le réfrigérant inférieures à 7 K pour 0.15 W cm⁻², et des gradients minimaux sur la surface chauffée.

Des tests expérimentaux en évaporation avec le réfrigérant C₄F₁₀ révèlent les mêmes performances thermiques qu'avec de l'eau, en indiquant que la résistance thermique dominante est par conduction dans le module, et pas convective à l'intérieur des tuyaux. L'utilisation d'un réfrigérant diphasique minimise l'inventaire de matériel du module à cause de la présence du vapeur. Les résultats d'une étude expérimentale sur la charge du réfrigérant diphasique dans un module ont été comparés avec des modèles de prédiction du taux de vide intégré numériquement le long des canaux de refroidissement, afin de trouver la meilleure méthode pour le calcul de l'inventaire du réfrigérant diphasique.

Finalement, une étude expérimentale du transfert de chaleur et de la perte de charge des écoulements diphasiques en ébullition convective du réfrigérant R245fa dans un canal de polyimide de 2.689 mm de diamètre a été réalisée. Des débits massiques entre 100 et 500 kg m⁻² s⁻¹, des flux de chaleur entre 15 et 55 kW m⁻², et trois températures de saturation (35, 41 et 47°C) constituent une base de données de 300 points. L'influence de ces paramètres sur le coefficient de transfert thermique moyen a été évaluée, avec l'indépendance du flux de chaleur comme conclusion principale. Les résultats ont été comparés avec d'autres études expérimentales et des modèles de prédiction dans la littérature.

Mots clés : haute conductivité, CFRP, polyimide, refroidissement ultraléger, inventaire du matériel, écoulements diphasiques, ébullition, perte de charge, micro-échelle, réfrigérants.

Contents

Acknowledgements	iii
Abstract/Version abrégée	v
List of Figures	xxi
List of Tables	xxv
List of Symbols	xxvii
List of Acronyms	xxx
1 Introduction	1
1.1 Objectives	3
1.2 Layout of the chapters	3
2 State of the art and literature survey	5
2.1 Introduction	5
2.2 Fundamentals of High Energy Physics particle detectors	5
2.2.1 Silicon detectors for High Energy Physics	5
2.2.2 Radiation in particle detectors	8
2.2.3 Material budget	10
2.3 Cooling systems for HEP particle detectors	13
2.3.1 Air and gas cooling systems	13
2.3.2 Single-phase cooling systems	13
2.3.3 Two-phase cooling systems	15
2.4 Review on material selection for HEP particle detectors	16
2.4.1 Structural materials	16

2.4.2	Thermally conductive materials	18
2.4.3	Resins and adhesives	21
2.4.4	Cooling channels	22
2.5	Review on two-phase flow boiling in small horizontal channels	26
2.5.1	Introduction	26
2.5.2	Macro-to-microchannel transition	26
2.5.3	Flow patterns	27
2.5.4	Cross-sectional void fractions and refrigerant inventory	29
2.5.5	Two-phase pressure drop	32
2.5.6	Flow boiling heat transfer	35
3	Cooling system R&D for the Upgrade of the ALICE Inner Tracker System	45
3.1	Introduction	45
3.2	The ALICE Inner Tracker System Upgrade detector	45
3.3	Thermal and material requirements of the ITS Upgrade	48
3.3.1	Thermal requirements	48
3.3.2	Material budget and general requirements	49
3.4	Status of the ITS Upgrade project at the start of this thesis	50
3.5	Air cooling	52
3.5.1	Layer-by-layer air cooling	52
3.5.2	Impinging jet air cooling proposal	56
3.6	Ultra-lightweight cooling systems	65
3.7	Choice of the refrigerant	70
3.7.1	Demineralised water	70
3.7.2	Fluorocarbons	71
4	Experimental setup, methodology and evaluation of the ultra-lightweight staves	73
4.1	Introduction	73
4.2	Experimental setup	73
4.2.1	Power dissipation and stave temperature monitoring	73
4.2.2	Experimental facilities	76

4.3	Experimental methodology	79
4.3.1	Heat exchange with the ambient	79
4.3.2	Stave thermal performance	85
4.3.3	Single-phase flow parameters	85
4.3.4	Two-phase flow parameters	87
4.3.5	Stave thermal resistance and heat transfer coefficient of the coolant	89
4.3.6	Calibration and error analysis	90
4.4	Comparison of the two ultra-lightweight concepts	93
4.5	Stave design optimisation	96
5	Results of the experimental cooling tests of the ALICE ITS Upgrade staves	99
5.1	Introduction	99
5.2	Inner Barrel staves	99
5.2.1	Description of the Inner Barrel stave layouts	100
5.2.2	Water cooling performance benchmarking of the Inner Barrel staves	102
5.2.3	Two-phase evaporative cooling for the Inner Barrel staves	107
5.3	Outer Barrel half-staves	116
5.3.1	Description of the Outer Barrel half-stave layouts	116
5.3.2	Water cooling performance benchmarking of the Outer Barrel half-staves	118
5.3.3	Two-phase evaporative cooling for the Outer Barrel half-staves	123
5.3.4	Two-phase heat transfer coefficient	134
5.4	Two-phase coolant inventory experimental studies	136
5.4.1	Introduction	136
5.4.2	Test facility	136
5.4.3	Sensitivity study	138
5.4.4	Experimental methodology	140
5.4.5	Void fraction methods	142
5.4.6	Results	142
5.4.7	Concluding remarks	146
5.5	Conclusions and recommendations	147

6	Experimental flow boiling heat transfer in a small polyimide channel	149
6.1	Introduction	149
6.2	Experimental apparatus	151
6.2.1	Test rig	151
6.2.2	Experimental facility	158
6.3	Experimental methodology	160
6.3.1	Heat flux	160
6.3.2	Heat transfer coefficient	162
6.3.3	Vapour quality	163
6.4	Water-water tests	164
6.4.1	Thermal resistance of conduction across the tube wall	164
6.4.2	Validation of the heat transfer coefficient correlation in the annulus	166
6.5	Validation tests	167
6.5.1	Single-phase flow tests	167
6.5.2	Singular two-phase flow pressure drop evaluation	169
6.6	Calibration, error analysis and stability of the experiments	173
6.7	Experimental results	175
6.7.1	Parametric analysis of the results	175
6.7.2	Comparison with experimental results from similar studies	181
6.7.3	Comparison with heat transfer prediction methods	182
6.8	Conclusion	186
7	Conclusions and recommendations	187
7.1	ALICE ITS Upgrade ultra-lightweight cooling system	187
7.1.1	Recommendations	188
7.2	Experimental flow boiling heat transfer in polyimide channels	189
7.2.1	Recommendations and suggestions on further research aspects	189
A	Correlations and methods	191
A.1	Pressure drop	191
A.1.1	Single-phase pressure drop correlations	191

A.1.2	Two-phase frictional pressure drop correlations	193
A.2	Heat transfer	197
A.2.1	Free convection	197
A.2.2	Single-phase forced convection in internal flows	199
A.2.3	Two-phase flow boiling heat transfer in internal flows	204
A.3	Two-phase void fraction models	211
B	Polyimide tubing characterisation	213
B.1	Introduction	213
B.2	Sectional stability of polyimide channels	213
B.2.1	Introduction	213
B.2.2	Dimensions and physical properties of the polyimide channels	214
B.2.3	Hoop stress elongation	215
B.2.4	Channel collapse	217
B.2.5	Recommended polyimide channel thicknesses	220
B.3	Water-polyimide channels long-term compatibility test	222
B.3.1	Introduction	222
B.3.2	Experimental setup	223
B.3.3	Specimens and test conditions	224
B.3.4	Inspection methodology	225
B.3.5	Results	226
B.3.6	Conclusions	228
B.3.7	Further studies	229
C	Thermophysical properties of the C₄F₁₀ and the R245fa fluids	231
D	Calibration procedure	233
D.1	Introduction	233
D.2	Calibration of the temperature measurements	233
D.3	Calibration of the water flow rate measurements	236
E	Limitations of the present studies	237

E.1 ALICE ITS Upgrade experimental cooling studies	237
E.2 Experimental flow boiling heat transfer studies in a small polyimide channel	238
Bibliography	239
Curriculum Vitae	255

List of Figures

2.1	Generic diode curve	6
2.2	Two schematic views of the present ALICE ITS detector	7
2.3	Air cooling system description at the STAR detector.	14
2.4	Support structures made with T300 carbon fibre composites.	17
2.5	Carbon foam and PEEK cooling channel used in a primitive ALICE ITS Upgrade module.	17
2.6	A view of a primitive ALICE ITS Upgrade module made of M55J CFRP.	18
2.7	K13D2U CFRP fibres placed in the same direction, with two fibre densities.	19
2.8	Thermal Pyrolytic Graphite (TPG) foil view.	20
2.9	Material budget comparison of a 2.1 mm ID, 2.4 mm OD cylindrical channel made of SAE 316LN stainless steel and made of polyimide.	23
2.10	Composite polyimide tubes: (a) pipe with reinforcement coil and outer surface made of Pebax [®] ; (b) pipe with a PTFE transition plus shaped polyimide section.	26
2.11	Flow patterns of R245fa refrigerant flow in a 1.1 mm inner diameter tube.	28
2.12	Effect of the liquid entrainment on the void fraction, calculated by Zivi [81], for two-phase R245fa refrigerant in a 2.7 mm ID channel.	30
2.13	Material budget of two-phase C ₄ F ₁₀ refrigerant with a void fraction of 0.85 and all liquid in a thin film adjacent to the wall of a 2.67 mm ID polyimide channel, compared to the same channel filled with water.	31
2.14	Flow pattern evolution in a boiling flow in a conventional horizontal tube. Figure adapted from Collier and Thome [75].	36
2.15	Heat transfer coefficient at three locations in the channel perimeter and two-phase flow images at three vapour qualities refrigerant, $G=100 \text{ kg m}^{-2} \text{ s}^{-1}$, $q=5 \text{ kW m}^{-2}$, $T_{sat}=22^\circ\text{C}$). From Tibiriça and Ribatski [103].	37
2.16	Heat transfer coefficient trend for R236fa refrigerant flow boiling, $G=2299 \text{ kg m}^{-2} \text{ s}^{-1}$ and base heat flux $q_b=48.6 \text{ W cm}^{-2}$ in 67 parallel $100 \mu\text{m}$ square channels by Szczukiewicz <i>et al</i> [105].	38

3.1	Location of the Inner Tracker System (ITS) at the ALICE Experiment, showing the detector modularity.	46
3.2	Cross-sectional views of the ITS Upgrade Inner, Middle and Outer Barrels.	47
3.3	Schematic view of the one-side access to the Inner Barrel staves.	50
3.4	Inner Barrel layer-by-layer air cooling concept.	53
3.5	Dimensions of the triangular duct cross-section for air inflow in the layer-by-layer air cooling solution.	53
3.6	Chip temperature map at a power density of 0.30 W cm^{-2} when cooling the Inner Barrel layer by layer with air injected at 20 m s^{-1} and 14°C	55
3.7	Heat flux dissipated by the two sides of the detector chips to the airflow at a power density of 0.30 W cm^{-2} when cooling the Inner Barrel layer by layer with air injected at 10 m s^{-1} inside the triangular ducts and 14°C	55
3.8	Air velocity map in a central longitudinal section of the CFD model at a power density of 0.30 W cm^{-2} when cooling the Inner Barrel layer by layer with air injected at 10 m s^{-1} inside the triangular ducts and 14°C	56
3.9	Impinging jet air cooling stave scheme.	57
3.10	Location and size of the nozzles for the air jets impinging on the detector chips.	58
3.11	CFD domain used to characterise the thermal performance of the impinging jet air cooling system and the dynamic pressure drop of the air on the chips.	61
3.12	Simulated chip temperature map when impinged with an air flow rate of $8.4 \cdot 10^{-3} \text{ L s}^{-1}$ per nozzle at 14°C and two nozzle-to-chip distances, 0.2 and 1 mm.	62
3.13	Total pressure over the chip surface when impinged with an air flow rate of $8.4 \cdot 10^{-3} \text{ L s}^{-1}$ per nozzle and two nozzle-to-chip distances, 0.2 and 1 mm.	63
3.14	Total pressure on the chip surface along the axis between two consecutive jets when impinged with an air flow rate of $8.4 \cdot 10^{-3} \text{ L s}^{-1}$ per nozzle and two nozzle-to-chip distances, 0.2 and 1 mm.	64
3.15	Total air pressure at the stave enclosure central symmetry plane at a total flow rate of 1.2 L s^{-1}	64
3.16	Air mass flow rate distribution in all stave nozzles and area-averaged mean air velocity in each nozzle, at a total stave air flow rate of 1.2 L s^{-1}	65
3.17	Schematic view of the two ultra-lightweight stave architectures proposed.	66
3.18	Thermal simulation of the stave and chip temperature map in a section of the water-cooled P1 prototype.	67

3.19 Views of prototypes P1 and P2 and their connectors.	69
4.1 Schematic view of the stave heated surfaces and the location of temperature sensors. . .	74
4.2 Single-phase thermal development length for the baseline Inner and Outer Barrel staves with water and C ₄ F ₁₀ as coolants.	76
4.3 Schematic view of the experimental water loop with an Inner Barrel stave.	77
4.4 Schematic view of the experimental two-phase C ₄ F ₁₀ loop with an Outer Barrel stave. . .	78
4.5 Inner Barrel stave and Outer Barrel half-stave connected to the cooling loops at CERN. .	79
4.6 Pictures of the leak-less water plant and two-phase C ₄ F ₁₀ plant used at the facilities at CERN.	79
4.7 Experimental and theoretical heat load exchanged with the air versus the difference between the mean heater temperature and the air temperature at the P2 Inner Barrel stave prototype.	84
4.8 Heater average temperature relative to the coolant mean temperature in the stave for water and two-phase C ₄ F ₁₀ refrigerant, at 0.30 W cm ⁻² , for the P1 and P2 staves.	93
4.9 Infrared images showing the heater temperature map for experimental tests with water and evaporative C ₄ F ₁₀ refrigerant at 0.30 W cm ⁻² on the P1 and P2 prototypes.	95
4.10 Water pressure drop increase if decreasing the stave cooling channel ID from 1.450 mm to 1.024 mm.	96
4.11 Material budget of the cooling plate assembly, cooling channels, and water as coolant of the P2 prototype if decreasing the stave cooling channel ID from 1.450 mm to 1.024 mm.	97
5.1 Schematic view of the Inner Barrel high-conductivity plate plus spaceframe stave concept.	100
5.2 Comparison of the cooling performance of the three Inner Barrel stave layouts with water.	103
5.3 Influence of the channel size on the cooling performance: comparison between the P2 stave (1.450 mm ID) and the IB1 stave (1.024 mm ID).	104
5.4 Water pressure drop of the three Inner Barrel staves and water temperature rise for the IB1 stave at 0.15 and 0.30 W cm ⁻²	105
5.5 Experimental and calculated water pressure drop at the IB1 stave versus the Reynolds number.	105
5.6 Infrared images displaying the water-cooled Inner Barrel IB1 stave heater temperature map for 0.15, 0.30 and 0.50 W cm ⁻²	107
5.7 IB2 stave material budget considering water or two-phase C ₄ F ₁₀ refrigerant as coolants. .	108

5.8	Experimental and calculated pressure drop at the IB2 stave versus the Reynolds number, for single-phase C_4F_{10} refrigerant.	109
5.9	IB2 stave energy balance and mean heat transfer coefficient with single-phase C_4F_{10} refrigerant at 0.10 W cm^{-2}	110
5.10	Cooling performance of the IB2 stave when cooling with single-phase water and two-phase C_4F_{10} refrigerant at 0.30 and 0.50 W cm^{-2}	111
5.11	Cooling performance variation with the mean vapour quality of the IB2 stave with two-phase C_4F_{10} refrigerant at 0.30 and 0.50 W cm^{-2}	112
5.12	Influence of the two-phase C_4F_{10} refrigerant mass flux and vapour quality on the temperature of the six thermistors on the IB2 stave heater, normalised to the coolant temperature.	112
5.13	Experimental versus predicted two-phase C_4F_{10} refrigerant pressure drop at the IB2 stave.	113
5.14	Saturation temperature drop trend with the mean stave vapour quality and its influence on the stave temperature non-uniformity for several two-phase C_4F_{10} mass fluxes in the IB2 stave.	114
5.15	Infrared images of the IB2 heater surface when cooling with water and two-phase C_4F_{10} refrigerant at nominal cooling conditions at 0.30 and 0.50 W cm^{-2}	115
5.16	Picture of an assembled Outer Barrel stave.	116
5.17	Comparison of the cooling performance of the two Outer Barrel half-stave layouts with water.	119
5.18	Water pressure drop of the two Outer Barrel half-staves and water temperature rise for the OB1 prototype at 0.15 and 0.30 W cm^{-2}	121
5.19	Experimental and calculated water pressure drop for the OB2 half-stave versus the Reynolds number.	121
5.20	Infrared images displaying the water-cooled Outer Barrel OB1 half-stave heater temperature map at nominal cooling conditions for the 0.15 W cm^{-2} power density.	122
5.21	Comparison of the temperatures measured by the thermistors on the heaters against the maximum and average temperatures recorded by the IR camera on the OB1 half-stave at nominal cooling conditions with water at 0.15 W cm^{-2}	123
5.22	Half-stave material budget considering water and two-phase C_4F_{10} refrigerant as coolants in the OB1 and OB3 Outer Barrel half-staves, respectively.	125
5.23	Experimental heat load transferred to the air versus the difference between the mean heater temperature and the ambient air temperature for the OB3 Outer Barrel half-stave.	126

5.24	Experimental and calculated pressure drop at the OB3 half-stave versus the Reynolds number with single-phase C ₄ F ₁₀ refrigerant.	126
5.25	Energy balance and mean stave heat transfer coefficient of the OB3 half-stave with single-phase C ₄ F ₁₀ refrigerant.	127
5.26	Cooling performance of the OB3 half-stave with two-phase C ₄ F ₁₀ refrigerant as coolant at several heater power densities.	128
5.27	Comparison between the cooling performance of the OB3 half-stave when using water and two-phase C ₄ F ₁₀ refrigerant at 0.15 and 0.30 W cm ⁻²	128
5.28	Sensitivity of the OB3 half-stave cooling performance with the mean vapour quality when cooled with two-phase C ₄ F ₁₀ refrigerant.	130
5.29	Influence of the two-phase C ₄ F ₁₀ coolant inlet conditions (subcooled liquid, saturated two-phase flow) on the temperatures measured by the 14 thermistors on the OB3 half-stave heaters. Cases are reported at 0.15 W cm ⁻² and G _{C₄F₁₀} = 365 kg m ⁻² s ⁻¹	131
5.30	Predicted versus experimental two-phase C ₄ F ₁₀ pressure drop values at the OB3 half-stave.	131
5.31	Saturation temperature drop trend with the mean stave vapour quality and its influence on the stave temperature non-uniformity for several two-phase C ₄ F ₁₀ mass fluxes in the OB3 half-stave.	132
5.32	Infrared images of the OB3 half-stave heated surface when cooling with water and two-phase C ₄ F ₁₀ refrigerant at nominal cooling conditions at 0.15 W cm ⁻²	133
5.33	Experimental two-phase heat transfer coefficients compared to the predicted values by the correlation of Liu and Winterton [121] for the Inner Barrel IB2 stave (a); and the Outer Barrel OB3 half-stave (b).	135
5.34	Schematic view of the two-phase coolant inventory experimental setup.	137
5.35	Technical drawings of the OB3 inlet/outlet connector and the Π-bend connecting the two polyimide channels.	138
5.36	Measured single-phase, adiabatic coolant inventories versus predicted values.	141
5.37	Measured two-phase coolant inventories versus predicted values from integrating void fraction methods from the literature along the cooling channels.	144
5.38	Experimental and predicted values of the two-phase C ₄ F ₁₀ coolant charge versus the mean vapour quality.	145
5.39	Absolute and relative deviations of the theoretical refrigerant charge values from the experimental measurements for the mean vapour quality range.	145
6.1	Schematic view of the test rig (not scaled).	152

6.2	A picture of the test rig assembled in the experimental facilities, with a detailed view of the outlet visualisation section.	153
6.3	Single-phase thermal entry length for the R245fa refrigerant in the 2.3 mm ID pre-heater versus R245fa mass flux in the pre-heater.	154
6.4	Micropictures of a section of the polyimide tube used in the experimental studies.	156
6.5	CFD simulation of the heating water flow thermal stratification.	159
6.6	Two-phase loop (adapted from [103]) and heating water circuit schemes.	159
6.7	Different ways of calculating the heat flux: as a constant or linear along the polyimide channel.	161
6.8	Water-water thermal resistances vs. annulus Reynolds number.	165
6.9	Comparison between the experimental single-phase R245fa pressure drop and the values obtained with correlations.	167
6.10	Single-phase energy balances at the pre-heater and the test section (polyimide tube).	168
6.11	Single-phase heat transfer coefficient in the polyimide channel: comparison between predictions and experimental values calculated from the heat loads measured in the water and the R245fa flows.	169
6.12	Experimental, theoretical (frictional and momentum pressure gradient), and singular two-phase adiabatic pressure drops for the R245fa refrigerant in the test rig versus mean vapour quality.	170
6.13	Theoretical versus the experimental pressure drop in several two-phase flow diabatic cases.	172
6.14	Repeatability of the diabatic two-phase flow boiling experimental tests.	174
6.15	Two-phase flow stratification recorded at the 2.1 mm ID visualisation section, at $G=200 \text{ kg m}^{-2} \text{ s}^{-1}$, $x=0.05$, $T_{sat}=35^\circ\text{C}$	175
6.16	Influence of the mass flux on the heat transfer coefficient. High-speed flow images of the four points with the highest vapour qualities at the lowest mass velocity are displayed illustrating the captured partial dryout conditions.	176
6.17	Influence of the mass flux on the mean heat transfer coefficient at two different saturation temperatures, 35 and 41°C.	177
6.18	Influence of the mass flux on the mean heat transfer coefficient versus the inlet, outlet and mean vapour quality in the polyimide tube, at $q_{ts,m}=25 \text{ kW m}^{-2}$ and $T_{sat}=35^\circ\text{C}$	177
6.19	Effect of the heat flux on the mean heat transfer coefficient, plotted against the mean vapour qualities, and the inlet and outlet vapour qualities in the polyimide channel.	178

6.20	Effect of the heat flux on the mean heat transfer coefficient plotted against the mean vapour quality at $G=400 \text{ kg m}^{-2} \text{ s}^{-1}$ and saturation temperatures of 35 and 41°C.	179
6.21	Effect of the saturation temperature on the mean heat transfer coefficient, versus the mean vapour quality in the test section.	180
6.22	Comparison of the experimental data taken in the present work with similar experimental studies with R245fa in a 2.3 mm ID stainless steel channel.	181
6.23	Influence of the mass flux on the heat transfer coefficient as computed by the methods from the literature, compared to the experimental data, at $q_{ts,m}=45 \text{ kW m}^{-2}$ and $T_{sat}=47^\circ\text{C}$	183
6.24	Influence of the heat flux on the heat transfer coefficient as computed by the methods by Liu and Winterton [121] and Cioncolini and Thome [130], compared to the experimental data, at $G=400 \text{ kg m}^{-2} \text{ s}^{-1}$ and $T_{sat}=41^\circ\text{C}$	183
6.25	Influence of the saturation temperature on the heat transfer coefficient as computed by the methods by Liu and Winterton [121] and Cioncolini and Thome [130], compared to the experimental data, at $G=300 \text{ kg m}^{-2} \text{ s}^{-1}$ and $q_{ts,m}=25 \text{ kW m}^{-2}$	184
6.26	Comparison of the experimental data with four heat transfer coefficient prediction methods in the literature at different conditions.	185
A.1	Ratio of the equivalent length and the channel diameter with the same pressure drop as that of a 90° bend.	196
B.1	Schematic view of the hoop stress in a thin-walled tube for internal positive gauge pressures and negative ones (sub-atmospheric).	215
B.2	Experimental burst failures in the Inner and Outer barrel staves.	217
B.3	Material budget of the OB1 stave with 2.052 mm ID channels with wall thicknesses of 32 μm and 60 μm , and water as coolant.	221
B.4	Overview of the long-term water circulation experimental facility.	223
B.5	Comparison of OM and SEM images at the same location in one sample.	227
B.6	SEM images of two samples from specimens 0 and 2.	228
B.7	SEM images of the inner surface local smoothing in specimen 2.	228
B.8	OM images of the inner surface of the two central samples from specimens 1 and 2.	229

List of Tables

2.1	Material budget value of a selection of solid materials assuming a 1 mm thickness	11
2.2	Material budget value of two refrigerants assuming a 1 mm thickness.	12
2.3	Structural CFRP material properties.	18
2.4	Thermal and mechanical properties of a selection of conductive CFRPs and and graphite foils.	20
2.5	Average material budget comparison of a 2.1 mm ID, 2.4 mm OD cylindrical channel made of different materials.	24
3.1	Architecture, power dissipation and radiation doses of the Inner, Middle and Outer Barrel.	50
3.2	Airflow characteristics of the layer-by-layer cooling proposal in a single triangular duct.	54
3.3	Analytical thermo-hydraulic characteristics of the impinging jet air cooling proposal for a single stave and three different nozzle array geometries.	60
3.4	Weight and material budget of the P1 and P2 prototypes.	70
3.5	Thermodynamic properties and X_0 of the coolants considered for the ITS Upgrade at 15°C.	72
4.1	Free convection heat exchange of the ITS Upgrade staves with the environment for several temperature differences between the plate and the air.	81
4.2	Radiative heat exchange of the ITS Upgrade staves with the environment for several temperature differences between the plate and the room or the neighbour staves.	82
4.3	Total heat exchange of the ITS Upgrade staves with the environment for staves at the sides of the Barrels assuming they are in a big room, for several temperature differences between the plate and the air.	82
4.4	Radiative heat transfer from the beam pipe at 40°C to each stave in the innermost Inner Barrel layer (layer 0), for several stave temperatures.	83
4.5	Type B uncertainties of the measured experimental variables.	91
4.6	Global uncertainties of the two-phase flow parameters.	92
4.7	Nominal cooling conditions for prototypes P1 and P2 at 0.30 W cm ⁻² with water.	94

4.8	Nominal cooling conditions for staves P1 and P2 at 0.30 W cm^{-2} with evaporative C_4F_{10} refrigerant.	94
4.9	Weight and material budget of the P2 prototype and the optimised IB1 stave.	97
5.1	Inner Barrel stave prototypes subjected to experimental cooling tests.	101
5.2	Nominal cooling conditions for the IB1, IB2 and IB3 prototypes at 0.15 W cm^{-2} with water.	106
5.3	Nominal cooling conditions for prototype IB1 with water at a flow rate of 3 L h^{-1} and power densities of $0.15, 0.30$ and 0.50 W cm^{-2}	107
5.4	Material budget of the IB2 stave with water and two-phase C_4F_{10} as coolants.	108
5.5	Nominal cooling conditions with evaporative C_4F_{10} refrigerant for the IB2 stave at 0.30 and 0.50 W cm^{-2}	115
5.6	Outer Barrel half-stave prototypes subjected to experimental water cooling tests.	117
5.7	Nominal cooling conditions for the OB1 half-stave with water at power densities of 0.15 and 0.30 W cm^{-2}	122
5.8	Outer Barrel OB3 half-stave developed for experimental two-phase cooling tests with C_4F_{10} refrigerant as coolant.	124
5.9	Material budget comparison between the OB1 half-stave with water and the OB3 half-stave with two-phase C_4F_{10} as coolant.	125
5.10	Average heat load transferred to the boiling C_4F_{10} refrigerant at the OB3 half-stave for the different power densities considered in the two-phase flow tests.	127
5.11	Five experimental cooling cases with boiling C_4F_{10} refrigerant for the OB3 half-stave at 0.15 W cm^{-2}	133
5.12	Four study cases with the predicted two-phase C_4F_{10} coolant inventory for the OB3 half-stave.	139
5.13	Influence of the inlet and outlet vapour quality variations on the predicted two-phase C_4F_{10} coolant inventory, for the OB3 half-stave at 0.15 W cm^{-2}	139
5.14	Statistical deviation parameters from the comparison of the charge predictions and the experimental values.	145
6.1	Thermophysical properties of C_4F_{10} and R245fa refrigerants at saturation temperatures of 15°C and 41°C	151
6.2	Dimensions and tolerances of the polyimide channel.	156
6.3	Summary of the conditions in the water-water tests and the experimental results of the thermal resistance of conduction across the polyimide channel wall.	166

6.4	Mean absolute error (<i>mae</i>) of the heat transfer coefficient between the water and the polyimide tube outer wall in the annulus given by four heat transfer correlations with respect to the experimental values.	167
6.5	Statistical analysis of the comparison between experimental and calculated two-phase pressure drops for the different methods used for evaluating the frictional component.	172
6.6	Experimental uncertainty of the measured variables.	173
6.7	Global uncertainties of the two-phase flow parameters at the experimental setup in EESC-USP.	173
6.8	Statistical analysis of the comparison between experimental and predicted mean two-phase flow boiling heat transfer coefficients in the polyimide channel.	182
B.1	Dimensions of the polyimide channels used in the ITS Upgrade staves.	214
B.2	Mechanical properties of the polyimide channels.	214
B.3	Hoop stresses and predicted increases of the inner diameter for all the polyimide channels used in the ITS Upgrade under positive gauge pressures.	216
B.4	Analytical, nominal, and measured burst pressures in the polyimide channels used in the ITS Upgrade.	217
B.5	Pressure difference between the external and internal tube surfaces ($\Delta p_{collapse}$) resulting in collapse of the polyimide channels of the ITS Upgrade staves, predicted by theoretical and analytical methods.	219
B.6	Pressure difference between the external and internal tube surfaces ($\Delta p_{collapse}$) resulting in collapse of the recommended polyimide channels with thicker walls, predicted by theoretical and analytical methods.	220
B.7	ITS Upgrade stove material budget if increasing the wall thicknesses of the the polyimide channels to the recommended values guaranteeing no channel collapse.	221
B.8	Test specimens, current status and total time of water circulation.	225
C.1	Thermophysical properties of the C ₄ F ₁₀ refrigerant.	232
C.2	Thermophysical properties of the R245fa refrigerant.	232
D.1	Calibration uncertainty parameters and correction constants for the temperature measurements.	236

List of Symbols

Roman Symbols

A_N	neutron number	
A	area	[cm ² , m ²]
CHF	Critical Heat Flux	[kW m ⁻²]
c_p	specific heat at constant pressure	[J kg ⁻¹ K ⁻¹]
CTE	Coefficient of Thermal Expansion	[K ⁻¹]
D	diameter	[m]
D_h	hydraulic diameter	[m]
df	degrees of freedom of a data distribution	[-]
E	heat load	[W]
E_y	Young modulus	[GPa]
e	entrained liquid fraction	[-]
$errA$	type A uncertainty	[dim]
$errB$	type B uncertainty	[dim]
F	two-phase convective multiplier	[-]
G	mass flux	[kg m ⁻² s ⁻¹]
g	gravity acceleration	[m s ⁻²]
h	heat transfer coefficient	[W m ⁻² K ⁻¹]
i	enthalpy	[J kg ⁻¹]
k	coverage factor defining a specific confidence interval of the uncertainty	[-]
L	length	[m]
mae	mean absolute error; $mae = \frac{1}{n} \sum_{i=1}^n \left \frac{X_{pred} - X_{exp}}{X_{exp}} \right $	[%]
mre	mean relative error; $mre = \frac{1}{n} \sum_{i=1}^n \frac{X_{pred} - X_{exp}}{X_{exp}}$	[%]

M	mass/coolant inventory	[g]
\dot{m}	mass flow rate	[kg s ⁻¹]
P_d	power density	[W cm ⁻²]
P	calibration precision coefficient	[dim]
p	pressure	[bar, kPa]
p_{crit}	critical pressure	[bar, kPa]
p_r	reduced pressure; $p_r = \frac{p}{p_{crit}}$	[-]
q	heat flux	[kW m ⁻²]
r	radius	[m]
R_a	average absolute surface roughness	[mm]
R	thermal resistance	[K W ⁻¹]
S	nucleate boiling suppression factor	[-]
SC	subcooling	[K]
SD	standard deviation of the measurements	[dim]
T	temperature	[°C]
T'	temperature	[K]
U	expanded uncertainty	[dim]
u	velocity	[m s ⁻¹]
\dot{V}	volumetric flow rate	[L h ⁻¹]
V	volume	[m ³]
ν	specific volume	[m ³ kg ⁻¹]
w	channel wall thickness	[m]
x	material thickness across particles go through in a particle detector	[cm]
x	vapour quality	[-]
X_0	radiation length	[cm]
X_{tt}	Lockhart-Martinelli parameter	[-]
Z	atomic number	[-]

Greek Symbols

α	thermal conductivity	[W m ⁻¹ K ⁻¹]
β	isobaric volume expansion coefficient	[K ⁻¹]

γ	surface tension	$[\text{N m}^{-1}]$
ϵ	emissivity	$[-]$
ε	two-phase refrigerant void fraction	$[-]$
ζ	Darcy friction factor, also called drag coefficient or coefficient of fluid resistance	$[-]$
κ	thermal diffusivity	$[\text{m}^2 \text{s}^{-1}]$
λ	strain	$[-]$
μ	dynamic viscosity	$[\text{Pa s}, \mu\text{Pa s}]$
ν	kinematic viscosity	$[\text{m}^2 \text{s}^{-1}]$
ν_P	Poisson ratio	$[-]$
φ	fraction of experimental data with error in a certain range	$[\%]$
ρ	volumetric mass density	$[\text{kg m}^{-3}]$
σ	stress	$[\text{Pa}, \text{kPa}]$

Subscripts

<i>air</i>	to/from ambient air
<i>ann</i>	annulus
<i>cond</i>	conduction
<i>conv</i>	convection
<i>cb</i>	convective boiling
<i>exp</i>	experimental
<i>e</i>	external
<i>frict</i>	frictional
<i>heated</i>	heated (length/section)
<i>in</i>	inlet
<i>i</i>	inner
<i>int</i>	internal
<i>lat</i>	lateral, for areas of tubes
<i>l</i>	liquid
<i>lv</i>	liquid-vapour
<i>LO</i>	Liquid-Only (all two-phase flow as liquid)
<i>m</i>	mean

<i>meas</i>	measured
<i>mom</i>	momentum
<i>nc</i>	natural/free convection
<i>net</i>	net (power, heat load)
<i>nb</i>	nucleate boiling
<i>out</i>	outlet
<i>pred</i>	predicted
<i>ph</i>	pre-heater
<i>rad</i>	radiative heat transfer
<i>ref</i>	reference
<i>sat</i>	saturation, or in saturated conditions
<i>sp</i>	single-phase
<i>sing</i>	singular
<i>ts</i>	test section
<i>tp</i>	two-phase
<i>v</i>	vapour
<i>VO</i>	Vapour-Only (all two-phase flow as vapour)
<i>wall</i>	wall

Dimensionless numbers

<i>Bo</i>	boiling number	$\left(Bo = \frac{q}{i_{lv}G}\right)$
<i>Bd</i>	Bond number	$\left(Bd = \frac{g(\rho_l - \rho_v)D_i^2}{\gamma}\right)$
<i>Co</i>	Confinement number	$\left(Co = \sqrt{\frac{\gamma}{g(\rho_v - \rho_l)D_i^2}}\right)$
<i>C</i>	convective number	$\left(C = \left(\frac{\rho_v}{\rho_l}\right)^{0.5} \left(\frac{1-x}{x}\right)^{0.8}\right)$
<i>Fr</i>	Froude number	$\left(Fr = \frac{G^2}{gD\rho^2}\right)$
<i>Nu</i>	Nusselt number	$\left(Nu = \frac{hD}{\alpha}\right)$
<i>Pr</i>	Prandtl number	$\left(Pr = \frac{c_p\mu}{\alpha}\right)$
<i>Ra</i>	Rayleigh number	$\left(Ra = \frac{g\beta(T_{wall} - T_{\infty})L^3}{\nu\kappa}\right)$
<i>Re</i>	Reynolds number	$\left(Re = \frac{GD}{\mu}\right)$
<i>We</i>	Weber number	$\left>We = \frac{G^2D}{\gamma\rho}\right)$

List of Acronyms

ALICE A Large Ion Collider Experiment

ATLAS A Toroidal LHC Apparatus

CERN European Center for Nuclear Research

CFD Computational Fluid Dynamics

CFRP carbon fibre-reinforced polymer

CMS Compact Muon Solenoid

DAQ Data Acquisition System

FC fluorocarbon

GWP Global Warming Potential

HEP High Energy Physics

ID Inner Diameter

ITS Inner Tracking System

LHC Large Hadron Collider

LS2 Long Shutdown 2

MAPS Monolithic Active Pixel Sensors

MB Material Budget

NIEL Non-Ionising Energy Loss

NTC Negative Temperature Coefficient

OD Outer Diameter

OM Optical Microscopy

PEEK	polyether ether ketone
PTFE	polytetrafluoroethylene
QGP	Quark Gluon Plasma
SEM	Scanning Electron Microscopy
TID	Total Ionising Dose
TPG	Thermal Pyrolytic Graphite

Chapter 1

Introduction

A Large Ion Collider Experiment (ALICE) is a heavy-ion detector apparatus at the European Center for Nuclear Research (CERN) Large Hadron Collider (LHC) focused on the Quark Gluon Plasma (QGP), the strong interaction sector of the Standard Model [1]. The ALICE apparatus consists of 18 High Energy Physics (HEP) detectors, most of them arranged concentrically around the beam pipe, the central duct inside which heavy ion beams, previously accelerated by the LHC, collide. In view of the LHC Phase-1 upgrade towards full design luminosity, planned for the Long Shutdown 2 (LS2) in 2019 [2], studies are ongoing at CERN to significantly improve the detection performance of the various LHC experiments, such as A Toroidal LHC Apparatus (ATLAS), the Compact Muon Solenoid (CMS) [3], and ALICE.

The Inner Tracking System (ITS) is the innermost HEP detector at ALICE. The goal of this vertex detector is to identify the decay phenomena of heavy particles after the collisions of the beams by recording accurately the location where they occur. An upgrade of the ITS detector is foreseen during the LS2, and a R&D program, covering all aspects of the detector (physics, electronics, integration, and lightweight mechanical and cooling systems) was launched: the ITS Upgrade Project. The upgrade of the ITS regards the replacement of the current silicon tracker with a new one [4], consisting of seven layers of more advanced silicon tracking detectors, presumably based on Monolithic Active Pixel Sensors (MAPS) technology. With coverage in radiuses from 22 mm to 400 mm from the interaction point and 10 m^2 of sensitive surface, the ITS Upgrade detector will be a 12.5 Giga-pixel “camera”, reading individual collisions at frequencies from 100 to 400 kHz. Accordingly, the design and implementation of a cooling system is foreseen as part of the ITS Upgrade project, in parallel to other activities, such as the physics scope development, the mechanics and electronics engineering, and services integration [5], and this is precisely the primary goal of the work described in this thesis. A dedicated mechanics and cooling working group has been developing and engineering solutions converging to the best practical arrangement from the points of view of detector resolution and operation.

The strictest requirement the ITS Upgrade cooling system must fulfil is that it should be lightweight. The amount of material inside the detector is quantified through the *material budget*, as described in section 2.2.3. This parameter accounts for the thickness, density, and atomic number of the different materials in the detector. The lower the material budget is, the better the tracking performance and momentum resolution of the detector are. On the other hand, the thermal requirements are not extreme: the detector chips must remain below 30°C at a maximum power density of 0.15 W cm⁻².

Each detector layer will be divided azimuthally into individual modules, named *staves*, which support and cool the silicon chips, circuit boards, and cables. The staves display different sizes: those closer to the beam pipe display a chip surface of 270 × 15 mm, while staves at the Outer Layer are each subdivided in two half-staves, each with chip surfaces up to 1475 × 30 mm. In total, there will be 346 independent staves and half-staves in a compact arrangement, especially at the innermost layers.

During the initial R&D phase, several cooling system concepts will be explored analytically and using Computational Fluid Dynamics (CFD) simulations, such as air cooling systems. Due to the extreme material budget limitations, the staves will require embedded, lightweight, on-detector cooling systems. Thin, non-metallic materials with low density and low atomic number (low-*Z*) are prioritised. The systems presented in this dissertation innovate in this direction, with the use of polyimide cooling channels in high thermal conductivity carbon fibre–reinforced polymer (CFRP) structures, allowing for extremely lightweight staves. Prototypes of the best designs will be manufactured and their cooling performance characterised experimentally with single- and two-phase refrigerants. Finding the array of cooling conditions providing the best compromise between all the ITS Upgrade requirements is the main target, quantifying the heat exchange with the ambient and the stave temperature non-uniformity.

Two-phase coolants are advantageous not only thermally, but also from the material budget point of view. The presence of a vapour phase, less dense than the liquid, results in a lower material budget and an overall lighter system. However, no consensus was found to calculate the material budget of a two-phase refrigerant. An experimental study will be conducted on an Outer Barrel half-stave to determine experimentally the two-phase coolant inventory and verify the validity of void fraction prediction methods that are used in the two-phase coolant material budget calculation.

Last, no data was found in the literature regarding flow boiling heat transfer in polyimide channels. A specific study, aimed to measure experimentally the mean flow boiling heat transfer coefficients in a small polyimide channel, will be presented. The facilities at CERN are not accurate enough to conduct these measurements, so this work was performed at the Heat Transfer Research Group (HTRG) lab at the Escola de Engenharia de São Carlos, University of São Paulo (EESC-USP), Brazil, with the support of the Swiss National Science Foundation (SNSF) through a Doctoral Mobility fellowship (project number 155264).

N.B.: This dissertation is written in long form so as to be a go-to reference at CERN for HEP pixel detector cooling systems. Please excuse the length of the document.

1.1 Objectives

The aim of this project is to design, develop, qualify and integrate a reliable lightweight cooling system for the Upgrade of the Inner Tracking System (ITS) of the ALICE Experiment at CERN. The main objectives of the project are the following:

- Benchmark different cooling proposals.
- Optimisation of the most promising solutions, towards the goal of meeting both the thermal and the material budget requirements using innovative high-conductivity, lightweight materials.
- Validate experimentally the cooling performance of the optimised stave cooling systems under operational conditions, for single-phase and evaporative coolants.
- Determine experimentally the inventory of an evaporative coolant in different operation conditions, comparing it with values obtained from integrating the void fractions obtained from prediction methods in the literature.
- Study the experimental mean flow boiling heat transfer coefficients and two-phase pressure drops of an evaporative coolant inside a small polyimide channel ($D_i < 3$ mm), comparing the results to methods in the literature.
- Provide the ITS Upgrade collaboration with a recommended lightweight cooling system as the project's final deliverable.

1.2 Layout of the chapters

Chapter 2 summarises the cooling and material requirements of HEP particle detectors, the current cooling systems, some general guidelines on material selection, and a brief literature survey on two-phase flow boiling in horizontal small channels.

Chapter 3 addresses the ITS Upgrade cooling system requirements. The different cooling solutions studied are outlined, focusing on the ultra-lightweight stave concepts finally optimised and tested.

In chapter 4, the experimental facilities used in the thermal tests at CERN, the methodology and the data reduction procedures are presented. Also, experimental results on the most promising lightweight cooling architectures are reported, as well as the actions taken for optimising their design.

Chapter 5 is devoted to the experimental cooling performance results for three Inner Barrel staves and three Outer Barrel half-staves with water and two-phase C_4F_{10} refrigerant. Results regarding the experimental measurements of the two-phase coolant inventory are discussed.

Chapter 6 is dedicated to the flow boiling heat transfer and two-phase pressure drop experimental studies in a small polyimide channel. Results are analysed parametrically with the two-phase flow parameters, and compared to heat transfer methods and similar experimental results in the literature.

Chapter 7 presents the conclusions of the project and recommendations.

Chapter 2

State of the art and literature survey

2.1 Introduction

This chapter is written in four parts: first, the fundamentals and general cooling requirements of HEP particle detectors cooling systems are introduced, followed secondly by a critical review on the most representative cooling systems used historically in HEP detectors. In the third part, a practical survey on structural and cooling materials used in HEP detectors is presented. The chapter ends with a literature review on two-phase flow boiling in horizontal small channels, with specific focus on two-phase HEP detector cooling systems to be address here.

2.2 Fundamentals of High Energy Physics particle detectors

2.2.1 Silicon detectors for High Energy Physics

A large fraction of the HEP particle detectors have active detection systems based on the ionisation of a continuum by particles originated in the collision of two beams of particles. It is often the case that such a continuum is a gas, although solid-state ionisation chambers have drawn substantial attention for specific detection tasks in the last decades. Silicon detectors constitute an excellent example of solid-state ionisation detectors, thanks to their structure of semiconductors. Its relevance not only comprises HEP particle detection applications but also other fields in industry, such as digital photography, where CCD and CMOS sensors are nowadays ubiquitous.

Generally speaking, silicon detectors in HEP are made by doping thin strips of silicon (50 to 200 μm thick) and transforming them into semiconductor diodes. Diodes are electronic devices with ideally

no resistance to current in one direction and infinite resistance in the opposite. Silicon diodes are made of two types of silicon, one that accepts electrons (named p-silicon) and other that has an excess of electron donors (named n-silicon). A junction between these two materials is what makes the diode.

If no electric potential is applied to a diode, it is unbiased. In that situation, a thin region existing between the n- and p-silicon remains devoid of available charge carriers and acts as an insulator, preventing current flow. This thin layer is known as the depletion region. When an external potential is applied in a way that current flow is permitted, the diode is forward biased. In that case, the depletion region becomes thinner until finally collapsing after a threshold potential, the forward voltage, is surpassed. In Fig. 2.1, this voltage is considered to be 0.7 V. Once exceeded, current will flow through with almost no resistance.

The opposite polarity prohibits current circulation and it is known as reverse bias. In an unbiased diode the depletion region gets thicker, resisting current circulation through it. However, a very small amount of current can and does go through a reverse-biased diode. It is called the leakage current. It can be seen at the left side of the plot in Fig. 2.1. As the external reverse-bias increases, the depletion insulating region becomes thicker. The external bias voltage at which the whole length of the diode is depleted is called the full depletion voltage. Finally, the ability of a diode to withstand reverse-bias voltages is limited. If the applied reverse-bias voltage becomes too great, over a threshold known as the breakdown voltage, the diode will collapse into a condition where current will flow through with no resistance (see Fig. 2.1). A full comprehensive review on semiconductor theory is given in [6].

Silicon detectors are reversely biased semiconductor diodes. Thus, as charged particles pass through the silicon strips, they leave behind ionisation charges that can be measured and used in HEP experiments. Only when the full depletion voltage is exceeded can all the created charge be collected. Therefore, arranging thousands of these detectors around a collision point in a particle accelerator gives an accurate picture of the paths the particles take. Silicon detectors have a much higher resolution in tracking charged particles than older technologies such as cloud chambers or wire chambers. This

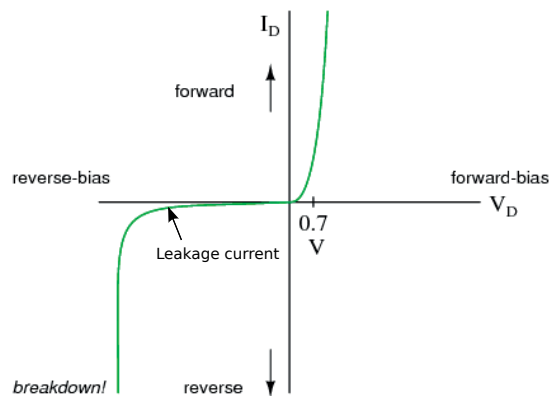


Figure 2.1: Generic diode curve.

is one of the reasons why silicon detectors are widely used as active elements in vertex detection systems. In such special HEP particle detectors (vertex detectors), the silicon detector modules are generally located close to the primary interaction point, or primary vertex, tracking particle trajectories and extrapolating them towards the primary interaction point or towards other regions of interest. Secondary and higher order vertexes are located depending on the precision of the detector. A general schematic view on the arrangement in concentric cylindrical layers of a silicon tracking device around the beam pipe is shown in Fig. 2.2a. Particle trajectories are reconstructed as displayed in Fig. 2.2b.

Signal retrieval is done by connecting the silicon chips to a power bus driving the signal to the electronics. Such connection operation is normally made using a metal between the chip and the cable at several points. One broken connecting spot would immediately increase currents in others nearby, leading to early detector failure. This suggests that minimal temperature gradients should be kept in each chip in order to minimise thermoelastic effects which could lead to chip-bus connection failure.

Several arrangements of the semiconductor structure -the p-implantation on the n-type silicon- are possible, resulting in a variety of architectures differing in resolution, energy ranges, readout frequencies and other detector parameters. Silicon strips, pads and pixels, to name a few, are detector architectures used in current particle detectors. Pixels are compact, single-sided detectors, presumably to be used in the ALICE ITS Upgrade underway at CERN, the detector of interest in this work.

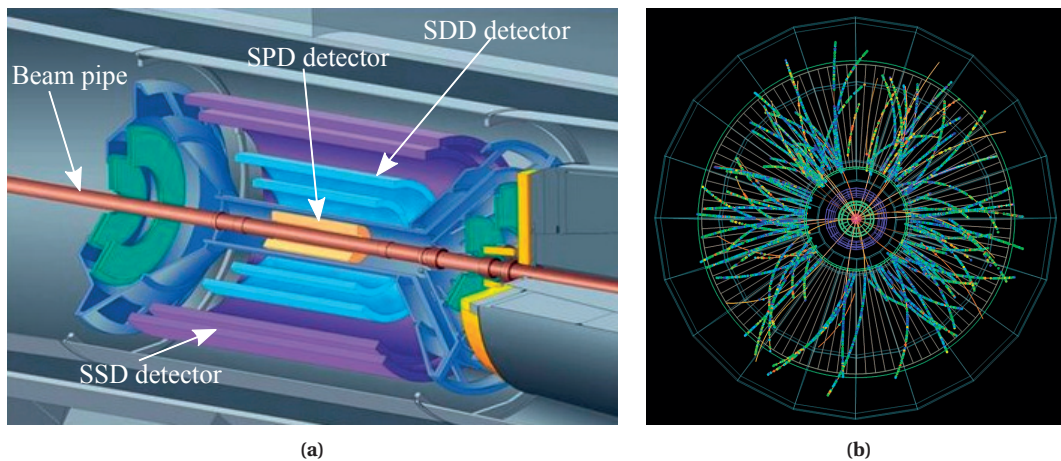


Figure 2.2: Two views of the present ALICE ITS detector: (a) the Silicon Pixel Detector (SPD), Silicon Drift Detector (SDD) and the Silicon Strip Detector (SSD) are disposed around the central beam pipe; (b) sample picture of particle trajectories at the ALICE Experiment. The ITS detector sits at the centre of the experiment.

2.2.2 Radiation in particle detectors

The need for cooling

When a charged particle traverses a silicon detector module, as depicted in Fig. 2.2b, it produces an ionising and a non-ionising energy loss. The magnitude of these two components is quantified through the Total Ionising Dose (TID) and the Non-Ionising Energy Loss (NIEL), respectively. The ionising component creates electron-hole pairs in the semiconductor. Once this external bias exceeds the full depletion voltage, all charge can be collected and processed, producing the signal relevant to the physics of the experiment. As detectors are reversely biased, a leakage current of small magnitude is always present during operation. Normally, the break-through voltage is higher than the full depletion voltage, so the detector would not, in theory, run into failure easily.

On the other hand, NIEL refers to the energy loss of charged particles coming from the interaction point due to the absorptivity of the materials in the detectors. It results in radiation damage to the detector. Silicon detectors are damaged by charged and neutral particles. Charged particles mainly damage the bulk material, while neutral particles damage surface structures. At a given bias voltage, the current across the silicon, I , is defined as in Eq. 2.1, being I_0 the ionising current (useful for the physics), I_d the leakage current, and Φ the radiation dose:

$$I = I_0 + I_d \cdot \Phi \quad (2.1)$$

The immediate consequence of radiation damage is that the leakage current rapidly increases, even for low radiation doses. Therefore, the signal-to-noise ratio decreases, resulting in a noisy output current and low detector resolution. At the same time, the depletion voltage to be applied in order to get the whole charge out of the detector increases and could eventually approach the break-through threshold. Ultimately, this magnification will lead to thermal runaway phenomena of the silicon sensors, and, as a result, unstable, unreliable detector operation, and even the destruction of the sensitive parts [7].

A damaged detector cannot be repaired; there is an integral dose of radiation the silicon detector can receive throughout its life before becoming inoperative and it is accounted for in the design stage. There are no radiation hard silicon detectors either. Cooling helps hereby reducing the leakage current magnitude, therefore prolonging the detector's life. Indeed, the leakage current produced in the bulk of a detector sustaining radiation damage at room temperature can be decreased by a factor 2 by decreasing its temperature by 7 K. Therefore, a cooling system is essential in a silicon particle detector to guarantee resolution and preventing noise in measurements throughout detector's life. Additionally, it is used to remove the heat load dissipated by electronics and readout structures.

Effects of radiation on materials

Radiation may not only damage the detector but may also interact with the rest of the parts involved in its construction and services, such as the mechanical and cooling structures. All of these should withstand the expected radiation levels without experiencing composition changes, chemical reactions, or physical damage throughout the life of the machine. Not only the reliability of the device is at stake, but also the safety of the staff and the facilities. Thus, materials that have a high *radiation hardness*, i.e. that withstand severe radiation levels without deteriorating, are preferred.

Typical effects resulting from the interaction of radiation with matter are:

- Alteration of the physical properties: mechanical and electrical properties may be affected by radiation doses. Considerable increases in thermal conductivity have been reported on different polymers after exposure to radiation [8]. Irradiation may induce accelerated ageing of some materials, with its properties rapidly degrading in time. Some types of carbon fibre composites experience premature ageing in radioactive environments, in particular the resins in CFRPs [9].
- Modification of the morphology of the material, especially its surface and crystallinity. Consequences are, among others: altered yield and tensile strength, abrasion resistance, hardness, and porosity. Some adhesives used in precision assemblies are known to experience weaker adhesion to surfaces [10].
- Radiolysis: dissociation of molecules by action of nuclear radiation. It is similar to photolysis, but irradiation is associated to radioactive decay. Products of radiolysis can be very reactive and dangerous for the detector and technical staff. For instance, a particular coolant might dissociate into different substances not compatible with the piping, and eventually cause leaks or obstructions in the cooling system. Studies have been conducted at CERN to qualify coolants and cooling channels for particle detectors [11].
- Chemical reactions: highly reactive substances may arise from radiolysis and interact with other substances. Refrigerants used as coolants having a high content in hydrogen and weak chemical bonds lose hydrogen atoms, which may recombine to form acids within the cooling flow, potentially corrosive to the cooling channels. Another possibility is that hydrogen atoms group as molecular hydrogen gas, highly explosive. Ozone is a typical product of radiolysis and is known to damage polyether ether ketone (PEEK). Usually, radiation levels in particle detectors are low enough to allow online purification and deionisation of an already high-radiation resistance irradiated cooling fluid.
- Deposition of substances derived from radiation damage, altering thermal resistances, obstructing cooling piping or transforming surfaces.

Being a subject of great interest in a large range of scientific fields, there are a great number of

compendiums and technical reports from institutions around the world regarding radiation damage and radiation compatibility of numerous engineering materials and fluids. CERN has collected information from extensive radiation damage testing of most engineering materials and fluids: cable insulating materials [12, 13], thermosetting and thermoplastic resins [14], composites [15], adhesives [10] and materials typically used in particle detectors [16]. This provides practical guidelines on material selection depending on the expected irradiation levels and compatibility with other materials. This large database expands continuously as new experiments are carried out in test beams and other facilities simulating radiation conditions to be expected in the particle detectors [17, 18].

Finally, CERN has safety instructions and regulations regarding the use of plastics and other non-metallic materials with respect to fire safety and radiation resistance [19]. The inviolability of this document determines ultimately the material selection for new particle detectors and its services at CERN.

2.2.3 Material budget

Typically, HEP vertex detectors do not involve high heat fluxes (values of 2 W cm^{-2} are rarely exceeded) nor extreme temperatures (detectors usually operate at a fixed temperature ranging from -25°C to 30°C). These design parameters are well below the high heat flux applications of power electronics that most advanced two-phase cooling systems are nowadays attempting to deal with. However, there is an extremely strict requirement unique to particle detectors which drives almost entirely the concept and design of the cooling system: the Material Budget (MB).

Resolution is one of the most important design targets in HEP particle detectors. It essentially depends on the technology and architecture of the silicon detector, and on the read-out technology. However, the actual resolution of a silicon detector system is usually not limited by the intrinsic resolution of the sensors. Particularly, the main limitation of vertex detector resolution comes from the presence of materials which are necessary for the detector's structural and operational needs, such as the beam pipe, mechanical structures, cooling, and the detector itself. Any object introduced in the sensitive area of the detector across the paths of the particles coming from the interaction point (the centre of the detector), causes multiple particle scattering, negatively affecting the detector's resolution. This negative effect highly depends on the type of material, and it is amplified in multi-layered detectors.

The following mathematical expression quantifies the material inventory in the detection area: the material budget (MB):

$$\text{MB} = \frac{x}{X_0} 100 [\%] \quad (2.2)$$

where x is the material thickness a particle coming from the interaction point would cross, and X_0 is the material radiation length, a characteristic that only depends on the kind of material and its physical state, and is related to energy loss of electromagnetic-interacting particles in the material. X_0

is calculated as follows:

$$X_0 = \frac{716.4 A_N}{Z(Z+1) \ln \frac{287}{\sqrt{Z}} \rho} [cm] \quad (2.3)$$

where X_0 depends on the atomic and mass numbers (Z and A_N , respectively) and on the material volumetric mass density, ρ .

Therefore, in order to minimise the material budget, thin, high- X_0 materials (also called *low-Z* materials) are preferred within the detector's sensitive zone. In other words, mechanical structures and cooling systems should be composed of low-atomic number, lightweight materials, tubes and refrigerants, especially at the innermost detector layers, where a maximum resolution is needed.

The material budget restriction in HEP particle detectors clashes with the designs of classic cooling technologies. Usually, cooling systems are made of standard industrial elements which involve thicknesses in the range of millimetres and, more importantly, metallic materials, since they are highly thermally conductive, mechanically robust, cheap and machinable. Such materials, like copper, aluminium and stainless steel cannot be used to build structures or cooling systems for HEP particle detectors with material budget restrictions. Table 2.1 provides a clear view on the influence of the kind of material in the material budget (x/X_0) for a selection of typical cooling engineering materials, including a CFRP. A value of $x=1$ mm thickness was chosen for calculating the material budget.

Minimising the material inventory per layer has become one of the main goals when conceiving HEP silicon detectors [4]. Extensive R&D is being carried out aiming towards new detection materials [20], thinning of silicon chips, electronics and, fundamentally, towards minimum material budget for the cooling systems and mechanical structures. Stricter material budget limits are imposed as detection technology improves. While a value of 1.5% of X_0 per layer was considered to be excellent a decade ago, values as low as 0.3% per layer are aimed for at present to achieve high sensitivity of HEP particle detectors.

Considering the ALICE ITS Upgrade detector maximum allowable material budget values, the

Table 2.1: Material budget value for a selection of engineering solid materials, assuming a thickness of $x=1$ mm.

Material	ρ [g cm ⁻³]	α [W m ⁻¹ K ⁻¹]	X_0 [cm]	x/X_0 [%]
Copper (pure)	8.90	405	1.4	6.94
Polyimide (Kapton [®])	1.42	0.12	28.5	0.34
CFRP K13D2U-2K	1.80	800 (fibre) ^a	23.7	0.42
Airloy [®] X103 UL Aerogel	0.034	0.017	1029.4 ^b	0.01

^a Thermal conductivity value in the direction of the carbon fibre. The effective thermal conductivity is lower due to the presence of resin binding the carbon fibre fibres all together.

^b Aerogel is more than 98.2% air. Determining its X_0 value is therefore difficult. In this comparison, the product ρX_0 similar to most polymers was assumed (35 g cm⁻²).

goals are 0.3% per layer at the Inner Barrel and 1.0% per layer at the Middle and Outer Barrel [4]. Thus it is clear metallic materials can not be used either in the mechanical or cooling structures. Polymeric materials, such as polyimide or CFRPs display a lower material budget, though its thickness must be carefully controlled since it is easy to exceed the material inventory limits. Higher thicknesses are locally tolerated, as long as the average material budget remains below the limit, but should be minimised, since local material budget peaks affect local detector resolution. Last, an aerogel was considered. This family of materials display an extremely low density and therefore provide an unmatched low material budget value. Although mechanical properties are acceptable for HEP particle detectors assemblies, its thermal conductivity is very low, as aerogels are mostly made of air.

Refrigerants used as coolants within the detector sensitive volume are subject to material limitations too. Table 2.2 displays a comparison between a $x=1$ mm thickness of two refrigerants: liquid water and two-phase R245fa refrigerant at a void fraction of $\varepsilon=0.85$, easily achievable in most two-phase boiling flows.

Two conclusions are drawn from the simple analysis in Table 2.2:

1. Minimising the cooling channel size is critical in order to reduce the average material budget and decrease the size of local material budget peaks.
2. For the same channel dimensions, two-phase refrigerants incur in a lower material budget than the same liquid refrigerant. This is due to a great volume of the channel being occupied by vapour; its high X_0 results in a lower material budget than if all the channel was full of liquid.

Estimations for two-phase R245fa material budget were done considering an $x(1-\varepsilon)$ thickness for the liquid phase and a $x\varepsilon$ thickness for the vapour phase. However, internal two-phase flows in channels involve different distributions of the liquid and vapour phases according to several flow parameters. No standard MB calculation methods for two-phase flows have been agreed so far by the scientific community; thus the method explained above is considered to yield a good approximation. Further discussion on this subject is presented in subsection 2.5.4.

Table 2.2: Material budget value for two refrigerants, assuming a thickness of $x=1$ mm.

Refrigerant	ρ_l [g cm ⁻³]	ρ_v [g cm ⁻³]	ε [-] ^a	X_{0l} [cm]	X_{0v} [cm]	x/X_0 [%]
Liquid Water	1.0	-	-	35.8	-	0.28
Liquid R245fa	1.4	-	-	26.0	-	0.39
Two-phase R245fa	1.4	0.006	0.85	26.0	5980.0	0.06

^a Assumed a typical value in two-phase boiling flows.

2.3 Cooling systems for HEP particle detectors

Depending on the field of interest HEP detectors are devoted to, along with their resolution, technology and read-out frequency, the requirements of the cooling system are controlled by various limiting factors. Over the last few years, the material budget constraints have become stricter in order to profit from the resolution increase in particle detector technologies and electronics. This has given birth to a variety of potential cooling systems sharing the philosophy of material budget reduction. A brief review on the current status of single- and two-phase cooling systems in HEP particle detectors is given below.

2.3.1 Air and gas cooling systems

According to Eq. 2.2, HEP vertex detectors should be ideally cooled with light gases, such as nitrogen, helium, or air. Their low density, combined with a low mass and atomic number would guarantee a minimal contribution of the refrigerant to the global material budget. For detectors operating at room temperature, gas/air cooling are promising solutions for some cases.

Air cooling is indeed the chosen cooling system of the STAR detector [21]. Here, the detector modules are mounted on hollow, lightweight individual structures made of carbon composites, arranged around the beam pipe perimeter, with three silicon modules longitudinally attached to each structure, as shown in Fig. 2.3a. The carbon composite structures have a mechanical and thermal purpose, as they not only support the silicon modules, but also serve as ducts for the airflow (Fig. 2.3b). The material budget remains below 0.3% of X_0 . Air at 8 m s^{-1} is used to remove the heat load corresponding to a detector power density of 0.1 W cm^{-2} , keeping the silicon temperature less than 12 K hotter than the air.

There are several limitations to air cooling systems. First, they are applicable only to low power density detectors operating close to room temperature. Also, mechanical problems derived from the cooling airflow may arise, such as structural dynamic and vibrational stresses propagated to the electronics. This issue requires from extensive qualification analysis and testing.

Experiments at the LHC are subject to air ventilation in the underground cavern. If temperatures on the detector are low enough, humidity in the air will condense on the sensitive parts, potentially leading to short-circuits and corrosion. To avoid this problem, nitrogen is constantly flushed across some detectors, cooling them down, but usually not entirely. Typically, nitrogen does not circulate at high velocity through the innermost detectors, resulting in virtually no local cooling power.

2.3.2 Single-phase cooling systems

Many detectors rely on single-phase cooling systems. The simplicity and the ability to cope with the typical low power dissipation of particle detectors are the main advantages. However, as seen in Eq. 2.2 and Table 2.2, liquid flows in a channel usually incur a higher average material budget than air cooling

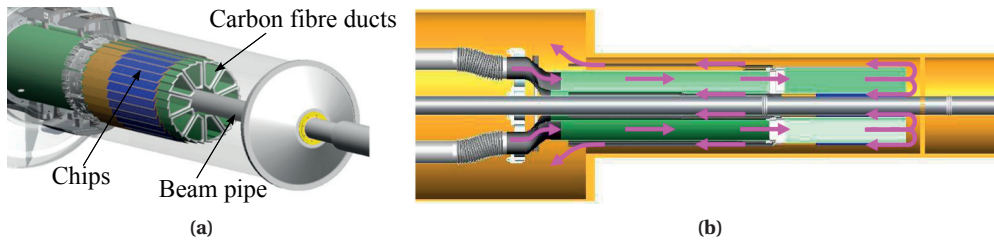


Figure 2.3: Air cooling system description at the STAR detector: (a) carbon structures around the beam pipe for cooling air circulation inside; (b) lateral view displaying airflow distribution. Figures adapted from [21].

or flow boiling cooling systems, where the air and the vapour phase, respectively, display higher X_0 than liquids.

The present ALICE ITS SSD and SDD detectors are equipped with single-phase demineralised water cooling systems [22, 23, 24]. A single cooling channel runs across every detector module. Demineralised water cooling is one of the initial proposals for the ITS Upgrade cooling. It consists of a polyimide microchannels structure with water in single-phase flow [25]. The microchannels body is held in place by the detector module structure from one side, with the silicon pixels glued to the other side. This system displayed good thermal behaviour but a high pressure drop.

Demineralised/deionised water is a poor electrical conductor. However, HEP particle detectors operate in radioactive environments, which might ionise water and any impurities present, and while purifiers and deionising systems are used, the presence of ionised water within the detector cannot be excluded. Ionised water is electrically conductive and will destroy electronics and circuits in case of a leak. To overcome this problem, water cooling systems in HEP particle detectors are usually conceived to work in leak-less mode (i.e. keeping water pressure always lower than atmospheric pressure) within the detector volume. This avoids damage to the detector in the event of leaks: air will be sucked into the loop instead of water leaking out. The cooling performance would decrease in this event but the sensor and electronics will be saved until technical intervention is possible. It is worth pointing out that HEP vertex detectors are usually installed several meters deep in the experiments, and access to the experiment underground areas is forbidden during operation because of radiation and safety risks. Thus, cooling fault risks should be minimised, as there is seldom a chance for intervention during the detector's multi-year use. Below atmospheric pressure operation restricts the water pressure drop to be less than 1 bar, which is a design limitation to these systems.

Under more extreme radioactive conditions than at the ALICE ITS Upgrade, water could undergo a radiolysis process that should be carefully controlled to limit the production of O_2 and H_2 (risk of explosion for the last). This was the main reason behind the rejection of an alcohol-water mixture liquid cooling system for the ATLAS Inner Detector [26].

Other refrigerants have been considered for single-phase detector cooling. Among them, fluoro-

carbons (FCs), with C_xF_y as general chemical formula, are suitable for cooling and cleaning electronics. They are used in several CERN cooling systems due to their good dielectric properties and their good radiation resistance. On the other hand, they are expensive refrigerants with high Global Warming Potentials (GWPs), and are not as good as water from a thermodynamic point of view. A CERN experiment, NA62, due to its exceptional geometry and power dissipation map, is cooled with C_6F_{14} in single-phase [27].

The experience gathered at the RICH detector at the Delphi Experiment at CERN gave a preliminary characterisation of fluorocarbons under radioactive conditions. As they became useful for detector cooling systems, compatibility with piping, polymers and electronics was extensively studied at CERN in close collaboration with the refrigerant supplier [28], as well as their radiation hardness [17]. At the current ALICE ITS SPD layer, a single-phase cooling system with C_6F_{14} was initially considered [29], but was finally substituted by evaporative C_4F_{10} , after the thermal load increased above what was expected.

The concerns regarding GWP and potential availability problems of fluorocarbons in the future motivates the consideration of other refrigerants. 3M Novec[®]-649 fluid is thermodynamically very similar to C_6F_{14} , while having a much lower GWP. Its use in HEP particle detector cooling depends upon pending radiation resistance qualification tests and compatibility to CERN standards.

2.3.3 Two-phase cooling systems

Over the past few years, the constraints in HEP particle detectors, especially those closer to the interaction point, have become more and more strict. The instruments are more compact and radiation levels are increased due to accelerator power upgrades. Developments in electronics and readout systems are focused on increasing data acquisition frequencies, thus the chip power dissipation has ramped up accordingly. In addition, higher resolution results in stricter material budget constraints that obliges one to resort to compact, lightweight mechanical and cooling services. Designing cooling systems complying with all requirements at the same time has proven to be quite a challenging task.

In this situation, two-phase cooling systems stand out as an effective and promising alternative to conventional single-phase designs. First of all, flow boiling cooling systems may normally yield higher heat transfer coefficients compared to single-phase systems. Secondly, a constant or slightly decreasing temperature of the refrigerant can be kept along the evaporator, depending on the pressure drop. These two characteristics make flow boiling cooling systems suitable for high heat flux technologies. Although the power density to be dissipated in particle detectors is low as compared to typical high heat flux applications, where two-phase cooling systems are essential [30], the presence of a large vapour fraction within a channel results in a lower refrigerant material budget than for the same channel with the same refrigerant in an all liquid state.

Several detectors implement two-phase cooling systems. For instance, the ATLAS Inner Detector uses evaporative C_3F_8 [31] and the ALICE ITS SPD uses a similar approach but with C_4F_{10} , due to

its temperature requirements: the ATLAS Inner detector requires the sensors to be kept below -7°C , whereas the SPD works at room temperature [29].

CO_2 evaporative systems have recently raised attention [32] and are implemented in many HEP particle detectors commissioned at the past LHC Long Shutdown 1 (LS1). The CMS Pix-Ph1 tracker, requiring two 15 kW plants, is an example. The ATLAS IBL detector, to be operated at -35°C , is cooled with CO_2 , needing two 3.3 kW plants [33]. Apart from the required low operation temperature, a big challenge to overcome in this detector is keeping low pressure drops, given the fact that the cooling lines are more than 6 m long. CO_2 cooling is present in experiments with stricter conditions, like the tracker of the Alpha Magnetic Spectrometer (AMS-02) at the International Space Station (ISS) [34], dealing with extreme temperature ranges. Many short- and long-term future HEP particle detectors are likely to be cooled with CO_2 . Microchannel CO_2 cooling is being considered for the LHCb-VELO tracker upgrade during the Long Shutdown 2 (LS2) scheduled in 2019 [35]. Long-term CO_2 cooling plans, beyond 2020, involve the ATLAS ITK and the CMS tracker at the future SLHC [36]. Multiple CO_2 plants, from 30 to 45 kW each, will be needed, demanding joint efforts between research centres, universities and industry in order to have access to components dealing with such power figures. Other projects involve the manufacturing and commissioning of mobile CO_2 cooling plants ranging from 0.1 to 1 kW, with the scope of launching them in the market targeted to refrigeration labs and test facilities.

2.4 Review on material selection for HEP particle detectors

Material selection in HEP particle detectors is not only driven by thermal and mechanical requirements but also by radiation resistance, material budget, and compliance to safety regulations as described in section 2.2.2. This section presents a brief survey on suitable materials for cooling HEP particle detectors, covering structural, thermal materials, adhesives, and cooling channels.

2.4.1 Structural materials

Mechanical structures in HEP particle detectors support and keep in place the chips and electronics while contributing as little as possible to the material budget. According to Eq. 2.2, metals and other dense materials are out of the question for detector construction, as their material budgets will easily exceed the acceptable limits even for the thinnest layout. Instead, lightweight, low- Z , large Young modulus (E_y) materials in thin arrangements are preferred.

CFRP composites provide high levels of stiffness at light weight and material budget, thanks to the possibility of selecting the best structural properties in the maximum stressed directions. Several types of structural shapes are possible. For instance, the T300 CFRP [37] can be made into a fabric by weaving the fibres together at 0 and 90 degrees. The result is a thin structure, which can be transformed to different shapes, keeping excellent mechanical behaviour and relatively good thermal properties in its planar dimension. Fig. 2.4a shows three mechanical supports proposed for the ALICE ITS Upgrade

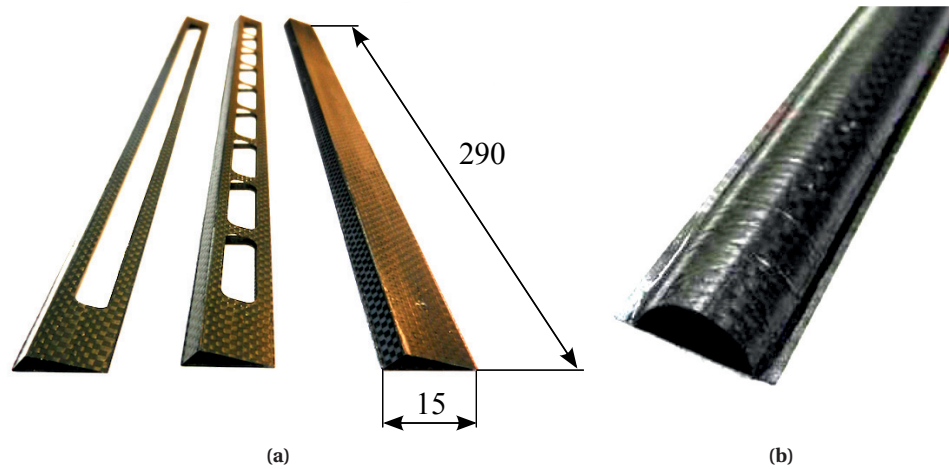


Figure 2.4: Support structures made with T300 carbon fibre composites. Dimensions in mm. Figures adapted from [4].

internal modules. They are 290 mm long and 15 mm wide each, and made of 100 μm -thick T300 ply. Their weights are, from left to right, 1.7, 1.8 and 2.0 grams. Fig. 2.4b displays a similar design with a curved top surface.

Carbon foams are lightweight composites used to provide mechanical support and, usually, thermal contact with an embedded cooling channel. This is the solution actually used in modules of the ATLAS IBL detector [33], where a titanium channel with flow boiling CO_2 is embedded inside a structure made of carbon foam. Fig. 2.5 displays an early module design for the ALICE ITS Upgrade, with an embedded pipe made of PEEK. Typically, these foams display relatively low, isotropic thermal conductivity (less than $25 \text{ W m}^{-1} \text{ K}^{-1}$)

More complex lightweight structures can be manufactured with CFRP rovings. These are carbon fibre threads pre-impregnated with resins, and can be wound, weaved or shaped in different ways. Examples are the M55J-3K [38] and the M60-6K fibres [39]. The numbers 3K and 6K designate the number of fibres in a bundle, each fibre being $5 \mu\text{m}$ in diameter. Fig. 2.6 shows a structure for the ALICE ITS Upgrade detector made of M55J-3K roving.

Carbon fleeces are very thin and light carbon plies with non-oriented fibres. A chemical binder holds the fibres together. This material is often used to encapsulate other CFRP parts and protect them, giving resistance to abrasion and peeling.



Figure 2.5: Carbon foam and PEEK cooling channel used in a primitive ALICE ITS Upgrade module, 290 x 15 mm in size, [4].



Figure 2.6: A view of a primitive ALICE ITS Upgrade module made of M55J CFRP. From [4].

Table 2.3: Structural CFRP material properties.

CFRP	Type	E_y [GPa]	Yield [GPa]	ρ_{fibre}	α_{fibre} [W m ⁻¹ K ⁻¹]	CTE_{fibre} [K ⁻¹]
M55J-6K	Impreg. thread	540	4.2	0.32 g m ⁻¹	150	-1.1 10 ⁻⁶
M60J-3K	Impreg. thread	588	3.9	0.15 g m ⁻¹	140	-1.1 10 ⁻⁶
T300	Fabric (0/90)	231	3.7	270 g m ⁻²	8.5/5	-0.6 10 ⁻⁶
Carbon fleece	Mat	240	4.4	8 g m ⁻²	-	-

The mechanical properties of all the materials in this subsection are summarised in Table 2.3. Note that ρ , α , and CTE in the table are specified for non-impregnated fibres only, except for the T300 fabric. The resin choice and impregnating process defines the density of the CFRP, as well as the effective thermal conductivity and the CTE .

2.4.2 Thermally conductive materials

The aggressive material budget requirements in HEP vertex detectors motivates the use of thin, highly conductive materials [40]. Again, CFRPs are one of the best choices, as not only do they display excellent mechanical properties, but they also have high thermal conductivities. Carbon fibre composites have been already used in many cooling applications apart from HEP detectors, like lightweight heat exchangers in space technology, or as thermal spreaders, for instance.

High-conductive pitch-based CFRPs, such as K13C2U-2K [41], K13D2U-2K [42], or K1100-2K Thornel [43] carbon fibres, display thermal conductivities in the direction of the conductive fibre of 620, 800 and 1000 W m⁻¹ K⁻¹, respectively, largely exceeding the fibre thermal conductivity values reported in Table 2.3. CFRPs of this kind are obtained as pre-preg: unidirectional fibres are impregnated with cyanate ester resins or epoxies, and then cured at high temperature (> 120°C). Multiple layers can be piled up in different directions in a mold prior to the curing process, depending on the thermal and mechanical needs of the final product. The elastic modulus and the thermal conductivity are larger in

the direction of the fibres. Depending on the curing and bleeding of the resin, plies down to 40 μm thick can be obtained.

Resins can make up to 50% of the volume of the final CFRP, thus influencing the effective thermal conductivity and elastic modulus of the CFRP. Some studies reported 40% of the original fibre thermal conductivity [44] for K13D2U-based CFRPs plies, whilst the elastic modulus can be decreased by 50% of the fibre value. Furthermore, transversal thermal conductivity values are low, on the order of $1 \text{ W m}^{-1} \text{ K}^{-1}$. Despite this, their lightness and their acceptable mechanical properties for the typical requirements of particle detector modules make them the best choice in terms of cooling power to material budget ratio. Using these materials in such a way that they provide mechanical and heat transfer capabilities simultaneously certainly minimises the material budget of the modules, sometimes sparing the need of extra mechanical structures.

At each heterogeneous mechanical interface, good *CTE* match between the two materials has to be guaranteed. This is especially critical at the interface between the mechanical/thermal structures and the silicon chips, with a $CTE = 2.6 \cdot 10^{-6} \text{ K}^{-1}$ at 20°C . Usually, composite materials and CFRPs display negative *CTE* in the direction of the conductive fibre, while in orthogonal directions, the presence of resin derives in neutral or positive *CTE*. Since CFRP plies can be layered with fibres oriented in different directions, and even embed other composites, a desired *CTE* can be obtained using the appropriate fibre layup. Fig. 2.7 displays K13D2U fibres ready to be cured. The CFRP in the right is more compact, with more fibre density.

Recently, thin foils made of Thermal Pyrolytic Graphite (TPG) (see Fig. 2.8) have become popular as thermal spreaders [46, 47] and as thin Thermal Interface Materials (TIMs) [48]. Unlike the carbon fibre composites described above, a thin graphite foil is not suitable for mechanical purposes; although it can be bent many times, it is weak and breaks easily, due to the layer stripping phenomena typical in graphite. Thermal conductivities up to $1500 \text{ W m}^{-1} \text{ K}^{-1}$ in-plane are reported [49]. Independent studies claimed out-of-plane thermal conductivities to be lower than stated by manufacturers [50]. Several manufacturers provide TPG in multiple thicknesses and coatings. For HEP cooling applications, thicknesses ranging between 30 and 100 μm are of highest interest.

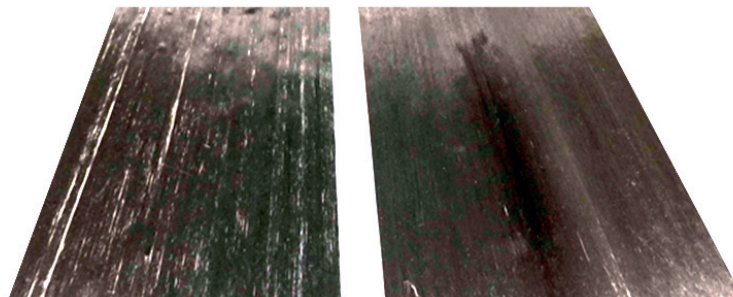


Figure 2.7: K13D2U CFRP fibres placed in the same direction, with two fibre densities. From [45].



Figure 2.8: Thermal Pyrolytic Graphite (TPG) foil view. From [45].

Table 2.4: Thermal and mechanical properties of a selection of conductive CFRPs and and graphite foils.

CFRP	Type	E_y [GPa]	Yield [GPa]	ρ_{fibre} [g cm ⁻³]	α_{fibre} [W m ⁻¹ K ⁻¹]	CTE_{fibre} [K ⁻¹]
K13C2U-2K	Unidir. pre-preg	896	3.8	2.2	620	-1.1 10 ⁻⁶
K13D2U-2K	Unidir. pre-preg	930	3.7	2.2	800	-1.2 10 ⁻⁶
K1100-2K	Unidir. pre-preg	931	3.1	2.2	1000	-1.5 10 ⁻⁶
TPG	Foil	-	-	1.6	1500 (planar)	-

Table 2.4 reports the thermal and mechanical properties of the CFRPs and the TPG described in this subsection. Note that the CFRP values are for the fibres only. Once the resin is added, the mechanical properties and the thermal conductivity slightly deteriorate, the CTE increases transversally to the fibres, and the volumetric density decreases to values ranging from 1.6 to 1.9 g cm⁻³.

Graphene has gathered recent attention due to its outstanding theoretical thermal properties [51]. In particular, the fewer layers of graphene are considered, the better thermal performance is obtained, with reported values of 1500-2000 W m⁻¹ K⁻¹ [52]. However, graphene layers need to be deposited over a substrate, as they are so thin that otherwise they would not have enough mechanical consistency. It was reported a dramatic decrease of the thermal conductivity after a layer of graphene was deposited by mechanical exfoliation over a silicon oxide (SiO₂) substrate [53], but still remaining about 500-600 W m⁻¹ K⁻¹ [54].

For the ITS Upgrade project, an experimental measurement of the thermal conductivity of a thin deposition of graphene over a substrate was performed. The chosen substrate was paper. The measured thermal conductivity was lower than 100 W m⁻¹ K⁻¹. This low value might have been originated in discontinuities in the graphene coating during the deposition process or by mechanical break of the graphene layer. At the time of the test, graphene was not a viable option. Still, it is a subject of investigation in HEP particle detectors cooling, since it could be potentially deposited on the silicon chips, increasing their superficial thermal conductivity.

Another thermally efficient material is graphite foam [55]. It has been used for the design of compact lightweight radiators [56] and evaporators [57], as the cooling surface is maximised. The open porosity provides permeability to fluids, and refrigerant evaporation may be possible through the foam. Several grades of foam are commercially available, displaying different pore size, thermal and mechanical properties. Specific thermal conductivities can reach values of $300 \text{ W m}^{-1} \text{ K}^{-1}$. Carbon foams, as described in subsection 2.4.1, are frequently used for enhancing thermal contact and provide mechanical stiffness. Their thermal conductivity is significantly lower than graphite foams. As a result, the graphite and carbon foams are not usually exchangeable. It is also very important to carefully select the foam grade, as their mechanical properties may vary greatly, from brittleness to plastic behaviours.

Recently, diamond became a realistic material for specific cooling applications. Chemical Vapour Deposited Diamond (CVD) is made of artificial polycrystalline structures with very low impurity contents. CVD displays a thermal conductivity similar to natural diamond, over $1800 \text{ W m}^{-1} \text{ K}^{-1}$. Also, CVD is being considered as the active media in future generations of HEP particle detectors [20], so the cooling could be directly integrated in the chips. However, current fabrication tolerances are not within the requirements and the process is still expensive.

The excellent thermo-physical properties of beryllium (low density, high X_0 , high thermal conductivity, good mechanical properties) would make it a top pick for HEP particle detector cooling applications, and indeed it is used in the beam pipe, to separate interaction points from the first detector layers. However, beryllium is toxic and prone to fracture. It also oxidises in ambient conditions and requires special equipment, facilities and safety measures to undergo fabrication processes. Thus, it is normally chosen only in applications where its presence is absolutely essential.

2.4.3 Resins and adhesives

CFRPs are impregnated with resins that keep the fibres together and allow creating a laminate or a thread. Resins are chosen depending mainly on the type and operating conditions of CFRPs, curing temperature, maximum service temperature, mechanical properties, moisture absorption, thermal conductivity, and material compatibility. In vertex detectors, additionally, resins must withstand well radiation for sustained time periods, and the *CTE* is an important parameter.

The EX-1515 cyanate ester resin [58] is widely used at CERN CFRP elements because of its high radiation resistance, low moisture absorption, and low curing temperature (127°C). Besides, its *CTE* of $61 \cdot 10^{-6} \text{ K}^{-1}$ partially compensates for the negative *CTE* values of carbon fibres. RS-3 [59] is an alternative cyanate ester resin extensively used at CERN. Cyanate ester resins are usually preferred to epoxy resins because of their lower moisture absorption and higher dimensional stability over time.

Adhesives are ubiquitous for assembling structural and cooling elements, detector chips, cables and printed boards. The choice of the adhesive is driven by bond strength stability, minimum thickness ensuring stable bond and dimensional tolerances, material budget, radiation hardness, chemical

stability, material compatibility (with interfacial materials, especially detector sensors, and coolants), contamination, cure temperature and cycle duration, application process, and creep. Additionally, *CTE* compliance should be verified, especially at high temperature curing processes. Last, glue re-workability could be needed when detector elements are to be removed independently, without damage. Such a broad spectrum of desired characteristics and the variety of adhesives available motivates tailored choices depending on the particular needs.

Epoxy resins are used in most structural joints. In cases where high thermal performance and high radiation hardness are needed, adhesives like Hysol EA9396 [60] are a good choice, as they can be easily filled with a high thermal conductivity micro-powder. Filling improves thermal conductivities by a factor of 5, from 0.3 to 1.5 W m⁻¹ K⁻¹ [44], compared to the values of epoxy adhesives, ~0.7 W m⁻¹ K⁻¹. The *CTE* of filled glued can dramatically change compared to the plain adhesive, and must be accounted for. Also, thermal conductivity stability with radiation must be carefully studied.

Electrically conductive adhesives are required for specific applications. Usually, such adhesives benefit by their high thermal conductivities. An example is the electrically conductive, silver epoxy EPO-TEK[®] H20E [61], which displays a thermal conductivity of 29 W m⁻¹ K⁻¹.

2.4.4 Cooling channels

Single- and two-phase cooling systems in HEP particle detectors require cooling channels for circulating the coolant. The choice of the channel material is driven by dimensional constraints, maximum/minimum coolant pressure, cross-sectional shape, radiation hardness, material/coolant compatibility, physical and chemical stability over time, integration requirements in the particle detector, and notably, material budget and wall thickness.

Traditionally, cooling channels in industrial cooling applications are made of metallic materials because of their good thermal conductivity, mechanical stability, price and availability. Copper and aluminium alloys, and stainless steel, to name a few, are materials widely used in multiple channel sizes, shapes and configurations. Metallic channels are used in HEP particle detectors too. An example is the ALICE SPD detector, cooled with flow boiling of C₄F₁₀ refrigerant in Phynox[®] tubes [29, 62]. The channels have an initial diameter of 2.6 mm and a wall thickness of 40 μm, and are squeezed to a flat profile of an overall thickness of 600 μm. Phynox[®] is a cobalt nickel chromium super-alloy with excellent fatigue resistance, low corrosion and non-magnetic properties. However, its low radiation length accounts for a high material budget, undesirable in new-generation vertex detectors.

Pure titanium and titanium alloy channels display excellent mechanical properties, corrosion resistance and material compatibility. With double the radiation length as Phynox[®] and a small wall thickness, the material budget is lower. Titanium tubes are used in high pressure cooling applications, such as the two-phase CO₂ system of the ATLAS Insertable B-Layer detector [33, 63].

Plastic tubes represent a big step towards material budget minimisation, thanks to their high

radiation length. PEEK (polyether ether ketone) is widely used as an engineering material. It provides excellent mechanical properties, chemical stability, durability and high radiation resistance, at low material budget. It can undergo a special treatment to keep a particular shape. Reinforcement with glass and carbon fibres is possible too. Pipe wall thicknesses down to 0.25 mm are available.

Polyimide [64], commercially known as Kapton[®], is a robust, radiation-resistant polymer [13] which takes wall thickness minimisation a step further: tubes of 1 mm Inner Diameter (ID) are available with 25 μm -thick walls, so even with similar X_0 as PEEK, its material budget for a pipe with the same ID is lower. Polyimide tubing is usually intended for electrical insulation and the medical industry, and has been seldom used in HEP particle detectors. An example at CERN is the straw tube technology for the LHCb tracking system [65], in which numerous straws 2.5 m long made partially in polyimide contain gas.

In order to compare the material budget differences the choice of the channel material would make, let us consider a 2.1 mm ID channel with 0.15 mm wall thickness. Fig. 2.9 plots the material budget of the empty channel if made of SAE 316 stainless steel (thin dashed line) and a polyimide channel with identical dimensions (thick line). The stainless steel channel displays a material budget 15 times higher than if made of polyimide. Furthermore, 2.1 mm ID polyimide tubes are readily available with 32 μm wall thickness [66]. Such pipe would display a material budget a 80 times lower than the initial stainless steel tube.

Table 2.5 summarises the average material budget of the same 2.1 mm ID, 2.4 mm Outer Diameter (OD) channel if made of the materials described in this subsection. Material radiation lengths are reported in the second column. The last column represents how many times higher is the channel material budget for a certain material compared to polyimide. PEEK slightly outperforms polyimide in

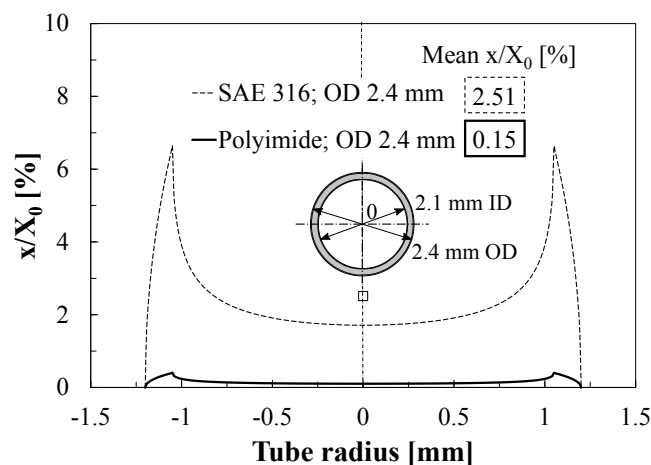


Figure 2.9: Material budget comparison of a 2.1 mm ID, 2.4 mm OD cylindrical channel made of SAE 316LN stainless steel and made of polyimide.

Table 2.5: Average material budget comparison of a 2.1 mm ID, 2.4 mm OD cylindrical channel made of different materials.

Material	X_0 [cm]	Channel x/X_0 [%]	$MB_{\text{material}}/MB_{\text{polyimide}}$ [-]
SAE 316	1.8	2.51	16.7
Phynox [®]	1.6	2.64	17.6
Titanium (pure)	3.6	1.20	8.0
Aluminium (pure)	8.9	0.48	3.2
PEEK	31.9	0.13	0.9
Polyimide	28.5	0.15	1.0
Polyimide (32 μm wall)	28.5	0.03	0.2

material budget at the same wall thickness, but polyimide tubes are available with thinner walls (see last row).

In addition to low wall thicknesses and low material budget, the advantages of polyimide channels are the following:

- High radiation hardness: according to [15], polyimide experiences no damage below 10^7 Gy and mild damage appears only after sustained irradiation over $5 \cdot 10^7$ Gy. The first layer of the ALICE ITS upgrade will be exposed to between 7000 and 27000 Gy per year (including a factor of safety of 10) [5], hence polyimide tubes will receive, over a 6-year operational life of the detector, a radiation dose more than 150 times lower than the 10^7 Gy safety threshold. It has to be considered that prolonged irradiation may increase the thermal conductivity of the tubes [8].
- Compatibility with refrigerants: polyimide is compatible with most fluids and no chemical reaction is expected with most of the coolants used at CERN [11]. Polyimide is not affected either by most solvents and can withstand weak acids. It is not compatible with some strong alkalis (such as potassium hydroxide or sodium hydroxide).
- Tightness: a 2.67 mm ID tube with 64 μm wall thickness withstands 40 bar before bursting.
- Thermal and mechanical stability: a thermoset polymer, polyimide cannot be re-shaped by heat at low temperatures ($<200^\circ\text{C}$) after extruding it. Its mechanical properties are: $E_y=2.3$ GPa; Yield=0.31 GPa; $CTE=45 \cdot 10^{-6} \text{ K}^{-1}$, $\rho=1.4 \text{ g m}^{-3}$.
- Dimensional stability: polyimide channels are made by extrusion, guaranteeing inner diameter uniformity. The outer surface is inspected after fabrication to verify the tube has no blimps.
- Low deterioration rate due to ageing: physical and chemical stability are good over time. Corrosion is not common in polyimide tubing.
- Surface hardness: a Shore hardness of 87D, similar to PEEK, is reported for polyimide [67].
- Fire safety: polyimide complies to CERN regulations in this aspect [19].

Some disadvantages of polyimide channels are:

- Low thermal conductivity: $0.12 \text{ W m}^{-1} \text{ K}^{-1}$ for pure polyimide tubes, 130 times lower than stainless steel. Low wall thicknesses help decreasing thermal resistances across the tube walls.
- Moisture absorption: up to 0.841% water absorption is reported [66], although it does not compromise the tube stability.
- Pinching or “kinking”: polyimide tubing can be bent and flexed. Pinching, or local permanent diameter reduction, might happen if flexed to a small radius. There is a threshold, linked to the relationship between the diameter of the tube to the wall thickness, that defines when the pipe would start to kink. If the tube kinks, it is possible to recover most of the original material mechanical properties by heating the pipe to 200°C , which is not always an option.
- Keeping sectional uniformity has to be carefully taken into account for any mechanical assembly process. Although the tube is flexible and robust, the section can be squeezed under relatively low forces and may remain “ovalised” afterwards. For this reason, polyimide channels should not be used for structural purposes, unlike PEEK.
- Potential brittleness: cured polyimide tubes will not easily break or tear. However, if the wall is very thin, piercing it during manipulation could be possible. Thus, polyimide channels should be always protected against external objects.

Polyimide tubing is commercially available in sizes from 0.25 to > 3 mm ID. In addition to pure polyimide, composite tubes (i.e. polyimide plus another material) provide specific properties. An example are polyimide channels with internal polytetrafluoroethylene (PTFE) liners, to decrease moisture absorption by 4 times and increase the thermal conductivity by 2 times. Pebax[®] is another widely used liner used to improve mechanical properties.

Tubes are also available with embedded, thin stainless steel braids or coils, increasing their flexibility and preventing them from kinking. During the manufacturing process, the tubes can also be bent to a shape, while keeping a circular cross-section. These two features open a wide range of possibilities for cooling systems for HEP particle detectors, where spatial constraints are strict. Fig 2.10a displays a 1.024 mm ID, 1.158 mm OD polyimide pipe reinforced with a 100 PIC (crosses per inch) stainless steel braid, the filament being 12 by $76 \mu\text{m}$. The braid is embedded under a layer of blue Pebax[®]. The pipe can be bent to an interaxis distance of 18 mm without the stressed section kinking. Fig 2.10b depicts a 0.993 mm ID, 1.194 mm OD natural polyimide tube with an intermediate section made of PTFE reinforced with a 75 WPI (wraps per inch), 25 by $76 \mu\text{m}$ stainless steel coil that allows for high flexibility. At the right, the polyimide is permanently shaped in a 'Z'.

It can be concluded that polyimide channels represent an appealing low-Z solution for vertex detector single- or two-phase cooling. On the other hand, their use opens several questions, particularly



Figure 2.10: Composite polyimide tubes: (a) pipe with reinforcement coil and outer surface made of Pebax[®]; (b) pipe with a PTFE transition plus shaped polyimide section. Dimensions expressed in mm.

in two-phase cooling, that must be addressed prior to considering them for long-term operation. Polyimide tubes are used in the ALICE ITS Upgrade cooling solution and in the two-phase flow tests.

2.5 Review on two-phase flow boiling in small horizontal channels

2.5.1 Introduction

The cooling system developed and tested in this thesis for the Upgrade of the ITS detector at the ALICE Experiment at CERN consists of new, lightweight cooling modules made of carbon fibre composites with embedded polyimide cooling channels. The choice of coolant is still open: single- or two-phase flow boiling refrigerants are considered. Generally speaking, convective flow boiling presents higher heat transfer coefficients than single-phase flows, and incurs higher pressure drops. One of the main advantages of two-phase cooling is the presence of usually large vapour fractions. As vapour is lighter than liquid, a two-phase flow boiling refrigerant is envisaged as a low material budget option, compared to single-phase cooling.

This section presents a short overview on two-phase flow boiling in horizontal channels, focusing on macro-to-microchannel transition criteria, flow patterns, void fractions and material inventory determination, two-phase pressure drop, and two-phase heat transfer mechanisms, methods and experimental measurements.

2.5.2 Macro-to-microchannel transition

It is frequently mentioned in two-phase heat transfer literature a transition between macro- and microscale regimes, which exhibit different flow patterns, two-phase pressure drops and heat transfer behaviours. The nature of this transition (continuous or abrupt), the criteria to identify it, or even its existence are subjects lacking agreement among researchers. In the last decades, numerous experi-

mental studies were aimed to identify key variables in the transitions, while mechanistic approaches were taken too. The most prominent studies are mentioned below.

Kandlikar and Grande [68] proposed a “rule-of-thumb” criterion based on the channel size and flow conditions. Conventional channels, or macrochannels, are those with hydraulic diameters equal or larger than 3 mm, minichannels belong in the 0.2 to 3 mm window, and microchannels are those below 0.2 mm ID. Kew and Cornwell [69] linked the transition to microscale conditions when vapour bubble growth is constrained by the channel diameter. Such confinement effects are relevant if the confinement number (Co), defined below, is higher than 0.5:

$$Co = \sqrt{\frac{\gamma}{g(\rho_v - \rho_l) D_i^2}} > 0.5 \quad (2.4)$$

Ong and Thome [70] based their transition criteria mainly upon liquid film thickness uniformity in the channel perimeter. For Co values between 0.3 and 1, the flow resides in a transitional regime (mesoscale), smoothly shifting from macroscale ($Co < 0.3$) to microscale regime ($Co > 1$).

There are mechanistic approaches, such as the study by Kandlikar [71], who analysed the balance among dominating forces during convective evaporations, while others have proposed several criteria based on bubble departure diameter.

Considering the multiple methods for predicting macro-to-mini-to-microchannel transition and the diverse flow regime nomenclature found in literature, still some common points of agreement are found. Generally, the macro-to-minichannel transition is accepted to occur at a diameter of 3 mm, according to Bertsch *et al.* [72], Cheng *et al.* [73] and Kandlikar and Grande [68]. Cooling channels in HEP particle detectors typically display diameters smaller than 4 mm, mainly due to spatial and material inventory constraints. The smallest modules of the ALICE ITS Upgrade will have polyimide tubes on the order of 1 mm ID, as described section 5.2.1. Two-phase flow in such channels is likely to fall in the minichannel category, with surface tension forces dominating over gravitational body forces. However, the biggest modules embed 2.667 mm ID polyimide channels, and hence boiling flows will fall in the macro-to minichannel transition [74]. Stratified two-phase flows in this case might occur depending on the flow conditions.

2.5.3 Flow patterns

The liquid and vapour phases in two-phase flows are distributed differently depending on the operating conditions. Generally speaking, one phase might be dispersed in the other, or they might flow as two separated continua, as purely stratified flows do. A combination of the two cases above is possible, with liquid or vapour entrainment in the other phase. Flow patterns in horizontal two-phase flows depend on the channel size (macro- or minichannel), heat transfer (adiabatic/diabatic), and flow conditions (mass flux, saturation temperature and pressure).

In conventional channels, Collier and Thome [75] identified seven flow patterns: bubbly, plug, stratified, stratified-wavy, slug, annular, and mist flows. Flow pattern maps, proposed by several authors, identify the transitions between these two-phase flow patterns or slight variations of them. Wojtan *et al.* [76] developed a flow pattern map including the flow patterns defined by Collier and Thome.

As the channel diameter decreases, surface tension dominates over gravity forces and liquid stratification tends to disappear. For small diameters, the vapour phase is reported to detach from the top of the channel, as indicated by Revellin *et al.* [77], and flow patterns differ from macroscale ones. Revellin and Thome proposed in their study [78] the following flow patterns:

- **Isolated bubbles (IB):** the vapour bubble generation rate is greater than the coalescence rate.
- **Coalescing bubbles (CB):** the bubble coalescence rate is greater than the bubble generation rate.
- **Annular (A):** at vapour qualities higher than the CB regime, bubbles coalesce to form a continuous vapour volume inside the channel, while a liquid film is present in the channel wall. Entrainment of liquid droplets in the vapour phase is possible.

Fig. 2.11 shows high-speed images of two-phase flow patterns of R245fa in a 1.1 mm ID channel by Tibirićá *et al.* [79], who also defined a 'churn' flow pattern between coalescing bubbles (slug) and annular flow.

The annular flow pattern occurs for both macro- and microscale, with the difference that the liquid film thickness in large, conventional channels might be thicker at the bottom due to stratification. Ordinarily, annular flow patterns are most advantageous in two-phase cooling systems for HEP particle detectors for two reasons:

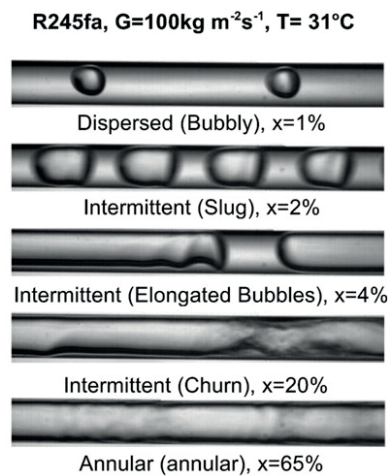


Figure 2.11: Flow patterns of R245fa refrigerant flow in a 1.1 mm inner diameter tube, by Tibirićá *et al.* [79]. Flow direction is from the right to the left of the images.

1. Annular flows display high heat transfer coefficients, as displayed in Fig. 2.16.
2. The presence of a continuous vapour phase in the core of the flow yields low material budget thanks to the low density of vapour, as described in section 2.2.3.

In multi-microchannel evaporators, the presence of restrictions at the entrance of each of the channels are included to guarantee uniform flow distribution and trigger the evaporation process earlier by saturation pressure drop flashing [80]. This effect usually involves an anticipation of the annular flow pattern. Thus, in multi-module HEP particle detectors cooling systems, which would feature capillary sections at the entrance of each module to ensure uniform parallel saturated flow distribution, the two-phase annular flow pattern could also be anticipated. Flow pattern modification might occur in other singular elements, such as U-bends, connectors and changes in diameter.

2.5.4 Cross-sectional void fractions and refrigerant inventory

The vapour void fraction is an important parameter in two-phase flows. It is used for defining flow pattern transitions, the velocity of each phase, two-phase pressure drop static and momentum components, and in mechanistic two-phase heat transfer methods. But, above all, it is a key parameter for estimating the refrigerant material budget and the coolant inventory in two-phase cooling systems in HEP particle detectors.

Void fractions may be defined as local, chordal, cross-sectional or volumetric. Usually, the cross-sectional void fraction is used and estimated by the different methods in literature, and hence it is referred to simply as 'void fraction'. The void fraction is mainly influenced by the channel dimensions and geometry, the flow pattern, and liquid entrainment in the vapour phase. Some prediction methods in the literature assume the same or different velocities for the vapour and liquid phases (homogeneous/separated models). Other methods recall the local void fraction and mass flux. Last, prediction methods based on mechanistic approaches are also available. However, most of the studies rely on correlations based partly or entirely upon experimental data (semi- and fully empirical methods). It is emphasised that measuring experimentally void fractions typically poses high uncertainty, especially in small channels, although technology advancements allow for more objective, non-intrusive, accurate measurements. A summary of the methods considered in the present work for material inventory determination and two-phase flow calculations is presented below. All these methods are described in detail in appendix A, section A.3.

The homogeneous void fraction method considers the two phases traveling at the same velocity. This approach is valid for disperse two-phase flows, where one phase moves entrained in the other (bubbly, mist flow patterns), or close to the fluid critical condition. In slug and annular flow patterns, homogeneous void fractions tend to overestimate the real void fraction. Several definitions of the two-phase mixture density are available in the literature.

Zivi [81] developed an analytical void fraction model where the superficial void fraction is obtained assuming the flow will minimise the kinetic energy flux of the two-phases across the cross-section of the channel. Such method was developed without regard to the flow pattern, although the author expanded his expression including the influence of liquid entrainment. The entrained liquid fraction, e , is the fraction of the liquid mass flow rate corresponding to entrained liquid droplets. Fig. 2.12 shows the effect of the liquid entrainment in the void fraction predicted by Zivi, with a higher influence at lower vapour qualities. It is also observed in the plot how the void fraction rapidly increases with vapour quality, exceeding in the depicted case values of 0.8 already at $x=0.1$.

Kanizawa and Ribatski [82] proposed a modification of the method by Zivi, considering non-uniformity effects in the velocity and distribution of the phases when computing the minimum kinetic energy flux across the channel cross-section. The result is a void fraction expression modified with the inclusion of the Froude number.

Drift-flux void fraction models account for different velocities of the two phases. Rouhani and Axelsson [83] developed an empirical void fraction method for annular flow in vertical channels, later adapted for horizontal channels by Steiner [84]. The method is widely referenced in the literature for two-phase flows of halogen refrigerants in conventional horizontal channels, being frequently applied to small channels too.

Niño *et. al* [85] put forward the first void fraction correlation for multi-microchannels. The method is based upon experimental data for annular flows in channel sizes between 1.02 to 1.54 mm ID. The Lockhart and Martinelli parameter (see Eq. 2.9) and the Weber number characterise the annular flow regime in small channels. These parameters affect the thickness of the liquid film of the annular configuration, and therefore have influence on the void fraction. The authors reported higher void

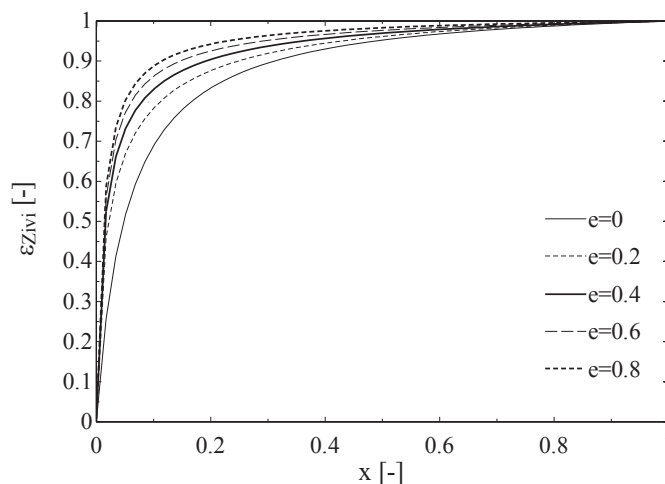


Figure 2.12: Effect of the liquid entrainment on the void fraction, calculated by Zivi [81], for two-phase R245fa refrigerant in a 2.7 mm ID channel.

fractions than for conventional channels.

Cioncolini and Thome [86] developed a void fraction model for conventional and small channels based on a large experimental database for annular flow for channel diameters from 1 to 45 mm. Contrary to drift-flux methods, this model does not include mass flux effects. The same authors elaborated a correlation for determining the entrained liquid fraction in annular flows [87].

At the beginning of the present section, it was stated that void fractions are needed to determine the effective material budget of boiling refrigerants in two-phase cooling systems in vertex detectors. Indeed, the void fraction indicates the fraction of the cross-section of the channel occupied by the vapour phase, but usually provides no direct answer about the liquid distribution, whether it is stratified at the bottom of the channel, in a thin film on the perimeter of the wall, or in liquid plugs between long vapour cores. Furthermore, the presence of singularities and changes of channel diameter in HEP particle detectors would motivate flow pattern and liquid distribution changes. As a result, there is currently no consensus for determining the material budget of two-phase flows.

Considering an annular flow and no stratification effects, the liquid phase can be assumed to be evenly distributed in contact with the channel wall in a thin liquid film. The material budget of the two separate phases, liquid and vapour, can be easily calculated for a given void fraction applying Eq. 2.2 to the liquid and vapour phases separately. Fig. 2.13 illustrates, as an example, the material budget of two-phase C_4F_{10} refrigerant with a void fraction of 0.85, compared to the material budget of the same channel filled with liquid water. The liquid C_4F_{10} is assumed to be a thin liquid film around the channel inner wall. The channel is 2.67 mm ID, 2.80 mm OD, made of polyimide.

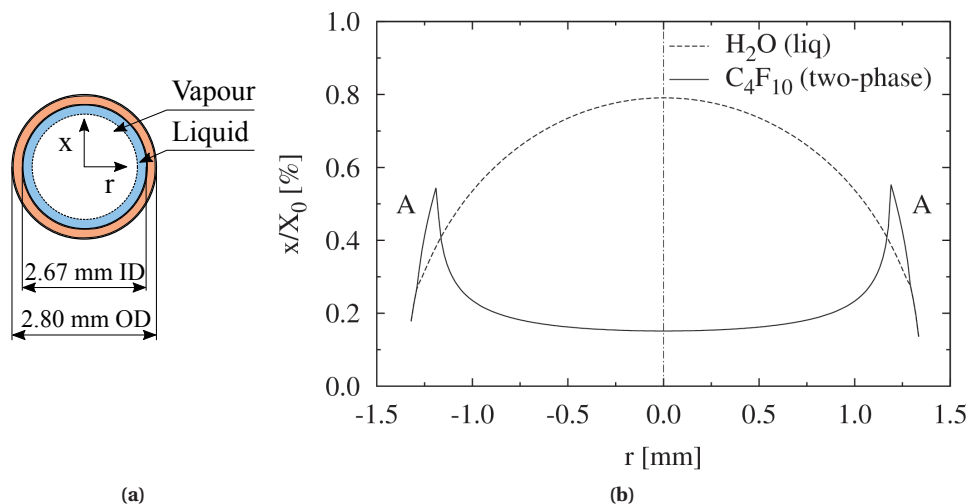


Figure 2.13: Material budget of two-phase C_4F_{10} refrigerant with a void fraction of 0.85 and all liquid in a thin film adjacent to the wall of a 2.67 mm ID polyimide channel, compared to the same channel filled with water: (a) vapour and liquid phases distribution in the 2.67 mm ID channel; (b) material budget calculation, including the channel walls.

Fig. 2.13b reveals that the channel width-averaged material budget of the case with the two-phase refrigerant is significantly lower than the case with liquid water, and that considering the liquid phase evenly distributed as a liquid film inside the channel accounts for the material budget peaks indicated by the letter 'A' at the plot. If a purely stratified liquid phase with a flat vapour-liquid interface was considered, the average material budget value would be the same, but the 'A' peaks would be smaller and due only to the channel wall thickness. Resolution in HEP particle detectors is affected by the presence of material budget peaks, therefore, considering the liquid as a thin film adjacent to the wall yields a safe approach to the two-phase material budget. All two-phase material budget calculations in this thesis are performed following this methodology, reviewed in section 5.3.4.

As described above, void fractions are key to determine two-phase coolant inventory. Studies in this direction typically involved the determination of the volumetric void fraction in the evaporator domain by using the quick-closing valves method, as initially proposed by Yashar [88]. Hoehne and Hnrjak [89] performed a parametric study on refrigerant charge minimisation techniques in a experimental system, using void fraction correlations in their work. In two-phase cooling systems in HEP particle detectors, the refrigerant charge can be calculated analytically by integrating the void fraction given by a correlation along the whole cooling channel assuming a linear vapour quality increase, i.e. a uniform heat flux boundary condition. This method is compared against experimental refrigerant inventory results as described later in section 5.4.

2.5.5 Two-phase pressure drop

The accurate estimation of two-phase pressure drops entrains great importance in evaporative cooling systems design. It is key to properly size the cooling channels and estimate two-phase saturation temperature drops. In general, the two-phase pressure drop along the channels of an evaporator has three components: the static, the momentum, and the frictional pressure drop, as follows:

$$\Delta p_{tp} = \Delta p_{static} + \Delta p_{mom} + \Delta p_{frict} \quad (2.5)$$

The static pressure drop component is defined below:

$$\Delta p_{static} = \rho_{tp} g Y \sin\Theta \quad (2.6)$$

where Θ is the angle between the horizontal plane and the tube axis, Y is the height from a reference, and ρ_{tp} is the density of the two-phase flow "mixture", for instance:

$$\rho_{tp} = \rho_v \varepsilon + \rho_l (1 - \varepsilon) \quad (2.7)$$

ε is the two-phase void fraction. This term, described in subsection 2.5.4, should be calculated beforehand, which needs from knowledge about the flow conditions. The static pressure drop component is

zero for horizontal flows.

The momentum pressure drop component is related to the change of velocities of the liquid and vapour phases. This might be due to phase change (heat transfer), changes in the channel size and shape, presence of singularities in the piping, and compressibility effects. This component is usually calculated by assuming separate or disperse liquid and vapour phases with different velocities. Applied to a circular channel of constant section and a length L between the inlet and the outlet, it is expressed as follows:

$$\Delta p_{mom} = G^2 \left\{ \left[\frac{(1-x)^2}{(1-\varepsilon)\rho_l} + \frac{x^2}{\varepsilon\rho_v} \right]_{out} - \left[\frac{(1-x)^2}{(1-\varepsilon)\rho_l} + \frac{x^2}{\varepsilon\rho_v} \right]_{in} \right\} \quad (2.8)$$

where ε is the two-phase void fraction, calculated using a prediction method from the literature. Again, determining correctly the void fraction is critical to estimate the momentum pressure drop component.

The frictional pressure drop component remains as one of the points of discussion between researchers in two-phase flows, since there is no analytical way to estimate it. This component can be experimentally determined using the measured global pressure drop value and the estimated momentum and static pressure drop components. Furthermore, in adiabatic two-phase flows in horizontal channels, the measured total pressure drop is just the frictional component. However, for microchannels, the momentum component may have a strong influence, as flashing effects related to local pressure drops may occur. Thus, accurate knowledge of the void fraction is needed, which is not typically the case for microchannels. This and other issues, such as thermal instabilities and/or compressibility effects, may affect the measured values and the models developed upon them, as reported by Consolini [90].

Most of the existing two-phase frictional pressure drop prediction methods are empirical, i.e. based on experimental databases. Traditionally, these methods are based on two-phase multipliers, which serve to correlate the two-phase pressure drop from the single-phase value. Lockhart and Martinelli [91] were first in proposing this approach in 1949. They defined two multipliers, one for each phase (liquid and vapour). From the ratio of the two two-phase multipliers, and considering the two phases as separate turbulent flows, the Lockhart and Martinelli parameter can be calculated:

$$X_{tt} = \left(\frac{1-x}{x} \right)^{0.9} \left(\frac{\rho_v}{\rho_l} \right)^{0.5} \left(\frac{\mu_l}{\mu_v} \right)^{0.1} \quad (2.9)$$

Several authors provided correlations of the two-phase multiplier based upon large experimental databases, using the Lockhart and Martinelli parameter and other non-dimensional groups. In particular, the correlation by Friedel [92] is widely used in literature as a first approach to the two-phase frictional pressure drop determination. The method by Müller-Steinhagen and Heck [93] proposes an interpolation between the pressure drop as “all-liquid” and “all-vapour” flows. This method is recommended as it provides good prediction of independent experimental databases [94]. Furthermore,

variations of the Müller-Steinhagen and Heck correlation were recently proposed [95, 96] to adapt it to a larger experimental database and to tubes with non-circular sections, respectively. All these methods are detailed in appendix A, section A.1.2.

Flow-pattern based pressure drop methods are regarded with interest. The model by Moreno Quibén [97] for horizontal channels captures the effect of a variety of local flow patterns and interfacial wave effects on the two-phase pressure drop. The authors report prediction of a larger fraction of experimental data than most of the two-phase multiplier methods, at the cost of a more complex model implementation and the need of specifying local flow patterns, which are not always possible to measure/observe accurately.

An example of a mechanistic pressure drop model is the one proposed by Cioncolini and Thome [98] for two-phase annular flows, as part of an unified annular flow modeling suite that includes methods to predict physical effects like entrained liquid fraction and liquid film thickness. It is based on a large pressure drop experimental database from the literature. The method yielded accurate predictions of the database by Tibirićá and Ribatski, and even good match with experimental pressure drop data in multi-microchannels [99].

As the ITS Upgrade staves have a Π -bend for returning the cooling fluid (see section 3.6), predicting two-phase pressure drops in these and other singular elements, like diameter changes, is necessary, along with straight pipe pressure drop predictions, with the aim of determining the size of the channel needed for two-phase flows and later validate the experimental two-phase pressure drop measurements. However, experimental research studies in U-bends indicate a large amount of parameters influencing the flow beyond the curvature to tube diameter ratio and the bend orientation: type of fluid, operating pressure, flow pattern, vapour quality and void fraction are some of the parameters which play a role in the results. Subsequently, singular two-phase pressure drops prediction methods are scarce in the literature and might fail to reproduce experimental data.

The flow pattern-based model by Da Silva Lima and Thome [100] yields accurate predictions of the experimental results. It is based on experimental data and flow patterns in smooth U-bends in large channels ($D_i > 8$ mm). The model requires the flow pattern as an input, which is uncertain in most two-phase cooling systems in HEP particle detectors. A simpler implementation is given by the model by Chisholm [101], although its results should be regarded as an approximation and as a guideline only.

Recently, Padilla *et. al* [102] carried out two-phase flow visualization and pressure drop measurements of HFO-1234yf and R-134a refrigerants in horizontal U-bends. They adopted an statistical approach to estimate the perturbation length before and after the U-bend. At lengths of ten times the tube diameter upstream and twenty times the diameter downstream, there was no difference in the measured two-phase pressure drop values. U-bend. They compared their experimental database against four models, including the one by Chisholm, yielding the four of them poor predictions of the experimental data.

2.5.6 Flow boiling heat transfer

The inverse of the thermal resistance between a surface and a fluid is known as the heat transfer coefficient and it is expressed by Newton's law of cooling:

$$h = \frac{q}{T_{wall} - T_{fluid}} \quad (2.10)$$

The most efficient cooling systems are those displaying the highest heat transfer coefficients, hence minimising the thermal resistance between the surface and the coolant. This results in more compact system configurations, reduced coolant inventory and low temperature differences between the fluid and the surfaces to be cooled. In this line, systems with two-phase coolants generally achieve higher heat transfer coefficients than single-phase ones, making them ideal for high heat flux applications.

However, unlike in single-phase flows, two-phase heat transfer coefficients are not easily predicted theoretically. This is mainly due to the high number of parameters they depend on, such as: heat flux, mass flux, vapour quality, saturation pressure, type of fluid, presence of gravity, channel orientation, channel size and length, channel geometry, boiling stability, surface finish and surface roughness, tube material, heat flux hysteresis, and purity of the fluid, among others. The sheer amount of independent variables in experimental two-phase heat transfer studies makes extremely difficult to study the influence of each one while controlling for the rest of them. As a consequence, disagreement on the parameters contributing to the heat transfer coefficient and their importance is common amongst researchers.

This subsection presents insight on the flow boiling heat transfer mechanisms in macro- and microscale flows, a brief review on the influence of several parameters on the heat transfer coefficient, to finish with a survey on several leading flow boiling heat transfer coefficient prediction methods.

Flow boiling heat transfer mechanisms

The heat transfer mechanisms identified in macroscale flow boiling are related to the flow conditions. Fig. 2.14 shows the evolution of the flow patterns during flow boiling in a macroscale horizontal tube. First, in region A, the fluid enters as single-phase liquid and heat exchange occurs by forced convection. As more heat is transferred to the fluid, bubbles start to grow, even with the fluid still in subcooled conditions, leading to the bubbly flow pattern in region B. The flow shifts to the plug flow pattern (region C) as the vapour quality increases. As vapour bubbles start to coalesce in large vapour volumes of nearly the same diameter of the tube, the flow moves on to the slug flow pattern (region D). In regions B-D, which display low vapour qualities, the dominating mechanism is in most cases identified as nucleate boiling, coupled to forced convection to the subcooled liquid at very low vapour qualities. Nucleate boiling is a similar mechanism to pool boiling and it predominates at high heat fluxes and low vapour qualities. Vapour bubbles grow consistently at specific locations of the tubes named nucleation

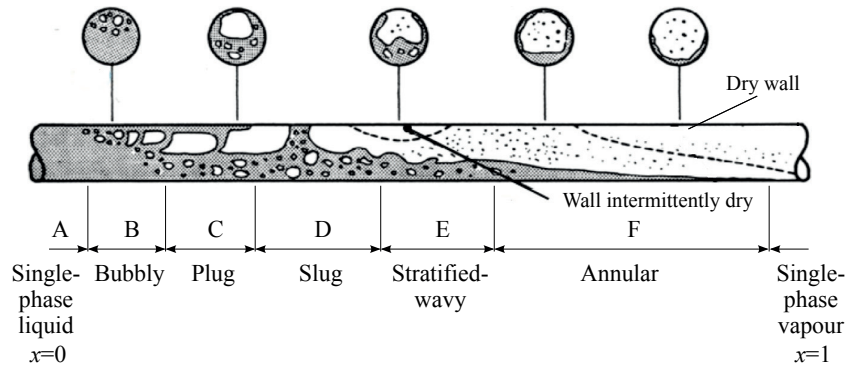


Figure 2.14: Flow pattern evolution in a boiling flow in a conventional horizontal tube. The flow is represented from left to right in the figure. Image adapted from Collier and Thome [75].

sites. Heat transfer coefficients under those conditions are usually high. Since nucleate boiling is a mechanism depending strongly on the surface micro-geometry and wettability, nucleate boiling heat transfer coefficient correlations display usually high dispersion in their results.

Nucleation effects are progressively suppressed as vapour quality increases. In macrochannels, stratification effects may appear, and the slug flow pattern will display a thicker liquid film at the bottom of the channels, as shown in region E in Fig. 2.14. As the vapour bubbles keep growing, convective boiling becomes a stronger heat transfer mechanism, involving conduction and convection through the liquid film at the tube periphery, with evaporation at the liquid-vapour interface. The liquid slugs become thinner to the point of disappearing, and the flow is then constituted by a central vapour core and a liquid film at the channel wall. This is known as the annular flow pattern (region F). Convective boiling is here the dominant heat transfer mechanism. Liquid evaporation occurs at the liquid-vapour interface until the wall dries out of liquid and the heat transfer coefficient drops to very low values, corresponding to single-phase forced convection to vapour. This flow pattern is usually referred as mist flow, and it is essentially a vapour flow with entrained liquid droplets.

In conventional channels, liquid phase stratification occurs related to gravity effects. Stratified flow patterns are characterised by a non-uniform heat transfer coefficient distribution around the channel periphery. This behaviour is illustrated in Fig. 2.15 for measurements taken by Tibiriçá and Ribatski [103]. At vapour qualities up to 0.85, heat transfer at the lower part of the channel is dominated by convective and nucleate boiling effects. Since the liquid film is thinner at the top of the tube, the thermal resistance across it is lower and the local heat transfer coefficient is higher than at the bottom. However, at vapour qualities over 0.85, the liquid film dries out from the tube wall and forced convection heat transfer to vapour occurs locally, resulting in a heat transfer coefficient drop. This effect starts at the top of the tube, where the liquid film is thinner, explaining the early local heat transfer coefficient drop at the top of the tube in Fig. 2.15. The biggest cooling modules for the ALICE ITS Upgrade developed in this thesis feature round 2.667 mm ID polyimide channels directly contacting the cooling plate at a fraction of their periphery. It is important to take into consideration stratification effects for the design

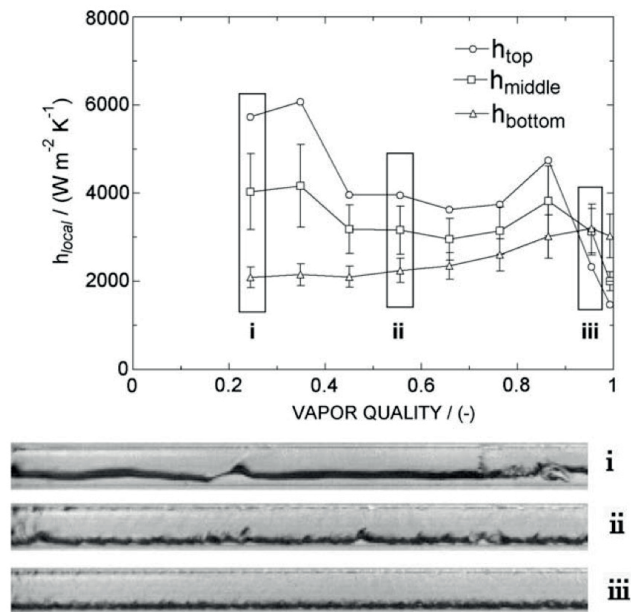


Figure 2.15: Heat transfer coefficient at three locations in the channel perimeter and two-phase flow images at three vapour qualities of R134a refrigerant in a 2.32 mm ID channel, $G=100 \text{ kg m}^{-2} \text{ s}^{-1}$, $q=5 \text{ kW m}^{-2}$, $T_{sat}=22^\circ\text{C}$). From Tibirić and Ribatski [103].

and operation of the cooling modules, if a two-phase evaporative coolant is chosen.

Microscale two-phase flows may differ significantly from the macroscale ones, as described in section 2.5.2. For instance, stratified flow patterns do not occur in microscale. Heat transfer mechanisms may also differ to those occurring in conventional channels, being this one of the main points of discussion amongst researchers in two-phase heat transfer. In annular flows, Kandlikar [104] indicated the presence of nucleate boiling effects in the formation of vapour bubbles within the liquid film next to the tube wall. The conjugate effect of this mechanism with conduction and convection across the liquid film was deemed to be the cause of the high heat transfer rates in micro-channels.

Fig. 2.16 illustrates the heat transfer coefficient versus vapour quality of two-phase flow boiling R236fa refrigerant in 67 parallel $100 \mu\text{m}$ square channels by Szczukiewicz *et. al* [105], overlaying flow visualisations recorded in a 0.79 mm ID sight glass at the exit of the test section by Revellin and Thome [106]. No stratified flow patterns were observed. The annular flow pattern occurs from low vapour qualities and presents a heat transfer coefficient rapidly increasing with vapour quality. In order to increase the heat transfer efficiency and compactness of the evaporator, annular flows will be preferred in this particular case.

Parameters of influence in flow boiling heat transfer

The large amount of parameters influencing flow boiling heat transfer and the exact extent of their importance causes discrepancies in experimental databases. A brief discussion on the effects of the

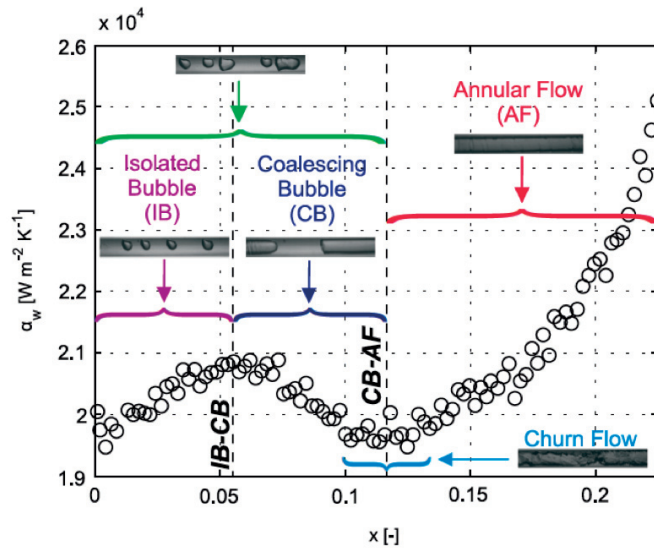


Figure 2.16: Heat transfer coefficient trend for R236fa refrigerant flow boiling, $G=2299 \text{ kg m}^{-2} \text{ s}^{-1}$ and base heat flux $q_b=48.6 \text{ W cm}^{-2}$ in 67 parallel $100 \mu\text{m}$ square channels by Szczukiewicz *et. al* [105]. Flow visualisation images in a 0.79 mm ID sight glass are overlaid, by Revellin and Thome [106].

main parameters is presented below.

Flow parameters may have a great influence on two-phase heat transfer coefficients depending on the dominant heat transfer mechanisms. Generally speaking, nucleate boiling is predominant when the heat transfer coefficient increases with heat flux but does not depend on the mass flux and vapour quality. However, the heat transfer coefficient increasing with increasing heat fluxes does not necessarily mean that the dominating heat transfer mechanism is nucleate boiling. Qu and Mudawar [107] reported that the heat transfer coefficient increases in annular flows with heat flux due to evaporation of the liquid film. On the other hand, convective boiling is the leading mechanism if the heat transfer coefficient increases with vapour quality and mass flux but is not influenced by the heat flux [108]. Increasing mass fluxes and vapour qualities lead to forced convection enhancement and higher temperature gradients in the fluid close to the channel walls. This effect is intensified by the presence of thinner liquid films. There are, however, discrepancies amongst researchers on the trends and the impact of the flow parameters on the heat transfer coefficients and subsequently, the ranges where convective and nucleate boiling dominate. Such discrepancies might be motivated by the lack of control over the rest of parameters influencing the heat transfer coefficient during experimental tests.

The fluid pressure^a may influence the flow boiling heat transfer coefficient. For instance, in most fluids, surface tension decreases as pressure increases. This typically results in lower bubble departure diameters, since this variable depends on surface tension. As a result, a higher density of nucleation sites is expected, with the subsequent intensification of nucleate boiling [108], and an

^a If saturated conditions are verified along the whole channel, the fluid saturation temperature can be used in equivalence to pressure via the fluid equation of state.

increase of the flow boiling heat transfer coefficient. Revellin *et al.* [109] observed that at higher saturation temperatures, nucleate boiling dominated over a larger range of vapour qualities. It must be noted though, that the trend with pressure of other fluid physical properties influencing flow boiling heat transfer mechanisms must be taken into consideration, such as the specific volume of vapour or the liquid thermal conductivity.

The large discrepancies frequently found among experimental databases are often related to the test section characteristics and operation, and to the intrinsic difficulties that working in microscale conditions entails [110]. Flow instability is claimed to be one of the top reasons of experimental result mismatch between similar experimental studies [108], especially for multi-microchannels. Thermal instabilities are related to compressibility effects in the flow, which increase liquid entrainment in the vapour flow and result in non-uniform liquid film distribution and evaporation. This may seriously affect the pressure drop and the heat transfer coefficient, which would not be stable in time. The occurrence of dryout might be advanced to lower vapour qualities too. For suppressing instabilities, Consolini and Thome [111] recommended the use of sectional restrictions at the entrance of the channels. Conversely, in stable boiling conditions, heat transfer coefficients increase up to very high vapour qualities due to stable liquid film evaporation. The liquid film wets the channel wall uniformly, minimising the presence of intermittent dry patches on the wall. Partial dryout is thus postponed to very high vapour qualities.

The channel surface characteristics, in particular the surface finish and roughness, are well known to influence the flow boiling heat transfer coefficient, at least at high heat fluxes [112]. Despite this, their impact is not usually considered in the experimental studies, with a few studies reporting only the average surface roughness. Karayiannis *et al.* [108] performed experimental flow boiling heat transfer studies on smooth and coarse tubes. They found out that surface characteristics seem to influence flow patterns at mostly low vapour qualities. Also, a high wall superheating was necessary to experience nucleate boiling conditions in the smooth tube, while this occurred at lower wall superheating for the rough channel. Finally, it was seen that the heat transfer coefficients increase with heat flux for coarse tubes, while for smooth tubes heat flux does not seem to have an influence. They concluded that smooth tubes would have fewer nucleation points and therefore convective boiling would presumably dominate over a wider vapour quality spectrum. Kandlikar and Spiesmann [113] stated that the presence of microcavities has a stronger influence on the heat transfer coefficient than the average surface roughness. A thorough characterisation of the channel surface is therefore needed, beyond the average surface roughness measurement. In a later work, Pike-Wilson and Karayiannis [114] studied the flow boiling heat transfer in three tubes made of copper, brass and stainless steel, after in-depth examination of the surface characteristics. They reported no clear correlation between the heat transfer coefficient and the surface finish at $x < 0.35$, with the heat transfer coefficient being higher for rougher surfaces at higher vapour qualities.

The channel material may have an influence on the heat transfer coefficient. In particular, in

microchannels, the axial heat conduction along the channel walls can become significant if the channel walls have a similar thickness as the channel width, in non-uniform heat flux scenarios, or if the flow is thermally developing. Celata *et al.* [115] proposed an expression to evaluate this effect in single-phase flows. Lower Nusselt numbers are obtained if not considering axial heat conduction in certain scenarios, according to Lin and Kandlikar [116]. They mentioned wall and fluid temperatures increasing as the cause. For two-phase flows, the axial temperature gradients are usually lower than for single-phase, and this effect is less important. Conjugate effects in two-phase flow boiling might be important if nucleate boiling dominates in channels with high wall thermal conductivity. When a vapour bubble grows in a nucleation site, it yields a locally high heat transfer coefficient. Afterwards, the required wall superheating for the growth of another bubble at the same nucleation site will be quickly reached, thanks to the high thermal conductivity of the channel wall. In low-thermal conductivity, thin-walled channels (such as the polyimide channels used in the ALICE ITS Upgrade cooling system), the needed wall superheating for bubble nucleation would be more difficult to be reached at the nucleation site after the previous vapour bubble detached, and thus nucleate boiling effects might be weakened. Pike-Wilson and Karayiannis [114] stated that the channel material did not influence strongly their flow boiling heat transfer results. In particular, they found out that among the three channel materials used in their study, the one with the highest thermal conductivity (copper) displayed the lowest boiling heat transfer coefficients.

Another parameter influencing the heat transfer coefficient is the test section length. Longer heated lengths result in lower heat fluxes and a development of the flow patterns along the channel, giving rise to different trends of the local heat transfer coefficients. Karayiannis *et al.* [108] evaluated the influence of the test section length for three circular 1.1 mm ID channels 150, 300, and 450 mm long. They first reported a decrease in the vapour quality at which the transition into annular flow occurs as the test section length increases. In the short tube it was observed a higher influence of the heat flux on the heat transfer coefficient, typically associated to nucleate boiling, whilst this does not occur in the longer channels. Mass flux effects on the heat transfer coefficient occur for the longer tubes at $x > 0.25$. This indicates that a shift from nucleate boiling to convective boiling as dominant heat transfer mechanism is expected as the tube length increases. Also, higher heat transfer coefficients were measured for the shorter lengths when comparing experimental cases with the same outlet vapour quality. Last, it was reported that the heat transfer coefficient drop measured at low vapour qualities, after boiling incipience, was higher for the longer channels. The authors attributed this effect to the assumption of a linear pressure drop along the section, which becomes less valid for longer tubes, and can result in heat transfer coefficient measured trends being different than the real ones. The findings in this work may partly explain the dispersion in the experimental data in the open literature, as channel heated lengths vary highly among similar studies.

Hysteresis effects are claimed to have an effect on the transitions in flow patterns when increasing or decreasing the heat flux [117]. The occurrence of hysteresis effects should be taken into consideration

when measuring the heat transfer coefficient, adopting measures to verify the flow pattern in studies where it is relevant.

Polyimide channels are to be used in the ALICE ITS Upgrade cooling system. These channels display very low thermal conductivity (130 times lower than stainless steel), very thin walls (values of 25 μm -thick walls for a 1 mm ID tube are readily available), and very smooth surfaces. Fiorenza *et al.* [25] measured the statistical average roughness of the surfaces of a polyimide microchannel heat sink using Atomic Force Microscopy (AFM), obtaining values ranging from 12 to 35 nm. Smooth metallic channels are rougher, with values in the order of 100-400 nm usually reported in experimental heat transfer studies [103]. A literature survey revealed a lack of experimental data regarding flow boiling in polyimide or plastic tubes. Hence, it is difficult to predict the flow boiling heat transfer characteristics in these channels, since they are too different from metallic tubes. The primary aim of the study presented in chapter 6 is to characterise the flow boiling heat transfer of R245fa refrigerant in a polyimide channel. By analysing parametrically the results, further insight will be provided on the influence of the flow parameters on the heat transfer coefficient.

Heat transfer coefficient methods and correlations

Many correlations and methods to determine two-phase flow boiling heat transfer coefficients in conventional and mini-/microchannels are available in the literature. Disagreement on the phenomena having an effect on the heat transfer coefficient and dispersion in experimental databases causes flow boiling heat transfer prediction methods to often yield scattered results. The methods can be fundamentally classified as mechanistic (built upon consideration of the physics of the flow, solving the mass, momentum and energy equations, and eventually turbulence), or empirical (where correlations are adjusted based on the effects of the relevant parameters on the heat transfer coefficient as observed in a reference experimental database). Other models are a combination of the two kinds, using physics criteria for the foundations of the model, which is later adjusted using experimental databases. Several heat transfer coefficient methods are described below. The methods used in this dissertation are detailed in appendix A, section A.2.3.

Most empirical heat transfer correlations consider the superposition of two heat transfer mechanisms, nucleate and convective boiling, in a power law fashion, as follows:

$$h_{tp} = \left[(S h_{nb})^n + (F h_{cb})^n \right]^{\frac{1}{n}} \quad (2.11)$$

where h_{nb} and h_{cb} are the nucleate and convective boiling heat transfer coefficients, respectively. S and F are multipliers that account for nucleate boiling suppression and convective boiling enhancement. Last, n is an exponent dimensioning the superposition of both effects. $n = 1$ would result in additive models. The pioneering model by Chen [118] assumes $n = 1$. The model by Saitoh *et al.* [119] is also an addition model. $n = 2$ refers to asymptotic models, where the aggregate two-phase heat transfer

coefficient tends to be larger between the nucleate and the convective boiling heat transfer coefficients components. There are methods that use $n = 3$ [120]. Even $n = \infty$ is possible, in order to use only the larger of the two heat transfer coefficients.

Liu and Winterton [121] developed an asymptotic correlation ($n = 2$). Their method is based upon a large experimental database comprising subcooled and saturated flow boiling data in channels of diameters from 2.9 mm to 32 mm. The nucleate boiling heat transfer coefficient (h_{nb}) is calculated according to the correlation by Cooper [122], and the convective boiling heat transfer coefficient is determined using the single-phase correlation by Dittus and Boelter [123]. The correlation also accounts for the roughness of the channel wall. The Liu and Winterton correlation is simple to implement and accounts for the combination of the basic nucleate and convective boiling effects. It has been widely applied in the literature, not only to conventional channels, for which it was developed, but also to mini- and microchannels.

Kandlikar and Balasubramanian [124] proposed a heat transfer coefficient correlation for flow boiling in the mini- and microchannel range, based on the model by Chen [118]. The authors put forward different expressions depending on the value of the liquid-only Reynolds number (Re_{LO}): $Re_{LO} > 3000$ (large diameter tubes), $1600 < Re_{LO} < 3000$ (laminar, transition flow region in minichannels) and $Re_{LO} < 1600$ (microchannels). Unlike other methods, this correlation includes constants accounting for the tube material and type of fluid. They reported heat transfer coefficient overestimation at low vapour qualities due to increased heat transfer rate associated to the onset of nucleate boiling in the experimental database they used as validation.

Kanizawa *et al.* [125] developed a heat transfer coefficient correlation for minichannels based upon more than 2000 experimental points in channels ranging from 0.6 to 2.6 mm ID. The correlation consists in calculating the flow boiling heat transfer term based on the additive method by Saitoh *et al.* [119]. In the dryout region, a linear interpolation is performed between the heat transfer coefficient at $x = x_{dryout}$ and the forced convection to vapour heat transfer coefficient value. The x_{dryout} is assumed to be the vapour quality at which the Critical Heat Flux (*CHF*) occurs. The authors suggest to determine it using the x_{crit} obtained by applying the *CHF* method by Zhang *et al.* [126].

Flow pattern-based heat transfer coefficient methods fall in the category of empirical methods with a phenomenological background. This approach certainly leads to accurate prediction of the heat transfer coefficient, as specific methods are fitted depending on the physical phenomena present in each flow pattern. However, the implementation of these methods is more complex than empirical ones, and requires determining or assuming the flow pattern as an additional step. This could lead to inaccurate results, especially if flow patterns are determined by subjective methods. Examples of these methods are the models by Kattan *et al.* [127] and by Wojtan *et al.* [128], which are widely referenced in literature. Also, Cheng *et al.* [129] developed a flow pattern-based heat transfer coefficient model for CO_2 .

Another semi-empirical heat transfer model is the one by Cioncolini and Thome [130]. The authors put forward an algebraic turbulence model for annular flows, as part of a unified annular flow modeling suite. The model is targeted to solve heat transfer and momentum across the liquid film in adiabatic and evaporating flows. Based on a database spanning channel diameters from 1.03 to 14.4 mm, the model provides heat transfer coefficient calculation capabilities and estimation of the liquid film thickness, void fraction, and entrained liquid fraction. No heat flux effects were included because no nucleate boiling was considered, as it is not expected to occur in annular flow except at high heat fluxes. The model reproduced well experimental databases and captured the main trends.

Most heat transfer coefficient prediction methods are built considering large experimental databases, but no model has been developed based on flow boiling data in polyimide channels, like the ones to be used in the ALICE ITS Upgrade cooling system. In chapter 6, a comparison between the experimental results of flow boiling R245fa refrigerant in a polyimide channel and the predicted values by the most appropriate heat transfer coefficient methods described in this subsection is presented. The aim is to assess the applicability of the models to another tube material and surface and understand which flow boiling heat transfer mechanisms rule for the polyimide tube in a range of flow conditions.

Chapter 3

Cooling system R&D for the Upgrade of the ALICE Inner Tracker System

3.1 Introduction

The present chapter describes the main requirements the cooling system for the Upgrade of the ALICE ITS detector shall fulfil. The R&D on the different cooling solutions is presented, focusing on the ultra-lightweight cooling structures that were finally optimised and tested.

3.2 The ALICE Inner Tracker System Upgrade detector

The Upgraded ALICE Inner Tracking System (ITS), to be commissioned during Long Shutdown 2 (LS2) [4], is 12.5 Giga-pixel “camera” with 10 m^2 of sensitive surface, detecting individual collisions and measuring the track of subparticles at read-out frequencies up to 400 kHz. The design and implementation of a cooling system is foreseen as part of the ITS Upgrade project, in parallel to other activities such as the physics scope development, the mechanics and electronics engineering, and services integration [5].

The ITS Upgrade is the innermost of the 18 particle detectors of the ALICE Experiment. Its morphology is illustrated in Fig. 3.1. The detector is arranged in seven concentric layers around a central cylindrical part, the *beam pipe*. Inside this thin cylinder, made of beryllium wrapped in several layers of different materials, beam collisions occur, emitting subparticles crossing the ITS layers. The silicon layers are arranged in radiuses ranging from 22 mm to 400 mm from the interaction point.

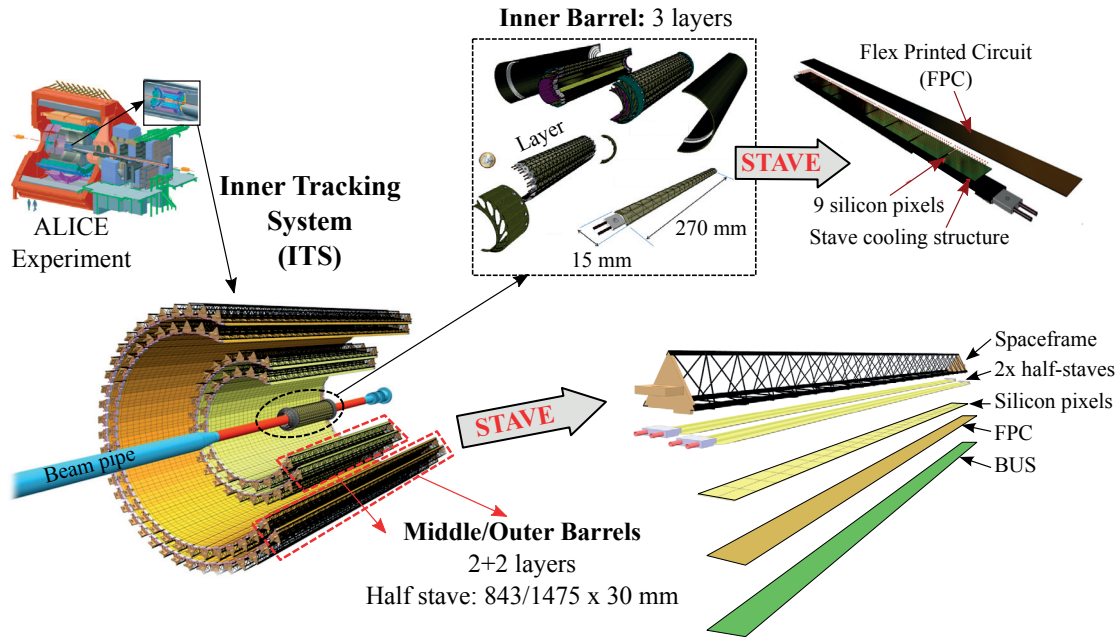


Figure 3.1: Location of the Inner Tracker System (ITS) at the ALICE Experiment, showing the detector modularity: from a whole assembly to the smallest independent part, the stave (right of the scheme). The surface occupied by the detector chips on each stave and half-stave is indicated.

The three innermost layers of the ITS constitute the Inner Barrel. It has a modular design; each layer is segmented in the azimuthal direction in individual modules called *staves*. The stave is the smallest individual part of the Inner Barrel. Each of the 48 staves in the Inner Barrel supports nine $15\text{ mm} \times 30\text{ mm}$, $50\text{ }\mu\text{m}$ -thick silicon pixel chips, aligned in z (barrel axial direction), making up a detection area of $15\text{ mm} \times 270\text{ mm}$ per stave that dissipates power during detector operation.

The remaining four layers are grouped in two barrels: the Middle and Outer Barrel. The staves are significantly bigger than the Inner Barrel ones: the staves in the two layers of the Middle Barrel are 60 mm wide by 870 mm long, while the staves at the two layers constituting the Outer Barrel are the same width but 1502 mm long. Because of dimensional and geometrical constraints, the staves are segmented in two halves, along the stave longitudinal axis. Each of the halves is named *half-stave* and they constitute a sub-modular stave design. The chips are glued in the central 843 mm and 1475 mm of each Middle and Outer Barrel half-stave, respectively. The half-staves are attached to a separate structure, named *spaceframe*, providing positioning and mechanical support.

A cross-sectional view of the Inner and Middle/Outer Barrels can be found in Fig. 3.2a and 3.2b, respectively, which illustrate the compactness and spatial constraints of the ITS Upgrade. The dimensions of the barrels, as well as a summary of the number of staves and power dissipation, are later summarised in Table 3.1.

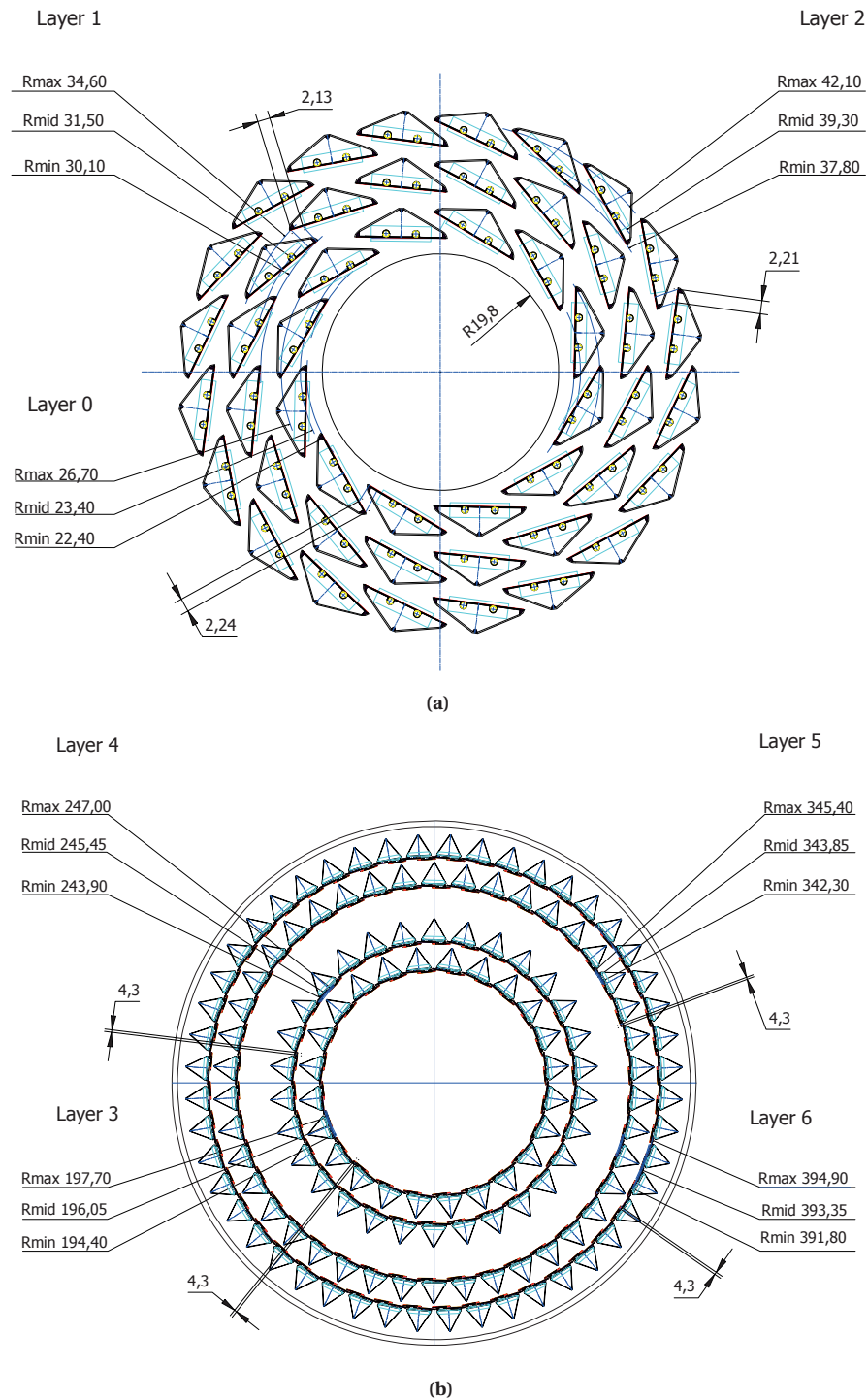


Figure 3.2: Cross-sectional view of the ITS Upgrade: (a) Inner Barrel (3 layers), with the beam pipe at the centre (radius=19.8 mm); (b) Middle and Outer Barrel (2+2 layers). The Inner Barrel would be a small cylindrical volume at the centre of (b) with a radius 5 times smaller than the Middle Barrel. All dimensions are expressed in mm. Images extracted from [5].

3.3 Thermal and material requirements of the ITS Upgrade

3.3.1 Thermal requirements

As described in section 2.2.2, silicon particle detectors dissipate heat due to Non-Ionising Energy Loss (NIEL) and front-end electronics in the silicon chips. At the time this document is written, the requirements the ITS Upgrade detector cooling system should comply with are the following [5]:

1. **Chip power dissipation:** the expected power density with the Alpide4 chip technology [5] is 0.058 W cm^{-2} at the Inner Barrel staves and 0.031 W cm^{-2} at the Outer Barrel staves. These figures consider also the power dissipated by the Flex Printed Circuit (FPC), and include a factor of safety of 1.5. However, at the time most of the stave thermal tests were performed, the feedback from the electronics working group was a nominal power density value from 0.10 to 0.20 W cm^{-2} for the Inner, Middle, and Outer Barrel staves, resulting in an effective input power density of 0.15 to 0.30 W cm^{-2} after applying a factor of safety of 1.5. Some thermal tests were performed at 0.50 W cm^{-2} . Cooling performance results obtained at such power densities provide a generous safety margin that accounts for hypothetical extra heat load intakes, such as from radiative heat transfer sources, and free convection with the surrounding air. A more detailed analysis is presented in section 4.3.1.
2. **Operational temperature and uniformity:** the chip temperature shall never exceed 30°C . As explained in section 2.2.2, if the chip temperature increases by 7 K, the radiation damage is doubled. Furthermore, chip temperature gradients should be minimal to experience uniform radiation damage, where the 5-10 K range is deemed acceptable.
3. **Minimum temperature:** the minimum temperature in the cooling system should be higher than the highest dew point of the air expected at the ITS Upgrade site, 12°C . This is to prevent condensation on the chips and electronics, which could destroy or severely damage them or create short-circuits.
4. **Thermal robustness:** the cooling system must operate over a wide range of conditions, coping with the highest power densities even in poor cooling conditions (i.e low coolant flow rate in one or more staves, high coolant temperature). At the same time, low sensitivity to load imbalances is desired.

At first glance, the thermal requirements are far from extreme. However, the challenge is to comply with them while coping with the strict material budget requirements presented below.

3.3.2 Material budget and general requirements

High detector resolution, compactness, and inaccessibility during operation drive the following requirements:

1. **Material budget:** values of x/X_0 [%] shall not exceed 0.3% per layer of the Inner Barrel and 1.0% per layer in the Middle and Outer Barrel. The material budget is the strictest constraint of all. The first layer in the present ITS detector has a material budget of 1.14% [29]. It is emphasised that the material budget limit per layer includes the influence of the slight overlap between staves, as seen in Fig. 3.2.
2. **Compliance with radiation and material safety directives:** all materials used in the cooling system must be radiation hard at the expected levels in the detector, compatible with each other, and comply with CERN material safety regulations [19].
3. **Modularity:** the stave should remain as the smallest individual part of the detector, facilitating the disassembly and the replacement of faulty chips. The Middle and Outer Barrel staves are each composed of two half-staves, that can be individually detached from the mechanical support.
4. **One-side accessibility:** due to integration requirements, the ITS Upgrade staves can only be accessed from the one side of the experiment, named the “A-Side”, as depicted in Fig. 3.3. Input and return cooling lines, as well as cables and other services, should all run at the same ITS extremity.
5. **Mechanical stability:** if the detector chips are mounted directly on the cooling system, it should guarantee precise chip positioning and planarity to the specifications of the detector [5]. These mechanical validation tests are the competence of the ITS Upgrade Mechanics working package and are out of the scope of this thesis.
6. **Reliability:** once in operation, the detector is not halted for months. Thus, technical intervention is not possible but once or twice a year, and only after the radioactivity in the experimental site has decayed. Hence, the system should require minimal maintenance and operate on simple principles.

Table 3.1 summarises the dimensional and thermal characteristics of the ITS Upgrade detector. The total dissipated heat loads expected for the Inner, Middle and Outer Barrel are, respectively, 111.9, 853.2 and 2467.5 W. The total power dissipation of the whole ITS Upgrade detector is 3332.6 W. The radiation doses per layer and year, NIEL and TID, are included in the last two columns, considering 6 years of operation and a factor of safety of 10, as stated in the ITS Upgrade Technical Design Report [5]. At the time of elaboration of the present document, the TID and NIEL radiation dose values were expected to be higher, with 2700 krad and $1.7 \cdot 10^{13} \text{ 1 Mev n}^{eq} \text{ cm}^{-2}$ at layer 0, and 100 krad and

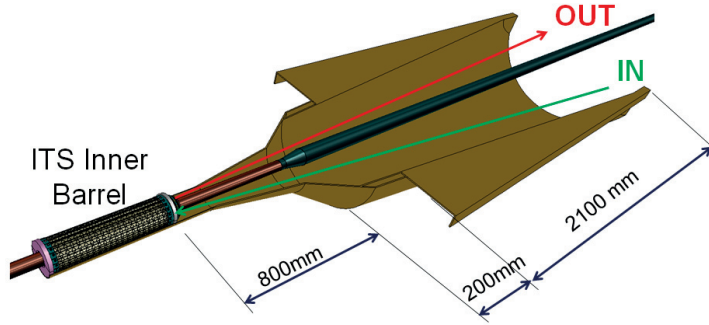


Figure 3.3: Schematic view of the one-side access to the Inner Barrel staves.

Table 3.1: Architecture, power dissipation and radiation doses of the Inner, Middle and Outer Barrel.

Layer	Radius [mm]	Nr. staves (half-staves)	Length ^a [mm]	Power dissipation				Radiation dose	
				P_d^b [mW cm ⁻²]	$E_{half-stave}$ [W]	E_{stave} [W]	E_{layer} [W]	NIEL ^c [1 MeV n _{eq} cm ⁻²]	TID ^c [krad] ^d
0	23.4	12					28.0	$9.2 \cdot 10^{12}$	686
1	31.5	16	270	58	-	2.33	37.3	$6.0 \cdot 10^{12}$	380
2	39.3	20					46.6	$3.8 \cdot 10^{12}$	216
Total power Inner Barrel [W]							111.9		
3	196.1	24 (48)	843	31	7.9	15.8	379.2	$5.4 \cdot 10^{11}$	15
4	245.5	30 (60)					474.0	$5.0 \cdot 10^{11}$	10
Total power Middle Barrel [W]							853.2		
5	343.9	42 (84)	1475	31	13.7	27.4	1152.3	$4.8 \cdot 10^{11}$	8
6	393.4	48 (96)					1315.2	$4.6 \cdot 10^{11}$	6
Total power Outer Barrel [W]							2467.5		
Total power ITS Upgrade [W]							3332.6		

10^{12} 1 MeV n^{eq} cm⁻² at layer 3. This increase in the radiation dose is estimated to have no severe consequences on the detector services specifications.

3.4 Status of the ITS Upgrade project at the start of this thesis

The work presented in this dissertation is the result of a collaboration between the CERN Projects section at the Cooling and Ventilation group at the Engineering department (EN-CV-PJ), in which the author worked, and the ALICE ITS Upgrade project, towards the development and validation of a cooling system for the future detector. The ITS Upgrade project had already started at the time the collaboration began, with early definitions of the physics scope, the development of the detector chips

^a Length of the stave/half-stave where the detector chips are installed. The staves at the Inner barrel are 20 mm longer. Middle and Outer barrel staves are 27 mm longer.

^b Power dissipation of the detector chips plus the flex cables. A factor of safety of 1.5 is included.

^c Includes a safety factor of 10.

^d 1 krad=10 Gy

and the definition of the detector geometry.

The development of a cooling system started with the work described in this thesis. The design, development, optimisation and validation of the cooling systems object of the dissertation is the result of a collaborative and iterative effort with the Mechanics team (this collaboration took place within the Mechanics and Cooling working package) and the whole ITS Upgrade project in general, regularly exchanging information on the progress of all detector parts and services.

In an initial R&D stage of this thesis, air cooling concepts were explored, as described next in section 3.5. These concepts were soon discarded due to insufficient cooling capabilities at the time (early detector chips were expected to dissipate between 0.3 and 0.5 W cm^{-2} instead of the current 0.10 - 0.15 W cm^{-2} or lower) and mechanical reasons (mainly potential vibration problems leading to chip destruction). Instead, a stave concept embedding lightweight tubing for coolant circulation, described in section 3.6, was developed and optimised in close collaboration with the Mechanics and Cooling working package coordinators R. Santoro, and later C. Gargiulo. The analytical thermal studies and experimental cooling tests were entirely performed by the author of this thesis, who actively participated in the optimisation process of the stave layouts.

It is worth emphasising that other research groups and universities initially proposed different cooling ideas. A group from INFN Bari suggested the use of microchannels made of polyimide (Kapton[®]) to be used with single-phase water [25]. The microchannels are glued to a stave structure, similar to the one depicted in Fig. 2.6, and the detector chips would be glued to the bottom surface of the microchannels. Such solution does not guarantee a chip positioning and planarity as accurate as the ultra-lightweight concept introduced in section 3.6, and it is more complex too. Another concept, proposed by Francescon *et al.* [131], consists in interconnected silicon micro-evaporators using boiling C_4F_{10} refrigerant as coolant. Similarly to the polyimide microchannels, the silicon micro-evaporators would be attached to the structure in Fig. 2.6. The results of the cooling tests of this solution revealed high pressure and saturation temperature drops due to the length of the stave to be cooled (270 mm). Besides, manufacturing a single micro-evaporator as long as one Inner Barrel stave is not currently achievable, obliging to bridge two micro-evaporators in series. This results in high local pressure and saturation drops at the bridging points. For these reasons, this solution is not operative at a stave level. Last, staves with impinging jet air cooling were put forward by a collaborating group from University of Saint Petersburg. The feasibility of this concept was analysed by the author by means of CFD (see section 3.5). Although this solution works from a thermal point of view at power densities up to 0.30 W cm^{-2} , it requires from very precise and laborious gluing of the chips to the stave, and local air velocities will exert high stresses over the $50 \mu\text{m}$ -thick detector chips, risking to break them. Subsequently, only the ultra-lightweight solution described and validated by the author in this thesis is currently considered for implementation in the ITS Upgrade detector.

3.5 Air cooling

In view of the example calculations in Tables 2.1 and 2.2 and the limitations of the ITS Upgrade in section 3.3.2, it can be acknowledged the challenge of developing a cooling system meeting the material budget constraints. Air cooling systems were considered in an early R&D stage. They are appropriate for the low power dissipation and room-temperature cooling conditions of the ITS Upgrade. Coupled with a light structure, they will provide low material budget too, as no liquid refrigerant or cooling channels are involved. Two configurations were studied from a thermal point of view through CFD simulations with the ANSYS Fluent software. The simulation setups and results are briefly described in the present section. No material budget calculations were done for the studied air cooling proposals.

3.5.1 Layer-by-layer air cooling

The first air cooling concept proposed consists of a layer-by-layer cooling approach, similar to the one used in the STAR experiment (see Fig. 2.3). The staves in each layer of the Inner Barrel would be made of triangular ducts as depicted in Fig. 2.4a, and in a similar fashion as shown in Fig. 3.2a. By then joining the triangular ducts in each layer in the Inner Barrel, the volumes between layers would be physically separated. Air would be injected in the triangular duct of each stave from the detector A-side and circulated back to that end through the gap between the beam pipe and layer 0. This is achieved by sealing the other Barrel end (C-Side), leaving 30 mm of additional longitudinal space for the air to be recirculated from the triangular ducts and into the gap between layers^a. The same process would happen in layers 1 and 2. The path followed by the air flow is depicted in Fig. 3.4a. The whole structure, which follows the geometry presented in Fig. 3.4b, would be made of thin, high-thermal conductivity CFRP to comply with the material budget requirements and, at the same time, provide mechanical support, spread the heat, and increase the heat exchange surface. The detector chips would be cooled from their top and bottom surfaces: one would face the inside of the triangular duct where the air is injected, and the other surface is facing the gap with the layer beneath or the beam pipe, where the airflow returns. Fig. 3.5 depicts the dimensions of the triangular ducts for the airflow entering the Inner Barrel, considering the geometric and mechanical needs of the barrel.

Prior to the CFD simulations, the thermo-hydraulic characteristics of the airflow in a single triangular duct were analytically calculated. In particular, the Reynolds number is expressed as follows:

$$Re_{D_h} = \frac{\rho u D_h}{\mu} \quad (3.1)$$

^a Air recirculation is necessary as only the front side of the barrel (A-side) is accessible, as mentioned in subsection 3.3.2.

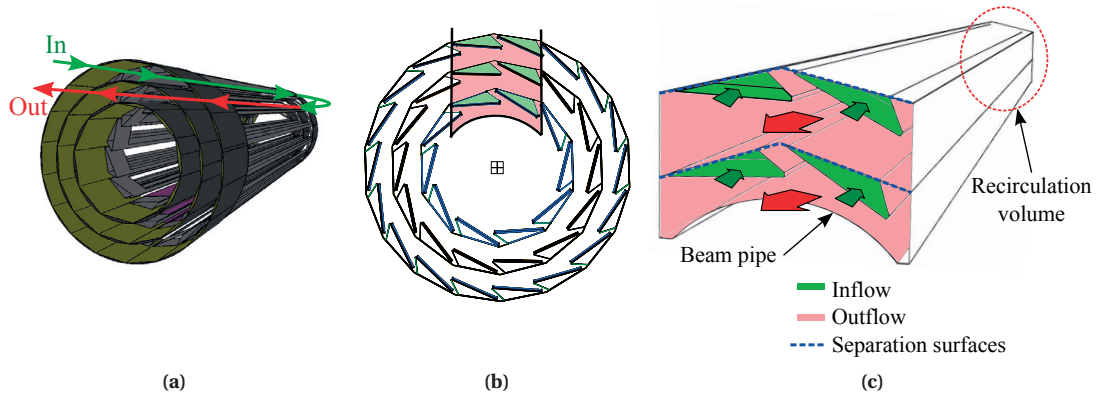


Figure 3.4: Inner Barrel layer-by-layer air cooling concept: (a) schematic airflow depiction; (b) Inner Barrel cross section, highlighting the gaps for the air in and outflows, and the domain considered in the CFD model (within the vertical lines); (c) CFD geometry considering the two innermost Inner Barrel layers. The inlet and outlet ducts for the air are indicated.

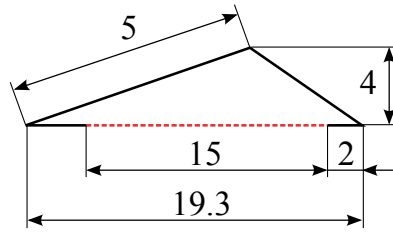


Figure 3.5: Dimensions of the triangular duct cross-section for air inflow in the layer-by-layer air cooling solution (not in scale). The dashed red line represents the location where the detector chips are to be glued. Dimensions expressed in mm.

where D_h is the triangular duct hydraulic diameter, defined below:

$$D_h = \frac{4A}{P} \quad (3.2)$$

where A is the sectional area of the triangular duct, and P is the perimeter. The dimensions of the triangular duct cross-section are displayed in Fig. 3.5.

The airflow temperature rise can be calculated using the following expression:

$$\Delta T_{coolant} = \frac{E_{chips}}{\dot{m}_{coolant} c_{p,coolant}} \quad (3.3)$$

E_{chips} is the total heat load dissipated by the 9 chips in each Inner Barrel stave. This figure is obtained using the power density, as follows:

$$E_{chips} = P_{d,chips} A_{chips} \quad (3.4)$$

A_{chips} is 270 x 15 mm for each Inner Barrel stave, corresponding to 7 chips 30 x 15 mm each.

Table 3.2 presents the analysis of the airflow characteristics inside a single triangular stave duct for different flow parameters. For the early nominal chip power density considered at the beginning of the ITS Upgrade project, 0.30 W cm^{-2} , flushing air at a velocity of 20 m s^{-1} results in an air temperature rise of 13.0 K . At the current 0.15 W cm^{-2} , air can be circulated at half the velocity (10 m s^{-1}) resulting in the same temperature rise. Low airflow velocities are preferred in order to prevent vibrations from occurring in the structure. At 10 m s^{-1} , the airflow is in the transitional regime ($Re_{D_h} = 2520$).

In order to assess the cooling performance of the layer-by-layer air cooling concept as an integrated solution (i.e. taking into account that the chips are cooled from inside the triangular structure and from the gap between the Inner Barrel layers as the air returns), a CFD model was built considering, for simplicity, only the two innermost layers (L0, L1), and an azimuthal sector comprising two staves, as depicted in Fig. 3.4b. The resulting CFD geometry is displayed in Fig. 3.4c. The boundary conditions presented for air in Table 3.2 were specified, with air being flushed at the inlet of the triangular ducts at 14°C . The detector chips are specified as pure silicon ($\alpha=150 \text{ W m}^{-1} \text{ K}^{-1}$), while for the CFRP structure, the K13D2U composite was chosen [42]. Planar and transversal conductivities are specified as follows: $\alpha_{planar} = 400 \text{ W m}^{-1} \text{ K}^{-1}$, $\alpha_{transversal} = 1.2 \text{ W m}^{-1} \text{ K}^{-1}$. These values are lower than the fibre thermal conductivity, and are taken considering that the effective sectional thermal conductivity of the CFRPs decreases with respect to the fibre values once the resin is added [44]. The SST $k-\omega$ turbulence model with corrections for low-Reynolds flows is used to solve the flow and heat transfer. The mesh on the CFD model is refined enough so that the boundary layer can be solved and an accurate heat transfer modeling is achieved.

The temperature map of the chip surface in steady-state at 0.30 W cm^{-2} and 20 m s^{-1} is illustrated in Fig. 3.6. In both the L0 and L1 layers, the chip surface exceeds the maximum allowable temperature of 30°C , although it should be noted that this CFD study was performed using the early power density specification for the ALICE ITS Upgrade of 0.30 W cm^{-2} , which is much higher than the value expected at the time this dissertation was written.

Table 3.2: Airflow characteristics of the layer-by-layer cooling proposal in a single triangular duct (stave, 9 chips, each $15 \times 30 \text{ mm}$). The changes introduced in each column are emphasised in bold font.

	Air at 20°C		Helium at 20°C
ρ [kg m^{-3}]	1.2		0.2
μ [Pa s]	$1.82 \cdot 10^{-5}$		$1.96 \cdot 10^{-5}$
c_p [$\text{J kg}^{-1} \text{ K}^{-1}$]	$1.5 \cdot 10^{-5}$		$9.8 \cdot 10^{-5}$
u [m s^{-1}]	20	10	20
Re_{D_h} [-]	5040	2520	777
$P_{d, chips}$ [W cm^{-2}]	0.30	0.15	0.15
E_{chips} [W]	12.2	6.1	6.1
$\Delta T_{coolant}$ [K]	13.0	13.0	7.6

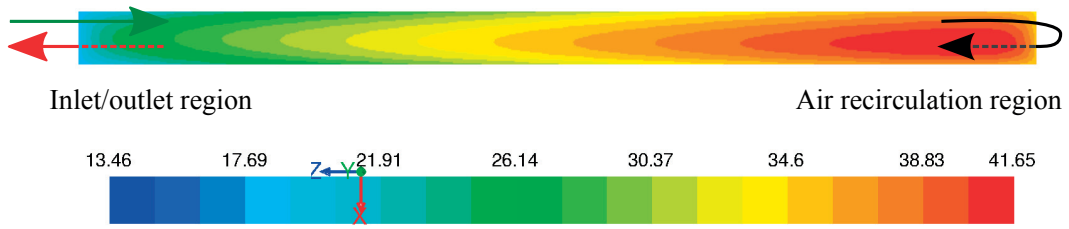


Figure 3.6: Chip temperature map at the innermost layer (L0), at a power density of 0.30 W cm^{-2} when cooling the Inner Barrel layer by layer with air injected at 20 m s^{-1} and 14°C .

By examining the heat flux from the detector chips towards the cooling air, it can be understood how the air cooling system can be optimised. Fig. 3.7a shows the heat flux from the chips in L1 to the air inside the triangular ducts (i.e. air inflow in the Inner Barrel), whilst Fig. 3.7b reports the heat flux of the chips in the same layer to the air in its way out the Inner Barrel (i.e. in the gap between L0 and L1). An imbalance on the heat transfer rate between both sides of the chips can be observed; in particular, a higher heat flux occurs to the air inside the triangular ducts. This is related to the fact that the airflow is more turbulent there, as the air velocity map in a longitudinal plane shows in Fig. 3.8.

This air cooling concept is simple and would cool the beam pipe too. However, it was put on hold because of its inability to cope with the high power densities assumed for the ITS Upgrade detector at

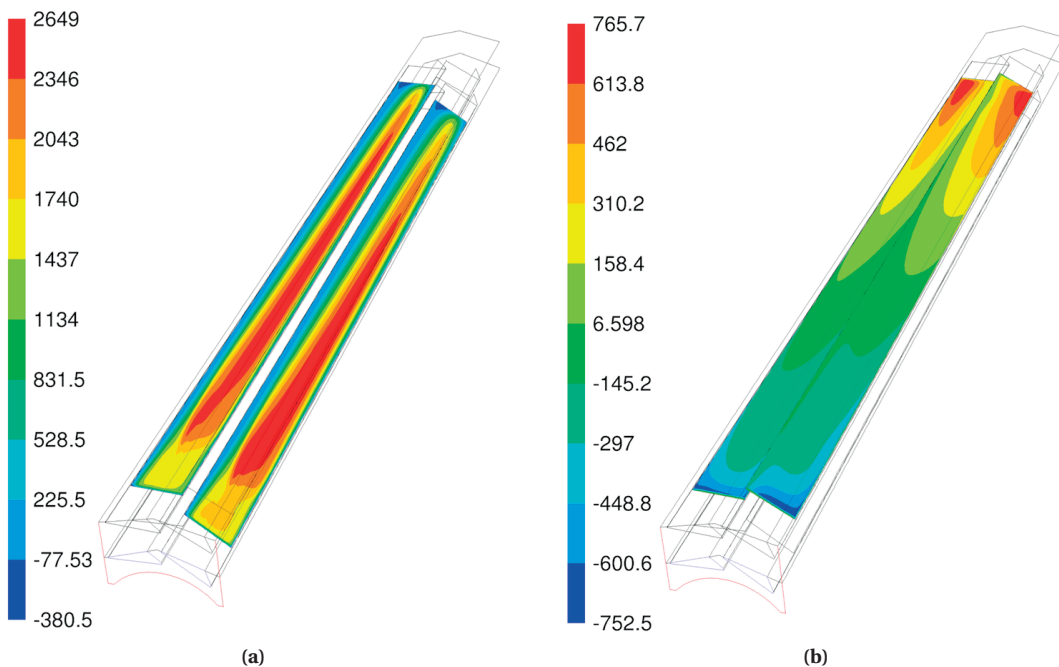


Figure 3.7: Heat flux [W m^{-2}] from the L1 layer detector chips to the airflow at a power density of 0.30 W cm^{-2} when cooling the Inner Barrel layer by layer with air injected at 10 m s^{-1} inside the triangular ducts and 14°C : (a) heat flux to the air inside the triangular ducts (inflow); (b) heat flux to the air flowing in the gap between the Inner Barrel L0 and L1 layers (outflow).

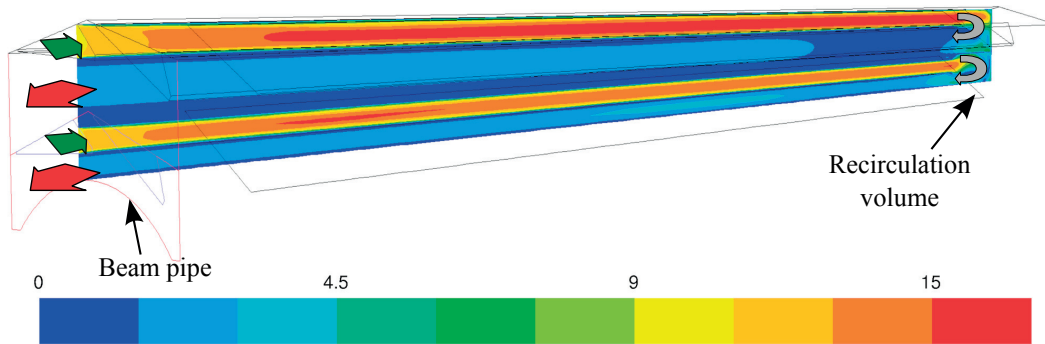


Figure 3.8: Air velocity map [m s^{-1}] in a central longitudinal section of the CFD model at a power density of 0.30 W cm^{-2} when cooling the Inner Barrel layer by layer with air injected at 10 m s^{-1} inside the triangular ducts and 14°C .

the time of the proposal, the lack of stave modularity, and potential mechanical problems involving vibration and stresses on the structures and the chips. Would the system be further developed, the magnitude of the pressure drop and the vibrations on the chip surfaces should be taken into consideration. Additionally, the implementation of the following measures is recommended for increasing the cooling performance:

1. Equalise the cross-sectional areas for the air inflow and outflow. This would balance the Reynolds numbers inside the triangular ducts and in the gaps between layers, thus balancing the heat transfer coefficients between the two sides of the chip with the airflows and increasing the global cooling performance.
2. Use helium as coolant. As reported in Table 3.2, helium can be flushed at high velocity (20 m s^{-1}) and the flow would still fall in the laminar regime, leading to vibrational stresses minimisation over the Inner Barrel structure. Moreover, the high specific heat capacity of helium results in a lower temperature rise than with air. On the other hand, a helium cooling system must be leak-tight to avoid the loss of the gas and incur in high operational costs.

3.5.2 Impinging jet air cooling proposal

This concept, proposed for the Inner Barrel staves by the University of Saint Petersburg ALICE working group, involves a stave-modular air cooling system based on air jets impinging directly on top of the chips. Air is injected in an enclosure in each stave and flows out through small holes in the lower flat part of the stave, directly impinging on the chips, which would be glued slightly separated from the stave. The concept is illustrated in Fig. 3.9. The top, semicircular enclosure and the plate where the holes are drilled are made of $100 \mu\text{m}$ -thick T300 fabric [37], resulting in a similar architecture as displayed in Fig. 2.4b.

The author was requested by the ALICE ITS Upgrade project to assess the cooling performance

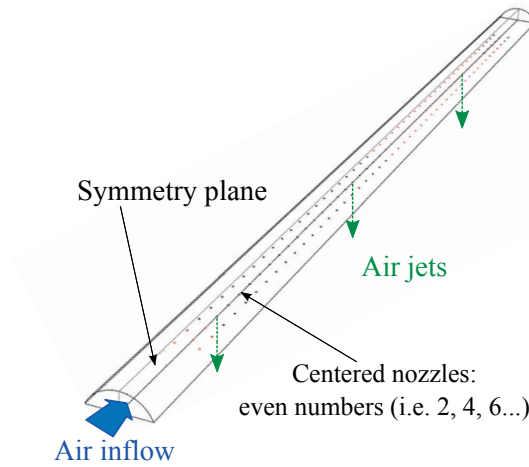


Figure 3.9: Impinging jet air cooling stave scheme. The ITS Upgrade detector chips are glued to the bottom of the stave enclosure, separated from the surface by a gap. The air jets impinge directly on the chips.

and the pressure distribution of the air on the chips with the geometry proposed by the University of Saint Petersburg group. Analytical calculations and CFD simulations are used to study this cooling concept, providing recommendations for optimising the design.

Analytical calculations

The first step is to perform an energy balance to estimate the air flow rate needed. It must be noted that the impinging jet solution was applied to an early design of the Inner Barrel staves that only had 8 chips per stave. Thus, the heated area was 240 x 15 mm per stave. Also, studies were carried out at the early maximum expected detector power density at the beginning of the ITS Upgrade project, 0.50 W cm⁻². Assuming air impinges on the chips at 14°C, a reasonable air temperature rise target may be $\Delta T_{air} = 26 - 14 = 12$ K. The required air flow rate per stave, in L s⁻¹, is calculated as follows:

$$\dot{V}_{air} = 1000 \frac{E_{chips}}{\rho_{air} c_{p,air} \Delta T_{air}} \quad [L s^{-1}] \quad (3.5)$$

By calculating E_{chips} with Eq. 4.5, $\dot{V}_{air} \approx 1.2$ L s⁻¹ per stave as of above.

Arrays of holes (also called “nozzles”) are used to establish impinging jets of air for heat and mass transfer. They are defined by four parameters:

1. **Number of nozzles (N):** a large number of nozzles is required to guarantee temperature uniformity of the surface to be cooled (the chips). The proposed number of nozzles by the University of Saint Petersburg group is 143 per stave, ~ 20 air jets impinging on each chip.
2. **Diameter of the holes (D):** it has a direct influence on the shape of the jet and the jet pressure drop. It should be chosen considering the nozzle-to-chip distance (H) in order to maximise the heat transfer. For the present solution, D should be small enough to minimise the loss of

mechanical rigidity of the plate and provide a high, dominating air pressure drop across the nozzles, guaranteeing all nozzles get a similar air flow rate. However, too small nozzles may lead to high air velocities and even to compressibility effects in the flow. This could potentially result in high stresses on the chips and instabilities in the air supply system. The University of Saint Petersburg group proposed an initial nozzle diameter of 0.35 mm.

3. **Pitch or distance between nozzles (L):** should be chosen so each nozzle cools an equal area of the chips. In the present concept, a square array of holes separated by a minimum distance of 3.54 mm is initially proposed (see Fig. 3.10).
4. **Nozzle-to-chip distance (H):** this parameter highly influences the heat transfer performance, as it affects the length of the jet core. In the proposed concept, values of H below 0.2 mm are not recommended as stresses by the air jet would become too high, and the dimensional tolerances of the gluing process would be too strict. On the other hand, nozzle-to-chip distances over 1 mm are not possible, since there would be no space for the required overlap between adjacent Inner Barrel staves, displayed in Fig. 3.2a.

The geometry put forward by the University of Saint Petersburg group is displayed in Fig. 3.10.

Empirical correlations are available in the literature to estimate the heat and mass transfer coefficients at the surface impinged by jets coming from an array of nozzles. The Nusselt number is defined by Martin [132] as follows:

$$Nu_{air} = \frac{hD}{\alpha_{air}} = G Re^{\frac{2}{3}} Pr^{0.42} \quad (3.6)$$

$$G = \frac{d^* (1 - 2.2 d^*)}{1 + 0.2 (h^* - 6) d^*} \left[1 + \left(\frac{10 h^* d^*}{6} \right)^6 \right]^{-0.05} \quad (3.7)$$

where, for the square-shaped nozzle arrangement in the present concept, the square root of the relative

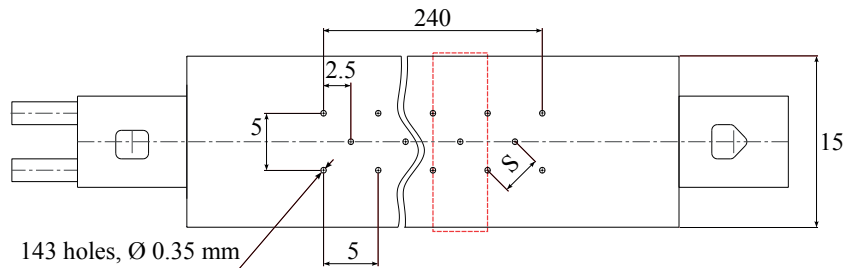


Figure 3.10: Location and size of the nozzles for the air jets impinging on the detector chips. The red dashed line rectangle represents the domain considered for the CFD thermal simulations (see Fig. 3.11).

nozzle area (f) is defined below:

$$d^* = \sqrt{f} = \sqrt{\frac{\pi D^2}{4L^2}} \quad (3.8)$$

and:

$$h^* = \frac{H}{D} \quad (3.9)$$

The range of validity of the correlation is:

$$\begin{aligned} 0.004 &\leq f \leq 0.04, \\ 2 &\leq h^* \leq 12, \\ 2000 &\leq Re \leq 100000 \end{aligned}$$

Applying the correlation by Martin [132], the thermo-hydraulic characteristics of the geometry proposed by the University of Saint Petersburg group are reported in Table 3.3 (case 1). Since the dimensions and the Reynolds numbers are within the range of validity, correlations are applicable to the cases reported in the three columns (cases outside the correlation validity ranges were not considered). It can be observed that the initial choice of $D=0.35$ mm and $N=143$ is a nearly optimal one from the point of view of the flow characteristics: the Reynolds number is low, just over 2000^a, and the mean velocity of the air out of a single nozzle is less than 30% the Mach number, thus none to low compressibility effects are expected in the airflow.

According to Martin [132], the nozzle geometry and arrangement can be optimised to maximise heat and mass transfer performance by choosing properly the D , H and L parameters. The following ratios ensure the optimal nozzle arrangement:

$$\left(\frac{H}{D}\right)_{optimal} \simeq 5 \quad (3.10)$$

$$\left(\frac{L}{H}\right)_{optimal} \simeq 1.4 \quad (3.11)$$

$$f_{optimal} = 0.0152 \quad (3.12)$$

The optimal value from Eq. 3.10 matches approximately the length of the jet's potential core, a region where local heat transfer coefficients display the maximum values. Considering a fixed $N = 143$ and $D = 0.35$ mm, the optimal value of H should be 1.75 mm, as reported in the last column of Table 3.3 (case 3). By choosing the optimal $L = 2.45$ mm, case 3 displays a heat transfer coefficient $\sim 17\%$ higher

^a Flows with $Re < 2300$ are not necessarily laminar in impinging jets, as the flow can be turbulent at Re as low as 100, according to [132]. However, $Re = 2000$ is low enough to obtain good cooling performance without exerting too high stresses on the chips.

Table 3.3: Analytical thermo-hydraulic characteristics of the impinging jet air cooling proposal for a single stave and three different nozzle array geometries, applying the correlation by Martin [132]. Cases 2 and 3 refer to optimised cases applying the optimal nozzle array arrangements reported in Eqs. 3.10 and 3.11.

Parameter	Case 1	Case 2	Case 3	
	Initial geometry	Optimised for $H=0.7$ mm	Optimised for $D=0.35$ mm	
Geometry	N [-]	143	143	143
	D [mm]	0.35	0.35	0.35
	L [mm]	3.54	1.70	2.45
	H [mm]	1.00	0.70	1.75
Flow characteristics	\dot{V}_{stave} [L s ⁻¹]	1.2	1.2	1.2
	u_{air} [m s ⁻¹]	87	87	87
	Re [-]	2044	2044	2044
Range of validity of correlations	L/D [-]	10.1	4.9	7.0
	H/D [-]	2.9	2.0	5.0
	L/H [-]	3.54	2.42	1.4
	f [-]	0.008	0.033	0.016
Heat transfer	h [W m ⁻² K ⁻¹]	781	1331	937

than the initial nozzle array geometry. However, the maximum H allowed is 1 mm due to the Inner Barrel staves spatial constraints. In the 0.2 to 1 mm nozzle-to-chip range, the configuration $H = 0.7$ mm, $L = 1.7$ mm with $D = 0.35$ mm described in case 2 in Table 3.3 results in the highest expected heat transfer coefficient, which is $\sim 41\%$ higher than for case 1. This case will result, nevertheless, in a high dynamic pressure on the chip surface due to the low nozzle-to-chip distance.

For further insight, the initial case 1 was studied from a thermal and hydraulic point of view using CFD simulations.

CFD studies on the impinging jet air cooling concept

The targets of the CFD simulations are indicated below:

1. Calculate the thermal performance of the nozzle array in case 1 (see Table 3.3) and back up the analytical estimates presented above.
2. Quantify the local pressure on the chip.
3. Study the air flow distribution between all the nozzles in one stave.

To fulfil the first two goals, a section of the stave, depicted in red dashed line in Fig. 3.10, was modeled in 3D and considered as the CFD domain. This domain is represented in Fig. 3.11. Since there is geometrical and physical symmetry in three planes of the domain, only one fourth of it had to be modelled and meshed. The boundary conditions imposed are the air flow rate at the jets corresponding to a total stave flow rate of 1.2 L s^{-1} (assuming uniform flow distribution, it corresponds to $1.2/143 = 8.4 \cdot 10^{-3} \text{ L s}^{-1}$ per nozzle) at a temperature at 14°C , and a power density at the chip surface of 0.50 W cm^{-2} . At

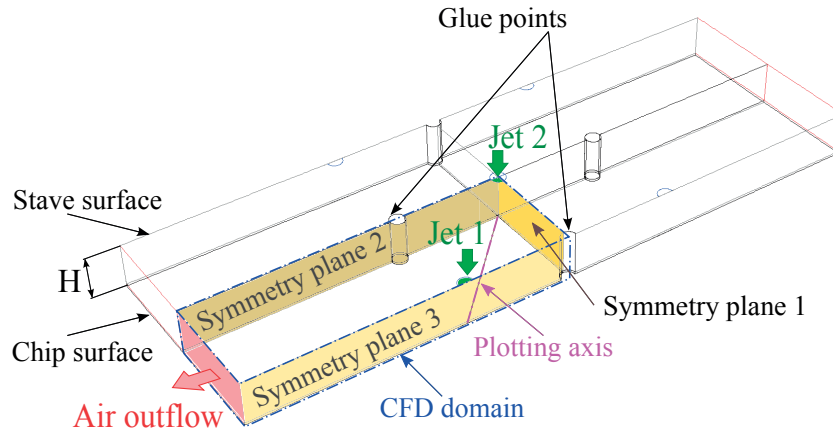


Figure 3.11: CFD domain used to characterise the thermal performance of the impinging jet air cooling system and the dynamic pressure drop of the air on the chips. CFD tests were performed for $H = 0.2$ mm and $H = 1$ mm.

the same time, the chip thickness, $50 \mu\text{m}$, and its thermal conductivity (silicon, $150 \text{ W m}^{-1} \text{ K}^{-1}$), were specified. Two sub-cases were studied, where the only difference is the nozzle-to-chip distance, H , set to the minimum and maximum admissible values, 0.2 and 1 mm.

Fig. 3.12 displays the chip temperature map for the two different nozzle-to-chip distances. While the maximum temperature is 1.5 K higher for the case at $H = 1$ mm, the chip temperature map is more uniform than at $H = 0.2$ mm, as the jet core has more space to develop and larger wall jets occur (i.e. the air spread parallel to the chip wall after first impinging on it). Both cases exceed the maximum allowable chip temperature of 30°C at 0.50 W cm^{-2} . The maximum temperatures occur at the sides of the domain. However, the nominal power density is expected to be, at the time this presentation is written, 3 to 5 times lower than 0.50 W cm^{-2} . As a result, the impinging jet air cooling solution would be expected to comply with the thermal requirements at the current power densities, though this solution was put on hold due to the issues described at the end of the present section. The ultra-lightweight cooling concept object of this thesis was developed instead.

Fig. 3.13 shows the pressure exerted on the chip surface by the air jets at the two aforementioned nozzle-to-chip distances. In general, the air exerts a higher pressure on the chip at $H = 0.2$ mm, reaching maximum values beneath the jets twice as high as for the $H = 1$ mm case. This last nozzle-to-chip distance is therefore preferred.

The total pressure on the chip surface along the axis separating the two jets, as represented in Figs. 3.11 and 3.13a, is plotted in Fig. 3.14. The case with $H = 1$ mm presents lower pressure on the chip, especially at the jet locations. This information was useful for the ITS Upgrade Mechanics working group to implement it in their FEM simulations. With the gluing points distributed in an equivalent arrangement as the nozzles (see Fig. 3.11), values of stress of 14 MPa are expected with $H = 0.2$ mm, along with a chip maximum sag of $1.74 \mu\text{m}$. It is unknown if the chip would withstand these stresses without breaking, since its strength will depend on the manufacturing process, and the stiffness and

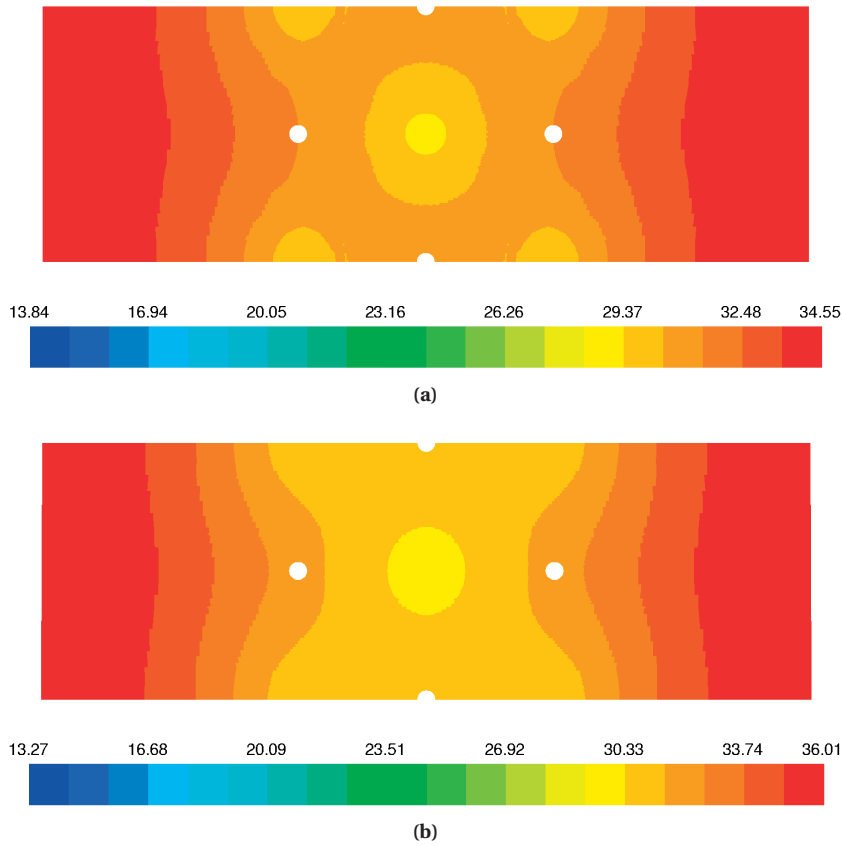


Figure 3.12: Simulated chip temperature map [C°] as viewed from the top when impinged with an air flow rate of $8.4 \cdot 10^{-3} \text{ L s}^{-1}$ per nozzle at 14°C and two nozzle-to-chip distances, 0.2 (a) and 1 mm (b). Only the bottom left quadrant of the domain is simulated, the rest is generated by symmetry. The white areas are the gluing points between the chip and the stave structure.

location of the gluing points. Experimental tests would provide here more information and would allow to cross-check the results of the simulations.

The third goal of the CFD studies is to study the air flow distribution between all the nozzles in one stave. A CFD model of the whole stave as depicted in Fig. 3.9 was built for this purpose. Symmetry was assumed along the central longitudinal plane. The nozzles are numbered, the ones at the central axis corresponding to even numbers. No chips are considered beneath the stave. The boundary conditions are the following: air flow rate at the stave inlet of 1.2 L s^{-1} and atmospheric pressure at the outlet at the nozzles. No compressible flow effects were considered, as the maximum velocity in the domain is below 30% of the Mach number.

Fig. 3.15 shows the total pressure at the central plane inside the stave enclosure. It can be seen that it decreases little along the stave, meaning that the main pressure drop occurs at the nozzles and thus uniform airflow distribution among them is expected. Indeed, Fig. 3.16a reports the mass flow rate in all the nozzles, with a maximum variation from those close to the inlet and those at the end of the stave enclosure of only 3.3%. It may be concluded that the flow is equally distributed between all

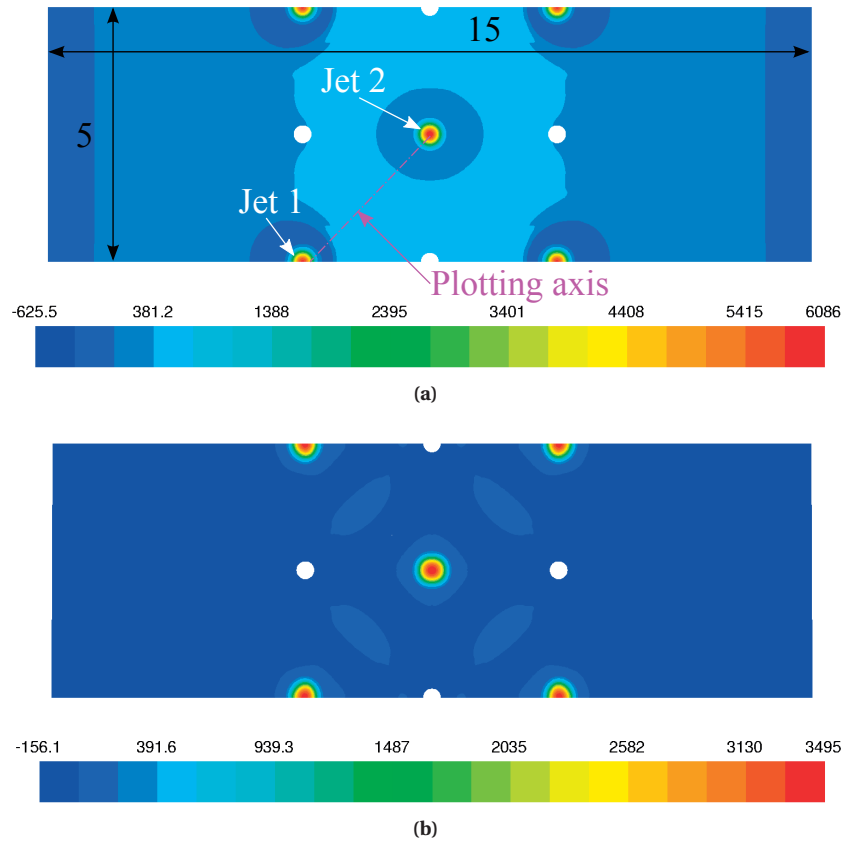


Figure 3.13: Total pressure [Pa] over the chip surface as viewed from the top when impinged with an air flow rate of $8.4 \cdot 10^{-3} \text{ L s}^{-1}$ per nozzle and two nozzle-to-chip distances, 0.2 (a) and 1 mm (b). In (a), the location of the two jets is indicated, as well as the plotting axis used in Fig. 3.14 and the dimensions of the domain, in mm. Only the bottom left quadrant of the domain is simulated, the rest is generated by symmetry. The white areas are the gluing points between the chip and the stave structure.

nozzles, and that, as a result, similar cooling performance will be achieved for all chips installed along the stave. Also, the mean air velocity in each nozzle is displayed in Fig. 3.16b.

The impinging jet air cooling solution with the architecture reported in case 1 in Table 3.3 provides a thermal performance close to the requirements at 0.50 W cm^{-2} , and it would be expected to comply to the thermal specifications at 0.30 W cm^{-2} and lower power densities. Two geometries that would enhance the thermal performance are recommended in Table 3.3 (cases 2 and 3). They consist in choosing an optimal nozzle-to-chip distance, and packing the nozzles closer to each other, which in turn would require a higher number of nozzles per stave to keep the same cooling area. Still, the influence of the pressure exerted by the air jets on the chip surface has to be characterised, preferably through experimental testing. Despite its modular approach and good cooling capabilities, the impinging jet air cooling system should faces the following challenges:

- Excellent gluing accuracy is required. If one chip is glued slightly closer to the stave, the airflow distribution might be less uniform among all air nozzles. Also, the gluing process must be reliable;

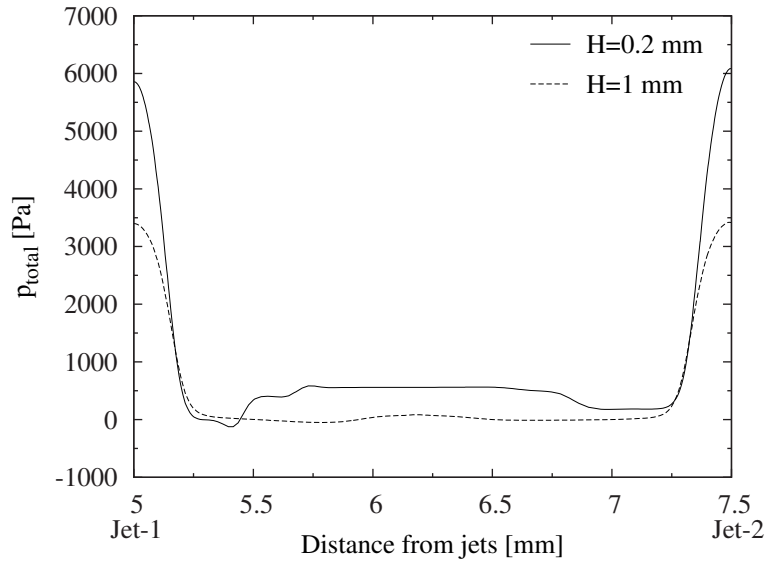


Figure 3.14: Total pressure on the chip surface along the axis between two consecutive jets (see Fig. 3.13a) when impinged with an air flow rate of $8.4 \cdot 10^{-3} \text{ L s}^{-1}$ per nozzle and two nozzle-to-chip distances (H), 0.2 and 1 mm.

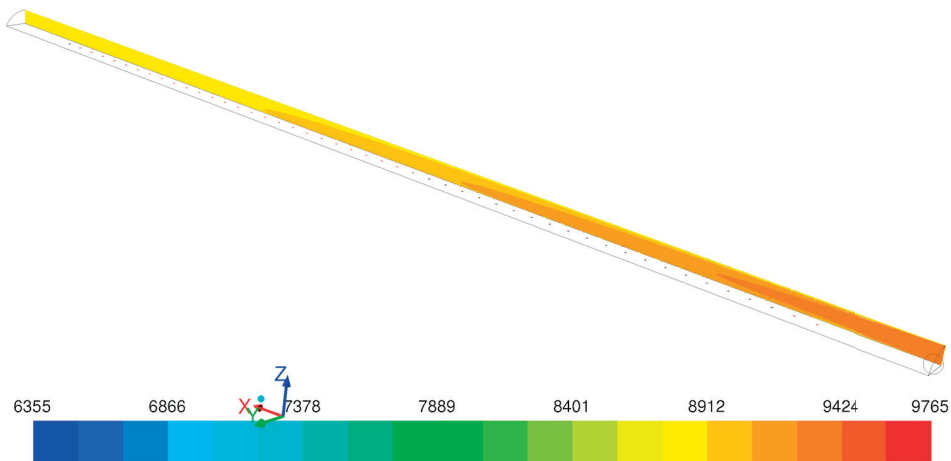


Figure 3.15: Total air pressure [Pa] at the stove enclosure central symmetry plane at a total flow rate of 1.2 L s^{-1} .

mechanical failure of gluing points may lead to loss of chip positioning and/or chip destruction.

- The system is prone to hotspots in the chips if one or more nozzles get blocked.
- The high local air velocities out of the nozzles and inside the test enclosure triggers the need of extensive, long-term experimental testing to discard mechanical damage of the chips.

The limitations of the two air cooling proposals presented in this section motivated, at the time of the initial ITS Upgrade R&D phase, the development of an ultra-lightweight liquid/two-phase cooling approach, which has been finally chosen as the baseline solution for the ALICE ITS cooling system.

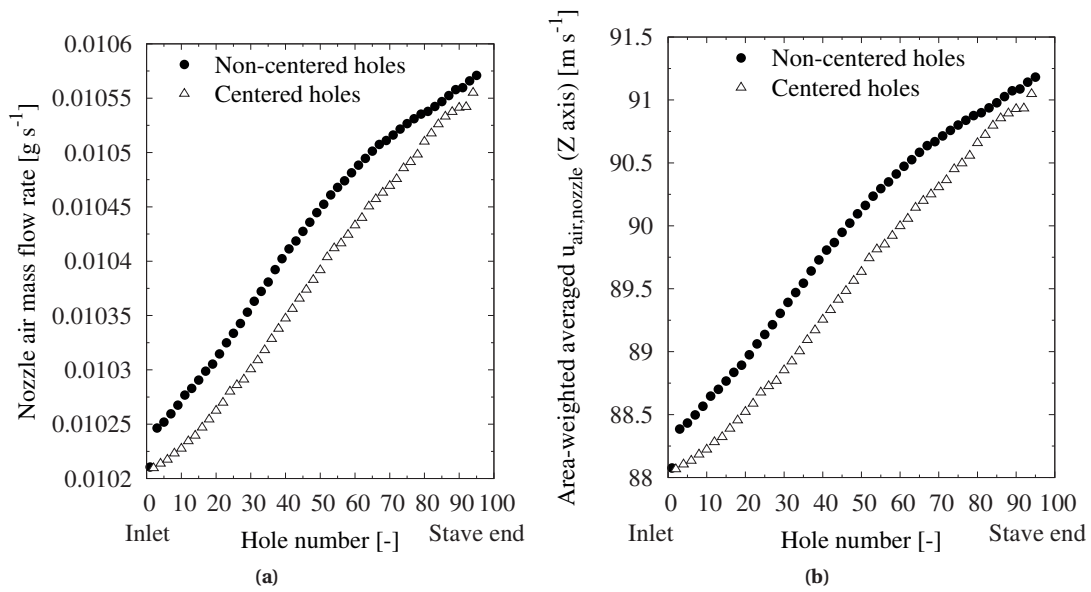


Figure 3.16: Air mass flow rate distribution in all stave nozzles (a), and area-averaged mean air velocity in each nozzle (b), at a total stave air flow rate of 1.2 L s^{-1} . No chips are considered at the bottom of the stave.

The rest of the chapter focuses on the development of this solution, the experimental setup and methodology, and the feedback from the first experimental test campaign.

3.6 Ultra-lightweight cooling systems

Ultra-lightweight cooling concepts were put forward as a technical solution involving single- or two-phase cooling and offering a good compromise among all constraints. The idea consists in embedding a lightweight cooling channel in an lightweight stave structure that provides mechanical and cooling capabilities at the same time. The materials delivering the best balance between material budget, thermal conductivity and stiffness are CFRPs, reviewed in section 2.4. Their directional behaviour allow for stave designs tailored for specific requirements, achieving the lightest concepts.

The development of operational ultra-lightweight cooling concepts requires considering the mechanical requirements (stiffness, dimensional constraints), the cooling performance (size of the cooling channels, CFRP fibre density, materials) and manufacturing feasibility (minimum CFRP bending radius, quality assurance). The two stave designs described in this section are the result of a collaborative effort in these three lines between the ITS Upgrade Mechanics team (with C. Gargiulo on the mechanics and S. Igolkin on the stave manufacturing) and the author on the cooling aspects, all within the ITS Upgrade Mechanics and Cooling working package. By exchanging information about mechanical features, manufacturing possibilities and results of cooling analysis and tests, the stave architectures described in the present section were developed and optimised in an iterative way, with the minimisation of the

material budget as the common primary goal.

Two ultra-lightweight Inner Barrel optimised stave architectures, shown in Fig. 3.17 and first described in [133], were ultimately considered and fabricated: a wound-truss structure and a high-conductivity plate with a spaceframe structure. The silicon pixel chips would be attached to the lower flat surface in each of these mechanical structures. A refrigerant providing the cooling power would flow inside the cooling pipes. The two channels are connected together at the inaccessible barrel end (C-side) by a Π -bend piece, while at the other end the refrigerant inlet and outlet are located (A-side). Therefore, the cooling flow passes twice on each stave, as indicated by the arrows in Fig. 3.17a.

The first optimised stave prototype (named hereafter P1) is made of a wound-truss structure, as shown in Fig. 3.17a. A 1.50 mm-wide, 70 μm -thick truss made of pre-impregnated unidirectional K13D2U-2K high-conductive pitch-based carbon fibre [42] is wrapped around the two cooling channels pipes, and constitutes the triangular cross-section of the stave. The fibre provides both mechanical stiffness and thermal capabilities. A winding angle of 90° between the tube axis and the winding truss is desired, as it would shorten the thermal path between the chip and the coolant. However, the truss minimum bending radius exceeds the cooling channel outer radius, 0.757 mm. Therefore, the winding angle is limited to 23° to avoid the risk of breaking the fibres. Since the truss is in contact with only some sections of the channels, a 30 μm -thick graphite foil (TPG) sleeve, with planar thermal conductivity rated to $1000 \text{ W m}^{-1} \text{ K}^{-1}$ [49], is wrapped to each channel as external liner, with the aim of spreading the heat coming from the truss longitudinally over the pipe. The influence of all the constructive parameters (fibre width, pitch, winding angle) was evaluated analytically and using computational

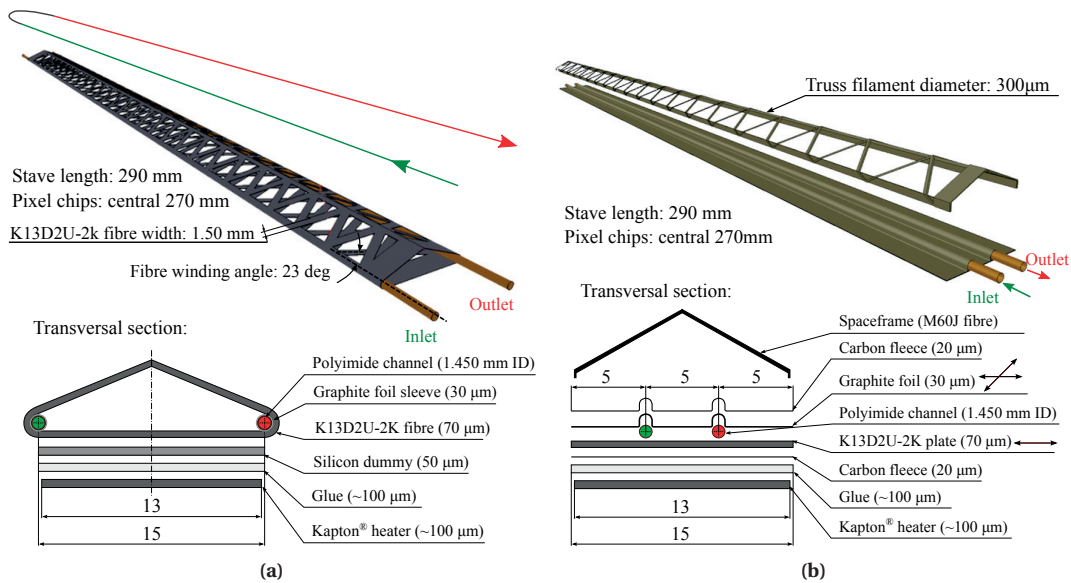


Figure 3.17: Schematic view of the two ultra-lightweight stave architectures proposed: (a) wound-truss structure, named P1; (b) high-conductivity plate plus spaceframe, named P2. The thicknesses of the different materials are indicated. All dimensions are in mm except where explicitly indicated.

simulations. The expected chip temperature map, calculated using CFD for the stave displayed in Fig. 3.17a, is illustrated in Fig. 3.18 when cooling with water at a 0.30 W cm^{-2} chip power density.

It is emphasised that the effective thermal conductivity of the CFRP truss is unknown due to the presence of the impregnating resins, as mentioned in subsection 2.4.2. Also, contact thermal resistances in all interfaces (channels, truss, silicon) are unknown. For these reasons, the analytical studies and thermal simulations provided only qualitative information on the influence of the constructive parameters cited above. Besides, the manufacturing capabilities of the Mechanics and Cooling working package facilitated having working stave prototypes at an early stage. Thus, it was possible characterising experimentally the cooling performance of different stave architectures and provide an accurate feedback to the Mechanics team and the technicians about the best working prototypes. This is the reason why analytical studies and simulations on the ultra-lightweight concepts are not described in detail in the present thesis.

The high-conductivity plate prototype (named hereafter P2) is depicted in Fig. 3.17b. While the P1 concept is made of a single structure, the P2 stave has two parts: a *spaceframe*, made of M60J-3K CFRP [39], which has mechanical but no cooling purposes; and a high-conductivity plate, made of pre-impregnated unidirectional $70 \mu\text{m}$ -thick K13D2U-2K CFRP [42]. The two parts are made in only one step, to avoid an intermediate gluing process, guarantee mechanical stability and planarity, and decrease the material budget at the edges. The use of a CFRP plate came up as an obvious solution from the mechanical and cooling points of view. The chips are attached to the bottom of the plate, where the fibres are oriented transversally to the stave and the cooling channels, as indicated in Fig. 3.17b. This feature provides a short path for the heat from the chips to the cooling channels. The two cooling

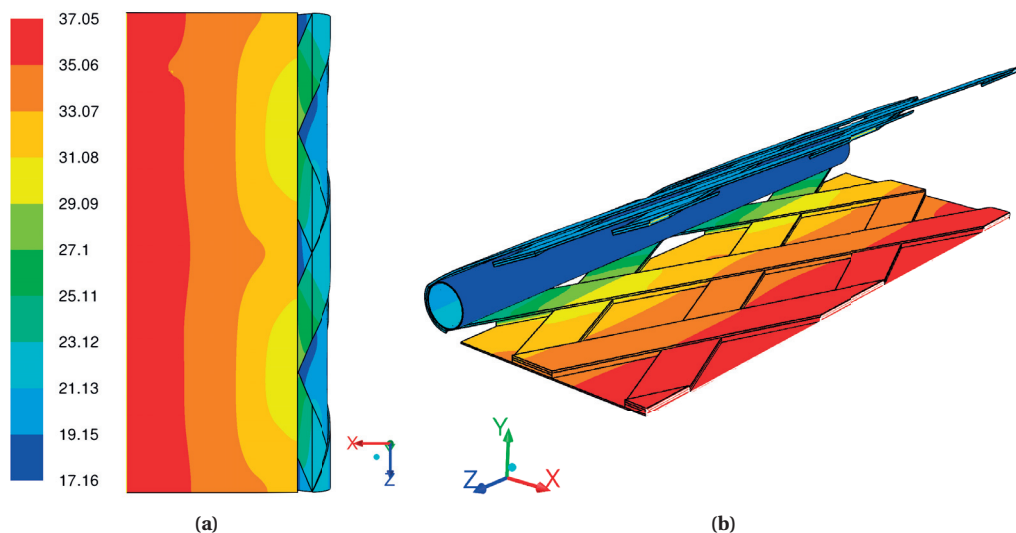


Figure 3.18: Thermal simulation of the stave and chip temperature map [$^{\circ}\text{C}$] in a section of the water-cooled P1 prototype. Boundary conditions: $T_{water}=15^{\circ}\text{C}$, $h=1700 \text{ W m}^{-2} \text{ K}^{-1}$, $Pd=0.3 \text{ W cm}^{-2}$, $h_{air}=10 \text{ W m}^{-2} \text{ K}^{-1}$; (a) view of the silicon chip from the bottom; (b) isometric view.

channels are not embedded in the plate nor pressed against it, but rather lie on it. A 30 μm -thick layer of TPG [49] covers the plate and the upper part of the tubes, creating a thermal bridge between the cooling plate and the top part of the cooling channels. Finally, 20 μm -thick carbon fleece plies are used to encapsulate the assembly, preventing its deterioration, and ensure firm positioning of the cooling channels on top of the cooling plate.

Like the wound-truss solution, the high-conductivity plate concept was initially evaluated using analytical calculations and simulations, but as working stage prototypes could be quickly manufactured, the results of cooling tests provided better feedback for optimising the concept. The optimal cooling channel size was proposed by the author after evaluating pressure drop correlations for single- and two-phase flows (see section 2.5.5 for more information) and experimental results, as later described in section 4.5. The plate thickness is the result of a compromise between mechanical properties, manufacturing feasibility, experimental thermal performance and material budget. J. Botelho Direito, from CERN EN-CV-DC group, is acknowledged for suggesting the use of the TPG foil over the plate-pipes assembly to provide a thermal bridge between the sides of the plate and the top of the cooling pipes. Finally, the distance of 5 mm between the cooling channels obeys spatial constraints at the A-side of the Inner Barrel and not cooling requirements.

The cooling channels in both prototypes constitute their most original innovation: they are made of polyimide [64], commercially known by DuPont's commercial name, Kapton[®]. This material was thoroughly described in section 2.4.4. It provides a series of advantages to the ultra-lightweight concepts. First, it is very light ($\rho=1.4 \text{ g cm}^{-3}$), it has a high radiation length ($X_0=28.5 \text{ cm}$, versus 1.4 cm of stainless steel), and tubes are available with thin walls: 32 μm for a 1.450 mm ID tube. These three characteristics provide an unbeatably low material budget. In chapter 2, a material budget comparison between a polyimide tube and a stainless steel tube of identical dimensions was displayed (see Fig. 2.9). The polyimide tube yields a material budget 15 times lower than a steel pipe of the same size, and 80 times lower if considering the polyimide channel is readily available with thinner walls. Besides, while PEEK may show a similar material budget, according to Table 2.5, PEEK channels are only available with thicker walls.

Additionally, polyimide features excellent mechanical properties, robustness, radiation resistance [15], compatibility with most refrigerants and materials, high burst pressure and tightness, low ageing rate, high hardness and flexibility. Downsides to polyimide tubes are its low thermal conductivity ($0.12 \text{ W m}^{-1} \text{ K}^{-1}$, 130 times lower than stainless steel), moisture absorption (up to 0.841% water absorption is reported [66], although it does not compromise the tube stability), and that it requires careful manipulation in order not to "pinch" the tubes and alter their section.

Concern might arise about the stability of the polyimide channel section: swelling or collapse might occur for high or sub-atmospheric pressurisation of the refrigerant, respectively. This subject has been studied analytically and experimentally. A summary is presented in appendix B. In any case,

the rigidity provided by the CFRP structures guarantees a solid assembly and stability of the cooling channels section. No signs of deformation of the channel section (pressure drop changes, pipe swelling or collapse) were observed after applying high pressure and vacuum inside the channel repeatedly.

The polyimide channels are connected at one end of the staves by a Π -bend made of PEEK, while in the accessible end (A-side) another PEEK block fitted with stainless steel tubes is installed for refrigerant input and output. The assembly is accomplished by gluing the polyimide tubes to the PEEK block with epoxy resin. A mandrel is kept inside the polyimide channel to ensure good contact during the glue curing process. These pieces are shown in the exploded view of prototype P1 in Fig. 3.19a. A detailed view of prototype P2 and its inlet/outlet connector is displayed in Fig. 3.19b.

Thanks to the use of CFRPs and polyimide channels, both staves achieve material budget values close to the 0.3% per layer required in the Inner Barrel. Their weights and material budgets are summarised in Table 3.4. Compliance with the 0.3% per layer limit is achieved for prototype P2 by decreasing the pipe size and improving the fabrication process (less material at the sides of the stave).

All the materials used for stave construction comply with the CERN safety regulations [19] and are radiation hard for the ITS Upgrade expected radiation doses listed in Table 3.1. A summary of the thermal and mechanical properties of the materials used can be found on Tables 2.3 and 2.4. It is emphasised that the values regarding the CFRPs in the aforementioned tables are referred to the fibre properties. Laminates and plates made of impregnated fibres display lower thermal conductivity and mechanical stiffness, and density, as mentioned in section 2.4.

The Middle and Outer Barrel staves are based on the same high-conductivity plate concept developed for the Inner Barrel ones (P2 prototype). Likewise, the stave optimisation process was based

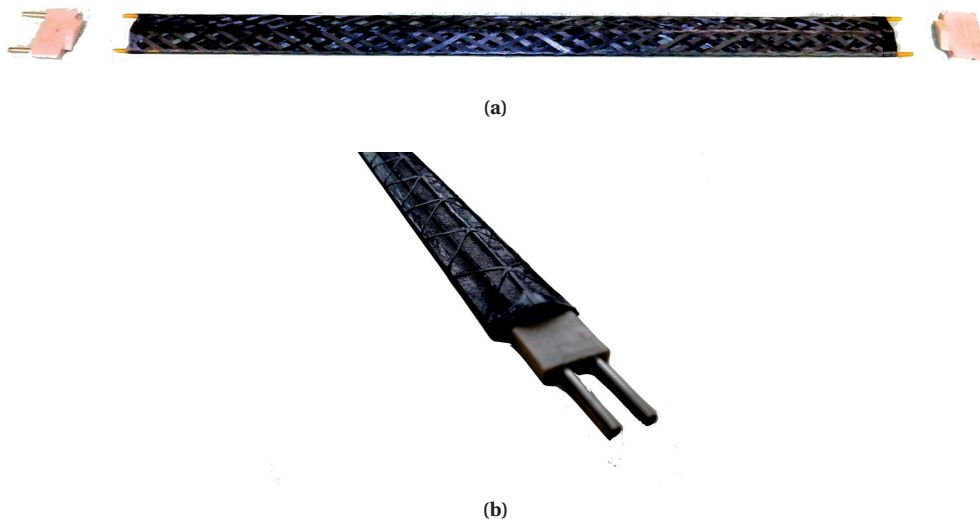


Figure 3.19: Views of the prototypes P1 and P2 and their connectors: (a) exploded view of P1; (b) inlet/outlet connector in P2. Images from [4].

Table 3.4: Weight and material budget of the P1 and P2 prototypes, as specified on [4].

	P1	P2 ^a
Weight ^b [g]	1.4	1.8
$[x/X_0]_{structure}$ [%]	0.20	0.25
$[x/X_0]_{full}$ ^c [%]	0.26	0.31
$[x/X_0]_{full,overlap}$ ^d [%]	0.32	0.38

on cooling performance results of the Inner Barrel staves and later prototypes of the Outer Barrel ones. These staves will be presented in detail in section 5.3. Only Inner and Outer Barrel stave prototypes were fabricated and tested, as the Middle Barrel staves share the design with the Outer Barrel ones.

3.7 Choice of the refrigerant

As indicated in subsection 3.3.1, the coolant should not be colder than 12°C within the detector to prevent moisture condensation on the electronics. Several refrigerants fulfilling this requirement were considered for the cooling of the ITS Upgrade. Their positive and negative characteristics for this application are pointed out below.

3.7.1 Demineralised water

Liquid water (H₂O) is widely used to dissipate low to medium heat loads in cooling applications in industrial and scientific facilities. Water cooling loops are simple to build and run, though they should operate in leak-less conditions in the ITS Upgrade: the maximum total pressure within detector bounds shall not exceed 1 bar, in order to prevent potential water leaks on the electronics. In case of a leak, air would enter the channels rather than water leaking out, which could destroy the detector and severely corrode essential components.

Previous experience with the ALICE SSD and SDD detectors [24], operating with water at roughly the same location as the future ITS Upgrade detector, showed that the pressure drop in the ITS Upgrade staves should not exceed 0.5 bar, in order to guarantee the return of the water to the cooling reservoir^e. For safety reasons, a target pressure drop value of 0.3 bar is aimed for if cooling with water in leak-less mode. Also, special care shall be made when designing the piping and distribution lines. An air flushing

^a The weights and material budget displayed correspond to the primitive P2 design, where the plate and the spaceframe are made separately and glued afterwards. Optimised staves, made in only one step, achieve lower weight and material budget, as reported later in Table 4.9.

^b Weight of the stave only, with no chips, glue or services. The inlet/outlet PEEK connector and Π -bend are not included, since they rest on the Barrel endwheels and hence are outside the detector sensitive area.

^c Includes: structure, water as coolant inside the channels, silicon chips, glue, and FPC (Flex Printed Circuit).

^d Full stave material budget (structure, water as coolant inside the channels, silicon chips, glue, FPC), plus the overlap between adjacent staves in each Inner Barrel layer.

^e In the ALICE site, ~ 50 m long piping is required from the location of the plant providing cooling water to the present SSD and SDD detectors. The water reaches the detector at slightly over 1 bar, is circulated in the staves at $p < 1$ bar and then returns to the plant. Accounting for a maximum 0.5 bar pressure drop in the 50 m long return lines falls well within safety.

system is to be installed in the ITS Upgrade with the aim of removing moisture and ensure dry air conditions in the detector site. Last, a drawback to using water is that, because it is in liquid state, it displays a higher material budget than gas and two-phase coolants.

The radiation dose per year expected in the ITS Upgrade, 700 to 2700 kRad per year with a factor of safety 10 at layer 0 (the closest to the beam pipe) [5], will cause mild radiolysis in the water. Products of radiolysis in water are ions, H_2 , and O_2 . Based on experience in accelerators and detectors, the presence of radiolysis products can be controlled by using ion exchangers and recombiners, microporous membrane contactors and demineralisation filters.

Demineralised water is compatible with polyimide channels. Moisture absorption slightly changes the electrical properties and thermal conductivity, though not at an important scale [134]. However, knowledge on the degradation of polyimide due to water radiolysis products is currently missing. A dedicated facility was commissioned in 2012 at the ALICE cavern site to continuously circulate water in several polyimide channels and it is still running in 2016. Furthermore, the facility is operating in radioactive conditions since the restart of LHC after the Long Shutdown 1 (LS1) in early 2015. Microscopy analysis on a 1.024 mm ID polyimide pipe sample revealed no surface damage after nearly 2 years of continuous demineralised water circulation at a flow rate 3 times higher than expected at the Inner Barrel staves. This study is ongoing with several pipe samples and a full Inner Barrel stave, and will certainly provide valuable feedback on channel-activated water compatibility. Further information can be found in appendix B, section B.3.

3.7.2 Fluorocarbons

Fluorocarbon (FC) fluids, also known by 3M's commercial name, Fluorinert™ fluids, have been used at CERN for cooling several detectors, such as the current ALICE ITS SPD (two-phase C_4F_{10}) [29] or the ATLAS Inner Detector (two-phase C_3F_8) [31]. Fluorocarbon fluids are non-toxic, thermally and chemically stable fluids, compatible with most materials, such as metals, plastics and elastomers, and, specifically, with polyimide. Water solubility is low, on the order of a few parts per million. The boiling point in atmospheric pressure conditions may range from 30°C to 215°C depending on the fluid.

These fluids are completely fluorinated; no chlorine or hydrogen atoms are present in the molecules. The strength of the carbon-fluorine bond contributes to their extreme stability and inertness. Indeed, fluorocarbon fluids are well known for complying with CERN standards and being radiation hard, as reported in tests performed at CERN [17, 18]. For radiation doses several times higher than those expected in the ITS Upgrade, the fluids experience mild radiolysis effects: acidity, appearance of new chemical species, measurable fluorine ion contents, and presence of polymers. On-line fluid cleaning and purification techniques are very effective counterweight measures to all these effects.

A substitute for water in single-phase cooling is a FC in particular, C_6F_{14} , which is dielectric and radiation hard [135]. Its disadvantages compared to water are its higher density, which results in a

higher global material budget than water, poorer thermodynamic properties, and a high GWP. 3M's Novec[®]-649 fluid is very similar to C₆F₁₄, with a much lower GWP. Its suitability to be used in HEP particle detector cooling is still to be assessed.

An evaporative refrigerant will display significantly lower material budget than a liquid system. It also allows cooling at fairly uniform temperature, minimising temperature gradients on the detector. This could be advantageous in case of large detector modules with long cooling channels, such as the Outer Barrel staves. A refrigerant considered for evaporative cooling for the ITS Upgrade is an FC fluid: per-fluorocarbon (C₄F₁₀). This fluid is radiation hard and dielectric, minimising harm to the detector if spilled out. In any case, leaks are not a primary concern due to the low fluid operating pressure: the saturation pressure at 15°C is 1.9 bar. Its thermodynamic properties can be found in appendix C.

Halocarbons, such as R245fa or R236fa were considered, but their use in radioactive environments has to be qualified; their molecules, where hydrogen atoms are present, may dissociate with radiation and create acids that could damage the cooling channels and parts of the cooling system. R245fa was used in the experimental flow boiling heat transfer studies in a small polyimide channel in chapter 6.

Two-phase cooling systems inherently feature more complex cooling circuits, compared to single-phase cooling. Additionally, ensuring good flow distribution in two-phase multi-channel systems is of paramount importance. For instance, the ITS Upgrade cooling system features 346 lines to be fed in parallel, with at least 2 diameters sizes and multiple heat loads to manage.

Table 3.5 reports the thermodynamic properties and radiation lengths of the refrigerants considered in this section. The size of the polyimide channels in the Inner and Outer Barrel staves was carefully chosen considering the stave pressure drop if using water and two-phase C₄F₁₀. A few examples of the theoretical calculations matching experimental results for water and single- and two-phase C₄F₁₀ are displayed later in Figs. 5.5, 5.8, and 5.13 in chapter 5. The baseline stave designs display a total material budget below the limit in the Inner and Middle/Outer Barrels using water as a coolant. Simplicity in the cooling system and thermal performance also encourage the use of water as coolant. However, two-phase C₄F₁₀ remains as a firm alternative if local material budget peaks have to be minimised and radiation doses are higher than expected.

Table 3.5: Thermodynamic properties and X_0 of the coolants considered for the ITS Upgrade at 15°C.

Property	Single-phase liquid			Two-phase	
	H ₂ O	C ₆ F ₁₄	Novec [®] -649	C ₄ F ₁₀ Liquid	C ₄ F ₁₀ Vapour
ρ [kg m ⁻³]	999	1701	1632	1534	21
μ [μ Pa s]	1137.6	743.3	818.5	246	12
c_p [J kg ⁻¹ K ⁻¹]	4188.5	1037.3	1096.6	1062.6	825.5
α [W m ⁻¹ K ⁻¹]	0.589	0.058	0.060	0.459	0.013
X_0 [%]	35.8	20.4	21.9	22.6	1651.9

Chapter 4

Experimental setup, methodology and evaluation of the ultra-lightweight staves

4.1 Introduction

This chapter is focused on the experimental facilities used in the thermal tests, the experimental methodology and the data reduction. In a second part, the experimental results providing feedback on the detector stave architecture yielding the best compromise between cooling performance and light weight, and the actions towards an optimised stave design, are presented.

4.2 Experimental setup

4.2.1 Power dissipation and stave temperature monitoring

Stave prototypes are equipped with very thin, Kapton[®]-encapsulated heaters providing a dummy heat load. These heaters consist of a copper resistance embedded in two Kapton foils. It can be easily seen that the future detector chips are more efficient spreading the heat compared to the Kapton[®]-encapsulated heaters for two reasons: the higher thermal conductivity of silicon compared to Kapton[®] (150 vs. $0.12 \text{ W m}^{-1} \text{ K}^{-1}$), and the fact that the copper resistance in the heaters has a longitudinal pattern, leaving transversal heat conduction to be ruled by the Kapton[®].

It can be observed in Fig. 3.17a that stave P1 relies on the thermal conductivity of the silicon chips to spread the heat load towards the cooling channels, and this was confirmed experimentally in early test campaigns. Thus, silicon dummies (i.e. silicon slabs the same size and thickness of the future

silicon chips, but dissipating no heat load) are glued to the bottom of the stave, and a Kapton[®] heater is then glued on top of the silicon dummies. This provides a slightly higher overall thermal resistance, but is a close configuration to the real stave assembly.

However, for high-conductivity plate stave prototypes like P2, heaters are glued directly to the cooling plate with no silicon dummies in between. In such prototypes, transversal heat transfer capabilities are provided by the high-conductivity plate, so the presence of silicon is not necessary. Including the silicon dummies would add one more layer of glue to the assembly, increasing the global thermal resistance and adding potential problems like hotspots due to the increased probability of gluing defects. Future staves will display better thermal performance in equal conditions than tested prototypes equipped with Kapton[®] heaters due to the presence of silicon chips only and an optimised gluing process.

Each Inner Barrel stave prototype is equipped with a single Kapton[®] heater displaying a 270×13 mm effective heating area. Outer Barrel prototypes are fitted with 14 heaters, each with an effective heating area of 195×10 mm. The total heated areas are smaller than the chip surface (25% smaller for the Inner Barrel staves and 35% for the Outer Barrel half-staves). Nevertheless, in the thermal tests, the indicated power density refers to the total chip surface, and the absolute heat load is set accordingly.

Negative Temperature Coefficient (NTC) thermistors, 6 for each Inner Barrel stave prototype and 14 for each Outer Barrel half-stave, are taped on the heaters with thermal paste enhancing the thermal contact. The location of the NTCs at the Inner Barrel staves is displayed in Fig. 4.1a. At the Outer Barrel half-stave prototypes, each of the 14 NTCs is located right at the center of each heater, as depicted in Fig. 4.1b. The thermistors are located in both cases far enough from the stave side edges and from the tube-plate contact surfaces. Their location with respect to the thermal entry region is discussed below.

A single-phase fluid flow entering a uniformly heated channel undergoes flow and thermal development during a certain channel length. This region is called thermal development (or entry) length.

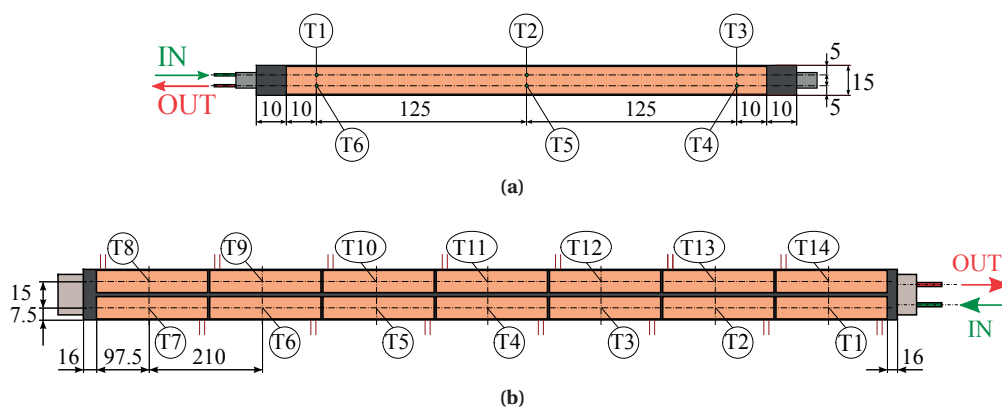


Figure 4.1: Schematic view of the stave heated surfaces and the location of temperature sensors (not in scale): (a) Inner Barrel prototypes; (b) Outer Barrel half-stave prototypes. Dimensions expressed in mm.

Theoretically, the heat transfer coefficient within the thermal development region is higher than for the fully developed flow [136], and even higher if the flow develops hydrodynamically and thermally at the same time. For laminar flows at a constant, uniform heat flux, the thermal development of the flow is generally expressed as follows [136]:

$$\frac{L_{th,dev,lam}}{D_i} \simeq 0.05 Re_D Pr \quad (4.1)$$

For single-phase turbulent flows, the thermal entry length is independent from the Prandtl number and it is similar in magnitude to the hydrodynamic entry length. Thus, the thermal development length in turbulent flows under a uniform, constant heat flux is defined as:

$$10 < \frac{L_{th,dev,turb}}{D_i} < 60 \quad (4.2)$$

In the present section, the most conservative approach of $\frac{L_{th,dev,turb}}{D_i} < 60$ is considered. It must be noted that the thermal entry lengths depend on the flow condition and hydrodynamic development at the entrance to the heated region.

For two-phase boiling flows, determining the thermal entry region is a problem ruled by many parameters at the same time, such as bubble growth and collapse, flow pattern or liquid entrainment. Consequently, thermal entry length prediction methods for two-phase flows would not guarantee accurate results, and would probably need from inputs like the flow pattern, that are not always possible to determine experimentally. Thus, the single-phase thermal entry length calculations reported above are used as a first approximation for two-phase flows.

Fig. 4.2 displays the expected thermal entry length for the baseline designs of the Inner Barrel staves and the Outer Barrel half-staves versus the actual ranges of water flow rate and C_4F_{10} mass flux tested, with the fluids at 20°C. As later reported in chapter 5, the cooling tubes are 1.024 mm in ID at the Inner Barrel staves (see Table. 5.1) and 2.052 mm ID at the Outer Barrel half-staves designed to work with water, as shown in Table 5.6. The Outer Barrel half-stave layout intended for two-phase cooling with C_4F_{10} refrigerant as coolant will have 2.667 mm ID tubes (see Table 5.8).

The first three temperature sensors on the Inner Barrel staves are well within the thermal development length for all the water flow rates in the laminar regime, as displayed in Fig. 4.2a. Only at the highest flow rates becomes the flow turbulent and the thermal entry length drops to 61 mm, leaving only thermistor T1 within the thermal entry length. With two-phase C_4F_{10} , the flow is laminar up to $G \simeq 550 \text{ kg m}^{-2} \text{ s}^{-1}$, being thermistors T1 to T3 within the thermal entry length up to that mass flux.

The thermal development of the water flow spans the first half of the inlet channel at the Outer Barrel half-staves with the lowest^a water flow rate of 6 L h^{-1} , according to the results in Fig. 4.2a. The

^a 6 L h^{-1} is the recommended water flow rate to effectively cool the Outer Barrel staves at a power density of 0.15 W cm^{-2} , as later reported in section 5.3.2.

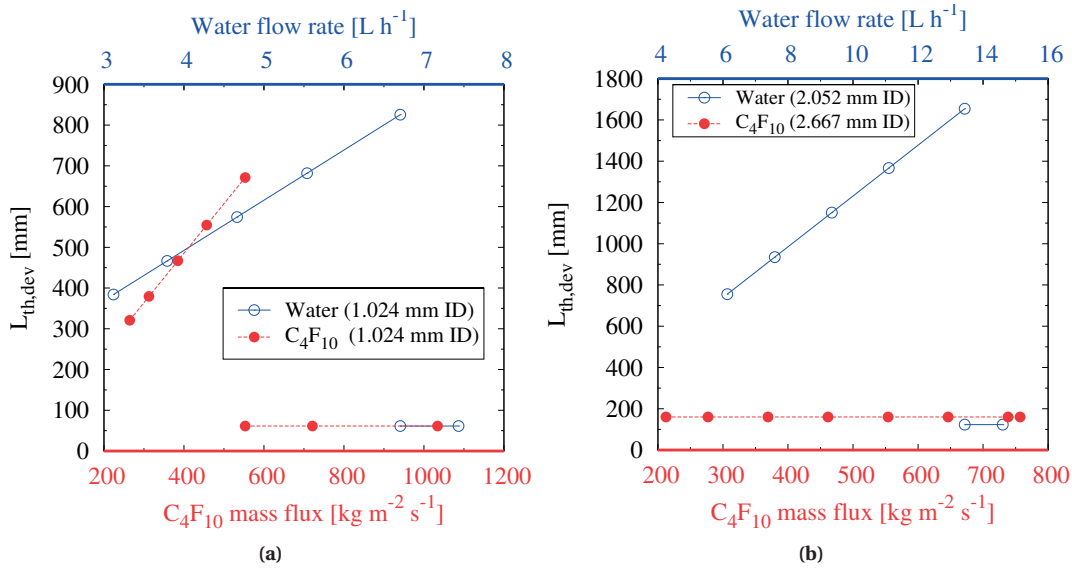


Figure 4.2: Single-phase thermal development length for the baseline Inner and Outer Barrel staves with water and C_4F_{10} as coolants, considering the cooling tubes uniformly heated in their perimeter and length.

thermal entry-length increases with the flow rate until $\sim 13.5\ L\ h^{-1}$, when the flow becomes turbulent and the thermal entry length decreases to just 123 mm. As it may be observed in Fig. 4.1b, that would leave all thermistors but T1 within the fully-developed flow region. With two-phase C_4F_{10} , the flow is always turbulent at the tested mass fluxes and a thermal entry length of 160 mm is expected.

It is worth emphasising that these calculations were made assuming an uniform heat flux around and along the cooling tubes in the staves, which, given their design and the fact that the wall thicknesses and thermal conductivity of the tubes are very low, might be far from reality. Also, since there are changes of diameter at the tubing connecting the staves to the cooling loops, it is unclear whether the fluid would be or not fully developed hydrodynamically at the beginning of the heated regions in the staves.

4.2.2 Experimental facilities

Experimental facilities were built at CERN to perform thermo-hydraulic tests with demineralised water and two-phase C_4F_{10} refrigerant. The water cooling circuit is displayed in Fig. 4.3. The stave prototypes are connected to an existing leak-less water plant providing a water flow rate at a controlled temperature. The absolute pressure at the stave outlet ranged from 0.6 to 0.7 bar. The volumetric water flow rate is adjusted with a needle valve (NV2) installed after a pallet flow meter (FM) working in the $3\text{--}30\ L\ h^{-1}$ range. Its calibration was verified before and after the tests. Water temperature and absolute pressure are tracked before and after the stave with PT100 sensors and pressure transducers respectively, at the stave inlet and outlet. The loop instrumentation was installed by the author.

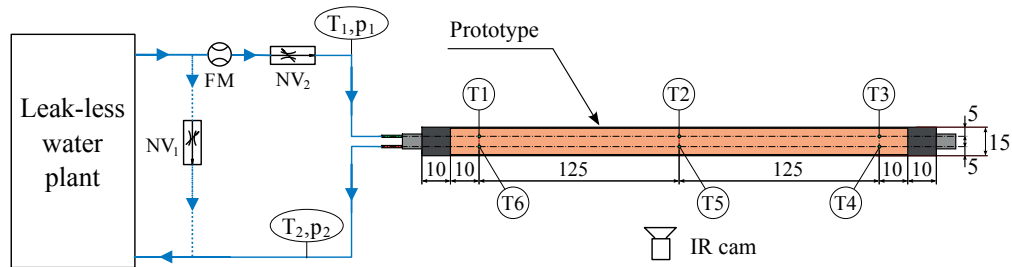


Figure 4.3: Schematic view of the experimental water loop with an Inner Barrel stove. Dimensions are expressed in mm.

Evaporative C_4F_{10} tests were run using an existing two-phase cooling plant [137], and a two-phase loop with instrumentation installed by the author to control the two-phase refrigerant condition at the stove inlet and monitor specific two-phase flow parameters. The two-phase C_4F_{10} loop is depicted in Fig. 4.4. Subcooled C_4F_{10} liquid leaves the plant and its pressure is tracked before reaching the bypass line linking to the return line through the needle valve ($NV1$). After the bypass, the liquid mass flow rate is measured in a Coriolis effect flow meter (CFM). The liquid is then subcooled by making it circulate in a coil inside a thermal bath. The refrigerant subcooling is controlled with an insulated electrical pre-heater (PH). Wall superheating is measured in the pre-heater by two NTC thermistors, to ensure the fluid does not reach two-phase conditions, and prevent potential burnout of the pre-heater in case of failure of the pump. The coolant then passes through a needle valve ($NV2$), which has three functions:

1. Control the coolant mass flow rate.
2. Provide an isenthalpic pressure drop. Such expansion triggers some flashing and the coolant reaches the stove inlet at saturation conditions.
3. Prevent flow instabilities. These phenomena are recurrently reported in several experimental two-phase flow studies. Their origin may be related to thermal instabilities caused by compressible volumes. A way to minimise instabilities is to install and control needle valves in the system, especially upstream the two-phase flow region [90].

Two-phase C_4F_{10} cooling tests were performed and recorded under stable boiling conditions in the staves. These conditions were verified by ensuring no pressure oscillations larger than the type B uncertainty of the pressure sensors were measured and also by checking visually that no flow instabilities occurred at the inlet and outlet connection tubes to the stove, which are made of transparent polyurethane. It must be emphasised that the needle valve $NV2$ and the sensors measuring T_3 , p_3 , and T_4 , p_4 are all installed over a short pipe distance and very close to the stove inlet/outlet ports. This short length between the start of vapour flashing and the stove inlet prevents bubble collapsing and compressibility effects leading to unstable boiling from occurring.

Pressure and temperature are tracked at the stove inlet and outlet by means of pressure transducers

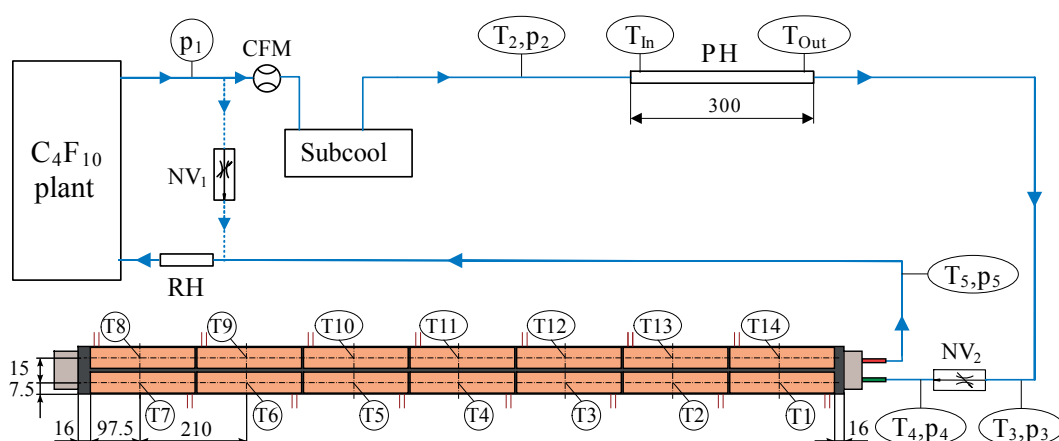


Figure 4.4: Schematic view of the experimental two-phase C_4F_{10} loop with an Outer Barrel stove. All dimensions are expressed in mm.

and PT100 sensors respectively. The refrigerant is returned to the plant through a large line and a return heater (*RH*), which fully evaporates the fluid, minimising the return pressure drop.

All tests were performed at a controlled room temperature of 21°C . All sensor signals are read by an ELMB data acquisition card [138] and then saved to a computer through a CAN OPC Server. The PVSS software is used to visualise and record data in real time. The author hereby acknowledges the help of M. Doubek configuring the CAN OPC Server and the PVSS software for data acquisition. Fluid physical properties were computed using NIST REFPROP [139]. A Fluke Ti10 thermal imager (*IR Cam*, as shown in Fig. 4.3) is used for recording the temperature of the heater in each prototype in a non-intrusive manner during the water and two-phase C_4F_{10} cooling tests. The thermo-camera is installed on a fixed support, using black opaque paper around the staves in order to prevent any reflections in the infrared images. The collaborating working group from the INFN Bari Institute measured the emissivity of the Kapton[®] heater experimentally in a climatic chamber using PVC tape as reference. A value of 0.86 was reported.

Two pictures of the stove prototypes connected to the experimental facilities are displayed in Fig. 4.5. Fig. 4.5a shows a view of an Inner Barrel stove in its support, with the 6 temperature sensors installed on the Kapton[®] heater. Fig. 4.5b displays the inlet/outlet port of an Outer Barrel half-stave, its connections to the C_4F_{10} loop via soft, transparent polyurethane tubing, and the needle valve (*NV2* in Fig. 4.4). The temperature and pressure sensors are hidden beneath the thermal insulation.

Pictures of the leak-less water cooling plant and the two-phase C_4F_{10} plant, which provides the subcooled C_4F_{10} liquid to the loop, are shown in Figs. 4.6a and 4.6b, respectively. More information on the two-phase C_4F_{10} cooling plant can be found in [137].

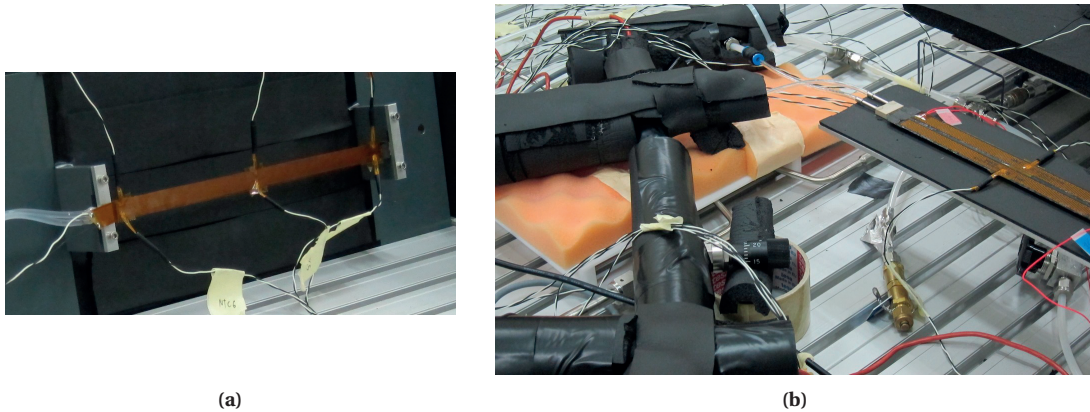


Figure 4.5: Cooling loops at CERN:(a) Inner Barrel stave in its support, as viewed from its heated surface; (b) Outer Barrel half-stave inlet/outlet end, connected to the C_4F_{10} loop.

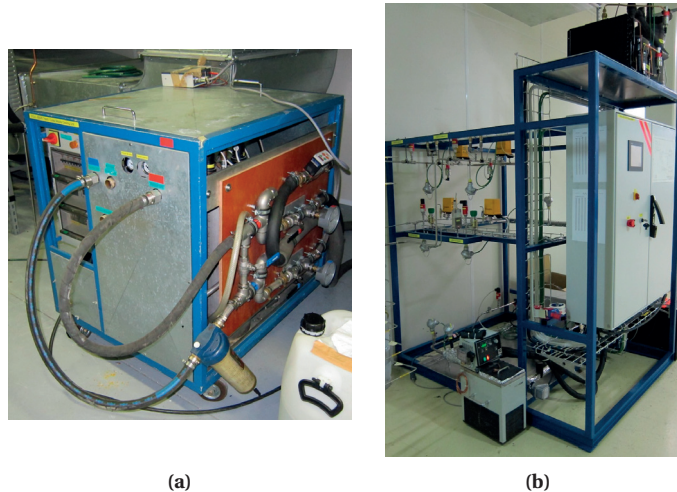


Figure 4.6: Pictures of the leak-less water plant (a), and the two-phase C_4F_{10} plant (b) used at the facilities at CERN.

4.3 Experimental methodology

4.3.1 Heat exchange with the ambient

During detector operation, the staves exchange heat with the ambient. The magnitude of such heat exchange has to be quantified during the thermal characterisation tests to understand the effective heat load transferred to the cooling fluid. If the stave is warmer than the ambient air, the air flushing system should be able to remove the heat load dissipated to the ambient. If the stave is colder than the surroundings, it has to be guaranteed that the stave cooling system can deal with the extra heat load intake. Theoretical and experimental analysis were performed to quantify heat exchange with the environment.

Theoretical analysis

Two heat transfer mechanisms are involved in the heat exchange with the environment: free convection and radiative heat transfer. The first highly depends on the position of the stave and its size. The second mechanism is influenced by the temperature of the surrounding air and objects. In this subsection, a theoretical analysis is made to determine the influence of each of the two heat transfer mechanisms. The sign convention is defined as follows: positive for heat transfer from stave to the ambient, and negative for heat transferred from the ambient to the stave.

Staves built with the same architecture as P2 (see Fig. 3.17b) can be considered as flat plates dissipating heat from both sides^a and with no spaceframe^b. In each Barrel layer, staves are installed parallel to the z-axis (i. e. Barrel central axis, horizontal) and, depending on the location of the stave in the layer, the plate can be horizontal (top and bottom of the Barrel), inclined, or vertical (sides of the Barrel), as displayed in Fig. 3.2. The correlation by Churchill and Chu [140] was used to quantify the free convection heat transfer for the staves at the sides of the Barrels (vertical), whilst the correlations by Stewartson [141] and by Churchill [142] were applied to the staves at the top/bottom of the Barrels (horizontal staves). The inclined staves represent an intermediate case between horizontal and vertical. All these correlations are detailed in appendix A, section A.2.1.

Despite the small characteristic dimension (the plate width), the highest heat exchange scenario would occur for a stave in vertical position, located at the sides of the Barrel. Free convection heat transfer rate with the ambient is reported in Table 4.1 for Inner and Outer Barrel staves at several mean stave-air temperature differences. It can be observed that up to 8.8% of the Inner Barrel stave heat load at a power density of 0.15 W cm^{-2} is dissipated by free convection if the stave is mounted at the sides of the Barrel (vertical). This would correspond to the case where the stave displays its maximum admissible temperature, 30°C , and the air is at 21°C . For the Outer Barrel half-staves, the maximum fraction of the nominal power at 0.15 W cm^{-2} dissipated by free convection in that case is 6.9%.

Two scenarios are assumed regarding boundary conditions for the radiative heat transfer:

1. Stave as a small body in a big volume (room).
2. Staves assembled in the Barrels.

The first scenario occurs during the experimental thermal tests, where the stave is not insulated and stays in a big room at a constant temperature of 21°C . The net radiative heat transfer between the stave and the room, considering both as gray surfaces^c, is:

$$E_{rad, stave-room} = \epsilon_{stave} \sigma A_{plate} (T_{stave}^4 - T_{room}^4) \quad (4.3)$$

^a The side of the cooling plate embedding the cooling pipes is assumed to have the same temperature as the chip side.

^b Heat exchange may occur in the spaceframe filaments close to the cooling plate, which would show temperatures similar to the cooling plate. This effect was not accounted for in theoretical heat exchange analysis.

^c Gray surface: surface for which the spectral absorptivity is independent of wavelength over the spectral regions of surface irradiation and emission

Table 4.1: Free convection heat exchange of the ITS Upgrade staves with the environment, absolute (E_{nc}) and relative to a stave power dissipation of 0.15 W cm^{-2} . Results reported for one stave or half-stave, and several temperature differences between the plate and the air.

Stave	Position	$\Delta T_{plate-air}$ [K]	-6	-3	-1	1	4	7	9
Inner Barrel	Vertical	E_{nc} [W]	-0.33	-0.14	-0.04	0.04	0.20	0.40	0.54
		% of 0.15 W cm^{-2} [%]	5.4	2.4	0.7	0.7	3.3	6.1	8.8
	Horizontal	E_{nc} [W]	-0.22	-0.10	-0.03	0.03	0.14	0.27	0.36
		% of 0.15 W cm^{-2} [%]	3.7	1.6	0.4	0.4	2.2	4.4	5.9
Outer Barrel ^a	Vertical	E_{nc} [W]	-2.82	-1.21	-0.32	0.32	1.72	3.41	4.64
		% of 0.15 W cm^{-2} [%]	4.2	1.8	0.5	0.5	2.6	5.1	6.9
	Horizontal	E_{nc} [W]	-1.84	-0.80	-0.21	0.21	1.13	2.22	3.00
		% of 0.15 W cm^{-2} [%]	2.7	1.2	0.3	0.3	1.7	3.3	4.4

where ϵ_{stave} is the emissivity of the stave surface, σ is the Stefan-Boltzmann constant ($5.67 \cdot 10^{13} \text{ W m}^{-2} \text{ K}^{-4}$) and T'_{stave} and T'_{room} are the mean stave and room temperatures, in K. In Eq. 4.3, it is assumed the stave is at a higher temperature than the room. A_{plate} is considered as twice the plate surface, as radiative heat transfer is assumed to occur at both sides of the plate.

The second scenario can be understood when considering the ITS Upgrade detector as concentric cylindrical layers at different temperatures exchanging heat by radiative heat transfer, dividing the transferred heat load among the number of staves or half-staves in one layer. Subsequently, two extreme cases are defined for the Inner and Outer Barrel staves. For the Inner Barrel, layer 2 (see Fig. 3.2a) will experience radiative heat exchange with layer 1 and layer 3, already in the Middle Barrel, assuming these layers stay at different temperatures. At the Outer Barrel, layer 6 is subject to radiative heat exchange with layer 5 and the ITS carbon fibre outer enclosure, depicted as the outermost shell in Fig. 3.2b, supposing once again these cylindrical layers are at a different temperature than layer 6. Eq. 4.4 is thus applied sequentially to the layers:

$$E_{rad,1-2} = \frac{\sigma}{\frac{1}{\epsilon_1} + \frac{1-\epsilon_2}{\epsilon_2} \left(\frac{r_1}{r_2}\right)} A_1 (T_1^4 - T_2^4) \quad (4.4)$$

Subindices 1 and 2 designate the smaller and bigger layers, with radiuses r_1 and r_2 respectively. Plate surfaces are considered as CFRP. Their emissivities depend on the type of composites; a value of 0.80 was chosen for the calculations. The chip surface will be covered by a Flex Printed Circuit (FPC) as displayed in Fig. 3.1, presumably encapsulated in polyimide. The emissivity previously reported for this material is used: 0.86. It is also the expected emissivity of the Kapton[®] heaters used in the thermal tests described in this thesis.

Table 4.2 reports the radiative heat transfer in the two scenarios for several temperature differences

^a Half-staves are considered in the calculation for the Outer Barrel.

Table 4.2: Radiative heat exchange of the ITS Upgrade staves with the environment, absolute (E_{rad}) and relative to a power density of 0.15 W cm^{-2} . Results reported for one stave or half-stave, and several temperature differences between the plate and the room (scenario 1) or the neighbour staves (scenario 2).

Stave	Case	$\Delta T_{plate-room/stave}$ [K]	-6	-3	-1	1	4	7	9
Inner Barrel	1. Stave in big volume	E_{rad} [W]	-0.23	-0.12	-0.04	0.04	0.16	0.29	0.37
		% of 0.15 W cm^{-2} [%]	3.8	1.9	0.7	0.7	2.7	4.8	6.2
Outer Barrel ^a	2. Stave assembled in Barrel	E_{rad} [W]	-0.19	-0.10	-0.03	0.03	0.13	0.24	0.31
		% of 0.15 W cm^{-2} [%]	2.7	1.3	0.5	0.5	1.9	3.3	4.3
Inner Barrel	1. Half-stave in big volume	E_{rad} [W]	-2.57	-1.30	-0.44	0.44	1.80	3.20	4.16
		% of 0.15 W cm^{-2} [%]	3.8	1.9	0.7	0.7	2.7	4.8	6.2
Outer Barrel ^a	2. Half-stave assembled in Barrel	E_{rad} [W]	-1.69	-0.86	-0.29	0.29	1.19	2.11	2.74
		% of 0.15 W cm^{-2} [%]	2.5	1.3	0.4	0.4	1.8	3.1	4.1

between each stave and the room (named scenario 1 above) and each stave and the neighbouring layers (scenario 2). For simplicity, it was assumed that the neighbouring layers will all display the same temperature difference with the studied stave. The case of an Outer Barrel stave in a big room would display the highest radiative heat exchange rate.

In view of the results depicted in Tables 4.1 and 4.2, it can be concluded that radiative heat transfer accounts for half of the heat load exchanged with the ambient, the other half being exchanged by natural convection. The highest heat exchange scenario would occur for a stave in a vertical configuration (i.e. at the sides of the Barrel), considering it is in a big room. Such conditions take place during the experimental test campaign, where the room is at a controlled temperature of 21°C .

Table 4.3 summarises the total heat exchange with the ambient for a vertical stave in a big room, in absolute terms and normalised to the power corresponding to the 0.15 W cm^{-2} power density, for several stave-ambient temperature differences.

Finally, the staves at the first layer of the Inner Barrel (layer 0) will see the beam pipe outer surface.

Table 4.3: Total heat exchange of the ITS Upgrade staves with the environment for staves at the sides of the Barrels (vertical) assuming they are in a big room. Absolute heat loads (E_{nc+rad}) and relative to a stave power dissipation of 0.15 W cm^{-2} are reported for a single stave or half-stave and several stave-air temperature differences.

Stave	$\Delta T_{plate-air}$ [K]	-6	-3	-1	1	4	7	9
Inner Barrel side stave in big volume	E_{nc+rad} [W]	-0.56	-0.26	-0.08	0.08	0.37	0.68	0.91
	% of 0.15 W cm^{-2} [%]	9.2	4.3	1.3	1.3	6.0	11.3	15.0
Outer Barrel side half-stave in big volume	E_{nc+rad} [W]	-5.39	-2.52	-0.76	0.77	3.52	6.61	8.80
	% of 0.15 W cm^{-2} [%]	8.0	3.7	1.1	1.1	5.2	9.8	13.0

^a Half-staves are considered in the calculation for the Outer Barrel.

The beam pipe dissipates heat too; a dedicated air cooling system is foreseen to be installed, keeping the outer surface temperature at around 40°C. Radiative heat transfer will occur between the beam pipe and the staves in layer 0. It can be quantified using Eq. 4.4 and dividing the heat load among the “viewable” 12 staves in the layer. The emissivity of the stave Flex Printed Circuit and the beam pipe is set to the value of polyimide, 0.86, since the beam pipe will be wrapped in Kapton® foil. Table 4.4 reports the heat load received by the staves in layer 0.

Overall, a stave from layer 0 at 15°C with an ambient air temperature of 21°C and the beam pipe outer surface at 40°C will receive ~ 1 W by free convection and radiative heat transfer, on top of the power dissipated by the chips. The nominal power dissipation of 58 mW cm⁻² means that each Inner Barrel stave dissipates 2.33 W as reported in Table 3.1. Adding the extra ~ 1 W, the total heat load corresponds to a power density of ~ 82 mW cm⁻². Subsequently, it can be concluded that the baseline power density of 0.15 W cm⁻² assumed in the Inner and Outer Barrel thermal tests, as stated in section 3.3.1, provides a generous margin accounting for extra heat load intakes. Besides, tests at 0.30 and 0.50 W cm⁻² were carried out to explore the limits of the ultra-lightweight concepts.

Experimental analysis

Theoretical heat loss analysis is useful to quantify the heat exchange with the ambient of the entire ITS Upgrade detector. However, the analysis strongly relies on assumptions. For instance, the geometry was simplified, assuming each stave as a plate and each Barrel layer as a perfect cylinder, but such assumptions do not work for a complex geometry such as the P1 stave architecture shown in Fig. 3.17a. Besides, no edge effects were taken into account. To overcome the limitations of the theoretical analysis, an experimental method to quantify the heat exchange with the ambient was devised and followed for each stave prototype prior to single- and two-phase tests. The method consists of three steps:

1. Before circulating any refrigerant (i.e. empty cooling channels) and with all connections and instrumentation to be used in the thermal tests installed, the stave is powered to a low heat load and left to reach a thermal balance with the ambient.
2. When steady-state conditions are achieved, the average heater surface temperature (i.e. the mean readings of the thermistors on the heated surface) and the ambient temperature are recorded.

Table 4.4: Radiative heat transfer from the beam pipe at 40°C to each stave in the innermost Inner Barrel layer (layer 0), for several stave temperatures. Absolute heat loads ($E_{rad,bp-stave}$) and relative to a stave power dissipation of 0.15 W cm⁻² are reported.

$T_{beam-pipe}$ [°C]	40	40	40	40	40	40	40
T_{stave} [°C]	15	18	20	22	25	28	30
$E_{rad,bp-stave}$ [W]	0.35	0.31	0.29	0.26	0.22	0.18	0.15
% of 0.15 W cm ⁻² [%]	5.8	5.1	4.7	4.3	3.6	2.9	2.5

3. The two steps above are repeated for several heat loads that give stave mean temperatures close to those expected during tests (20 to 35°C).

Fig. 4.7 shows the power applied to the uncooled Inner Barrel P2 stave prototype described in Fig. 3.17b versus the difference between the mean heater temperature and the ambient air temperature. A linear correlation is found between these two parameters. The power dissipated to the ambient by free convection and radiative heat transfer mechanisms, calculated analytically as described in the previous subsection, is overlaid on the plot, displaying also a linear trend. Good agreement between the analytical and experimental values is found, with deviations lower than 26% at $\Delta T_{stave-amb} \leq 10$ K.

The experimental heat loss determination method is performed for each stave prototype right before the cooling tests, with the same experimental layout, obtaining a linear correlation as displayed in Fig. 4.7. Later, in the cooling tests, the temperature difference between the stave and the ambient air is recorded and input in the aforementioned linear correlation, obtaining the heat load dissipated to the air. For instance, for the prototype in Fig. 4.7, if the temperature difference between the stave heater and the air is 10 K during a water cooling test, the heat load dissipated to the air is 1.3 W.

This simple methodology is based on the assumption that the temperature distribution on the stave is similar when powering it with and without coolant. The validity of this assumption was confirmed upon examination of the experimental data recorded during the cooling tests. The infrared images showed low temperature gradients on the powered stave prototypes with and without cooling. At the same time, due to the low heat loads applied, the coolant flow experiences low temperature differences resulting from liquid heat-up in single-phase tests and saturation temperature drop in two-phase cooling. Thus, it can be concluded that the experimental method for determining heat exchange with ambient represents a valid approach for the cooling tests.

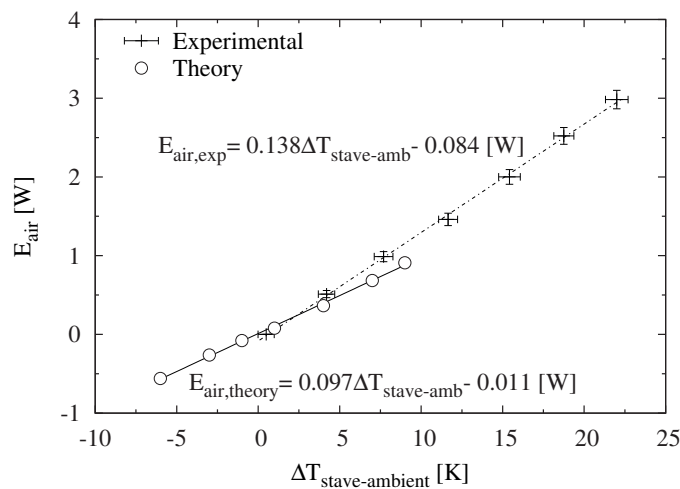


Figure 4.7: Experimental and theoretical heat load exchanged with the air versus the difference between the mean heater temperature and the air temperature at the P2 Inner Barrel stave prototype.

4.3.2 Stave thermal performance

The power density, or stave heat flux, in W cm^{-2} , for a electrical power applied to the heater (E_{heater}) is calculated as follows:

$$P_d = \frac{E_{heater}}{A_{plate}} \quad (4.5)$$

The difference between the mean heater temperature, calculated from the n thermistors on top of the heaters in each stave, and the mean fluid temperature is used to measure thermal performance, as expressed in Eq. 4.6 below. Since the room temperature and humidity are controlled, similarly to the conditions in the ALICE Experiment, this is a reliable thermal performance assessment parameter:

$$\Delta T_{heater-coolant} = \frac{1}{n} \sum_{i=1}^n T_{NTC,i} - \frac{T_{in} - T_{out}}{2} \quad (4.6)$$

Current figures of merit regarding $\Delta T_{chips-coolant}$ in HEP particle detector cooling systems oscillate between 7 and 10 K for a power density of 0.5 W cm^{-2} .

4.3.3 Single-phase flow parameters

Cooling tests with water were performed to assess the stave thermal performance. Single-phase C_4F_{10} tests were aimed to validate the setup prior to the two-phase flow tests.

Pressure drop

Pressure drop tracking is key when cooling with water. Since a water cooled system in the ITS Upgrade has to be leak-less, the pressure drop should remain well below 1 bar in order to guarantee the return of the water flow. As described in section 3.7.1, based on previous experiences [24], a maximum stave pressure drop limit of 0.5 bar would ensure suitable flow circulation from and back to the cooling plant, located approximately 50 m away from the ITS detector. For an increased safety margin, a value of 0.3 bar is set as the maximum admissible. In addition, prior to the two-phase C_4F_{10} tests, single-phase tests with the same fluid are run to validate the pressure drop measurements and verify there are no obstructions in the piping.

Experimental pressure drop values are calculated from the difference between the readings of the two pressure transducers. They are compared with values from frictional pressure drop prediction methods in the literature, as follows:

$$\Delta p_{pred} = \Delta p_{frict} + \Delta p_{sing} \quad (4.7)$$

where Δp_{frict} is the frictional pressure drop in straight channels, expressed below for a channel of length

L , inner diameter D_i , and a fluid of density ρ flowing at a velocity u :

$$\Delta p_{frict} = \zeta \frac{L}{D_i} \frac{\rho u^2}{2} \quad (4.8)$$

where ζ is the Darcy friction factor. In laminar regime ($Re < 2300$ in a circular channel), the friction factor is related to the Reynolds number according to the Hagen-Poiseuille's law:

$$\zeta = \frac{64}{Re} \quad (4.9)$$

For fully turbulent flows ($Re > 8000$), the friction factor is related to the Reynolds number through the implicit equation of Colebrook [143]. While the Moody chart provides a quick way of obtaining the friction factor, explicit approaches to this problem can be found in the literature. The basic correlation by Blasius [144] is limited to smooth tubes as it does not include the influence of the tube roughness. The correlation by Churchill [145] is recommended by the author since it spans all regimes, from laminar to turbulent. The transitional regime, spanning Reynolds numbers from 2300 and up to 8000-10000, the flow regime will strongly depend on the inlet conditions. The Churchill correlation provides a smooth transition between the laminar and the turbulent flow regimes, including the transitional regime. Its implementation can be found in appendix A.

Δp_{sing} is the pressure drop in the singularities, in particular the diameter changes at the inlet/outlet connections, and the Π -bend element connecting the two polyimide tubes. Singular pressure drops are expressed as follows:

$$\Delta p_{sing} = \zeta_{sing} \frac{\rho u^2}{2} \quad (4.10)$$

where ζ_{sing} is the friction factor due to the presence of a singularity. Generally, this parameter depends on the flow regime, the type of singularity and its geometry, but it is also sensitive to the presence of other singularities upstream and downstream a particular singularity. Predictive methods of ζ_{sing} are mostly empirical and account for a variety of pipe configurations and flow conditions. The author recommends the use of the methods by Idelchik [146] to obtain approximate values of pressure drops in the singularities. The methods used in this dissertation are described in appendix A. These methods, together with the Churchill correlation for straight channels, were used to find the optimal channel diameter of the ITS Upgrade staves for single-phase water cooling. For a desired water flow rate, the total pressure drop in the ITS Upgrade staves is estimated, decreasing the cooling channel diameter iteratively until the expected water pressure drop in the stave remains near 0.3 bar.

Energy balance

The energy balance is performed in a control volume comprising the stave prototype only. The electric power provided to the stave heater (E_{heater}) is compared to the enthalpy rise of the liquid coolant along

the stove ($E_{coolant}$), taking into consideration the experimental heat exchange rate with the ambient (E_{air}), as described in section 4.3.1:

$$\frac{\Delta E}{E} = \frac{E_{coolant} - E_{heater} - E_{air}}{E_{heater} - E_{air}} \quad (4.11)$$

The heat load transferred to the fluid is determined using the readings from the PT100 sensors at the stove inlet and outlet, as follows:

$$E_{coolant} = \dot{m}_{coolant} c_p (T_{out} - T_{in}) \quad (4.12)$$

This analysis provides valuable feedback on the test setup and the heat exchange with the ambient. It is particularly important in the single-phase C_4F_{10} test as a validation of the two-phase experimental setup.

4.3.4 Two-phase flow parameters

Prior to the two-phase C_4F_{10} cooling tests, the staves were subjected to single-phase water and C_4F_{10} tests, carefully cleaning the channels with nitrogen, allowing time to dry, and vacuuming the stove lines before changing the coolant. This methodology provides validation of the experimental setup (pressure drop, energy balance) and direct cooling performance comparison between water and two-phase C_4F_{10} .

For a given power density, the required two-phase C_4F_{10} mass flow rate, in kg s^{-1} , is estimated as follows:

$$\dot{m}_{tp} = \frac{E_{heater}}{i_{lv} \Delta x_{in-out}} \quad (4.13)$$

where i_{lv} is the coolant latent heat at the desired saturation temperature, and Δx_{in-out} is the vapour quality increase between the stove inlet and outlet (x_4 and x_5 in Fig. 4.4). Setting this parameter to a desired value, typically 0.4 or 0.5, and choosing the fluid saturation temperature, the required mass flow rate is easily calculated.

The coolant mass flux, G , is the ratio between the two-phase mass flow rate, \dot{m}_{tp} , and the internal sectional area of the polyimide channels, A_i , as expressed below:

$$G = \frac{\dot{m}_{tp}}{A_i} \quad (4.14)$$

$$A_i = \frac{\pi D_i^2}{4} \quad (4.15)$$

The configuration of the two-phase loop allows tracking of the fluid vapour quality at the stove

inlet. Indeed, as one can observe in the loop scheme in Fig. 4.4, the enthalpy of the subcooled liquid leaving the pre-heater is determined through pressure and temperature measurements in point 3. The value of i_3 was validated by applying Eq. 4.12 in the pre-heater. The needle valve *NV2* triggers fluid evaporation through an isenthalpic expansion; hence the enthalpy in point 4 (stave inlet) is assumed to be the same as at point 3, as stated in Eq. 4.16:

$$i_3 = i_4 = f(p_3, T_3) \quad (4.16)$$

Pressure and temperature readings in point 4 are used to verify that the fluid is in saturated conditions and, together with i_4 , allow determining x_4 , as indicated below:

$$x_4 = f(p_4, i_4) \quad (4.17)$$

The stave outlet vapour quality, x_5 , may be used to predict the fluid flow pattern and anticipate the onset of dryout conditions, which result in low local heat transfer coefficients and thus, locally high wall superheating and hotspots on the chip surface. x_5 is calculated assuming thermodynamic equilibrium (see Eq. 4.18), which can be assumed during the steady-state conditions in the tests. The liquid enthalpy and latent heat at the stave outlet conditions ($i_{5,l}$ and $i_{5,lv}$) are determined from pressure and temperature measurements, p_5 and T_5 :

$$x_5 = \frac{\frac{E_{heater} - E_{air}}{GA_i} + i_4 - i_{5,l}}{i_{5,lv}} \quad (4.18)$$

Two-phase pressure drop

Monitoring the two-phase pressure drop is of great importance to guarantee the two-phase saturation temperature does not fall below the minimum admissible at the ITS Upgrade, 12°C. Comparing it with analytical predictions gives feedback on the stave construction i.e. no blocks or pinched channels.

Two-phase pressure drops can be calculated analytically as the sum of the two-phase frictional pressure drop at the channels and the Π -bend, and the momentum pressure drop in diabatic tests (test conditions where the vapour quality increases along the stave). No gravitational effects are considered as the cooling channels are at the same horizontal plane. The momentum pressure drop is calculated by assuming a separate liquid-vapour flow, the two phases having different velocities:

$$\Delta p_{mom} = G^2 \left\{ \left[\frac{(1-x)^2}{(1-\varepsilon)\rho_l} + \frac{x^2}{\varepsilon\rho_v} \right]_{out} - \left[\frac{(1-x)^2}{(1-\varepsilon)\rho_l} + \frac{x^2}{\varepsilon\rho_v} \right]_{in} \right\} \quad (4.19)$$

where ε is the two-phase void fraction, calculated for the staves using a void fraction prediction method from the literature. A widely used method, appropriate for the channel sizes in the staves, is Steiner's version [84] of the Rouhani and Axelsson drift flux void fraction correlation [83].

The predicted two-phase pressure drop in evaporative conditions is calculated as follows:

$$\Delta p_{tp,pred} = \Delta p_{tp,frict} + \Delta p_{mom} \quad (4.20)$$

The straight line frictional pressure drop is calculated using the correlation by Friedel [92]. The singular pressure drop at the singularities (Π -bend, diameter changes), is estimated with the correlation by Chisholm [101]. However, as described in section 2.5.5, the results of this calculation should be regarded as an approximation, due to the amount of factors having an impact on the two-phase pressure drop in singularities, including the flow conditions upstream and downstream each singularity. The reader is referred to appendix A, section A.1.2, for a full description of the two-phase frictional pressure drop correlations here used.

4.3.5 Stave thermal resistance and heat transfer coefficient of the coolant

A calculation method is proposed below to calculate the average heat transfer coefficient of the coolant in the stave channels, although obtaining this parameter for the staves is not a target of this work. The global thermal resistance between the stave heater and the coolant flow is defined as follows:

$$R_{global} = \frac{\Delta T_{heater-coolant}}{E_{heater} - E_{air}} = R_{cond} + R_{conv} \quad (4.21)$$

where R_{cond} is the conductive thermal resistance in the stave, from the heater to the inner wall of the channel, and R_{conv} is the thermal resistance of convection between the channel inner wall and the coolant. The last can be defined as:

$$R_{conv} = \frac{1}{hA_{lat}} \quad (4.22)$$

where h is the average heat transfer coefficient, and A_{lat} is the internal wall area of the two channels on the stave, calculated as $A_{lat} = \pi D_i (2L_{stave})$.

In certain conditions, R_{conv} can be calculated quite accurately by using a heat transfer coefficient model. The correlations described in chapter G1 of the VDI Heat Atlas [147] take into consideration a variety of flow conditions and regimes. For instance, Spang [148] put forward an expression to determine the local heat transfer coefficient for thermally and hydrodynamically developing laminar flows ($Re < 2300$) inside the channels with a constant heat flux. Local heat transfer coefficients in the transition region between laminar and fully developed turbulent flow ($2300 \leq Re \leq 10000$) can be estimated by using the correlation proposed by Gnielinski [149], though in this region the heat transfer depends highly on the pipe inlet and the flow conditions upstream the pipe inlet. By discretising the pipe length and applying these correlations in each discrete element, accurate heat transfer coefficient results can be obtained for each of the channels in the staves in constant heat flux conditions. For fully developed turbulent flows, a larger choice of correlations is available in the literature. The author used,

for that flow condition, the simplified correlation by Gnielinski [150] and its advanced version, based on the correlation by Petukhov [151]. All the correlations referenced in this paragraph are detailed in appendix A, section A.2.2.

Once h is determined, the value of R_{conv} is calculated through Eq. 4.22, and the thermal resistance of conduction in the stove can be estimated by using Eq. 4.21. This parameter only depends on the stove and not on the coolant or the flow regime.

It is best to calculate R_{cond} as indicated above from a series of experimental cooling tests with low uncertainty. For instance, water cooling tests in the laminar regime and at a heat load providing a reasonably high water temperature rise, thus yielding accurate estimates of R_{global} (see Eq. 4.21). It must be verified that the values of R_{cond} obtained using the methodology above remain uniform for the whole experimental test series considered.

The average heat transfer coefficient of any single- or two-phase flow cooling case in a stove may be estimated by using the value of R_{cond} previously obtained for the same stove. As R_{global} can be always measured experimentally, R_{conv} is determined via Eq. 4.21. The mean heat transfer coefficient is given by Eq. 4.22. However, this method yielded very high uncertainties with the present experimental setup. Therefore, heat transfer coefficient measurements in the staves are not accurate, as later reported in section 5.3.4. This is the main reason why the tests described in chapter 6 were carried out.

Determining the local experimental heat transfer coefficient of a fluid flow inside a channel requires measuring the wall superheating. Unfortunately, this is not possible in the tested staves.

4.3.6 Calibration and error analysis

Periodical calibration and verification of the instrumentation and the Data Acquisition System (DAQ) were performed in order to ensure accurate experimental measurements. The pallet flow meter at the water loop was calibrated using a frequency-to-voltage converter, averaging the voltage value over 100 individual readings, and measuring the water flow rate using a stopwatch and a scale. The ELMB channels and CAN OPC server were calibrated using reference electrical resistances.

The experimental uncertainty of each measured variable, expressed as expanded uncertainty, U , is calculated as:

$$U = \sqrt{errA^2 + errB^2} \quad (4.23)$$

The expanded uncertainty has two components. The type A uncertainty ($errA$) is a consequence from taking repeated, independent observations. According to the ISO Guide to the Expression of Uncertainty in Measurement [152], this component is defined for a set of measurements as the standard deviation of the mean. In order to evaluate in this experimental study the Type A error at a confidence interval of 95%, it is considered as two times the standard deviation (SD) of the measurements, assuming

a normal probability distribution^a:

$$errA = 2 SD \quad (4.24)$$

The type B uncertainty ($errB$) accounts for systematic errors, calibration of the instruments and specifications from the manufacturer. The type B uncertainties of the experimental setup are reported in Table 4.5 evaluated at a 95% confidence interval. Thus, considering Eq. 4.24, the expanded uncertainty of the measurements U , calculated with Eq. 4.23, is expressed at a 95% confidence interval.

The uncertainty of the thermophysical properties of the coolant (density, viscosity, enthalpy, thermal conductivity, specific heat, surface tension) is taken into consideration. The uncertainties of these values as indicated by Christians in appendix A of his Ph.D thesis [153] are assumed. In any case, these uncertainties are negligible compared to the error in the measured variables.

The uncertainty of the derived variables described in the present section is propagated from the measured variables using the equations below. Let us assume a variable y which depends of n measured variables:

$$y = f(X_1, X_2, \dots, X_n) \quad (4.25)$$

Assuming the X_i variables and their uncertainties are independent from each other and that their uncertainties follow a Gaussian distribution, the propagated uncertainty of y , $U(y)$, is calculated as

Table 4.5: Type B uncertainties of the measured experimental variables.

Parameter	Type B uncertainty (95% CI)
Tube ID	(1.024 ± 0.013) mm (1.450 ± 0.013) mm (2.052 ± 0.025) mm (2.667 ± 0.025) mm
Temperature (PT100)	± 0.4 K
Temperature (NTC)	± 0.9 K
Thermal imager	± 5 K
Absolute pressure	± 0.05 bar
Water flow rate	± 0.67 L h ⁻¹
C ₄ F ₁₀ mass flow rate	± (0.2% \dot{m} + 8) g h ⁻¹
Electrical power applied to heater ^b	± 0.8-3% E_{heater} W

^a For a normally distributed variable, a 95% coverage level corresponds to two times the standard deviation.

^b The uncertainty depends on the power applied, being higher for lower absolute heat loads.

Table 4.6: Global uncertainties of the two-phase flow parameters.

Parameter	Global uncertainty (95% CI)
Mass flux (G)	$\pm 2-3.5\%$
Vapour quality (x)	$< 10\%^a$
Pressure drop (Δp_{stave})	± 0.07 bar (5-38%)
Average stave heat transfer coefficient (h)	$\pm 8-70\%$

follows:

$$U(y) = \left[\sum_{i=1}^n \left(\frac{\partial y}{\partial X_i} U(X_i) \right)^2 \right]^{\frac{1}{2}} \quad (4.26)$$

Provided that all $U(X_i)$ are expressed at 95% confidence interval, $U(y)$ will be already evaluated at the same confidence interval.

Uncertainty results are often normalised to the absolute value of y . Table 4.6 displays the propagated uncertainties of the experimental parameter evaluating the cooling performance of a stave ($\Delta T_{heater-coolant}$) and the main two-phase experimental parameters. Note that uncertainty values are expressed as well with error bars in the plots.

^a Uncertainties at the stave inlet up to 70% were recorded due to the values of $x_4 \sim 0$.

4.4 Comparison of the two ultra-lightweight concepts

Inner Barrel stave prototypes with the P1 and P2 architectures, displayed in Fig. 3.17, were manufactured and tested thermally with demineralised water and two-phase C_4F_{10} refrigerant with the aim of understanding which concept yields better cooling performance: the lighter P1 or the more robust P2 stave. The results of this cooling performance comparison were first published in [133]. The prototypes were tested in a controlled environment at 21°C on a mechanical support and in a horizontal position with the flat surface where the heater is glued to slightly inclined. The experimental setup was always left to achieve stability and steady-state conditions for at least 15 minutes between two experimental cases. The plots in Fig. 4.8 report the temperature difference between the heater and the coolant flow versus the coolant flow rate for P1 (Fig. 4.8a) and P2 (Fig. 4.8b) staves at a heater power density of 0.30 W cm^{-2} . The top horizontal axis, in blue, indicates the water volumetric flow rate corresponding to the empty points in the same colour, while the bottom horizontal axis, in red, refers to two-phase C_4F_{10} mass flux and the filled red points.

A few observations are made in view of the results. First, comparing the two plots, it is observed the P2 prototype provides a better thermal performance than P1. Indeed, P2 can keep the heater less than 8 K hotter than the coolant flow, be it water or evaporative C_4F_{10} . Since the minimum fluid temperature shall be above the air dew point at the ITS Upgrade site, 12°C , the P2 prototype can easily comply with the thermal requirements with the coolant at a mean temperature up to 20°C , even at a power density of 0.30 W cm^{-2} , twice the nominal value of 0.15 W cm^{-2} . The P1 stave displays not only a poorer cooling performance but also higher temperature non-uniformity, as reported in Fig. 4.9.

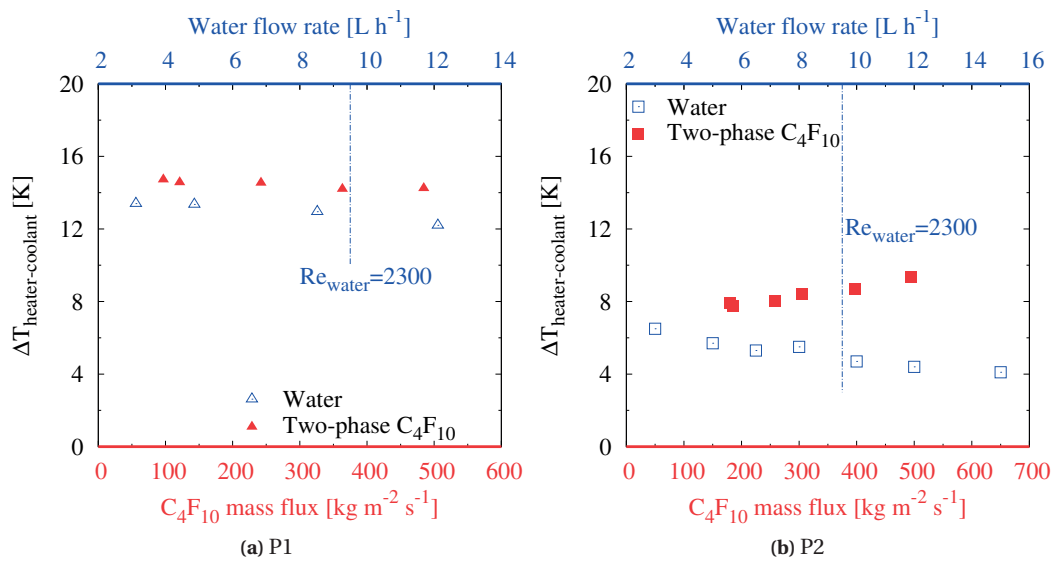


Figure 4.8: Heater average temperature relative to the coolant mean temperature in the stave for water and two-phase C_4F_{10} refrigerant, at 0.30 W cm^{-2} : (a) P1; (b) P2.

Second, regarding water cooling, no significant improvement of the cooling performance is observed when increasing the flow rate. This low flow sensitivity is seen in both prototypes. Below 10 L h^{-1} , the mild improvement at low water flow rates is due solely to the reduction of the water temperature rise, since the flow regime is laminar. Above 10 L h^{-1} , the Reynolds number exceeds 2300 and the flow enters the transitional regime, presumably anticipated thanks to the singularities in the stave (connections, Π -bend). However, though heat transfer coefficients are higher in the transitional and turbulent regimes than in laminar flows, no significant improvement of the thermal performance is observed.

Last, the influence of the refrigerant on the cooling performance is assessed. As displayed in Fig. 4.8, the temperature difference between the stave and the coolant does not change significantly if cooling with water or two-phase C_4F_{10} , especially at the nominal operating points with the evaporative refrigerant reported in Table 4.8. Such a comparison is displayed in Figs. 4.9 b and 4.9 d too. Taking into account the last two conclusions, it can be deduced that the conductive thermal resistance across the stave dominates over the convective thermal resistance between the tube wall and the coolant.

Table 4.7 reports two experimental cases, one per prototype, yielding the best compromise between cooling performance and water flow rate for the P1 and P2 prototypes. Table 4.8 summarises the points rendering the best cooling conditions with two-phase C_4F_{10} . The four cases displayed in the two tables constitute the nominal operating conditions for the P1 and P2 staves.

The use of an infrared camera at the experimental facility provided the capability to record the stave heater temperature map in a thermographic picture. The thermal images were compared with the information given by the thermistors on the stave heaters, finding a good match (see Fig. 5.21 for an Outer Barrel stave). Fig. 4.9 depicts the stave temperature map for the P1 (warmer) and P2 (colder) prototypes when cooling with water and two-phase C_4F_{10} and a power density of 0.30 W cm^{-2} at the nominal conditions reported in Tables 4.7 and 4.8. The average heater temperature of the P2

Table 4.7: Nominal cooling conditions for prototypes P1 and P2 at 0.30 W cm^{-2} with water.

Stave	\dot{V}_{water} [L h^{-1}]	$u_{mean,water}$ [m s^{-1}]	$T_{mean,water}$ [$^{\circ}\text{C}$]	$T_{mean,heater}$ [$^{\circ}\text{C}$]	ΔT_{water} [K]	Δp_{water} [bar]
P1	3.1	0.52	16.3	29.7	2.4	0.08
P2	3.0	0.52	16.4	22.9	2.4	0.23

Table 4.8: Nominal cooling conditions for staves P1 and P2 at 0.30 W cm^{-2} with evaporative C_4F_{10} refrigerant.

Stave	$G_{\text{C}_4\text{F}_{10}}$ [$\text{kg m}^{-2}\text{s}^{-1}$]	$T_{mean,\text{C}_4\text{F}_{10}}$ [$^{\circ}\text{C}$]	$T_{mean,heater}$ [$^{\circ}\text{C}$]	x_{in} [-]	x_{out} [-]	$\Delta p_{\text{C}_4\text{F}_{10}}$ [bar]	$\Delta T_{sat,\text{C}_4\text{F}_{10}}$ [K]
P1	242	14.0	28.5	0.07	0.36	0.14	1.1
P2	258	17.3	23.6	0.01	0.33	0.35	3.4

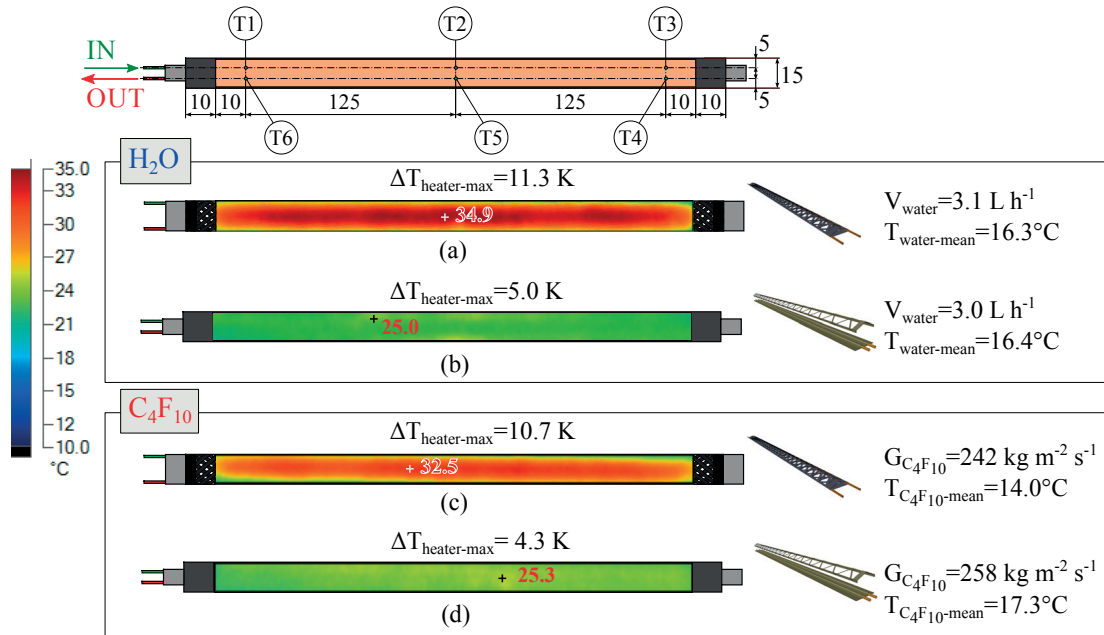


Figure 4.9: Infrared images showing the heater temperature map [C°] for tests at 0.30 W cm^{-2} on the P1 (a, c) and P2 (b, d) prototypes: (a, b) water; (c, d) evaporative C₄F₁₀ refrigerant. Dimensions in mm.

prototype is always clearly lower than for P1 at similar or warmer coolant temperatures, proving that the high-conductivity plate and spaceframe stave thermally outperforms the wound-truss structure.

The P1 prototype displays higher heater temperature non-uniformity, even though silicon dum-mies are installed beneath the heater. The stave structure lacks efficiency in channeling the heat load towards the cooling channels at the sides, resulting in maximum heater temperatures above 30°C even for coolant temperatures below 15°C. The P2 prototype displays temperature gradients between 4.3 and 5.0 K, depending whether the stave is cooled with evaporative C₄F₁₀ or with water. Infrared imaging is useful to locate hotspots on the prototypes. For the tested prototypes, the heater temperature map showed good uniformity and no evidence of gluing defects or poor local cooling was found.

In view of the results, it can be concluded that the P2 stave prototype provides better cooling capabilities than P1. In addition, due to the stave architecture and manufacturing process, the P2 prototype achieves better chip planarity and positioning control. Thus, the P2 ultra-lightweight concept has been chosen and developed for the Inner Barrel staves. The Outer Barrel half-staves, introduced in the next chapter are based on the same concept.

Either water or two-phase C₄F₁₀ refrigerant may be used, at least for the Inner Barrel staves. The coolant choice will result from a compromise between thermal needs, complexity of the system and especially, material budget. For the same tube, a two-phase flow will display large vapour fractions, resulting in a significantly lower average flow density and thus, lower material budget than the same liquid refrigerant. The two staves are thermally robust and can be cooled with a wide range of coolant flow rates and mass fluxes, thanks to the main thermal resistance being of conduction at the stave.

4.5 Stave design optimisation

As reported in Table 3.4, the material budget of the P2 stave still exceeds 0.3% for a fully equipped stave with water as coolant, especially when assembled in the Inner Barrel due to the overlap existing with the neighbouring staves. The stave concept was optimised to comply to the material budget target without compromising the thermal performance.

Several CFRP layups based on the P2 concept were tested and their performance experimentally assessed in the next chapter, but they all share a critical improvement: the minimisation of the polyimide channel diameter. Fig. 4.10 reports the experimental pressure drop with water in the P2 prototype, which has 1.450 mm ID polyimide channels, compared against the pressure drop expected if the channel size is decreased to 1.024 mm ID with channels walls 25 μm thick. The correlation by Churchill [145] is used to calculate the pressure drop in straight sections, while the singular pressure drops in the connections and the Π -bend are quantified by the methods by Idelchik [146]. Please see section A.1.1 for more information on these correlations.

In the previous section, it was observed that a 3 L h^{-1} water flow rate is enough to keep the P2 stave heater less than 8 K hotter than the coolant flow at 0.30 W cm^{-2} . At such a volumetric flow rate, the pressure drop is expected to be 0.3 bar in a stave equipped with a 1.024 mm ID. As later shown in Figs 5.5, the experimental pressure drop matches the theoretically predicted values, and minimising the diameter channel does not greatly affect the thermal performance (see Fig. 5.3).

The cooling channel size minimisation also decreases the mean material budget of the stave and the magnitude of the material budget peaks due to the presence of the cooling channels. This is critical when using a liquid refrigerant as a coolant. Fig. 4.11 shows the material budget across the P2

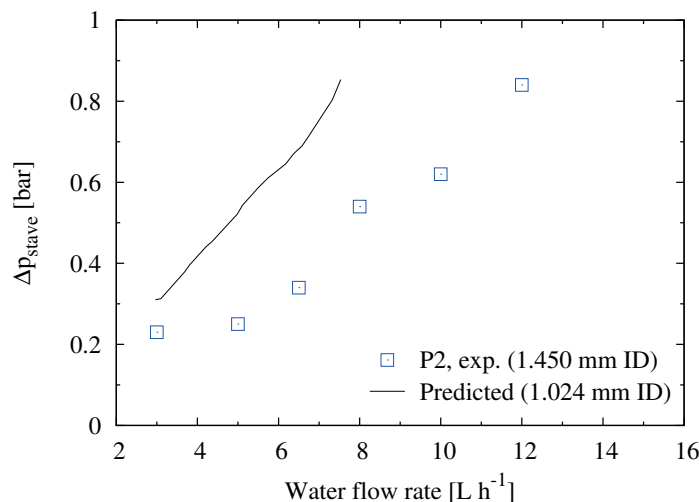


Figure 4.10: Water pressure drop increase if decreasing the stave cooling channel ID from 1.450 mm (experimental measurements in the P2 prototype) to 1.024 mm, predicted using the Churchill correlation [145] and the methods by Idelchik [146].

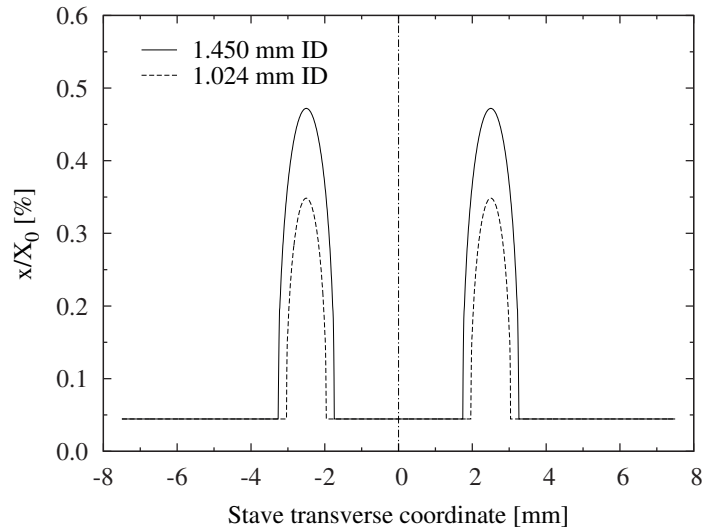


Figure 4.11: Material budget of the cooling plate assembly, cooling channels, and water as coolant of the P2 prototype if decreasing the stave cooling channel ID from 1.450 mm to 1.024 mm.

stave plate when cooling with water, with the original 1.450 mm ID channels and with the minimum diameter ones of 1.024 mm ID. Only the plate assembly, the cooling channel and water as coolant are considered in the calculation, i.e. no spaceframe, glue, chips or cables are accounted for. The material budget peaks are almost 30% smaller with the smaller cooling channels. The average material budget also decreases, as reported in Table 4.9.

Another step towards material budget minimisation was achieved by optimising the manufacturing process. While P2 is made in two separate parts, the spaceframe and the cooling plate, later glued together, optimised staves are made in just one step, decreasing the thickness at the sides of the stave due to the glue and extra CFRP presence. This, together with the pipe diameter minimisation, allow for a material budget reduction below the 0.3% threshold, as reported in Table 4.9. The IB1 stave is considered as the baseline Inner Barrel stave for the ITS Upgrade detector. Cooling performance results for this stave and other alternative stave layouts are presented in the next chapter.

Table 4.9: Weight and material budget of the P2 prototype and the optimised IB1 stave (1.024 mm ID channels). Sources: [4, 5]

	P2	IB1
Weight ^a [g]	1.8	1.4
$[x/X_0]_{full}$ ^b [%]	0.31	0.26
$[x/X_0]_{full,overlap}$ ^c [%]	0.38	0.28

^a Weight of the stave only, with no chips, glue or services. The inlet/outlet PEEK connector and Π -bend are not included, since they rest on the Barrel endwheels and hence are outside the detector sensitive area.

^b Includes: structure, water as coolant inside the channels, silicon chips, glue, and FPC (Flex Printed Circuit).

^c Full stave material budget (structure, water as coolant inside the channels, silicon chips, glue, FPC) and the overlap between adjacent staves in each Inner Barrel layer.

Chapter 5

Results of the experimental cooling tests of the ALICE ITS Upgrade staves

5.1 Introduction

This chapter reports the results of the experimental cooling tests performed with water and two-phase C_4F_{10} refrigerant on three Inner Barrel staves and three Outer Barrel half-stave prototypes. Additionally, an experimental study on the two-phase coolant inventory in an Outer Barrel half-stave is described, before closing the chapter with the concluding remarks and recommendations.

5.2 Inner Barrel staves

In this section, three Inner Barrel stave architectures featuring different properties are described and their cooling performance reported with water, and for one of the stave prototypes, with two-phase C_4F_{10} refrigerant as well. The three stave layouts considered here provided, to the best of the knowledge of the ITS Upgrade Mechanics and Cooling working package and the author, the best compromise between cooling and mechanical capabilities, low material, and quality of the manufactured staves. They are the result of an optimisation process that involved the evaluation of cooling test results and analysis obtained by the author, and mechanical tests by the mechanics team.

5.2.1 Description of the Inner Barrel stave layouts

In chapter 4, results from the first experimental cooling test campaign reported that the stave architecture offering the best compromise between good thermal performance and low material budget is given by the high-conductivity plate plus spaceframe concept, used in the stave prototype named P2 (see Fig. 3.17b). A schematic 3D view of this stave layout is displayed in Fig. 5.1. The P2 stave displayed better cooling performance than the wound-truss structure in the P1 prototype. The P2 stave was thus further developed by minimising the cooling channel size and optimising the manufacturing process.

Table 5.1 summarises the three stave layouts to be considered as baselines for the Inner Barrel staves. The second column displays a cross-section view of the cooling plate/channel assembly on each prototype. The spaceframe is identical for the three staves and it is not included in the cross sectional views.

IB1 represents an optimised version of the P2 prototype described in the previous chapter. It consists of a high thermal conductivity plate made of pre-impregnated unidirectional K13D2U-2K high-conductivity CFRP [42], 70 μm thick. The carbon fibres are oriented transversally to the stave, enhancing the heat spreading towards the cooling channels from the sides of the stave. Two polyimide cooling tubes for refrigerant circulation [64], with an inner diameter of 1.024 mm and a wall thickness of 25 μm , are located beneath a 30 μm -thick graphite foil [49], which enhances the thermal contact between the top of the cooling pipes and the plate. Two 20 μm -thick carbon fleece plies, at the top and the bottom of the assembly, encapsulate the whole plate layout providing mechanical stiffness and protection to the polyimide channels, guaranteeing its section remains circular. The upper structure, the spaceframe, is made of M60J-3K carbon fibre [39] in one step, at the same time as the cooling plate. It provides mechanical stiffness but no cooling capabilities. The total weight of this stave prototype is 1.4 grams, considering the cooling plate assembly, the spaceframe, and the polyimide channels only. The material budget of a single stave, including all services (silicon pixel chips, Flex Printed Circuit, glue and water) is estimated to be 0.26%, lower than the Inner Barrel maximum admissible material budget per layer at the ITS Upgrade, 0.30%. The IB1 stave cooling performance will be assessed with liquid water.

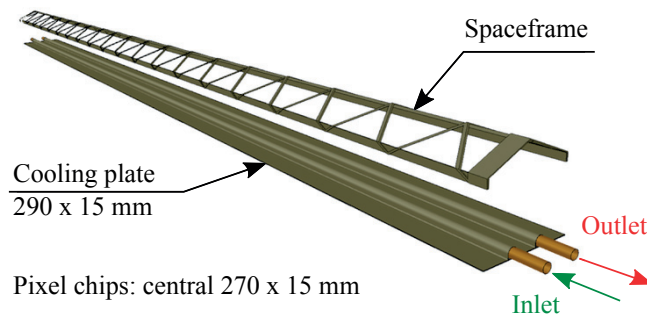


Figure 5.1: Schematic view of the Inner Barrel high-conductivity plate plus spaceframe stave concept.

Table 5.1: Inner Barrel stave prototypes subjected to experimental cooling tests. The high thermal conductivity directions are indicated in the schemes. All dimensions are in mm, except where explicitly indicated.

Name	Layout	$[x/X_0]^a$ [%]	Weight ^b [g]	Features
IB1		0.079	1.4	Baseline Lowest x/X_0
IB2		0.096	1.8	High cooling performance
IB3		0.092	1.7	Zero-CTE

The IB2 stave has a 90 μm -thick K1100-2K high-conductivity CFRP plate [43] instead of the 70 μm -thick K13D2U-2K one in the IB1 stave. The carbon fibres remain equally oriented transversally to the stave. The cooling channels are identical to the IB1 prototype ones: 1.024 mm ID, made of polyimide. Also, like in the IB1 stave, the channels-plate assembly is covered by a 30 μm -thick graphite foil, and the whole structure is encapsulated in two layers of 20 μm -thick carbon fleece. The IB2 stave is aimed to provide better thermal performance than the IB1, thanks to the thicker cooling plate and its higher thermal conductivity in the fibre direction (1000 $\text{W m}^{-1} \text{K}^{-1}$ for the fibre only, compared to 800 $\text{W m}^{-1} \text{K}^{-1}$ for the K13D2U fibres). It is emphasised that the presence of resin in the laminar plate causes the effective thermal conductivity to be significantly lower. The presence of a thicker plate of denser CFRP has an impact on the weight and material budget: 1.8 g and 0.096% respectively, for the stave only (no coolant or services included), compared to 1.4 g, and 0.079% for the IB1 stave. On the other hand, the IB2 stave was proven by experimental means to be mechanically more robust than the IB1 one. Experimental cooling performance results with water and two-phase C_4F_{10} refrigerant of the IB2 stave are later reported in subsection 5.2.3.

^a Includes: cooling plate, cooling channels, and water as coolant inside the channels. No spaceframe, silicon chips, glue, or FPC (Flex Printed Circuit) are considered.

^b Includes: cooling plate, spaceframe, and cooling channels only (no coolant).

The IB3 prototype has no graphite foil and no carbon fleece plies. Instead, the cooling plate is composed of three layers of K13C2U-2K CFRP laminate [41] 45 μm thick each, piled one onto another, as depicted in Table 5.1. The fibres in the central layer are set transversally to the stave, in the so-called 90° direction, as in the IB1 and IB2 concepts. However, the layer beneath displays the fibres oriented in the longitudinal direction (0° direction). Finally, the third layer completes the assembly by being placed on top of the cooling channels with its fibres oriented longitudinally too. This stave architecture is expected to have no or little thermal expansion. It is well known carbon-fibre reinforced polymers display negative thermal expansion in the direction of the fibre i.e. their fibres shrink with temperature increases, as reported in Table 2.4, while they display the opposite behaviour in the perpendicular directions due to the presence of the resin, which has a positive coefficient of thermal expansion (*CTE*). This prototype anticipates the zero-*CTE* layout proposed for the Outer Barrel half-staves, where thermal expansion can be an issue due to the length of the staves. The cooling channels are identical to the IB1 and IB2 staves: 1.024 mm ID, made of polyimide. The IB3 stave displays a weight of 1.7 g and a material budget of 0.092% for the stave alone. Its cooling performance is thermally characterised with water.

5.2.2 Water cooling performance benchmarking of the Inner Barrel staves

The IB1, IB2 and IB3 prototypes were subjected to thermal tests with water at temperatures ranging from 15 to 18°C, as presented in [154]. Prior to the tests, heat exchange with the ambient was quantified using the experimental methodology described in section 4.3.1, obtaining a characteristic similar to the one plotted in Fig. 4.7 for each prototype. Heat exchange with the ambient is considered in the interpretation of the results from the cooling tests.

The thermal performance of each stave prototype is represented by plotting the difference between the mean heater temperature and the mean flow temperature versus the water flow rate, as expressed in Eq. 4.6. Results are reported in Fig. 5.2 for two power densities, 0.15 and 0.30 W cm^{-2} , corresponding to absolute electric heat loads at the heater of 6.1 and 12.2 W respectively. The heat load (in W) removed by the coolant is indicated on the plots for each experimental point.

In view of the results, the IB1 stave provides, for the nominal power density of 0.15 W cm^{-2} , a temperature difference between the heater and the water flow always lower than 3 K for the tested flow rate range. In other words, the detector can be effectively cooled with water at a mean temperature of 25°C and the cooling system will be keeping the chips 2 degrees below the maximum admissible temperature, 30°C, even at flow rates as low as 3 L h^{-1} . At 0.30 W cm^{-2} , 5 times the nominal chip power density, the detector mean temperature would be only 5 K higher than the mean water flow.

The IB2 prototype shows the best thermal performance, slightly outperforming the IB1 stave thanks to its thicker and more conductive high thermal conductivity plate. On the other hand, IB3 displays the poorest thermal performance of the three stave prototypes, although it is acceptable: the $\Delta T_{\text{heater-water}}$ is lower than 6 K at a power density of 0.15 W cm^{-2} . The poorer cooling capability

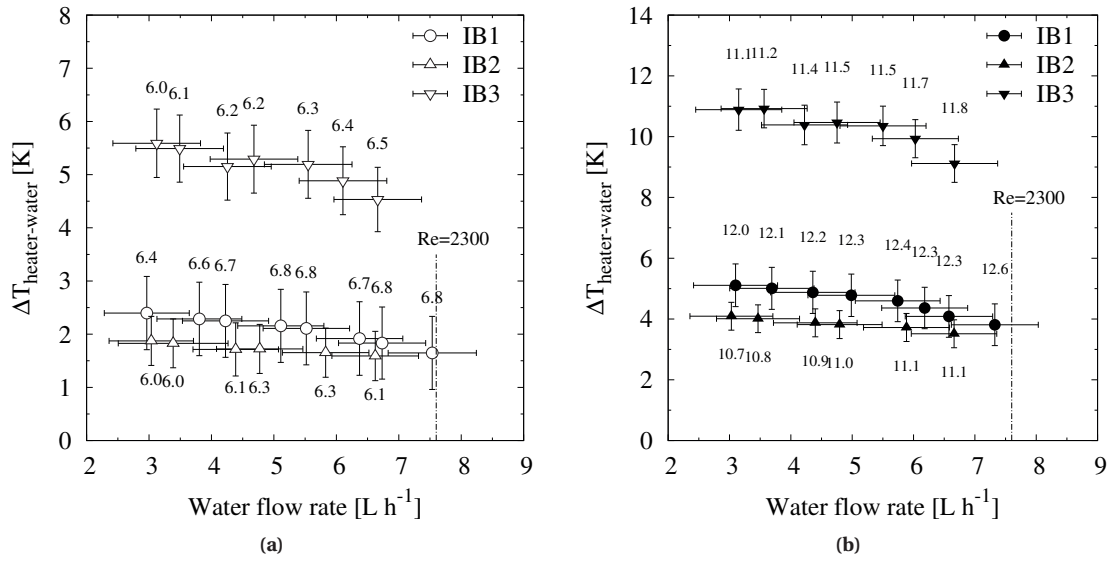


Figure 5.2: Comparison of the cooling performance ($\Delta T_{\text{heater-water}}$ vs. water flow rate) of the three Inner Barrel stave layouts with water, at: (a) 0.15 W cm⁻²; (b) 0.30 W cm⁻². The estimated heat load (in W) transferred to the coolant is indicated for each experimental point in the plot.

compared to the IB1 stave is due to the lower thermal conductivity of the K13C2U-2K CFRP used: 620 W m⁻¹ K⁻¹ in the fibre direction, compared to 800 W m⁻¹ K⁻¹ for the K13D2U-2K fibres in IB1, and 1000 W m⁻¹ K⁻¹ for the K1100-2K CFRP at IB2. A similar 3-layer, 0°/90°/0° design with K13D2U-2K CFRP tested for the Outer Barrel half-staves delivered almost identical thermal performance as the baseline, as later shown in section 5.3.2. Therefore, the use of K13D2U-2K pre-preg CFRP might improve the cooling performance of the IB3 layout.

As acknowledged for the P2 prototype in section 4.4, increasing water flow rates involve no significant improvement of the cooling performance of the staves. In the 3.0-7.6 L h⁻¹ range, this is explained by the fact that the flow is laminar ($Re < 2300$) in that range in a 1.024 mm ID circular channel. Laminar heat transfer coefficients do not depend on the water flow rate. Above ~ 6.0 L h⁻¹ ($Re \approx 1800$), only a feeble drop of $\Delta T_{\text{heater-water}}$ is observed at 0.30 W cm⁻² for the IB1 stave, perhaps anticipating the transition flow regime. This behaviour confirms what was observed for prototype P2: the main thermal resistance in the system is by conduction in the stave, from the heater to the cooling channels, dominating over the convective thermal resistance between the coolant and the tube inner wall. In high heat flux applications, minimising the conductive thermal resistance of the heat sink is always a primary system design target. Yet, a high conductive thermal resistance is actually positive for the ITS Upgrade detector staves: the system is thermally robust and can work with multiple flow rates and temperatures.

Fig. 5.3 shows the impact of decreasing the cooling channel size from 1.450 mm ID to 1.024 mm ID by displaying a comparison between the thermal performance of the P2 and the IB1 staves. The

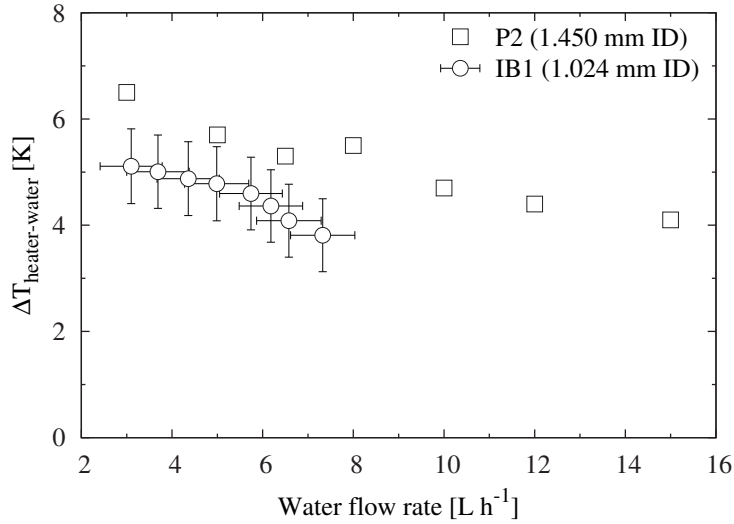


Figure 5.3: Influence of the channel size on the cooling performance: comparison between the P2 stave (1.450 mm ID) and the IB1 stave (1.024 mm ID). Both staves display the same cooling plate layout.

influence of the channel size, which is strong regarding the pressure drop, does not greatly affect the thermal performance, and it can be said both staves show the same thermal performance. Specifically, decreasing the pipe size to 1.024 mm ID (IB1) results in a decrease of $\Delta T_{heater-water}$ of roughly 1 K, which is not a significant improvement in terms of cooling performance.

The water pressure drop is plotted versus flow rate in Fig. 5.4a for the IB1 stave. The three prototypes exhibit the same pressure drop characteristic, as their channel dimensions and geometries are identical. The maximum admissible pressure drop threshold of 0.3 bar is exceeded at flow rates higher than 3.5 L h^{-1} , which is not a problem, as the cooling system guarantees sufficiently low $\Delta T_{heater-water}$ already at 3 L h^{-1} . Lower water flow rates are possible if the water temperature rise remains low, in order to avoid heater temperature non-uniformities. The water temperature rise trend is plotted for the IB1 stave in Fig. 5.4b versus flow rate. At 3 L h^{-1} and 0.15 W cm^{-2} , the water temperature rise does not exceed 1.5 K, so a lower flow rate could be used to effectively cool the detector and benefit from lower pressure drops.

The values calculated analytically using the frictional pressure drop correlation by Churchill [145] and the methods by Idelchik for the singular pressure drops [146], as already reported in Fig. 4.10, are overlaid to the experimental water pressure drop measurements recorded in the IB1 stave in Fig. 5.5. A good match is found, especially at flow rates below 6 L h^{-1} ($Re \approx 1800$ in Fig. 5.5). This indicates that the stave fabrication process did not alter the section of the polyimide channels nor caused obstructions in the piping. At flow rates higher than 6 L h^{-1} , the predictions from the literature seem to underestimate the pressure drops, as the flow starts shifting from the laminar to the transitional flow regime. The pressure drop at the singularities, mostly at the Π -bend, makes up for 28% of the total pressure drop.

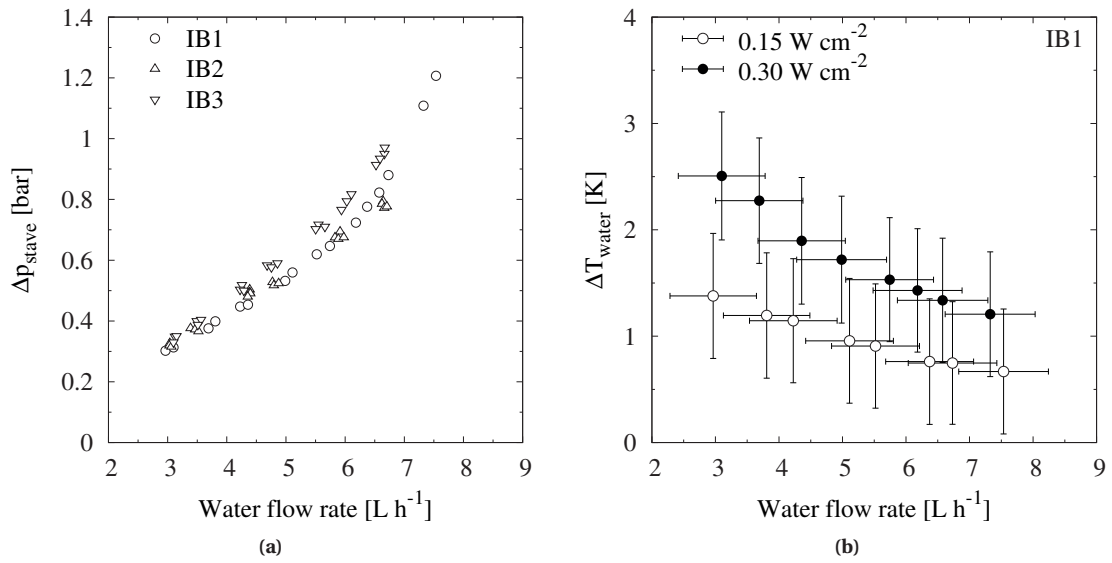


Figure 5.4: Water pressure drop of the three Inner Barrel staves (a); and water temperature rise for the IB1 stave at 0.15 and 0.30 W cm⁻² (b).

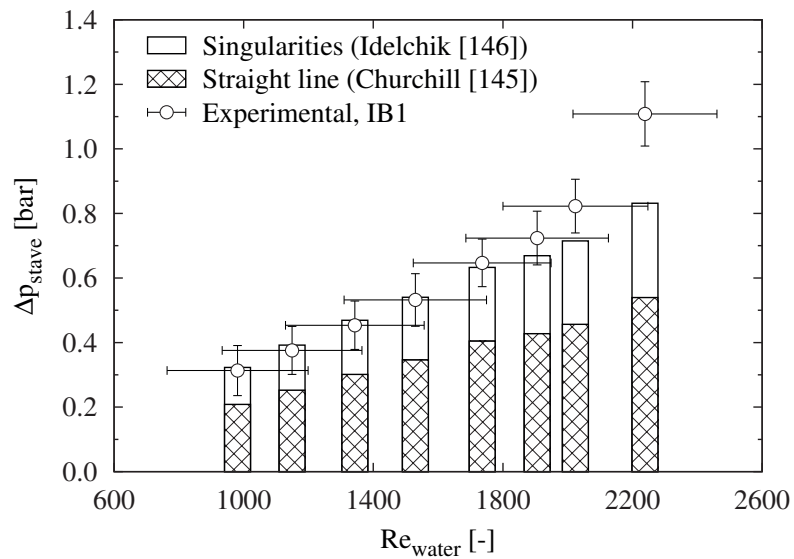


Figure 5.5: Experimental and calculated water pressure drop at the IB1 stave versus the Reynolds number. The calculated values are the sum of the frictional pressure drop in the straight channels, by Churchill [145], and the singular pressure drops, estimated by Idelchik [146].

Nominal cases

The nominal cases for the water-cooled Inner Barrel IB1, IB2 and IB3 staves at 0.15 W cm⁻² are summarised in Table 5.2. The water mean velocity in the polyimide channels is 1 m s⁻¹. The ASHRAE Fundamentals Handbook [155] reports potential issues associated to fluid flows inside piping systems. Noise, originated by turbulence, air entrainment, cavitation or change of flow direction or pipe size, can induce vibrations. Erosion due to the presence of air bubbles is a concern too. To prevent the

Table 5.2: Nominal cooling conditions for the IB1, IB2 and IB3 prototypes at 0.15 W cm^{-2} with water.

Stave	\dot{V}_{water} [L h ⁻¹]	$u_{mean,water}$ [m s ⁻¹]	$T_{mean,water}$ [°C]	$T_{mean,heater}$ [°C]	ΔT_{water} [K]	Δp_{water} [bar]
IB1	3.0	1.0	16.2	18.6	1.4	0.30
IB2	3.0	1.0	15.6	17.5	1.4	0.33
IB3	3.1	1.1	16.2	22.5	1.4	0.34

occurrence of these phenomena, recommendations on the maximum fluid velocity are given in [155]. It is indicated that, for piping smaller than 50 mm ID, nominal fluid velocities should not exceed 1.2 m s^{-1} . Erosion effects are in general negligible for fluid velocities up to 3 m s^{-1} , even at workloads over 6000 hours per year (~ 250 days, nearly the operational time of the ITS Upgrade detector). Last, guidelines by other authors include recommended velocities between 0.9 and 2.1 m s^{-1} [156]. Therefore, the 1 m s^{-1} velocity is well within the recommendations. Furthermore, as it results in a laminar flow inside the 1.024 mm ID pipes, erosion or vibration effects are expected to be insignificant. For all nominal cases, the water temperature at the inlet is higher than 15°C and the mean temperatures on the heated surface do not exceed 22°C .

Since tests with water were carried out so that the heater temperatures are similar to the ambient temperature, heat loads transferred from/to the air only reached $\sim 10\%$ of the electric power applied to the heater for experimental cases at the highest power density, 0.50 W cm^{-2} . Nevertheless, energy balances were performed to assess the match of the electric power input and the heat load absorbed by the fluid. Heat loads absorbed by the cooling water calculated from the temperature rises and flow rates are 15 to 25% lower than the applied electric heat loads. However, these results are not very precise due to the low water temperature rise measured for all the Inner Barrel prototypes, and thus should be regarded as qualitative indicators.

The IB1 Inner Barrel provides an excellent compromise between cooling performance and low weight and material budget. Mechanical tests confirmed the high flexural rigidity of the system and chip planarity complying with the target values. The IB2 stave is mechanically more robust than the IB1 one, but at a higher material budget and weight, with no significant improvement of the cooling performance. Last, the IB3 stave displays a higher weight, a more complicated fabrication process and poorer cooling capabilities. Subsequently, the IB1 stave design is finally chosen as the baseline for the Inner Barrel. However, the IB2 stave was tested with two-phase C_4F_{10} (see next subsection) and the IB3 stave concept is used at the Outer Barrel half-staves, where no thermal expansion might be a desirable feature.

Fig. 5.6 displays the temperature map of the IB1 stave Kapton[®] heater in the nominal cases summarised in Table 5.3. Good temperature uniformity on the heated surface was achieved, barely reaching 6 K at 0.30 W cm^{-2} . A cooler region is located close to the prototype inlet, at the top left corner

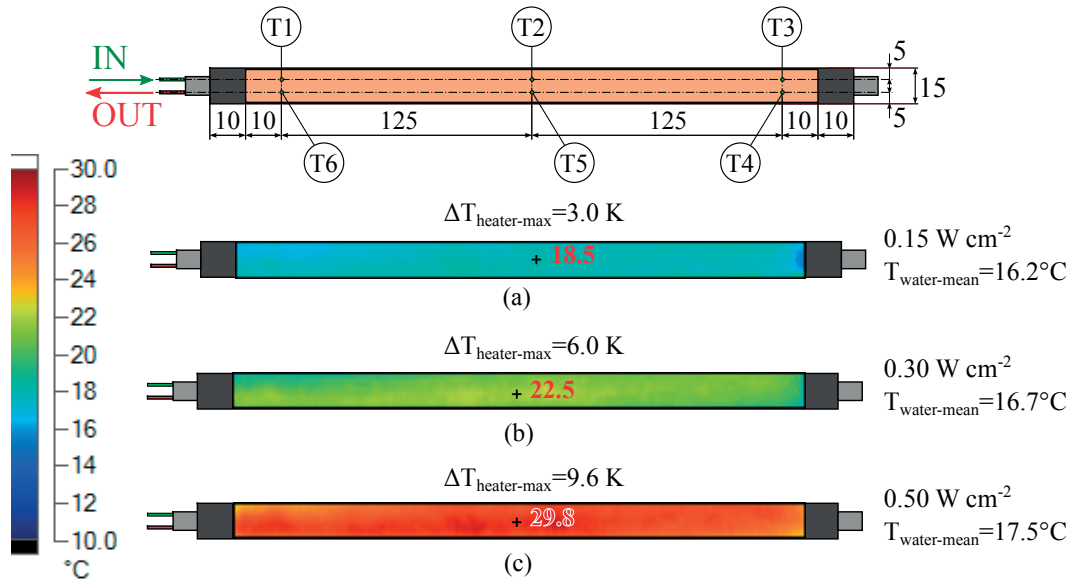


Figure 5.6: Infrared images displaying the water-cooled Inner Barrel IB1 stave heater temperature map [°C] at the nominal conditions in Table 5.3: 3 L h^{-1} and (a) 0.15 W cm^{-2} ; (b) 0.30 W cm^{-2} ; (c) 0.50 W cm^{-2} . The maximum temperatures on the heater are reported in red text. Dimensions in mm.

Table 5.3: Nominal cooling conditions for prototype IB1 with water at a flow rate of 3 L h^{-1} and power densities of 0.15 , 0.30 and 0.50 W cm^{-2} .

$P_{d,heater}$ [W cm^{-2}]	\dot{V}_{water} [L h^{-1}]	$u_{mean,water}$ [m s^{-1}]	$T_{mean,water}$ [°C]	$T_{mean,heater}$ [°C]	ΔT_{water} [K]	Δp_{water} [bar]
0.15	3.0	1.0	16.2	18.6	1.4	0.30
0.30	3.1	1.1	16.7	21.8	2.5	0.30
0.50	3.0	1.1	17.5	26.5	4.2	0.29

of each thermographic image; everywhere else on the plate, the temperature distribution is uniform. The maximum temperatures measured in the thermographic images are reported. They do not differ significantly from mean heater temperatures, confirming again the temperature uniformity the cooling plate provides.

5.2.3 Two-phase evaporative cooling for the Inner Barrel staves

Introduction

Two-phase cooling is considered as a realistic alternative to water. The most immediate advantage of evaporative coolants in HEP particle detectors is the reduction of the coolant material budget and the average stave material budget. Since the inception of boiling, the fraction of the cooling channel section occupied by the vapour (void fraction) is usually quite large. As vapour is many times lighter than liquid, the material budget of the coolant is very low, minimising the size of the local material budget peaks a liquid coolant typically displays.

The IB2 Inner Barrel stave, with a 90 μm -thick K1100 CFRP cooling plate and 1.024 mm ID channels (see Table 5.1), was subjected to experimental two-phase cooling tests with a per-fluorocarbon refrigerant, C_4F_{10} . The physical properties of this fluid can be found in appendix C. In Fig. 5.7, the material budget of the IB2 stave is compared with water and with two-phase C_4F_{10} as coolants. The cooling plate, the cooling channels, and the coolant are included in the calculation. For the two-phase coolant material budget calculation, the void fraction is estimated according to the values given by the correlation by Steiner [84], based on the Rouhani-Axelsson drift flux void fraction map [83]. Void fractions over 0.85 are expected in the whole saturated region, starting from small vapour qualities. Therefore, a value of 0.85 can be safely considered for the material budget calculations. Also, a uniform distribution of the liquid phase as a film around the periphery of the channel inner wall is assumed. In addition to decreasing the coolant budget peaks, using two-phase C_4F_{10} refrigerant results in a reduction of the overall stave assembly material budget of 10.4%, as reported in Table 5.4.

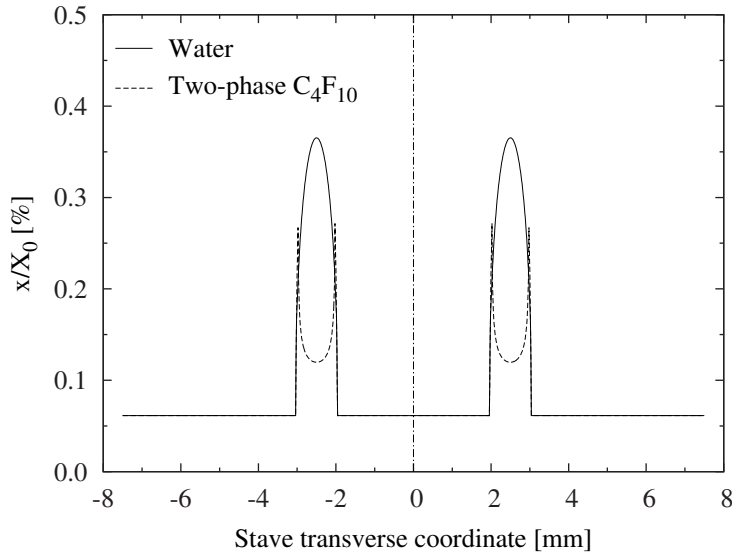


Figure 5.7: IB2 stave material budget considering water and two-phase C_4F_{10} refrigerant ($\varepsilon = 0.85$) as coolants. Only the plate assembly, the cooling channels and the coolant are considered in the calculation.

Table 5.4: Material budget of the IB2 Inner Barrel stave with water and two-phase C_4F_{10} as coolants.

Coolant	$[x/X_0]_{plate+coolant}$ ^a [%]	$[x/X_0]_{full}$ ^b [%]
Water	0.096	0.293
Two-phase C_4F_{10}	0.065	0.263
% of x/X_0 saved if using two-phase C_4F_{10} [%]	-31.9	-10.4

^a Includes: plate assembly, channels and coolant inside the channels. No spaceframe included.

^b Includes: plate assembly, channels, coolant inside the channels, spaceframe, silicon chips, glue, and FPC (Flex Printed Circuit). No overlap is considered between adjacent staves.

Single-phase C_4F_{10} tests

The two-phase C_4F_{10} cooling experimental setup was first validated with single-phase flow tests with the same refrigerant, assessing single-phase parameters like pressure drop and the energy balance.

Fig. 5.8 expresses the single-phase pressure drop measured experimentally and compares it with predicted values, calculated by using the correlation by Churchill for straight pipes [145] and the methods indicated in Idelchik's handbook [146] for singular pressure drops. A good match was found between the two parameters for a range of Reynolds numbers in the transitional regime. Similarly to the cases with water, singular pressure drops make up for roughly 30% of the total pressure drop, and are mostly concentrated at the Π -bend (25% of the frictional pressure drop).

The energy balance at a power density of 0.10 W cm^{-2} is plotted in Fig. 5.9a versus the liquid C_4F_{10} mass flux. Deviations between -15% and -20% were obtained. This is mostly due to the low power applied which results in low coolant temperature rise. Thus, the uncertainties are very high, in some cases reaching up to 100% of the energy balance. The energy balance is more accurate in the larger half-staves of the Outer Barrel, where the absolute heat load applied is significantly higher.

A second heat transfer check was done by comparing the experimental mean heat transfer coefficient (h) with predicted values from the literature. The mean heat transfer coefficient was calculated using the method described in subsection 4.3.5. For the single-phase C_4F_{10} tests on the IB2 stave, the value of R_{global} is known, so by inputting the R_{cond} parameter, previously determined for the IB2 stave with water cooling test results^a, $R_{conv,C_4F_{10}}$ can be calculated using Eq. 4.21. Ultimately, Eq. 4.22 yields

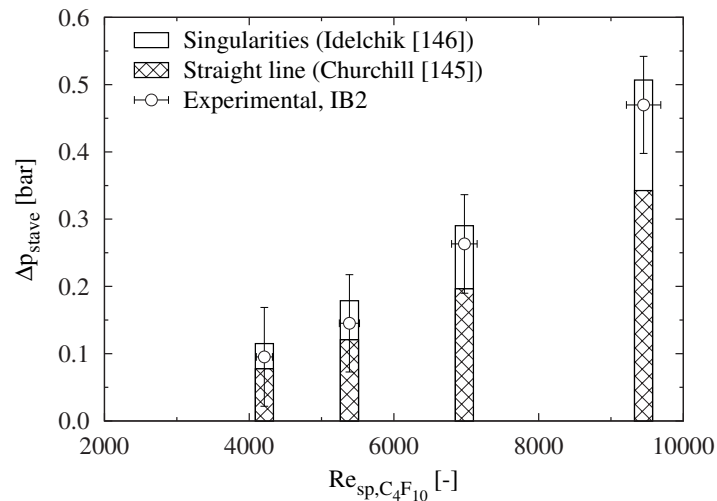


Figure 5.8: Experimental and calculated pressure drop at the IB2 stave versus the Reynolds number, for single-phase C_4F_{10} refrigerant. The calculated values are the sum of the frictional pressure drop in the straight channels, by Churchill [145], and the singular pressure drops, estimated by Idelchik [146].

^a R_{cond} is calculated from tests with laminar water flow rates at a 0.30 W cm^{-2} , achieving accurate results. It was verified that the obtained value of R_{cond} remained constant in the experimental data series used for its calculation.

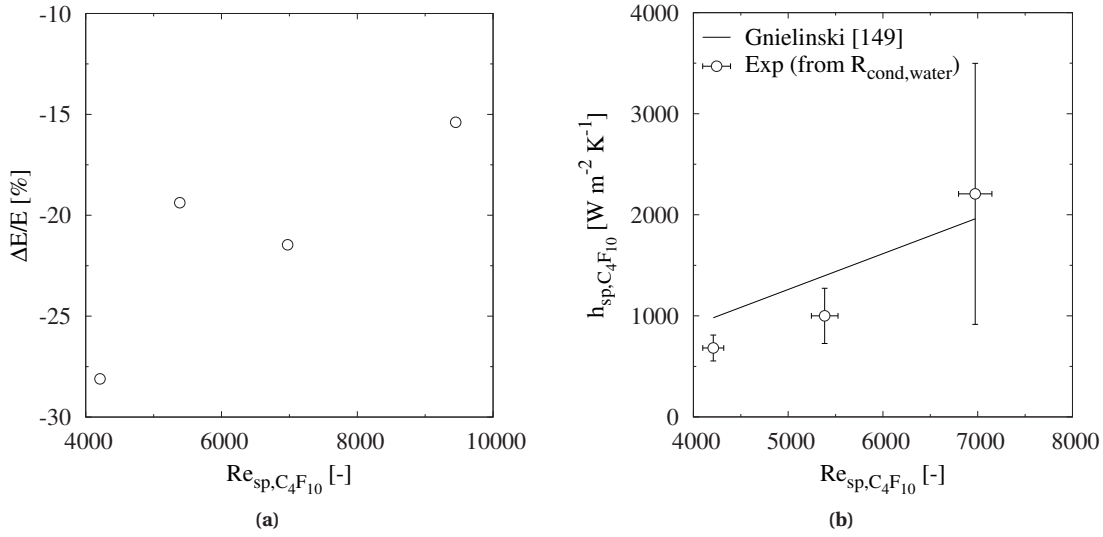


Figure 5.9: IB2 stave energy balance (a) and mean heat transfer coefficient with single-phase C_4F_{10} refrigerant at $0.10 W cm^{-2}$ (b).

the average single-phase C_4F_{10} heat transfer coefficient, $h_{sp,C_4F_{10}}$, displayed in Fig. 5.9b. It is then compared with the predicted values estimated with the correlations by Gnielinski [149]. The calculated values match the predictions, although the uncertainty is quite high for the point with the highest C_4F_{10} flow rate. This is due to the fact that at high C_4F_{10} flow rates $R_{conv,C_4F_{10}}$ decreases as the heat transfer coefficient increases, to the extent that the uncertainty of $R_{conv,C_4F_{10}}$ becomes of the same order as the measured variable. Thus, the propagation of uncertainty in Eq. 4.22 results in the high heat transfer coefficient uncertainty reported for the highest Reynolds number in Fig. 5.9b.

In view of the single-phase test results, the facility is considered validated and ready for two-phase flow cooling tests.

Two-phase C_4F_{10} cooling test results

Fig. 5.10 reports the cooling performance of the IB2 prototype when cooling with water and two-phase C_4F_{10} for power density inputs of 0.30 and $0.50 W cm^{-2}$. The absolute power transferred to the cooling fluid is reported for each experimental point. Note that there is no relationship between the C_4F_{10} mass flux and the water flow rate. Generally, the prototype is well cooled with water and with two-phase C_4F_{10} , with a maximum $\Delta T_{heater-coolant}$ not exceeding $7 K$ at $0.30 W cm^{-2}$ and below $10 K$ at $0.50 W cm^{-2}$, two power densities well above the nominal value of $0.15 W cm^{-2}$.

A few observations can be drawn. First, for the mass flow rate range, water provides better cooling performance than two-phase C_4F_{10} , as seen for the P1 and P2 prototypes in section 4.4. Indeed, the mean heat transfer coefficient of the water in the whole flow rate range (laminar) is $2500 W m^{-2} K^{-1}$, while two-phase C_4F_{10} heat transfer coefficients, according to the correlations by Cooper [122] for pool

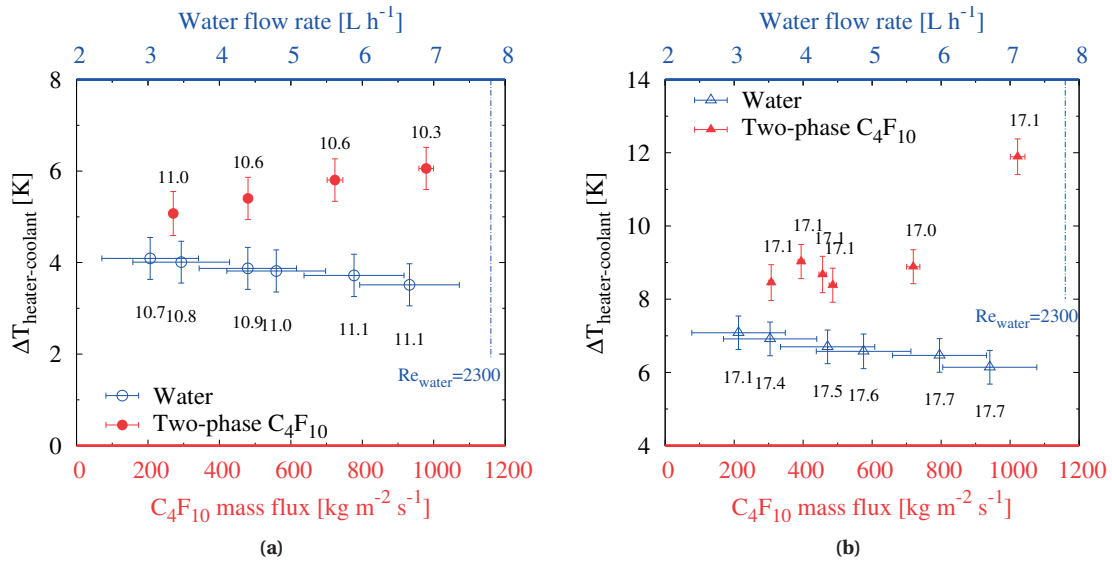


Figure 5.10: Cooling performance of the IB2 stave when cooling with single-phase water and two-phase C_4F_{10} refrigerant at: (a) 0.30 W cm^{-2} and; (b) 0.50 W cm^{-2} . The power transferred to the coolant is indicated for each experimental point.

boiling and by Liu and Winterton [121] for convective flow boiling, range from 1200 to $2000 \text{ W m}^{-2} \text{ K}^{-1}$.

Also, it can be seen that, if the C_4F_{10} mass flux is increased, the cooling performance slightly deteriorates. The worst case is found in Fig. 5.10b at the highest mass flux. High mass flux conditions involve low mean vapour qualities, which yield low heat transfer coefficients. Furthermore, higher subcooling before the pre-heater was measured in these conditions, resulting in the coolant displaying low vapour qualities at the stave entrance. In such scenario, and due to the low heat flux in the stave, which does not enhance nucleate boiling, forced convection to the liquid could be the dominating heat transfer mechanism. The cooling capabilities of this mechanism are very inefficient due to the low thermal conductivity of liquid C_4F_{10} , 10 times lower than water. This explains the poor cooling performance at high C_4F_{10} mass fluxes. On the other hand, it should be noted that, since the main thermal resistance is of conduction in the stave, the real deterioration of the cooling performance when increasing the C_4F_{10} mass flux cannot be accurately quantified by using the stave test results.

The importance of cooling at high enough vapour quality is expressed in Fig. 5.11. Here, the stave cooling performance is plotted versus the mean vapour quality. The heater-coolant temperature difference decreases for increasing mean vapour qualities. This trend is more pronounced for the Outer Barrel half-staves, as later shown in Fig. 5.28.

The plots in Fig. 5.12 display the temperature recorded by each of the six thermistors on the IB2 stave heater normalised to the coolant temperature. NTC 1 is close to the stave inlet and NTC 6 nearby the outlet, as described in Fig. 4.1a. Two extreme cases at 0.30 W cm^{-2} , each represented by a C_4F_{10} mass flux, are reported in each plot. In Fig. 5.12a, the same relative temperature close to the stave inlet

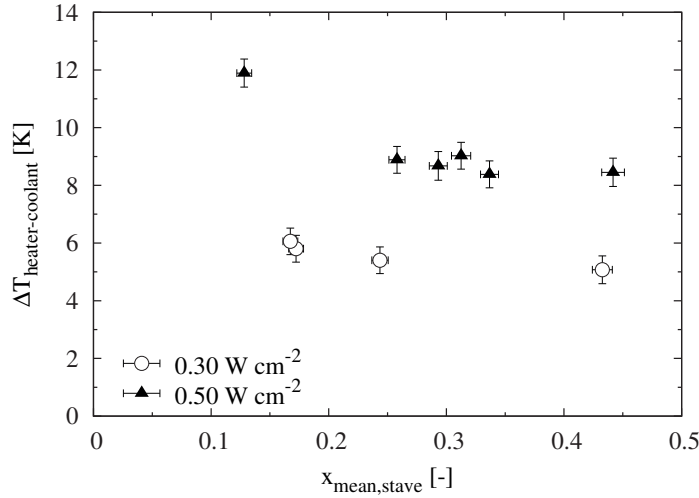


Figure 5.11: Cooling performance variation with the mean vapour quality of the IB2 stave with two-phase C_4F_{10} refrigerant at 0.30 and 0.50 W cm^{-2} . The mass flux is different for each point.

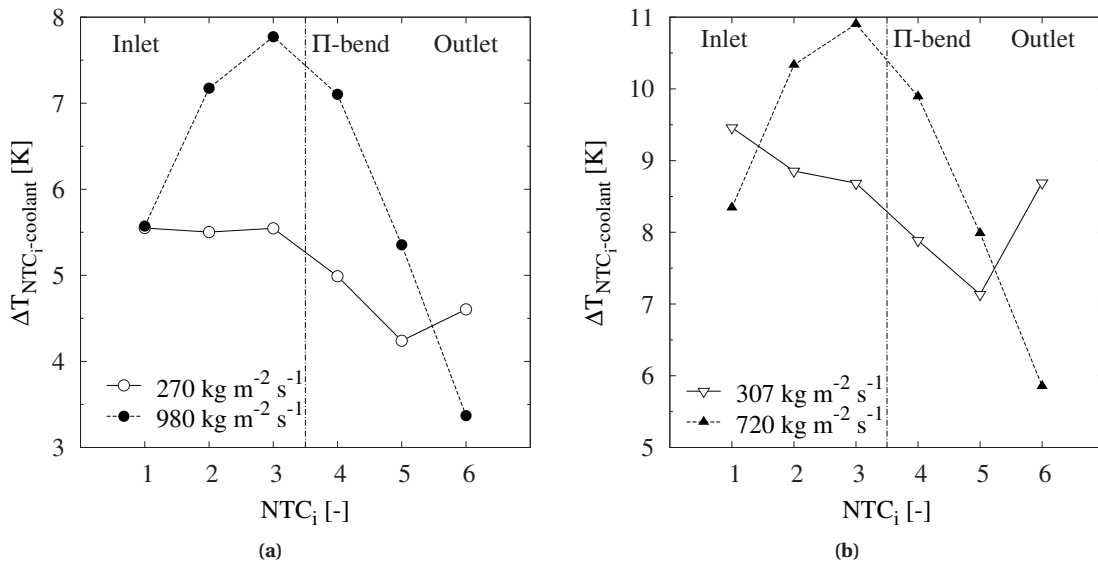


Figure 5.12: Influence of the two-phase C_4F_{10} refrigerant mass flux and vapour quality on the temperature of the six NTCs on the IB2 stave heater, normalised to the coolant temperature, at: (a) 0.30 W cm^{-2} ; (b) 0.50 W cm^{-2} .

(NTC 1) is measured for the two cases. However, at $980 \text{ kg m}^{-2} \text{ s}^{-1}$ it rapidly increases before dropping after the fourth thermistor. Poor heat transfer conditions take place in the first part; indeed, the flow enters the stave barely in saturated conditions. The temperature drop at the return line is due to higher heat transfer coefficients, typical at higher vapour qualities (the stave outlet vapour quality is 0.30). The cooling plate, with the high-thermal conductivity fibres oriented transversally to the stave, moderates the temperature differences on the heater over the two lines. On the other hand, the coolant enters the stave at $x_4=0.15$ and leaves it at $x_5=0.57$ for the case at $270 \text{ kg m}^{-2} \text{ s}^{-1}$, resulting in a more uniform

heater temperature profile. The temperature drop at the thermistors 4 and 5 is probably caused by the local pressure drop at the Π -bend. Fig. 5.12b shows two similar cases at 0.50 W cm^{-2} . Again, it is important to carefully choose and guarantee appropriate and stable two-phase flow conditions.

Tracking the two-phase pressure drop is vital in order to ensure the two-phase saturation temperature of the coolant does not decrease below the minimum admissible at the ITS Upgrade, 12°C . The two-phase pressure drop readings are compared to analytical predictions. As described in subsection 4.3.4, Eq. 4.20 expresses the theoretical two-phase pressure drops as the sum of the two-phase frictional pressure drop at the channels and the Π -bend, and the momentum pressure drop in diabatic tests. Frictional components are estimated with the correlation by Friedel [92] in straight sections of the channel and the model by Chisholm [101] in the Π -bend singularity^a. The momentum pressure drop is determined via Eq. 4.19, considering separated phases in the two-phase flow.

The scatter plot in Fig. 5.13 compares the measured pressure drop and the predicted values using Eq. 4.20. The expected values fall within the $\pm 20\%$ range. The points outside this range, at high predicted pressure drop values, correspond to low vapour quality conditions. The frictional two-phase pressure drop correlations provide overestimated results in these conditions.

It is interesting to examine the relationship between two-phase saturation temperature drops and heater temperature non-uniformities, which can be expressed as the standard deviation of the readings of the six thermistors on the stove heater. Fig. 5.14a reports a saturation temperature drop positive trend with the mean vapour quality in the stove for several C_4F_{10} mass fluxes. In Fig. 5.14b, the saturation temperature drop is matched against the stove temperature non-uniformity characteristic,

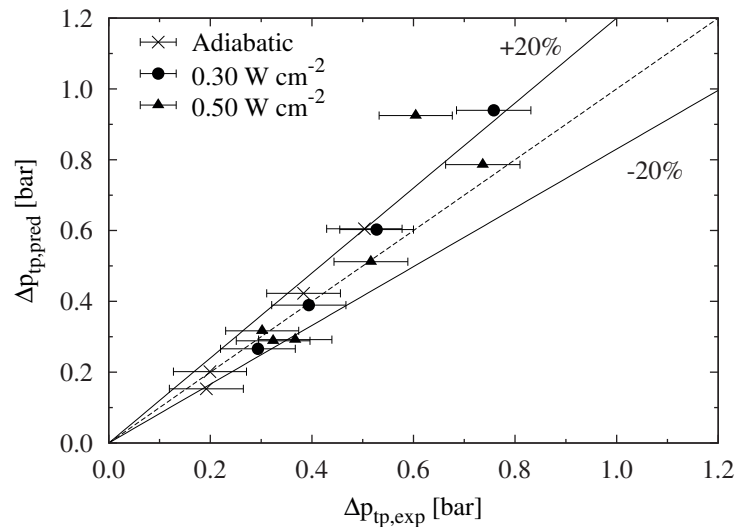


Figure 5.13: Experimental versus predicted two-phase C_4F_{10} refrigerant pressure drop at the IB2 stove. For the calculation of the predicted frictional two-phase pressure drop, the correlations by Friedel [92] for straight channels, and by Chisholm [101] for the Π -bend, are used.

^a Frictional pressure drops in a Π -bend are strongly influenced by flow conditions upstream and downstream. Thus, analytical two-phase pressure drop results should be considered as an approximation.

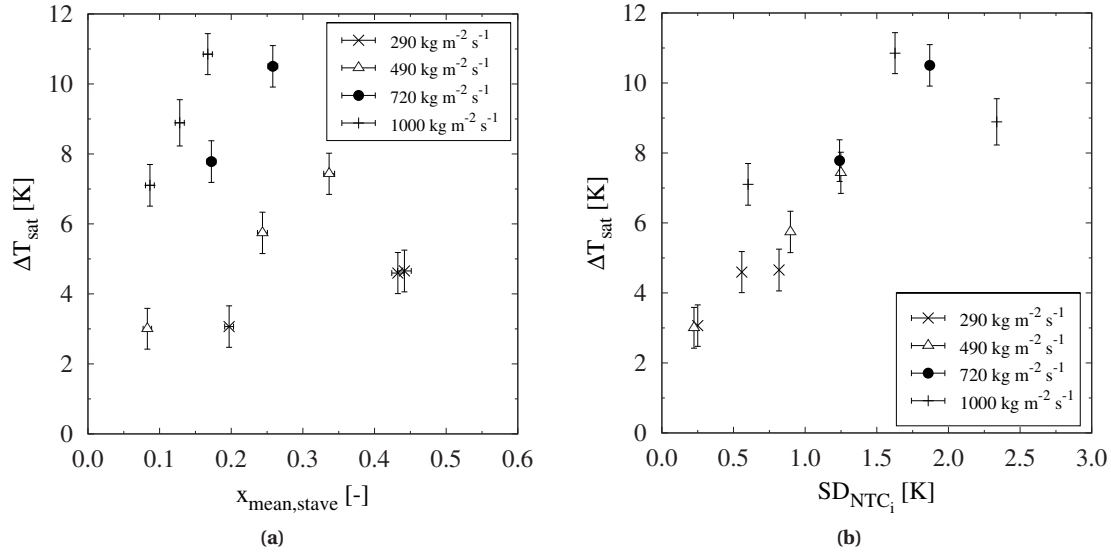


Figure 5.14: (a) Saturation temperature drop trend with the mean stave vapour quality; and (b) its influence on the stave temperature non-uniformity for several two-phase C_4F_{10} mass fluxes in the IB2 stave.

showing a positive trend too. Thus, there is a relationship between the saturation temperature drop and the heater temperature non-uniformity, despite the heat spreading capabilities of the cooling plate.

With the results in mind regarding the stave thermal performance ($\Delta T_{heater-coolant}$), saturation temperature drops (ΔT_{sat}) and the stave temperature non-uniformity aspects, it can be concluded that:

- Low mass fluxes (280-400 $kg\ m^{-2}\ s^{-1}$) and high mean vapour qualities (on the order of 0.4-0.5) are preferred in order to obtain low $\Delta T_{heater-coolant}$ values.
- With the aim of minimising temperature gradients on the stave, the mean stave vapour quality should remain in the 0.2-0.4 range.

A compromise must be sought between these features in order to find optimal two-phase flow boiling nominal cooling conditions. Also, in order to prevent potential dry-out close to the stave outlet, it is recommended not to use very low C_4F_{10} mass fluxes and to prioritise the control of this parameter in the integrated system. This is especially critical in case of high chip power densities. The proposed nominal cooling conditions are presented below, referred to the IB2 stave.

IB2 stave two-phase nominal cooling conditions

Considering the aforementioned remarks, nominal cooling conditions with two-phase C_4F_{10} refrigerant as coolant for the IB2 stave are proposed in Table 5.5, for power densities of 0.30 and 0.50 $W\ cm^{-2}$.

Fig. 5.15 shows the temperature map of the Kapton[®] heater at the nominal cases in Table 5.5, compared to water nominal conditions at 0.30 $W\ cm^{-2}$. Similar temperature non-uniformity was achieved with two-phase C_4F_{10} and water, with gradients on the active area of 6 K at 0.30 $W\ cm^{-2}$.

Table 5.5: Nominal cooling conditions with evaporative C_4F_{10} for the IB2 stave at 0.30 and 0.50 W cm^{-2} .

$P_{d,heater}$ [W cm^{-2}]	$G_{C_4F_{10}}$ [$\text{kg m}^{-2}\text{s}^{-1}$]	$T_{mean,C_4F_{10}}$ [$^{\circ}\text{C}$]	$T_{mean,heater}$ [$^{\circ}\text{C}$]	x_{in} [-]	x_{out} [-]	$\Delta p_{C_4F_{10}}$ [bar]	$\Delta T_{sat,C_4F_{10}}$ [K]
0.30	270	13.9	19.0	0.15	0.72	0.29	4.6
0.50	307	16.9	25.3	0.05	0.83	0.32	4.7

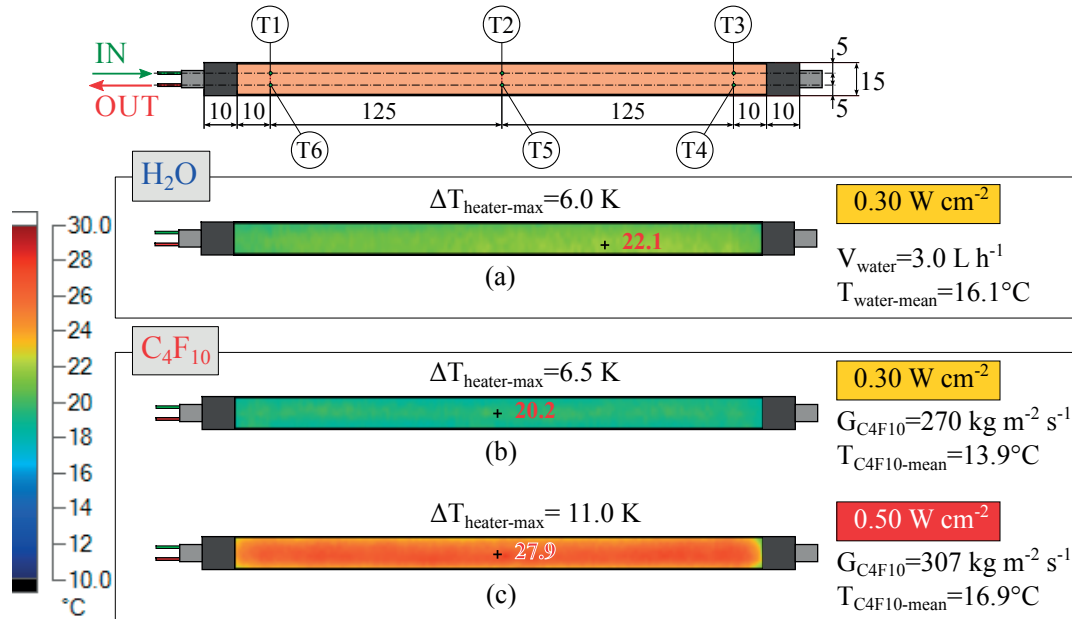


Figure 5.15: Infrared images of the IB2 heater surface temperature map [$^{\circ}\text{C}$] at nominal cooling conditions with: (a) water at 0.30 W cm^{-2} , and two-phase C_4F_{10} refrigerant at: (b) 0.30 W cm^{-2} and; (c) 0.50 W cm^{-2} . The maximum temperature gradients are indicated in each case. The maximum temperatures on the heater are reported in red text. Dimensions are expressed in mm.

Saturation temperature drops are higher than the water temperature rise, 2.4 K in the case in Fig. 5.15a.

5.3 Outer Barrel half-staves

This section is devoted to assessing the cooling performance of two optimised Outer Barrel half-staves with water, and to study the thermal capabilities of another half-stave concept with two-phase C_4F_{10} refrigerant. The prototypes and results in this section only regard Outer Barrel half-staves, since they are almost twice as long as the Middle Barrel ones.

5.3.1 Description of the Outer Barrel half-stave layouts

The morphology of the Middle and Outer Barrel was described in chapter 3. The Barrels consist of two layers of staves each, being the staves made of three parts: a spaceframe, and two half-staves. Each half-stave is a flat surface where the silicon chips, the Flex Printed Circuit (FPC) and the power bus are glued. The half-staves are attached by several “U-legs” (i.e. small, lightweight structural CFRP pieces in a shape of a ‘U’) to the spaceframe, which provides mechanical support and keeps the positioning and dimensional tolerances. The architecture of the Middle and Outer Barrel staves obeys chip location requirements, modularity and ease of manufacturing. A picture of a single Outer Barrel stave prototype is shown in Fig. 5.16.

To keep the system modular, each half-stave has its own cooling system, based on the concept used at the Inner Barrel staves: two polyimide channels on a high-thermal conductivity plate layout. The inlet/outlet of the two half-staves can be seen in Fig. 5.16. The main difference with the Inner Barrel staves is the size: each Outer Barrel half-stave is twice as wide (30 mm), to accommodate two rows of chips, and more than 5 times longer than one Inner Barrel stave. The detector chips, being the same size as for the Inner Barrel, are arranged in a 2 x 28 matrix on each Middle Barrel half-stave, and a 2 x 49 matrix on each Outer Barrel half-stave. This increase of the total heat load and its distribution in

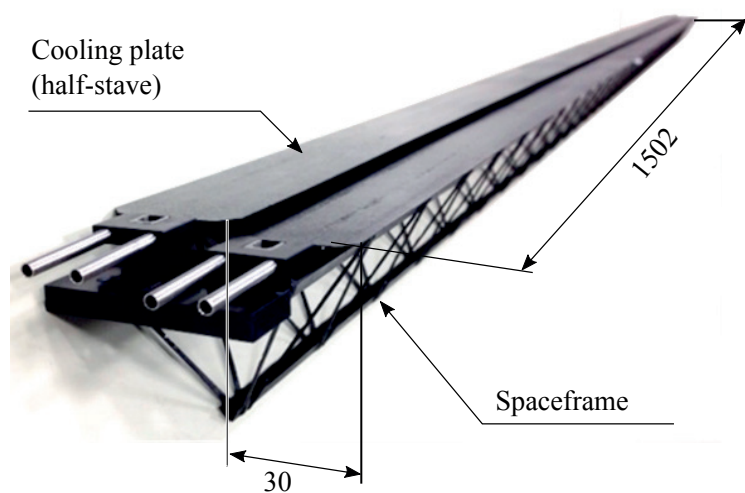


Figure 5.16: Picture of an assembled Outer Barrel stave. The detector chips will occupy the central 1475 mm of each half-stave. Dimensions expressed in mm.

a larger area requires from thicker cooling plates and a rearrangement of the cooling pipes, which need an increased diameter to allow higher coolant flow rates at no pressure drop increase.

The required plate thickness was calculated using analytical calculations (1-D thermal conduction) and the cooling pipe size was estimated through pressure drop correlations, as this was the limiting factor in the Inner Barrel staves. For single-phase water, the correlation by Churchill for straight pipes [145] and the methods indicated in Idelchik's handbook [146] for singular pressure drops were used to ensure that $\Delta p < 0.3$ bar in a half-stave. These correlations were selected for these calculations after achieving good predictions of the experimental data recorded in the Inner Barrel staves. This optimisation process resulted in the plate thicknesses and cooling channel sizes reported in Table 5.6.

The cooling performance of the two optimised half-stave layouts described in Table 5.6 are compared in the present section. The OB1 half-stave consists of a cooling plate made of the same CFRP as the Inner Barrel IB1 stave, K13D2U-2K [42], with its fibres equally arranged transversally to the stave. An increased plate thickness, $120 \mu\text{m}$, is needed in order to cope with the heat load distributed in the 30 mm -wide plate, and to guarantee mechanical stability of the half-stave. The two cooling channels, made of polyimide, are 2.052 mm ID, twice as large as the channels in the Inner Barrel staves. Connectors, assembly blocks, and the Π -bend piece are properly scaled to the new channel size. A 30

Table 5.6: Outer Barrel stave prototypes subjected to experimental water cooling tests. The high thermal conductivity directions are indicated in the cross-section schemes. Dimensions in mm, except where explicitly indicated.

Name	Layout	$[x/X_0]_{full-stave}^a$ [%]	Weight ^b [g]
OB1		0.770	20.4
OB2		0.770	20.7

^a For a fully-equipped stave: spaceframe, half-stave, water as coolant, pixel chips, Flex Printed Circuit (FPC) and power bus. The small overlap between half-staves is considered too.

^b For a single half-stave. It includes: cooling plate and cooling channels only (no coolant).

μm -thick TPG foil [49] is present to enhance the thermal contact between a now wider plate and the upper perimeter of the cooling channels. Last, another difference with the Inner Barrel IB1 stave is the presence of three layers of carbon fleece for constructive reasons, with the third one placed between the plate and the polyimide tubing. This half-stave alone, with water as coolant and no spaceframe, chips or cables, displays a material budget of 0.134%. Additionally, if taking into account the presence of all these elements and the slight overlap between two adjacent half-staves (see Fig. 5.16), the material budget of the whole stave is 0.770%. Thus, a stave made of OB1 half-staves complies with the material budget requirements for the ITS Upgrade Middle and Outer Layers, limited to 1.0% per layer.

Thermo-elastic effects are not negligible in the Outer Barrel staves due to their longitudinal dimension. Experimental tests revealed that the OB1 half-stave will expand up to 1.5 mm within the 20-80°C temperature range, due to the presence of resin in the cooling plate. This phenomenon could cause stave buckling and subsequent loss of spatial positioning and planarity of the detector chips, thermal mismatch between the chips and the plate, and delamination of the plate. The OB2 stave constitutes a good approach to a zero-*CTE* half-stave design, and indeed it was proven experimentally that it displays no thermal expansion in the temperature range mentioned above. The plate layout is inspired in the 0°/90°/0° architecture of the IB3 Inner barrel stave. The cooling plate is decomposed in three laminate layers of K13D2U-2K CFRP 40 μm thick each. The fibres in the central layer are set transversally to the stave (90° direction), like in the OB1 half-stave. The layer beneath and the top one, display the fibres oriented in the stave longitudinal direction (0°). Unlike the IB3 stave, the OB2 half stave does have a 30 μm -thick layer of TPG foil and a 20 μm -thick carbon fleece ply on top of the cooling channels. The cooling channels are identical to the OB1 ones. The assembly is depicted in Table 5.6. The OB2 stave displays almost the same weight as OB1, 20.7 g, and because it is made of the same amount of identical materials, the material budget is considered the same as the OB1 one^a.

5.3.2 Water cooling performance benchmarking of the Outer Barrel half-staves

The two half-stave prototypes, each equipped with 14 Kapton[®] heaters as depicted in Fig. 4.1b, were subjected to thermal tests with water at temperatures ranging from 14 to 18°C. Results were interpreted in a similar fashion as for the Inner Barrel stave prototypes. The cooling performance of the OB1 and OB2 half-staves is represented by the difference between the mean temperature recorded by the thermistors on top of the 14 heaters of each half-stave and the mean water flow temperature. Fig. 5.17a displays the cooling performance versus the water flow rate for the nominal power density, 0.15 W cm^{-2} , and Fig. 5.17b reports the results for double the nominal power density, 0.30 W cm^{-2} . These correspond to absolute electric heat loads of 66 and 132 W applied to the heaters, respectively. The power transferred to the coolant is displayed for each experimental point.

The results show that the OB1 and the OB2 half-staves exhibit similar cooling performances.

^a The OB1 half-stave has an extra carbon fleece layer, but its density is so low that contributes negligibly to the overall material budget.

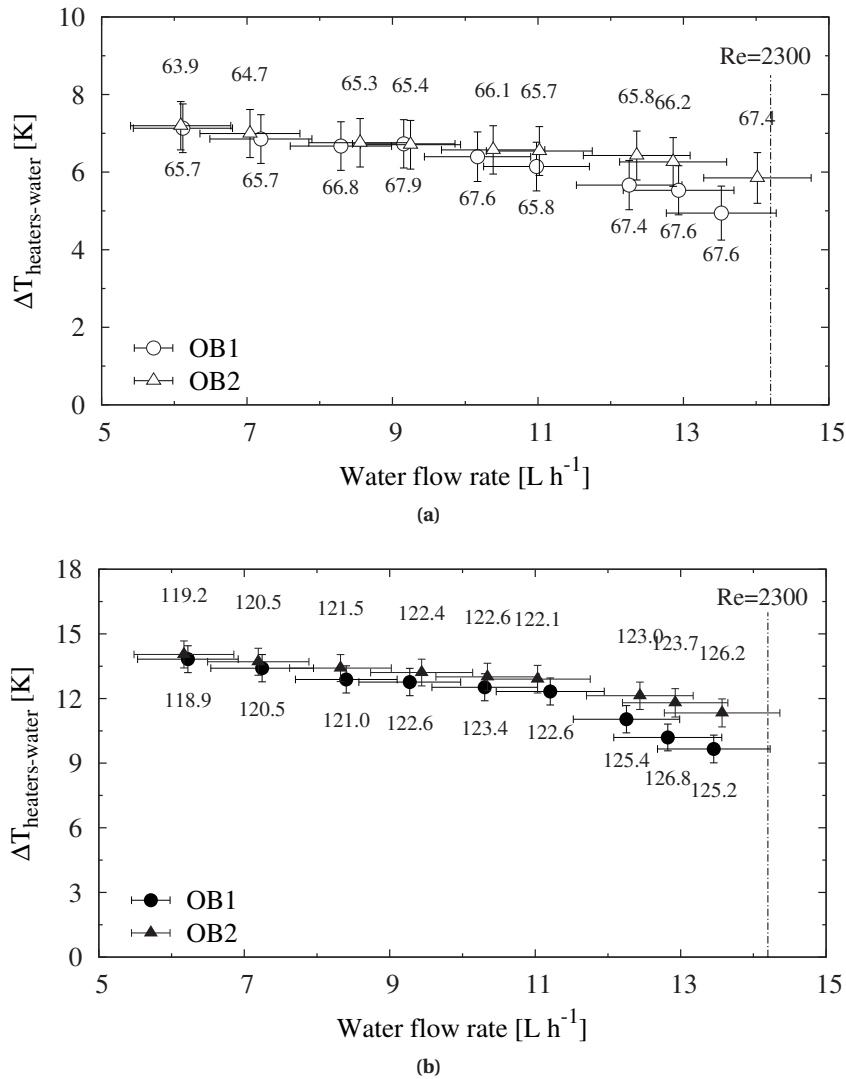


Figure 5.17: Comparison of the cooling performance ($\Delta T_{\text{heaters-water}}$ vs. water flow rate) of the two Outer Barrel half-stave layouts with water, at: (a) 0.15 W cm^{-2} ; (b) 0.30 W cm^{-2} . The heat load transferred to the coolant is indicated for each experimental point in the plot.

The different plate layout does not greatly influence the cooling performance, indicating that the dominating thermal resistance is located in the plate-channel contact, across the polyimide channel wall, or in the wall-fluid convection heat transfer mechanism. The OB1 half-stave displays a slightly better thermal performance than OB2 at higher water flow rates.

Both half-staves maintain a temperature difference between the mean value recorded at the heaters and the water flow lower than 7 K for flow rates higher than 6 L h^{-1} and a power density of 0.15 W cm^{-2} . The detector can be effectively cooled in these conditions with water at a mean temperature of 20°C and the cooling system will keep the chips 3 degrees below the maximum admissible temperature, 30°C , even at flow rates as low as 6 L h^{-1} . However, it is emphasised that the expected power dissipation

in the Middle and Outer Barrel staves at the time this document was written is 31 mW cm^{-2} , almost 5 times lower than the nominal power density used in the cooling tests. Thus, these thermal performance results provide a generous safety margin against occurrences, such as failure of the ITS Upgrade air flushing system or low coolant flow conditions.

If the nominal power density is doubled to 0.30 W cm^{-2} , almost 10 times the expected power dissipation, $\Delta T_{\text{heaters-water}}$ approaches the limit of 15 K. Thus, the coolant flow is required to be at an average temperature of less than 15°C . The coolant temperature rise experienced at the stove implicates supplying the coolant at the half-stave inlet at a temperature several degrees lower than 15°C . This would get too close to the ITS Upgrade detector requirement of keeping the coolant warmer than 12°C , although such a power density scenario is unlikely during detector operating conditions and is limited only to the cooling tests hereby presented.

No significant improvement in the stove thermal performance is observed when increasing the water flow rate. In the $6\text{-}14 \text{ L h}^{-1}$ range, this is explained by the fact that the flow is laminar ($Re < 2300$) inside the 2.052 mm ID circular channel. Laminar heat transfer coefficients do not depend on the water flow rate. $\Delta T_{\text{heaters-water}}$ only decreases slightly at water flow rates higher than $\sim 13 \text{ L h}^{-1}$ as the water starts entering the transitional flow regime. This behaviour, more noticeable in the OB1 half-stave, suggests the main thermal resistance in the system is concentrated in the conduction mechanism in the stove-cooling channel assembly. A similar conclusion was taken for the Inner Barrel staves, especially when comparing cooling performance results with water and two-phase C_4F_{10} . High conductive thermal resistance across the half-stave is not a negative feature, as the system becomes thermally robust around an specific $\Delta T_{\text{heaters-water}}$ and thus can work over a wide range of cooling conditions.

The water pressure drop is plotted versus water flow rate in Fig. 5.18a for the two prototypes. In order to have a water pressure drop lower than 0.3 bar, the flow rate should be lower than 8 L h^{-1} , which is enough to guarantee good thermal performance at 0.15 W cm^{-2} , as displayed in Fig. 5.17a. The water temperature rise is plotted in Fig. 5.18b versus flow rate for the OB1 half-stave. The OB2 half-stave displays the same values. At 6 L h^{-1} , the water temperature rise is 6.8 K at 0.15 W cm^{-2} . A lower flow rate involves a higher temperature rise, causing potentially undesired temperature non-uniformities in the heaters. Thus, a water flow rate of 6 L h^{-1} provides good thermal performance, low pressure drop at 0.15 W cm^{-2} , and surely will cope well with the actual Outer Barrel chip power density of 31 mW cm^{-2} .

The experimental pressure drop was compared with the values calculated analytically using the frictional pressure drop correlations by Churchill [145] and by Idelchik for the singular pressure drops [146] in the OB2 half-stave in Fig. 5.19. The predicted values match the experimental ones, confirming that the fabrication process did not alter the section of the polyimide channels nor caused obstructions in the piping. Deviations are higher at Reynolds numbers approaching the transitional regime, with underestimated predicted values. The pressure drop at the singularities, mostly at the Π -bend, make up for 15-20% of the total pressure drop.

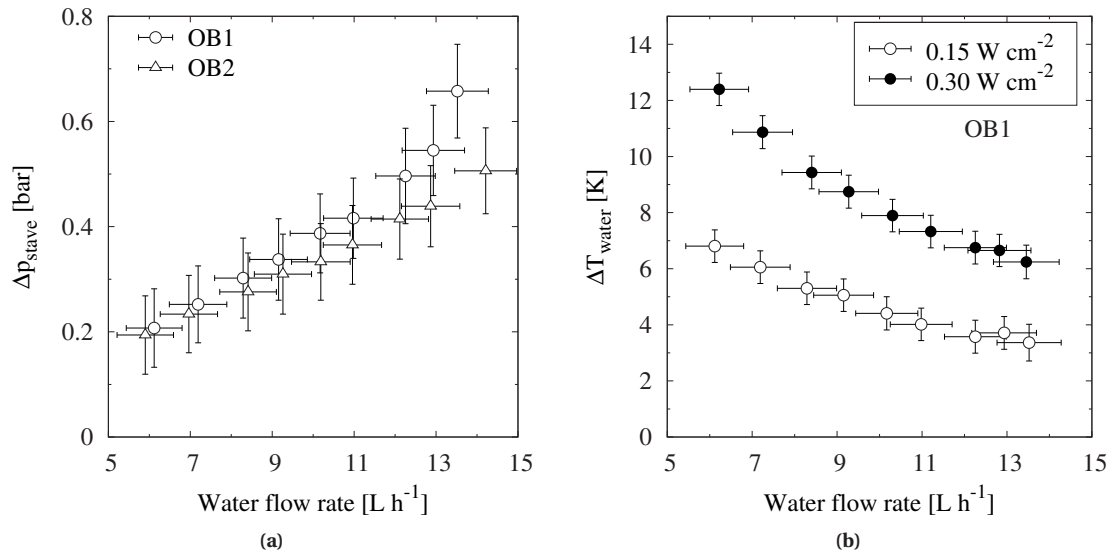


Figure 5.18: (a) Water pressure drop of the two Outer Barrel half-staves and; (b) water temperature rise for the OB1 prototype at 0.15 and 0.30 W cm⁻² (b).

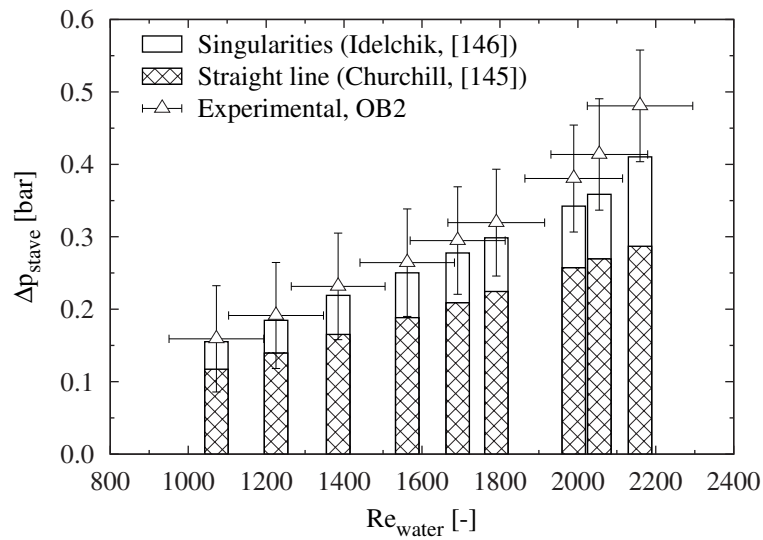


Figure 5.19: Experimental and calculated water pressure drop for the OB2 half-stave versus the Reynolds number. The calculated values are the sum of the frictional pressure drop in the straight channels, by Churchill [145], and the singular pressure drops, estimated by Idelchik [146].

Tests with water were carried out at coolant temperatures yielding heater temperatures close to the ambient air. Thus, heat loads transferred from/to the air reached $\sim 9\%$ of the total power applied to the electric heaters only for some experimental cases at the highest power density, 0.30 W cm⁻², and 5% at 0.15 W cm⁻². Extra losses are originated by ohmic heating of the heater cabling and equipment due to the high electric currents involved in the Outer Barrel half-stave tests.

Nominal cases

The nominal conditions for the water-cooled Outer Barrel OB1 half-stave are summarised in Table 5.2 for the nominal power density, 0.15 W cm^{-2} , and twice its value, 0.30 W cm^{-2} . The water mean velocity in the polyimide channels ranges from 0.5 to 0.8 m s^{-1} , well within the recommended velocity values for pipe flows [155, 156]. Further detail on this subject was presented in page 105. In the 0.15 W cm^{-2} case, the water inlet temperature is 14°C and the mean temperature of the heated surface does not exceed 25°C . The OB2 half-stave exhibits identical cooling conditions for the 6 L h^{-1} flow rate.

Fig. 5.20 displays infrared images of the OB1 half-stave Kapton[®] heaters at the 0.15 W cm^{-2} nominal case (see first row of Table 5.7). At the right side of the image, the temperatures of the heaters 1 and 14, those closer to the inlet/outlet end, are reported. The temperature maps of heaters 7 and 8, those close to the Π -bend, are displayed on the left. In general, good temperature uniformity on the heated surface was achieved: 7 K at 0.15 W cm^{-2} . The maximum temperature of the whole half-stave heated surface is reached on heater 7, and the lowest at heater number 1, the coldest region. The cooling plate balances the temperatures of heaters 1 and 14, and that is the reason why the maximum temperature on heater 14 is moderate, despite it being cooled with water at its hottest temperature.

Last, Fig. 5.21 compares the temperature readings from the thermistors on each of the 14 heaters

Table 5.7: Nominal cooling conditions for the OB1 half-stave with water at 0.15 and 0.30 W cm^{-2} .

$P_{d, \text{heaters}}$ [W cm^{-2}]	\dot{V}_{water} [L h^{-1}]	$u_{\text{mean, water}}$ [m s^{-1}]	$T_{\text{mean, water}}$ [$^\circ\text{C}$]	$T_{\text{mean, heaters}}$ [$^\circ\text{C}$]	ΔT_{water} [K]	Δp_{water} [bar]
0.15	6.1	0.5	17.4	24.5	6.8	0.21
0.30	9.3	0.8	18.0	30.8	8.7	0.32

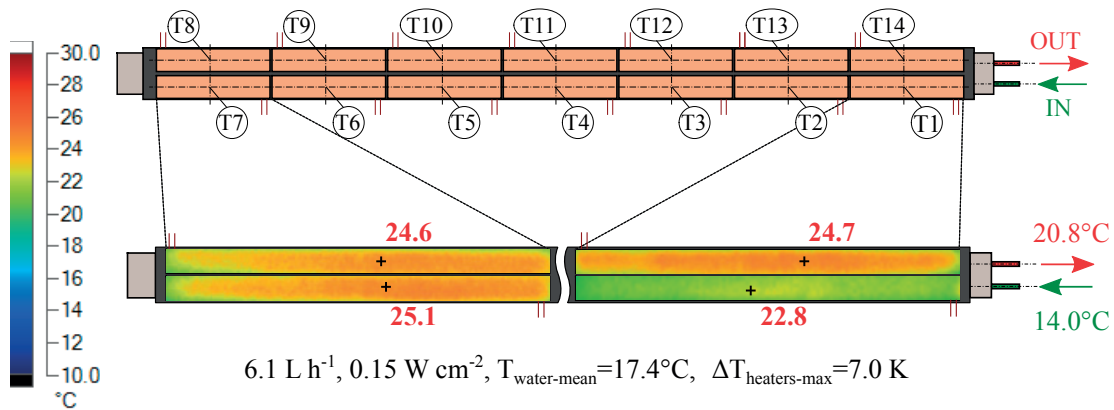


Figure 5.20: Infrared images displaying the water-cooled Outer Barrel OB1 half-stave heater temperature map [$^\circ\text{C}$] at nominal cooling conditions for the 0.15 W cm^{-2} power density, reported in the first row of Table 5.7. Only the surface temperature maps of the heaters close to the inlet/outlet (heaters 1 and 14, at the right) and the ones next to the Π -bend (heaters 7 and 8, at the left) are shown. The maximum temperatures on the heaters are reported in red text.

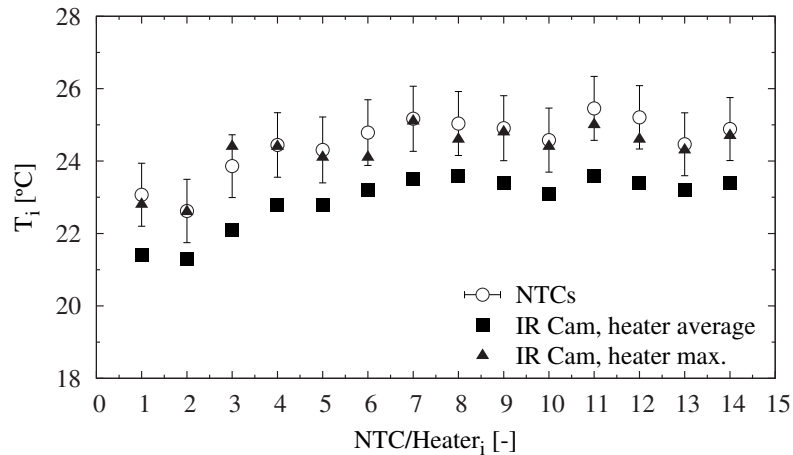


Figure 5.21: Comparison of the temperatures measured by the thermistors on the heaters against the maximum and average temperatures recorded by the IR camera on the OB1 half-stave at nominal cooling conditions with water at 0.15 W cm^{-2} , as reported in the first row of Table 5.7.

with the average and maximum temperatures recorded using the infrared camera. The values do not differ significantly, despite the high uncertainty typically involved in thermographic imaging. Besides, the temperature trend is reproduced. This validates the data acquisition procedure and the results.

To conclude, the OB1 and OB2 half-staves offer an excellent compromise between cooling performance and low weight and material budget. Mechanical tests on the half-staves-spaceframe assembly showed good flexural properties complying with the ITS Upgrade requirements. The thermo-mechanical behaviour, particularly the thermoelastic characteristics, of a fully-assembled stave, i.e. half-staves, spaceframe, detector chips, FPC, glue and power bus cable, is still to be tested, since most of the services mentioned are still being developed. The outcome of these studies will drive the decision of choosing between the OB1 or the OB2 half-staves, the two of them conforming to the cooling requirements.

5.3.3 Two-phase evaporative cooling for the Outer Barrel half-staves

Half-stave description

The Outer Barrel half-staves presented above, due to their bigger channels compared to the Inner Barrel staves, display large material budget peaks if water is used as a coolant. Thus, an evaporative coolant provides an important advantage towards the preservation of the local detector resolution by decreasing the local and the overall stave material budget.

While the Inner Barrel staves may operate with water or two-phase C_4F_{10} refrigerant without any adjustment, larger cooling channels are needed for the Outer Barrel half-staves due to their 1.5 m length. The half-stave tested with two-phase C_4F_{10} refrigerant is named OB3, and it is based on the OB1 half-stave. They share the same layout, but the OB3 half-stave has larger polyimide channels, 2.667

mm ID instead of 2.052 mm in the OB1 half-stave, in order to keep the two-phase saturation pressure and temperature drop reasonably low. The correlation by Friedel [92] in the straight channels, and the model by Chisholm [101] in the Π -bend were implemented to estimate the two-phase pressure drop in the half-stave and ensure it results in a $\Delta T_{sat} < 10$ K. The 2.667 mm ID channels fulfil this condition in a wide range of mass fluxes. Other differences with OB1 include one less carbon fleece layer and an interaxis channel distance of 13 mm instead of 10 mm, which was the initial required gap between the channels (the OB3 half-stave is an older design than the OB1 and OB2 half-staves). The layout, material budget and weight of the OB3 stave are summarised in Table 5.8.

Fig. 5.22 displays the material budget of the OB3 half-stave considering the cooling plate, the cooling channels, and two-phase C_4F_{10} as the coolant, compared with the OB1 half-stave with water. Similar to the Inner Barrel staves, the void fraction for the two-phase flow material budget calculation is estimated according to the void fraction correlation by Steiner [84], based on the Rouhani-Axelsson drift flux void fraction map [83], finally choosing a value of 0.85. The liquid phase is assumed to be uniformly distributed as a film around the periphery of the channel inner wall. Cooling with two-phase C_4F_{10} refrigerant diminishes the height and width of the coolant material budget peaks with respect to water, and, even with a 25% larger channel, the global material budget of the stave assembly is decreased by 3.8%, as reported in Table 5.9.

The OB3 stave was subjected to heat loss experimental characterisation, as well as single-phase and two-phase cooling tests with C_4F_{10} refrigerant. Cooling tests with water were performed for the sake of comparison. Fig. 5.23 displays the heat loss characteristic of the OB3 half-stave. At a prototype-ambient temperature difference of 5 K, the stave will dissipate less than 5 W to the air.

Table 5.8: Outer Barrel OB3 half-stave developed for experimental two-phase cooling tests with C_4F_{10} refrigerant as coolant. All dimensions are expressed in mm, except where explicitly indicated. The high thermal conductivity directions are indicated in the scheme.

Name	Layout	$[x/X_0]_{full-stave}^a$ [%]	Weight ^b [g]
OB3		0.741	22.0

^a For a fully-equipped stave: spaceframe, half-stave, two-phase C_4F_{10} as coolant with a void fraction of 0.85, pixel chips, Flex Printed Circuit (FPC) and power bus. The small overlap between half-staves is considered too.

^b For a single half-stave. It includes: cooling plate and cooling channels only (no coolant).

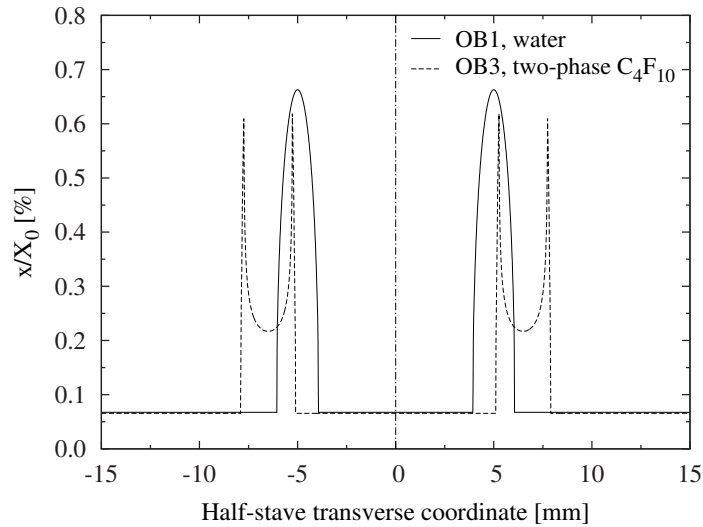


Figure 5.22: Half-stave material budget considering water and two-phase C_4F_{10} refrigerant as coolants in the OB1 and OB3 Outer Barrel half-staves, respectively. A void fraction of $\varepsilon = 0.85$ is assumed. Only the cooling plate assembly, the cooling channels and the coolant are considered in the calculation.

Table 5.9: Material budget comparison between the OB1 half-stave with water and the OB3 half-stave with two-phase C_4F_{10} as coolant.

Half-stave	Coolant	$[x/X_0]_{plate+coolant}^a$ [%]	$[x/X_0]_{full}^b$ [%]
OB1	Water	0.134	0.770
OB3	Two-phase C_4F_{10}	0.105	0.741
% of x/X_0 saved with OB3 with two-phase C_4F_{10} [%]		-21.6	-3.8

Single-phase C_4F_{10} tests

Fig. 5.24 shows the measured single-phase pressure drop and the predicted values according to Churchill's correlation [145] and the singular friction factors calculated by Idelchik [146]. As for the Inner Barrel staves and with Outer Barrel half-staves with water as coolant, consistency was found between measurements and predictions. Singular pressure drops account for roughly 15% of the total pressure drop, and are mostly concentrated at the Π -bend.

Results of the energy balance are displayed in Fig. 5.25a at adiabatic conditions, i.e. considering the heat exchange with the ambient as quantified in Fig. 5.23, and power densities of 0.0225 and 0.0450 W cm^{-2} . Generally, the experimental points fall within the $\pm 20\%$ error band, even in adiabatic conditions. At an equal coolant temperature rise, the uncertainty of the energy balance for single-phase C_4F_{10} cooling is lower than with water thanks mainly to the lower uncertainty of the Coriolis effect mass flow meter.

^a Includes: plate assembly, channels and coolant inside the channels. No spaceframe included.

^b Includes: plate assembly, channels, coolant inside the channels, spaceframe, silicon chips, glue, FPC (Flex Printed Circuit) and power bus. The overlap between adjacent half-staves is included too.

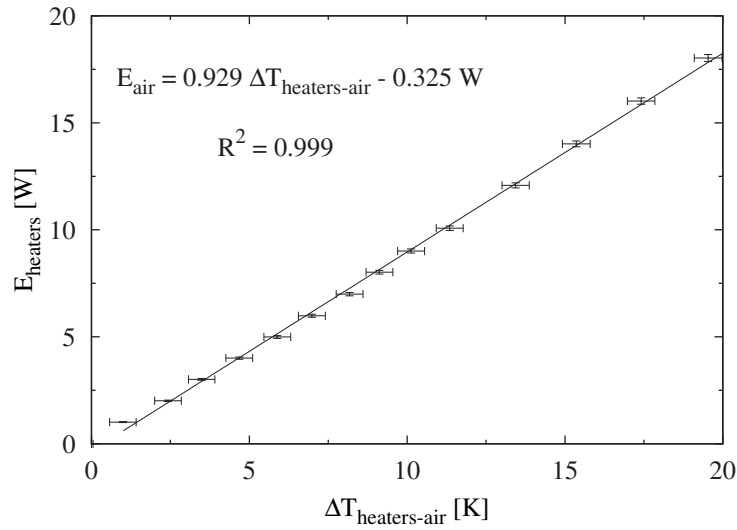


Figure 5.23: Experimental heat load transferred to the air versus the difference between the mean heater temperature and the ambient air temperature for the OB3 Outer Barrel half-stave.

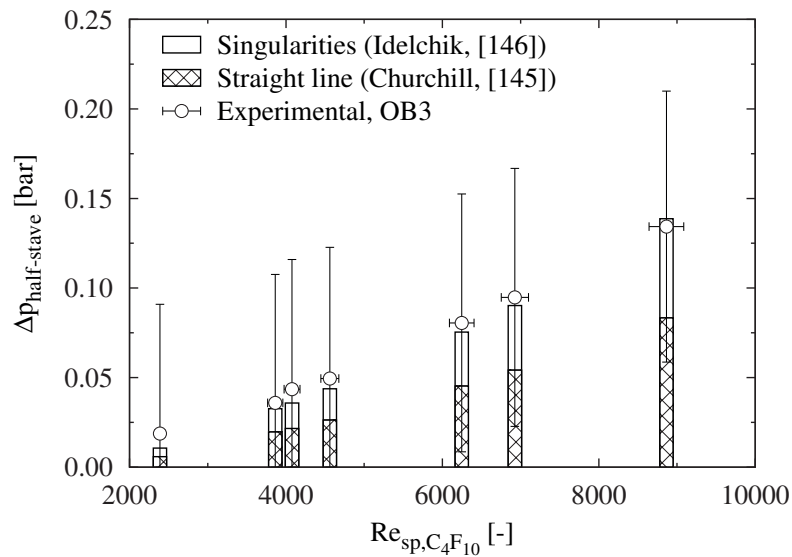


Figure 5.24: Experimental and calculated pressure drop at the OB3 half-stave versus the Reynolds number with single-phase C_4F_{10} refrigerant. The predicted values are the sum of the frictional pressure drop in the straight channels, by Churchill [145], and the singular pressure drops, estimated by Idelchik [146].

The experimental mean heat transfer coefficients ($h_{sp,C_4F_{10}}$), calculated following the thermal resistance method described in Eqs. 4.22 and 4.21 in subsection 4.3.5, are compared to predicted values with the correlation by Gnielinski [149] in Fig. 5.25b. This method required determining the conduction thermal resistance in the stave using water as coolant and a power density of 0.30 W cm^{-2} . Although the trend given by the correlations is reproduced experimentally, the uncertainty becomes quite high at $Re > 6000$, for the same reasons explained in page 110. The two-phase cooling facility and instrumentation are thus validated and now two-phase flow cooling tests are performed.

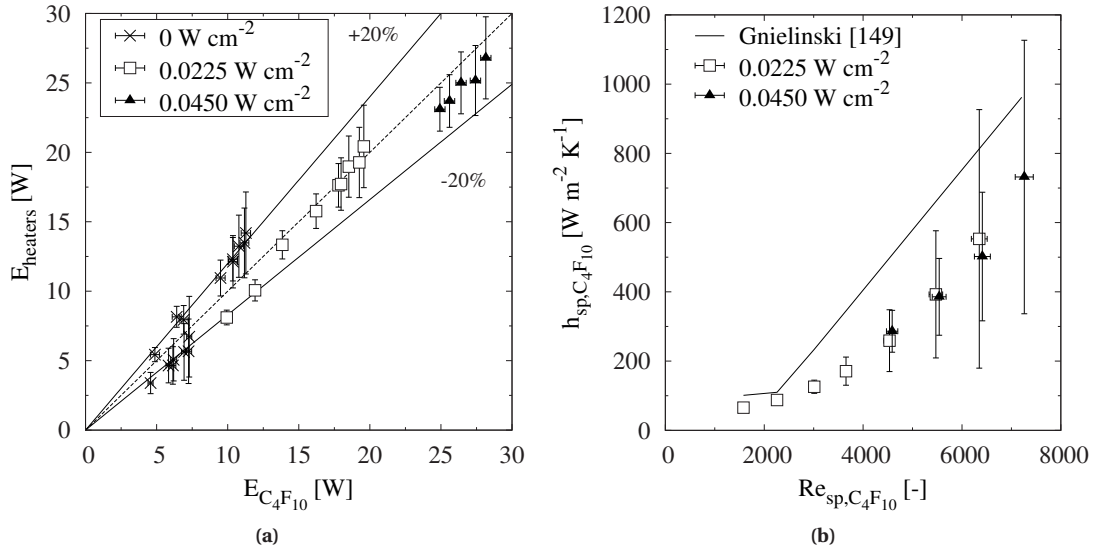


Figure 5.25: Energy balance (a) and mean stave heat transfer coefficient of the OB3 half-stave with single-phase C_4F_{10} refrigerant at 0.0225 and 0.0450 $W\ cm^{-2}$ (b). The energy balance was calculated in adiabatic conditions too, considering the heat exchange with the ambient.

Two-phase C_4F_{10} cooling test results

Cooling tests with two-phase C_4F_{10} refrigerant were run for the OB3 half-stave at several power densities. The average absolute power transferred to the boiling coolant (i.e. the difference between the electric power applied to the 14 heaters and the heat transfer rate with the environment calculated using the characteristic in Fig. 5.23) is summarised in Table 5.10 for a series of power densities.

The cooling performance of the OB3 half-stave with two-phase C_4F_{10} refrigerant as coolant for all the considered power densities is reported in Fig. 5.26. Up to 0.20 $W\ cm^{-2}$, more than 6 times the current expected power dissipation of the detector chips, the half-stave is kept less than 10 K hotter than the coolant. Only at 0.30 $W\ cm^{-2}$ is the 15 K temperature difference surpassed.

The two-phase C_4F_{10} cooling performance is compared to that of water in the OB3 half-stave, as presented in [154], in Fig. 5.27 at 0.15 and 0.30 $W\ cm^{-2}$. Besides, the cooling performance results for

Table 5.10: Average heat load transferred to the boiling C_4F_{10} refrigerant at the OB3 half-stave for the different power densities considered in the two-phase flow tests.

P_d [$W\ cm^{-2}$]	$E_{heaters} - E_{air}$ [W]
0.10	42.2
0.125	51.2
0.15	61.0
0.20	81.2
0.30	121.1

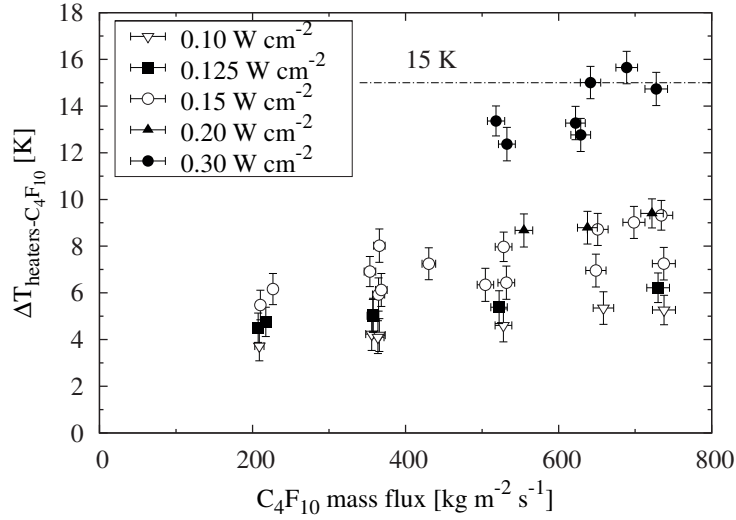


Figure 5.26: Cooling performance of the OB3 half-stave with two-phase C_4F_{10} refrigerant as coolant at several heater power densities. The average power transferred to the fluid is reported in Table 5.10.

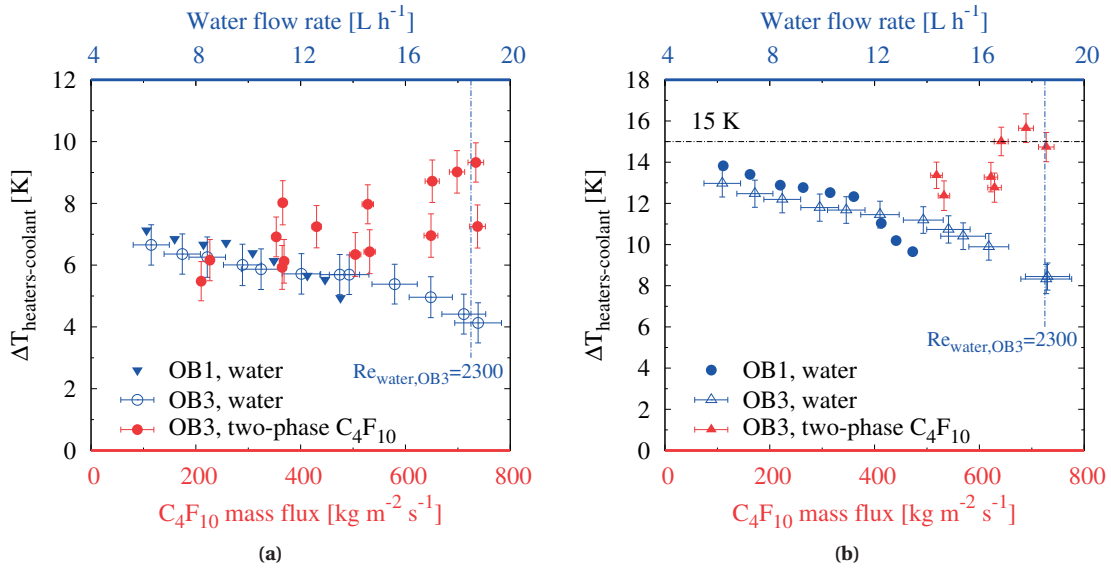


Figure 5.27: Comparison between the cooling performance of the OB3 half-stave when using water and two-phase C_4F_{10} refrigerant at 0.15 and 0.30 W cm^{-2} , compared against the results for the water-cooled OB1 half-stave.

the water-cooled OB1 half-stave prototype are overlaid in the plots. In view of the full set of results, the following behaviours are observed:

- The OB3 prototype is well cooled with water and with two-phase C_4F_{10} , with a maximum $\Delta T_{heaters-coolant}$ not exceeding 10 K at the nominal power density of 0.15 W cm^{-2} .
- Similar cooling performance is observed with water and two-phase C_4F_{10} refrigerant, at least at 0.15 W cm^{-2} . However, unlike the Inner Barrel staves, the expected heat transfer coefficient with

water is $1000 \text{ W m}^{-2} \text{ K}^{-1}$ (laminar flow), lower than values predicted for the two-phase C_4F_{10} refrigerant using the Liu and Winterton correlation [121], which range from 1000 to $4000 \text{ W m}^{-2} \text{ K}^{-1}$. Further analysis is presented at the end of this section.

- The cooling performance decreases at increasing mass fluxes. As explained for two-phase cooling tests on the IB2 stave, this is related to the fact that higher mass fluxes involve lower mean vapour qualities in these tests and lower heat transfer coefficients. Stronger presence of liquid C_4F_{10} promotes forced convection to the liquid as the dominating heat transfer mechanism, which, given the low liquid thermal conductivity of liquid C_4F_{10} , increases the global thermal resistance. As for the IB2 stave, the extent of the cooling performance drop due to the increase of C_4F_{10} mass flux cannot be accurately quantified using the experimental data obtained in these tests, since the dominating thermal resistance is by conduction in the stave.
- The OB1 and OB3 half-staves present a similar cooling performance with water, where the only differences are the size of the polyimide channels and the interaxis distance between them. It is observed that the cooling performances of OB1 and OB3 improve when the coolant flow approaches the transitional flow regime ($Re = 2300$), which occurs at a lower flow rate for the OB1 half-stave due to its smaller channels.

Fig. 5.27a shows an interesting feature: values of $\Delta T_{\text{heaters-coolant}}$ differing up to 2.5 K at the same mass flux are obtained with two-phase C_4F_{10} cooling in the OB3 prototype. The vapour quality is the parameter behind this behaviour. Fig. 5.28a pictures the trend of $\Delta T_{\text{heaters-coolant}}$ with the mean vapour quality for several power densities. Generally, working at high vapour qualities results in improved cooling performances. A particular case is presented in Fig. 5.28b. Here, $\Delta T_{\text{heaters-coolant}}$ is plotted against the mean vapour quality for cases at 0.15 W cm^{-2} and different mass fluxes. The worst cooling performances are achieved at the lowest vapour qualities, usually connected to the higher mass fluxes.

An extreme case regarding low cooling performance corresponds to a scenario where subcooled liquid reaches the half-stave entrance. In that case, liquid forced convection occurs in the first section of the channels and thus the cooling rate locally decreases. Fig. 5.29 depicts three cases at 0.15 W cm^{-2} and $365 \text{ kg m}^{-2} \text{ s}^{-1}$, where the coolant reaches the stave as liquid with a subcooling of 3.5 K, and in saturated conditions with $x_4=0.03$ and $x_4=0.16$. The cooling performance of the case with the coolant entering as subcooled liquid is the worst by up to 3 K. The saturated cases present a similar behaviour, with the one reaching higher vapour qualities experiencing a slightly better cooling performance at the end of the return line.

Thermal results have to be framed within the two-phase pressure drop measurements, following the same methodology as for the Inner Barrel staves, in section 5.2.3. The experimental readings were compared with predicted values, expressed in Eq. 4.20 as the sum of the two-phase frictional pressure drop and the momentum pressure drop (see Eq. 4.19), in conditions where the vapour quality increases along the stave. The frictional pressure drop components were estimated with the correlation by Friedel

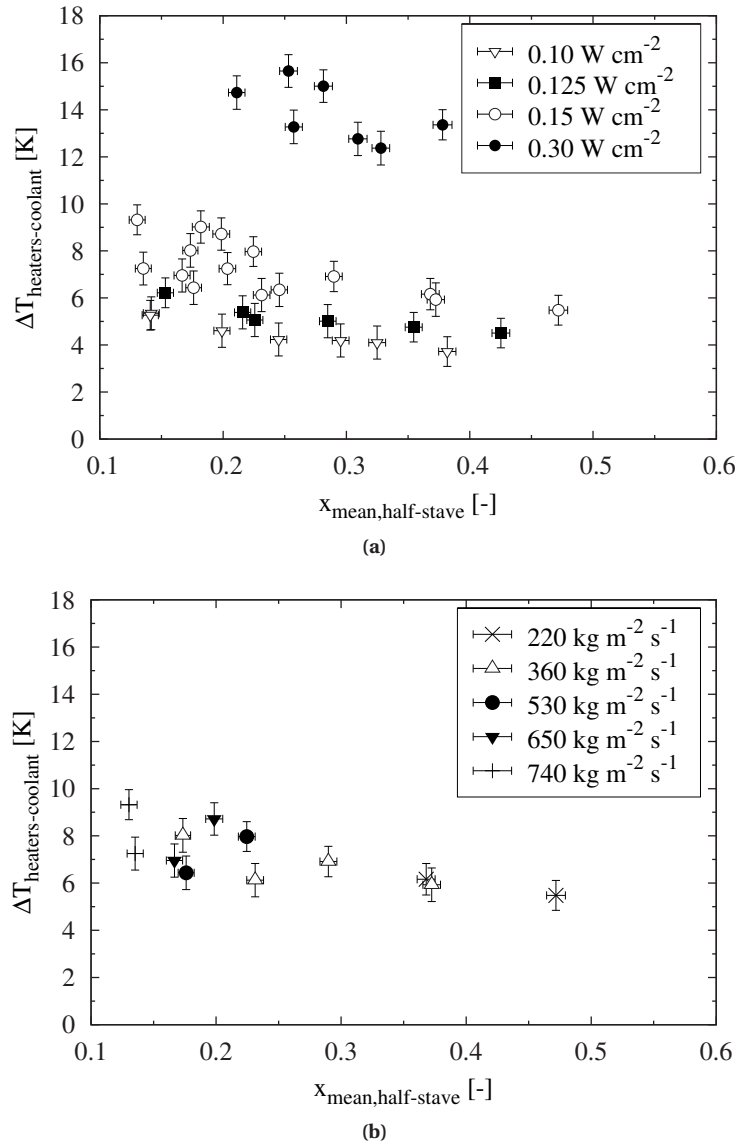


Figure 5.28: Sensitivity of the OB3 half-stave cooling performance with the mean vapour quality when cooled with two-phase C_4F_{10} refrigerant: (a) influence of the power density; (b) influence of the mass flux, at a power density of 0.15 W cm^{-2} .

[92] in the straight channels, and according to the method by Chisholm [101] in the Π -bend. Fig. 5.30 compares the measured pressure drop to the predicted values. A $\pm 30\%$ agreement was observed for the experimental matrix, with most of the cases within the $\pm 20\%$ error range.

The main goal of studying the two-phase pressure drop is to quantify the corresponding saturation temperature drop. For a selection of experimental cases at several mass fluxes and power densities, Fig. 5.31 reports the saturation temperature drop in the whole half-stave matched against the mean vapour quality and the standard deviation of the measurements of the 14 thermistors on the half-stave heaters. In general, low mass fluxes and low vapour qualities yield low saturation temperature drops (see Fig.

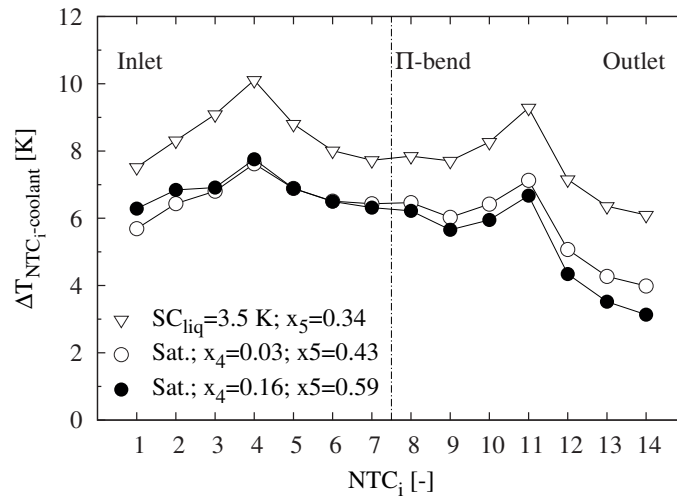


Figure 5.29: Influence of the two-phase C_4F_{10} coolant inlet conditions (subcooled liquid, saturated two-phase flow) on the temperatures measured by the 14 thermistors on the OB3 half-stave heaters. Cases are reported at 0.15 W cm^{-2} and $G_{C_4F_{10}} = 365 \text{ kg m}^{-2} \text{ s}^{-1}$.

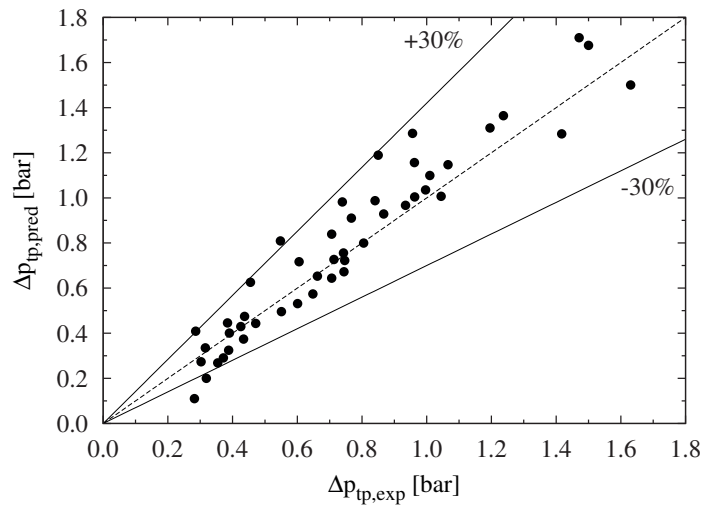


Figure 5.30: Predicted versus experimental two-phase C_4F_{10} pressure drop values at the OB3 half-stave. For the calculating the predicted frictional two-phase pressure drop, the correlations by Friedel [92] for straight channels, and by Chisholm [101] for the Π -bend, are used.

5.31a). At the same time, high saturation temperature drops result in high half-stave temperature non-uniformity, as displayed in Fig. 5.31b, thus the operation points should be carefully chosen.

The main trends of $\Delta T_{heater-coolant}$, ΔT_{sat} , and half-stave temperature non-uniformity characteristics have been identified. In view of the results, it can be stated that:

- Low mass fluxes ($200\text{-}400 \text{ kg m}^{-2} \text{ s}^{-1}$) and high mean vapour qualities (on the order of 0.4-0.5) are preferred in order to obtain low $\Delta T_{heaters-coolant}$ (i.e. good cooling performance). The use of too low C_4F_{10} mass fluxes is discouraged, as they might lead to partial dry-out of the coolant.

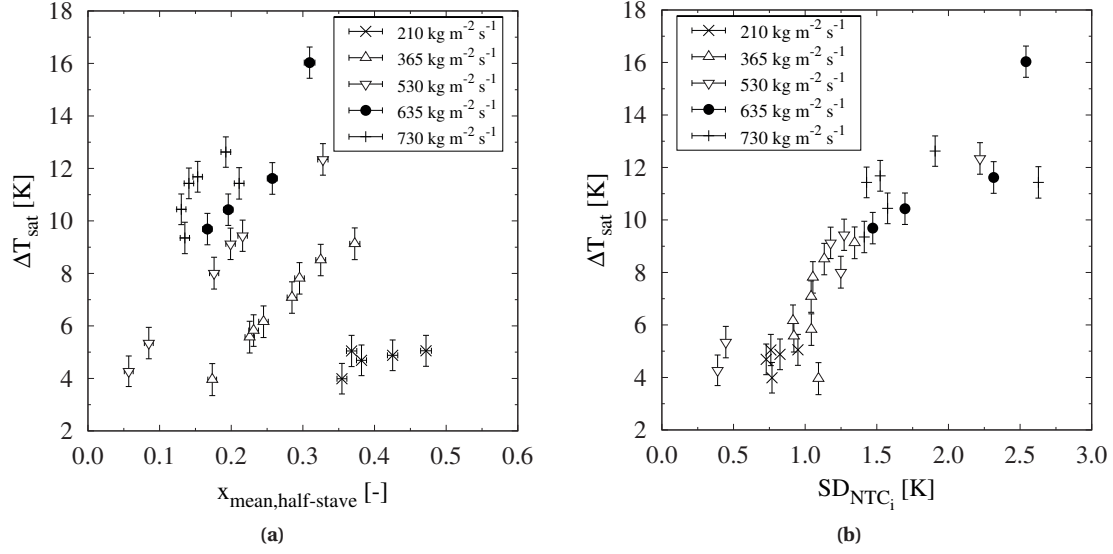


Figure 5.31: (a) Saturation temperature drop trend with the mean stave vapour quality; and (b) its influence on the stave temperature non-uniformity for several two-phase C_4F_{10} mass fluxes in the OB3 half-stave.

- At high mass fluxes, low vapour qualities at the half-stave inlet are desired, in order to minimise the coolant saturation temperature drop and hence decrease the temperature gradients on the half-stave. Also, high inlet vapour qualities could lead to partial dryout conditions and poor local cooling performance. The mass flux is thus a critical parameter to control.
- The coolant should enter the stave at saturated conditions.

The experimental conditions yielding the best compromise between these requirements are summarised below.

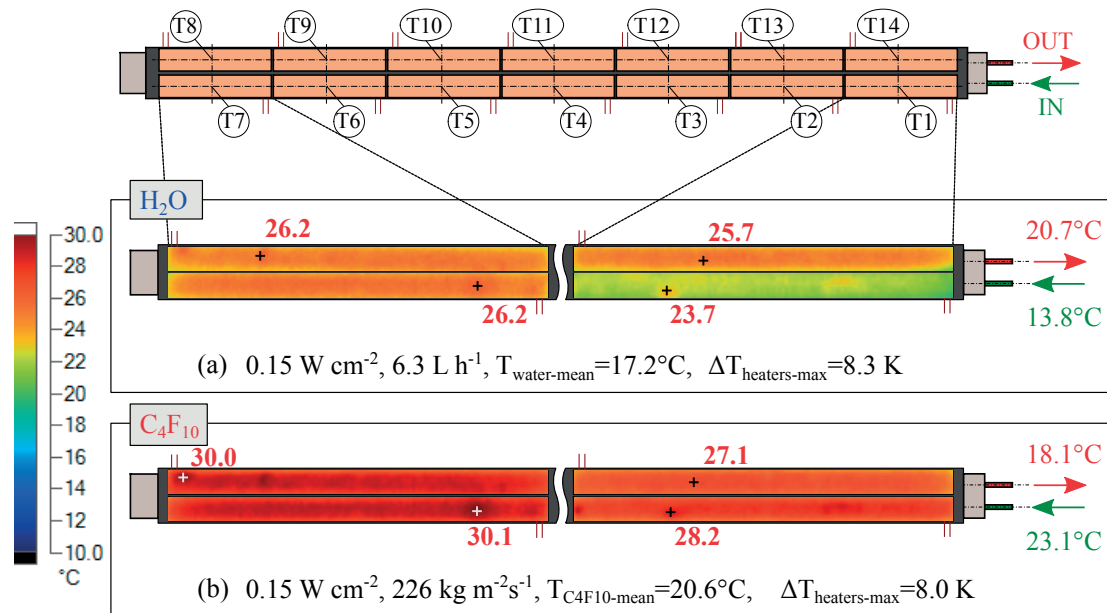
OB3 stave two-phase nominal cooling conditions

Considering the remarks above, five experimental points at 0.15 W cm^{-2} are selected and their conditions summarised in Table 5.11. Cases 1 and 2 are similar except for the vapour qualities. Saturated conditions are expected at the half-stave inlet for the first case, while for the second one a considerable fraction of saturated liquid refrigerant enters the stave, resulting in a slightly poorer cooling performance, although acceptable. Besides, case 2 exhibits an outlet vapour quality far from the onset of partial dryout conditions and a low saturation temperature drop. Cases 3, 4, and 5 involve identical, higher mass fluxes, and the inlet coolant flow conditions range from saturated conditions to saturated liquid and, finally, subcooled liquid. Local heater temperatures were reported for these three cases in Fig. 5.29. Cases 3 and 4 display the best cooling performances of all three, though case 4 is preferred due to its lower saturation temperature drop. Case 5, with subcooled liquid entering the stave, incurs the lowest pressure and saturation temperature drops, but its thermal performance is the worst of all cases, with $\Delta T_{\text{heaters-coolant}} \sim 8 \text{ K}$. Subsequently, case 2 is chosen as the best nominal cooling condition.

Table 5.11: Five experimental cooling cases with boiling C_4F_{10} refrigerant for the OB3 half-stave at 0.15 W cm^{-2} .

Case	$G_{C_4F_{10}}$ [$\text{kg m}^{-2}\text{s}^{-1}$]	$T_{mean,C_4F_{10}}$ [$^{\circ}\text{C}$]	$T_{mean,heaters}$ [$^{\circ}\text{C}$]	x_{in} [-]	x_{out} [-]	$\Delta p_{C_4F_{10}}$ [bar]	$\Delta T_{sat,C_4F_{10}}$ [K]
1	210	20.2	25.7	0.15	0.80	0.39	5.1
2	226	20.6	26.6	0.07	0.67	0.39	5.0
3	365	20.4	26.3	0.16	0.59	0.71	9.1
4	365	19.3	25.4	0.03	0.43	0.44	5.8
5	365	16.4	24.5	SC=3.5 K	0.34	0.29	4.0

Fig. 5.32 displays the thermographic images of the OB3 half-stave Kapton[®] heaters at 0.15 W cm^{-2} with water at 6 L h^{-1} (Fig. 5.32a), and with evaporative C_4F_{10} (Fig. 5.32b) at the conditions reported in case 2 in Table 5.11. At the right side of the image, the temperatures of the heaters 1 and 14, which are adjacent to the inlet/outlet ports, are reported. The temperature maps of the heaters 7 and 8, neighbouring the Π -bend, are displayed at the left side of the images. In general, similar temperature uniformity on the heated surface was achieved with water and two-phase C_4F_{10} . The maximum gradients reach 8.3 and 8.0 K in each case, similar to those displayed in the OB1 and OB2 prototypes cooled with water. Small differences are attributed to the absolute temperature of the prototypes during the tests (directly depending on the refrigerant temperature), which involves different heat exchange rates with the ambient in the cooling tests conditions, and constructive differences.

**Figure 5.32:** Infrared images of the OB3 half-stave heated surface temperature map [$^{\circ}\text{C}$] when cooling at nominal cooling conditions at 0.15 W cm^{-2} with: (a) water at 6 L h^{-1} ; and (b) two-phase C_4F_{10} refrigerant at the conditions corresponding to case 2 in Table 5.11. The maximum temperature gradients measured in the whole heated surface are indicated. The maximum temperatures on the heaters are reported in red text.

The temperature map on the half-stave looks qualitatively different whether the coolant is water or two-phase C_4F_{10} . With water, the area occupied by heater 1 is the coldest, as the coolant is colder at the inlet. This affects the neighbouring heater 14, that gets cooled thanks to the heat spreading capabilities of the cooling plate. Heaters from 4 to 11 display the highest temperatures. On the other hand, with two-phase C_4F_{10} , the coolant enters in saturated state, thus at its hottest temperature, and at low vapour quality, subsequently displaying low heat transfer coefficients. Heater 1 should be hence the hottest, but it is cooled by the colder area across the plate beneath heater 14, where the coolant leaves the half-stave after experiencing a saturation temperature drop. Besides, the heat transfer coefficient is locally high at the outlet. Heaters 7 and 8 see a higher temperature, as the coolant temperature is locally high and its vapour quality still quite low, yielding low local heat transfer coefficients.

Concluding this section, two-phase C_4F_{10} refrigerant can be used as coolant for the ITS Upgrade Outer Barrel staves as an alternative to water, with the sole major change with respect to the OB1 and OB2 designs (tested with water) being the need of larger cooling channels. Still, an advantageous material budget will be achieved, compared to the aforementioned water-cooled staves. However, it is important to carefully choose the operation points in order to avoid feeding subcooled liquid to the staves, ensure no coolant dryout conditions are reached in the half-stave and, due to the stave length, prevent coolant saturation temperature dropping below 12°C . Likewise, it is important to properly size the piping from the cooling facilities, distribution lines, and capillaries in the fully integrated Outer Barrel, tasks that fall outside of the scope of this thesis.

The latest Outer Barrel nominal power density of 31 mW cm^{-2} stated by the ITS Upgrade project collaboration was announced at the time this dissertation was written. The closest power density tested with two-phase C_4F_{10} refrigerant is 0.10 W cm^{-2} , with satisfactory cooling performances (see Fig. 5.26). It is expected that two-phase cooling will perform well at lower power densities too, though it is strongly recommended to verify it experimentally.

5.3.4 Two-phase heat transfer coefficient

Although studying the flow boiling heat transfer coefficient is not a primary target of the stave cooling tests described in this chapter, it could deliver some understanding of the two-phase heat transfer characteristics in channels not normally used in research or industrial cooling, and that are radically different from metallic tubing. Polyimide channels are smoother, display low thermal conductivity and small wall thickness. Thus, the flow boiling heat transfer coefficient determination was attempted using the methodology summarised in subsection 4.3.5, particularly in Eqs. 4.21. and 4.22.

The scatter plot in Fig. 5.33a displays the measured two-phase mean heat transfer coefficient in the IB2 Inner Barrel stave with C_4F_{10} as coolant versus the values predicted by the correlation by Liu and Winterton [121] (see section A.2.3). The heat transfer coefficient calculated with the referred experimental method fails to approach the trends displayed by the values predicted by the correlation.

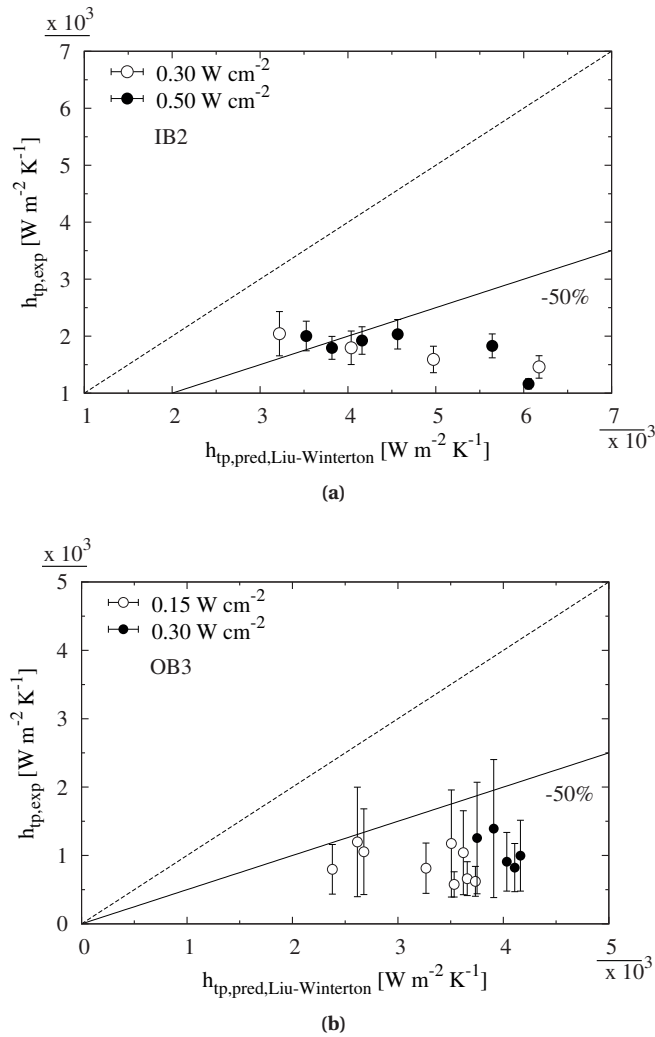


Figure 5.33: Experimental two-phase heat transfer coefficients compared to the predicted values by the correlation of Liu and Winterton [121] for the Inner Barrel IB2 stave (a); and the Outer Barrel OB3 half-stave (b), with C_4F_{10} as the evaporative coolant.

Here, the heat transfer coefficient increases with mass flux, regardless of the low vapour quality values recorded in the experimental tests. The same comparison is performed for the OB3 half-stave from the Outer Barrel, with a channel of 2.667 mm ID, in Fig. 5.33b, and the results display the same trend.

It was not possible to characterise the flow boiling heat transfer in the polyimide tubes at CERN, as the instrumentation used is too inaccurate. This motivated the development of a dedicated test section at the Heat Transfer research Group (HTRG) at the School of Engineering of São Carlos (University of São Paulo, Brazil) to experimentally measure the flow boiling heat transfer coefficient of a refrigerant inside a 2.689 mm ID polyimide tube. The extended research visit to carry out the experimental work was financed by the Swiss National Foundation for Science (SNSF) through a Doctoral Mobility fellowship (project number 155264). The results from this study are described in chapter 6.

5.4 Two-phase coolant inventory experimental studies

5.4.1 Introduction

In chapter 2, it was stated that the cross-sectional void fraction in two-phase flows is a key parameter for estimating the material budget of an evaporative coolant flow in a two-phase cooling system of a HEP particle detector (see subsection 2.5.4). In subsections 5.2.3 and 5.3.3, two-phase cooling with C_4F_{10} refrigerant was presented as a low material budget alternative for the cooling of the Inner and Outer Barrel staves of the ALICE ITS Upgrade detector at CERN. The material budget of the staves was compared with water and with the evaporative coolant. For the last, it was necessary to calculate the two-phase flow void fraction, which was determined using the void fraction correlation by Steiner [84], based on the Rouhani-Axelsson drift flux void fraction map [83], for a set of generic two-phase flow parameters. However, the validity of this correlation in the experimental cooling conditions was not verified. At the same time, neither the experimental facilities nor the staves are appropriate to experimentally measure two-phase void fractions.

An alternative way to experimentally validate the use of this or other void fraction prediction methods in the literature for estimating the material budget of the staves tested with the evaporative coolant consists in measuring the two-phase coolant inventory. This can be achieved in the OB3 half-stave by using a scale and a methodology to eliminate the potential stresses on the half-stave by the tubing connecting it to the two-phase loop. This section is devoted to the description of the experimental methodology and the comparison of the experimental coolant inventory results with the predictions obtained using a selection of void fraction methods.

5.4.2 Test facility

The experimental setup is the same as the one used for the two-phase C_4F_{10} cooling tests, depicted in Fig. 4.4. The Outer Barrel OB3 half-stave is the test section used in the coolant inventory tests. Its characteristics are summarised in Table 5.8. With a weight of 22 g and 2.667 mm ID channels, this half-stave operates with the highest two-phase coolant inventory of all tested prototypes.

The experimental tests consist in positioning the OB3 half-stave prototype on a high-precision scale and then connecting it to the two-phase loop by means of flexible, soft tubing. The goal is to ensure the whole prototype's weight is supported by the scale and not by the connection tubing, which should be under minimal or no stress. The connection tubes used are made of polyurethane, and display a 2.5 mm ID and a 4 mm OD. Their flexural modulus is very low, and were cut to a short length so the pressure and temperature sensors are close to the half-stave inlet and outlet, but long enough so they remain flexible and transmit minimal stresses on the prototype. A good compromise was found for a length of 100 mm for each of the tube sections. A rigid, slender support made of aluminium is placed atop the scale and it is used to hold the half-stave and keep it horizontal, without flexing due to

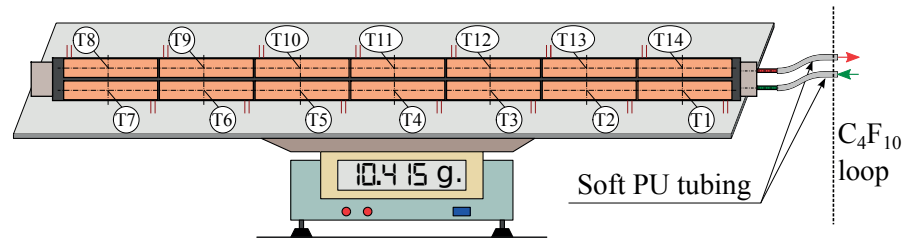


Figure 5.34: Schematic view of the two-phase coolant inventory experimental setup. The two-phase C_4F_{10} loop is depicted in Fig. 4.4.

its own weight and length (1.5 m). An schematic representation of this configuration is depicted in Fig. 5.34.

An Ohaus Explorer EX10202 Class I high-precision scale is used in the tests. This instrument has a resolution of 0.01 g, a linearity of measurements of ± 0.02 g, and a repeatability^a of 0.01 g. The scale is connected to the data acquisition system and synchronised with the rest of the instrumentation, enabling to measure the coolant inventory simultaneously to the two-phase cooling tests. The scale was configured to take weight measurements every second and save them to a data file. Measurements taken under unstable or unsteady conditions are automatically pinpointed; this feature allowed selection of the data taken in stable conditions during the data post-processing, after verifying stable two-phase flow measurements were recorded simultaneously. For each experimental point, the setup was left to reach steady-state conditions for more than 20 minutes, and measurements were taken for at least 10 minutes. Afterwards, the weight measurements were examined to exclude large fluctuations or oscillations. In practice, the weight of the empty, connected section is first measured, then the experimental process proceeds as described later in subsection 5.4.5.

The uncertainty of the weight measurements are calculated using Eqs. 4.23 and 4.24, assuming ± 0.02 g as the type B error of the scale. The median experimental coolant inventory expanded uncertainty of the whole test results array is ± 0.08 g. Individual uncertainty values for each case depend on the flow stability conditions.

This setup is different to others specifically developed for measuring the inventory of a two-phase coolant, described in experimental studies in the literature. These typically involve expensive and delicate equipment, such as quick-closing valves [88, 89], as they typically aim for determining the charge in an specific component of a two-phase loop, like the evaporator. The present facility provides a fast, simple way of directly measuring the coolant charge at the same time two-phase cooling tests are performed.

^a This parameter can be understood as a measure of precision, or standard deviation of a series of measurements in steady-state conditions.

5.4.3 Sensitivity study

An analytical study on the expected absolute two-phase coolant charge and its sensitivity depending on the variations of the main two-phase parameters was performed. The following assumptions were made:

- A linear variation of the vapour quality with the channel length (z) was assumed, since uniform heat fluxes are applied to the stave. In the inlet/outlet connector and the Π -bend it is considered constant, with the same value as upstream each specific element.
- The predicted two-phase coolant charge ($M_{tp,C_4F_{10},pred}$) is calculated according to the following integral:

$$M_{tp,C_4F_{10},pred} = \int_0^{L_{total}} [\varepsilon \rho_v + (1 - \varepsilon) \rho_l] A_i dz \quad (5.1)$$

where L_{total} is the total length of the channel, A_i is the channel internal cross-section, and ε the cross-sectional void fraction, which varies along the longitudinal coordinate along the channel.

- The cross-sectional void fraction in this sensitivity study is calculated using Steiner's version [84] of the Rouhani-Axelsson void fraction method [83].

The two-phase coolant inventory was calculated considering the OB3 half-stave. The channel consists of two 2.667 mm ID, 1504 mm long polyimide tubes, plus the inlet/outlet connector and the Π -bend, both depicted in Fig. 5.35. The evaporative refrigerant is C_4F_{10} at 20°C. Table 5.12 summarises four cases initially considered.

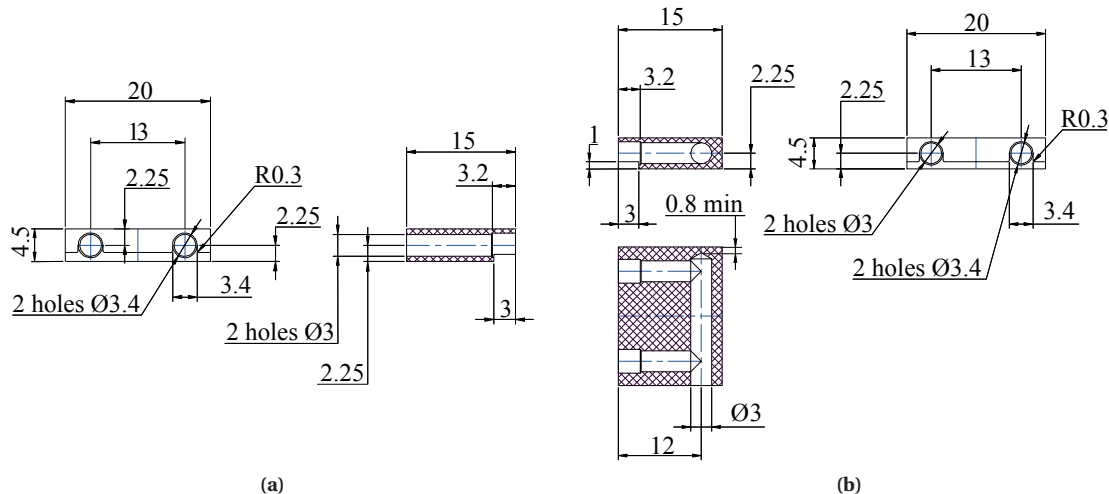


Figure 5.35: Technical drawings of the OB3 half-stave inlet/outlet connector (a); and the Π -bend connecting the two polyimide channels (b). A plug is installed in the Π -bend piece to close the lateral hole. Dimensions in mm. Drawings provided by the ITS Upgrade Mechanics and Cooling working package.

Table 5.12: Four study cases with the predicted two-phase C₄F₁₀ coolant inventory for the OB3 half-stave.

Case	x_{in} [-]	x_{out} [-]	E [W]	$G_{C_4F_{10}}$ [kg m ⁻² s ⁻¹]	$M_{tp,C_4F_{10},pred}$ [g]
A	0.2	0.7	67.6	271	2.775
B	0.1	0.6	67.6	271	3.543
C	0.1	0.5	67.6	338	3.792
D	0.1	0.5	45.1	225	3.982

Case A is based upon the nominal conditions defined for the OB3 half-stave (see case 2 in Table 5.11) for a power density of 0.15 W cm⁻². By defining the inlet and outlet vapour qualities, the mass flux is determined. The coolant inventory in the OB3 half-stave in these conditions, calculated according to Eq. 5.1, is expected to be 2.775 g. Case B envisages a shift of the inlet vapour quality towards a lower value, 0.1. This results in a coolant inventory of 3.543 g, more than 20% higher. If then the two-phase mass flux is increased to 338 kg m⁻² s⁻¹, the coolant inventory increases almost by 7%, to 3.792 g. Finally, if keeping the same conditions of case C, the power density decreases to 0.10 W cm⁻², the heat load is 45.1 W and the required mass flux is 225 kg m⁻² s⁻¹. This results in a decrease of the void fraction and an overall increase of the coolant inventory of 5%. Thus, determining experimentally the different coolant inventory in these conditions is feasible with the available instrumentation, as the scale provides accurate measurements in the ± 0.08 g range.

On the other hand, the most sensitive parameter is the inlet vapour quality, as the void fraction experiences the greatest variations at low vapour qualities (see Fig. 2.12 for $e=0$). Table 5.13 proposes a series of scenarios starting from the case A reported above where the inlet and outlet vapour qualities change by ± 0.04, a variation that can be measured in the two-phase experimental facilities. The predicted coolant inventories are reported, as well as the difference between each case and case A, on the last column.

As expected, changes of the inlet vapour qualities yield the biggest inventory differences, reaching at least ± 0.16 g for a x_{in} (or x_4 in Fig. 4.4) varying within ± 0.04. Cases A3 and A4 involve the same

Table 5.13: Influence of the inlet and outlet vapour quality variations on the predicted two-phase C₄F₁₀ coolant inventory, for the OB3 half-stave at 0.15 W cm⁻².

Case	x_{in} [-]	x_{out} [-]	$G_{C_4F_{10}}$ [kg m ⁻² s ⁻¹]	$M_{tp,C_4F_{10},pred}$ [g]	$\Delta M_{Case\ i - Case\ A}$ [g]
A	0.2	0.7	271	2.775	-
A1	0.175	0.7	251	2.959	0.184
A2	0.225	0.7	295	2.616	-0.159
A3	0.2	0.675	295	2.853	0.078
A4	0.2	0.725	251	2.698	-0.077

vapour quality change but at the half-stave outlet (x_{out} , or x_5). The impact this has on the two-phase coolant inventory is smaller, with the differences with base case A barely reaching ± 0.08 g.

Accounting for an expanded uncertainty of the coolant inventory measurements of ± 0.08 g, differences in the two-phase coolant inventory due to vapour quality variations as low as ± 0.04 can be captured. Thus, the experimental setup is considered appropriate for the measurements.

5.4.4 Experimental methodology

This section focuses on the methodology followed to obtain two-phase coolant inventory measurements independently from stresses potentially exerted by the connection piping on the prototype. The experimental procedure consists of the following steps:

1. Place the half-stave, dry and clean from any previous coolant, on top of the support on the scale on a stable position, connecting it to the two-phase loop via the soft polyurethane tubing. Then, the cooling lines are set under vacuum, and the weight is measured (M_{empty}).
2. Circulate single-phase C_4F_{10} in the OB3 half-stave, measuring the weight of the whole assembly ($M_{OB3,sp}$). Since the total volume of the channels, the inlet/outlet connector and the Π -bend is known, the inventory of the liquid C_4F_{10} refrigerant can be calculated as follows:

$$M_{sp,C_4F_{10},pred} = \rho_{l,C_4F_{10}} V_{channels} \quad (5.2)$$

3. The apparent weight due to the stress exerted by the connection tubing is quantified as follows:

$$M_{stress,tubing} = M_{OB3,sp} - M_{empty} - M_{sp,C_4F_{10},pred} \quad (5.3)$$

where $M_{OB3,sp}$ is the weight measurement of the OB3 half-stave full of liquid C_4F_{10} refrigerant.

4. $M_{stress,tubing}$ is evaluated. If it is too high, the procedure must be repeated for another configuration of the connection tubing exerting lower stresses on the stave.

The methodology assumes that the polyurethane connection tubing exerts similar stresses to the half-stave in single-phase and two-phase flow conditions. This assumption is conservative, since in general, ~ 28.5 g of liquid C_4F_{10} are measured in the half-stave and the connection tubes, while 4 to 10 g are expected in two-phase conditions, and the tubing is placed so the stresses are downwards. Thus, if stresses are small in single-phase, it is safe to assume no extra stress will be exerted by the plastic tubing when circulating a boiling C_4F_{10} flow.

Once the stresses due to the connection tubes can be considered as negligible, two-phase flow cooling tests may be performed. The two-phase coolant inventory is then determined as follows:

$$M_{tp,C_4F_{10},exp} = M_{measured} - M_{empty} \quad (5.4)$$

The experimental coolant inventory values are finally compared to the results obtained by integrating void fractions from methods in the literature along the half-stave cooling channel length (see Eq. 5.1).

Experimental validation

Prior to each two-phase coolant inventory test session, the scale was set to self-calibrate and particularly, the stresses due to the connecting tubing were quantified using the methodology described above with single-phase C_4F_{10} refrigerant. This is a way of validating the experimental setup, obtaining the weight of the empty, connected half-stave (M_{empty}) to be used later in the two-phase coolant inventory tests, and assess the global uncertainty of the coolant inventory measurements.

Fig. 5.36 displays the expected weight of the liquid C_4F_{10} inside the OB3 half-stave, computed with Eq. 5.2, compared to the measured weight of the OB3 half-stave with single-phase liquid C_4F_{10} inside the channels once no stresses by the connection tubing are observed. This is calculated as follows:

$$M_{sp,C_4F_{10},exp} = M_{OB3,sp} - M_{empty} \quad (5.5)$$

Good agreement was found in all the test campaigns. The maximum deviation between the

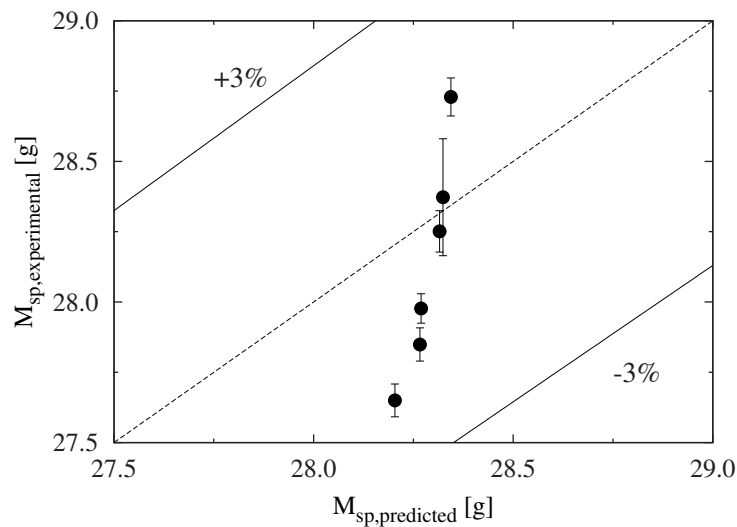


Figure 5.36: Measured single-phase, adiabatic coolant inventories versus predicted values using the C_4F_{10} liquid density and the total channel volume (see Eq. 5.2).

predicted and the measured liquid inventories is 0.8 g, which represents less than 3% of the weight of the liquid inside the half-stave. In order to safely interpret the results, this value is hereafter considered as the global two-phase coolant inventory uncertainty.

5.4.5 Void fraction methods

Six void fraction prediction methods from the literature, described in section 2.5.4, were considered for comparing the integrated two-phase refrigerant charge they yield with the experimental results obtained in this study. Their implementation equations are detailed in appendix A, section A.3. This selection of models provides a view on the different types of existing methods to estimate the sectional two-phase void fraction in the channels of the ITS Upgrade Outer Barrel staves:

- Homogeneous method: used as reference, although it tends to overestimate the void fraction and thus yields low coolant inventories. Its results may be used to establish a minimum inventory limit.
- The analytical void fraction model by Zivi [81], with and without inclusion of liquid entrainment. If included, the value of the entrained liquid fraction (e) is calculated by the method by Cioncolini and Thome [87]. However, this effect does not yield great differences in the integrated coolant inventory.
- The empirical void fraction method for annular flow in vertical channels by Rouhani and Axelsson [83], later adapted for horizontal channels by Steiner [84].
- The void fraction correlation for microchannels by Niño *et. al* [85].
- The model by Cioncolini and Thome [86] for conventional and small channels.
- A modification of the method of Zivi by Kanizawa and Ribatski [82].

The void fraction is calculated with each of the methods and integrated along the cooling channels using Eq. 5.1 in order to obtain the two-phase coolant inventory. The vapour quality is assumed to increase linearly along the channel, since the heat load is applied uniformly on the half-stave plate and thus constant heat flux conditions can be assumed.

By comparing the coolant charge results of the models with the experimental values, the method delivering the best void fraction predictions can be then used for calculating the material budget of the two-phase coolant.

5.4.6 Results

Each of the plots in Fig. 5.37 displays the comparison of the two-phase coolant charge values obtained by integrating each of the void fractions calculated following the methods described above, and the

experimentally measured coolant inventories. According to Fig. 5.37a, coolant charge values obtained by integrating the homogeneous two-phase void fraction model result in the highest deviation from the experimental measurements. It is well known that assuming an homogeneous two-phase flow typically results in overestimated void fractions compared to separated flows models. The rest of the methods provide better match with the experimental results. In particular, the void fraction methods by Niño *et al.* (Fig. 5.37d), Zivi with liquid entrainment (Fig. 5.37b), Steiner (Fig. 5.37c), and Kanizawa and Ribatski (Fig. 5.37f), in that order, show the lowest dispersion with the experimental values, typically underestimating the refrigerant charge.

Generally speaking, the methods fail to predict the coolant inventory at low vapour qualities. For instance, the results with the methodology by Niño *et al.* are well grouped within the $\pm 20\%$ error band, but some high coolant charge points are underestimated. A similar trend was observed for predictions by Cioncolini and Thome, which as well failed predicting the coolant inventories at medium to high vapour qualities. The method by Zivi, contrary to that of Niño *et al.*, overestimates the coolant inventory at low vapour qualities, with and without liquid entrainment (not shown in Fig. 5.37, as it provides nearly the same results as its version with liquid entrainment). The methods by Steiner and by Kanizawa and Ribatski exhibit a similar behaviour, as expected for the last, since it is based on the method by Zivi.

Fig. 5.38 reports how good is the match of the selected prediction methods with experimental data in the whole mean vapour quality range. All the predictions shown in the plot reproduce the refrigerant charge trend with vapour quality, displaying an offset from the experimental values. Overestimation of the refrigerant charge by the four considered methods occurs mostly at mean vapour qualities over 0.3. One reason that might explain this behaviour is that at high vapour qualities, the measured refrigerant charge is low, better exposing possible setup uncertainties and measurement errors.

Fig. 5.39 displays the absolute and relative differences between experimental and theoretical coolant charges, versus mean vapour qualities. Mean relative errors (*mre*) are calculated with Eq. 5.6. The methods predict the coolant charge within a $\pm 30\%$ error band at vapour qualities above 0.2.

Finally, Table 5.14 reports the statistical parameters resulting from comparing the two-phase coolant inventories calculated by integrating the void fraction models considered in this study, and the values measured experimentally. The fraction of results predicted within the $\pm 30\%$ and $\pm 20\%$ error range ($\varphi_{30\%}$ and $\varphi_{20\%}$, respectively) are reported, along with the mean relative errors (*mre*) and the mean absolute errors (*mae*), defined as follows:

$$mre = \frac{1}{n} \sum_{i=1}^n \frac{M_{pred} - M_{exp}}{M_{exp}} \quad (5.6)$$

$$mae = \frac{1}{n} \sum_{i=1}^n \left| \frac{M_{pred} - M_{exp}}{M_{exp}} \right| \quad (5.7)$$

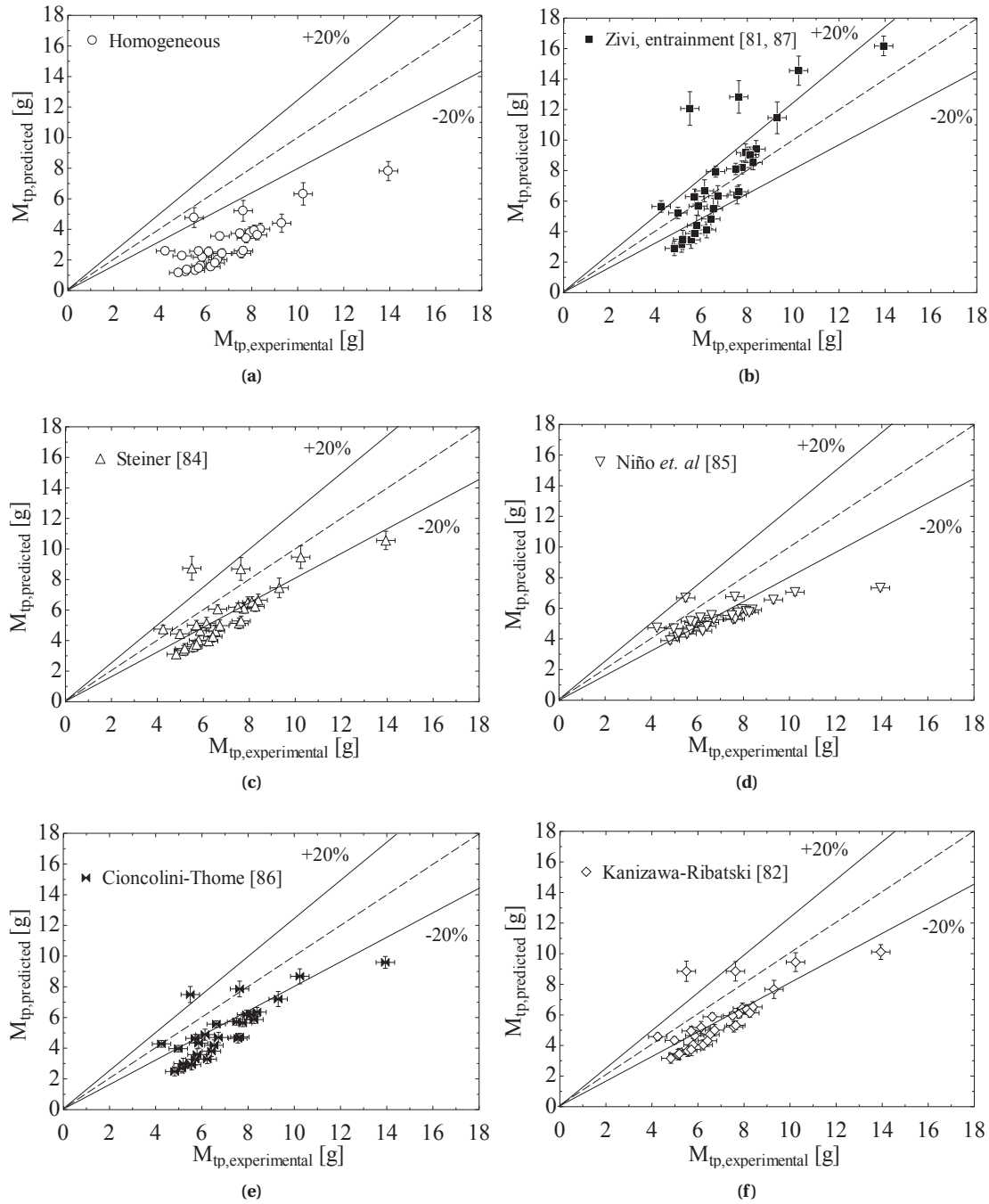


Figure 5.37: Measured two-phase coolant inventories versus predicted values from integrating the following void fraction methods from the literature along the cooling channels: (a) Homogeneous; (b) Zivi [81], with the liquid entrainment fraction calculated according to Cioncolini and Thome [87]; (c) Steiner's version [84] of the method by Rouhani and Axelsson [83]; (d) Niño *et. al* [85]; (e) Cioncolini and Thome [86]; (f) Kanizawa and Ribatski [82].

In view of the statistical parameters of the comparison between prediction methods and experimental measurements, it can be concluded that integrating the void fractions obtained by the method

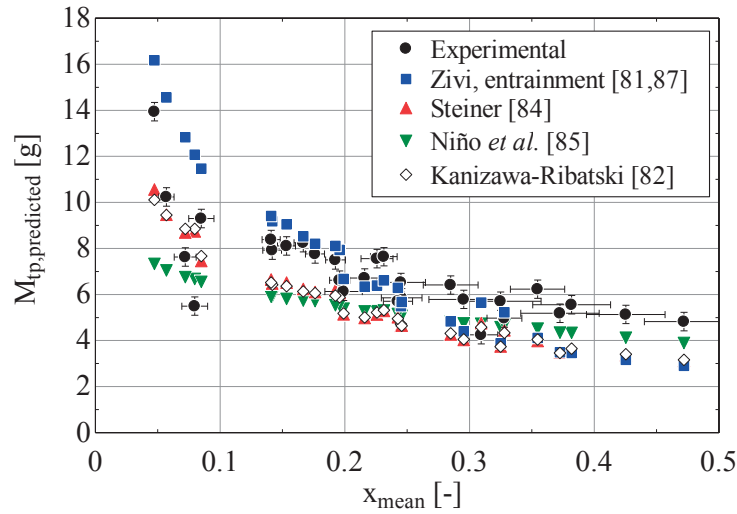


Figure 5.38: Experimental and predicted values of the two-phase C_4F_{10} charge versus the mean vapour quality.

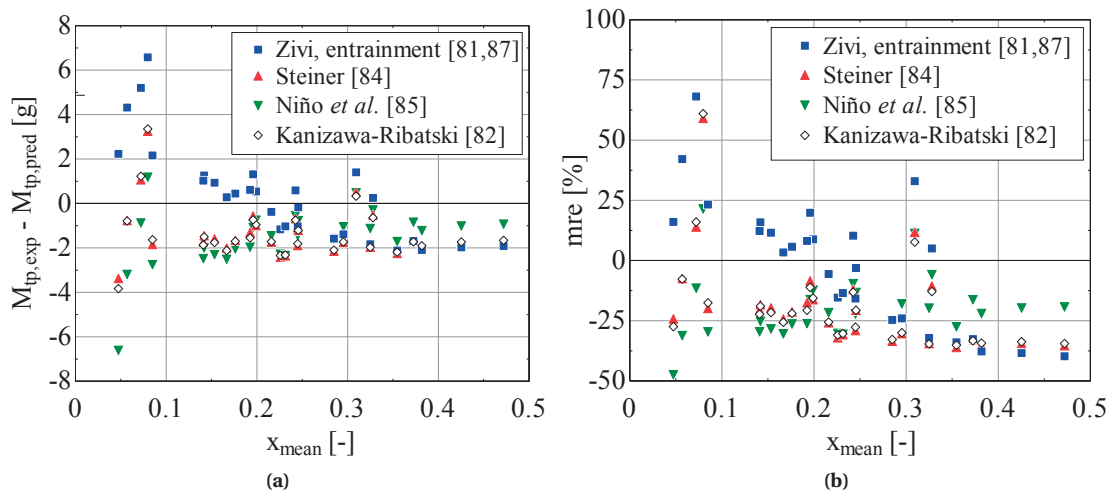


Figure 5.39: Deviation of the theoretical refrigerant charge values from the experimental measurements for the mean vapour quality range; (a) absolute difference [g]; (b) relative difference [%] (see Eq. 5.6).

Table 5.14: Statistical deviation parameters from the comparison of the charge predictions and the experimental values.

Method	$\varphi_{30\%}$ [%]	$\varphi_{20\%}$ [%]	mre [%]	mae [%]
Homogeneous	3	3	-58	58
Zivi [81]	66	52	5	26
Zivi, with liquid entrainment [81, 87]	66	55	3	25
Steiner [84]	62	38	-19	25
Niño <i>et al.</i> [85]	83	41	-20	22
Cioncolini and Thome [86]	52	17	-27	30
Kanizawa and Ribatski [82]	66	31	-19	25

by Niño *et al.* yields the overall most accurate two-phase coolant inventories, since it predicts 80% of the experimental measurements within the $\pm 30\%$ error band and displays the lowest mean absolute error (*mae*). The method by Zivi, with and without considering liquid entrainment in the vapour phase, yields good results too, within 55% of the experimental data predicted with an error band of $\pm 20\%$. The methods by Steiner and by Kanizawa and Ribatski give the worst but still reasonable predictions. The method by Cioncolini and Thome provides acceptable agreement at low vapour qualities. Lastly, considering two-phase homogeneous void fractions is very far from reality, and predictions strongly underestimate the coolant inventories.

5.4.7 Concluding remarks

In the whole mean vapour quality range, integrating the correlation by Niño *et al.*, although conceived for two-phase flows in multi-microchannels, yields the most accurate two-phase coolant inventory predictions, closely followed by the methods by Zivi, and Steiner's version of the method Rouhani and Axelsson.

Last, it should be emphasised this study is made for a wide range of vapour qualities, mass fluxes and heat fluxes. If needed, a more thorough analysis can be done by identifying which methods predict best a specific fraction of the experimental results. This way, the two-phase coolant inventory calculation method can be tailored to provide accurate predictions for a set of nominal cooling conditions in real-time, during the operation of the ITS Upgrade detector.

5.5 Conclusions and recommendations

In this chapter, cooling performance results were reported and discussed for three Inner Barrel staves and three Outer Barrel half staves with water and two-phase C_4F_{10} refrigerant as coolants. The following conclusions were reached:

- The Inner and Outer Barrel staves surpass the ITS Upgrade cooling requirements either using water or flow boiling C_4F_{10} refrigerant. The only adjustment to be done for using the two-phase refrigerant concerns the need of larger channels at the Outer Barrel (2.667 mm ID), but no other changes must be done to the stave architecture. A fair reduction on the material budget may be achieved relative to water cooling, especially at the Inner Barrel staves, in exchange for a more complex cooling system at the detector integration level.
- Since the cooling performance displays low sensitivity to the type of coolant or flow rate, it can be deduced that the main thermal resistance dominating is by conduction in the stave, and not of convection between the channel wall and the coolant. This results in thermally robust staves.
- The IB1 stave and OB1 half-stave provided the best compromise between cooling performance with the two refrigerants, material budget, mechanical properties and easiness of fabrication. The OB2 half-stave represents an alternative if no thermal expansion properties are required.
- Choosing appropriate nominal cooling conditions is critical, especially with two-phase coolants. The best cases were indicated for each stave prototype and coolant.
- Pressure drops at the Π -bend, making up for 25-30% of the pressure drop in the Inner Barrel staves, and 15-20% at the Outer Barrel half-staves, may be minimised if using U-bends with smooth corners, ideally semi-circular [146]. 3D-printing technologies allow for the manufacturing of the pieces in one step, without any glued or bonded interfaces. A mock-up U-bend was manufactured and tested, but the polymer was not completely leak-tight, although there are currently capabilities of printing in non-permeable polymers. This solution is considered if the mechanical tolerances can be met and if the polymers to be used comply with CERN regulations.
- Experimental coolant inventory measurements were performed online in the existing two-phase cooling facility using a precision scale. The void fraction method in the literature that provides the best two-phase coolant inventory predictions after integrating it along the cooling channel length is the one by Niño *et al.* [85], followed by the methods by Zivi [81] and the version by Steiner [84] of the drift flux void fraction method by Rouhani and Axelsson [83].
- Two-phase experimental points might be grouped depending on cooling performance, mass flux, vapour quality or heat flux, and their coolant inventories compared separately to the methods in the literature, with the aim of identifying ranges of applicability of each method. This would help creating an accurate array of two-phase cooling conditions yielding minimal coolant inventories and, subsequently, minimal local material budget.

Chapter 6

Experimental flow boiling heat transfer in a small polyimide channel

6.1 Introduction

Chapter 3 focused on the cooling system proposed for the Upgrade of the ALICE ITS detector, to be commissioned at CERN in 2019. The system includes lightweight circular cooling channels made of polyimide with the aim of minimising the material budget within the detector sensitive area, essential for preserving detector resolution [5]. In this line, an evaporative coolant circulating inside the polyimide channels is one of the potential solutions for cooling the detector, as the vapour fraction would minimise the material budget, compared to a liquid cooling system [133]. As reported in chapter 5, all the detector modules, named *staves*, can be cooled with water or two-phase C_4F_{10} refrigerant, although experimentally determining the two-phase heat transfer coefficient was not possible using those cooling test sections (see section 5.3.4).

The characteristics of polyimide channels were described in section 2.4.4. As reported in section 2.5.6, a literature survey revealed a lack of experimental data in the literature regarding flow boiling in polyimide channels. First, these channels are smoother than metallic channels used in industrial heat transfer applications. Fiorenza *et al.* [25] measured the statistical average roughness of the surfaces in a polyimide heat sink using Atomic Force Microscopy (AFM), obtaining values ranging from 12 to 35 nm. Smooth metallic channels are rougher, with values on the order of 100-400 nm [103]. Wall roughness has been often reported to have an effect on the flow boiling heat transfer coefficient (h). For instance, the three-zone model by Dupont, Thome and Jacobi [157] uses the measured surface roughness to

set the dryout thickness and hence the onset and size of the dry zone with a substantial influence on its three-zone-averaged heat transfer coefficient. Furthermore, Karayiannis *et al.* [108] performed experimental studies on smooth and coarse mini-tubes, concluding that the heat transfer coefficients increased with heat flux for the coarse tube, while for the smooth tube the heat flux does not seem to have an influence. Smooth tubes would have fewer nucleation points and therefore convective boiling would dominate over a wider vapor quality spectrum. Also, most heat transfer coefficient prediction methods in the literature are based upon extensive experimental databases that typically do not include tests with plastic channels. In particular, the polyimide channels of interest in this thesis feature small inner diameters, ranging from 1.024 to 2.667 mm ID, which, according to the classification presented in section 2.5.2, would fall in the mini- and macrochannel categories. They also present very thin wall thicknesses (e.g. 64 μm for the 2.667 mm ID polyimide channel in the ITS Upgrade Middle and Outer Barrel half-staves) and low thermal conductivity ($0.12 \text{ W m}^{-1} \text{ K}^{-1}$ for pure polyimide).

This chapter presents new experimental flow boiling results in a 2.689 mm ID water-heated polyimide channel with 285 mm of heated length, R245fa refrigerant as the evaporating fluid, at mass fluxes ranging from 100 to 500 $\text{kg m}^{-2} \text{ s}^{-1}$, heat fluxes from 15 to 55 kW m^{-2} and at three saturation temperatures, 35, 41 and 47°C. The goals of this study are to provide insight into the ALICE ITS Upgrade two-phase cooling proposal, to expand the experimental flow boiling heat transfer database to another tube material and characteristics, and to understand the influence of the key flow parameters (saturation temperature, mass flux and heat flux) on the mean flow boiling heat transfer coefficient. Two-phase pressure drops and wall thermal resistance measurements are also evaluated. This experimental work was carried out at the Heat Transfer Research Group (HTRG) lab at the Escola de Engenharia de São Carlos, University of São Paulo (EESC-USP), Brazil, under the on-site supervision of Prof. G. Ribatski, and with the support of the Swiss National Science Foundation (SNSF) through a Doctoral Mobility fellowship (project number 155264). The research carried out during the visit at the HTRG lab involved: the design and construction of a new dedicated test section to measure average heat transfer coefficients in a polyimide minichannel, its characterisation via validation tests, the calibration of the instrumentation, the execution of the experimental flow boiling tests, and the interpretation of the results and their comparison against leading heat transfer coefficient methods in the literature and similar experimental data by other authors.

R245fa refrigerant was used instead of C_4F_{10} in this study for three reasons: it was readily available at the HTRG lab at the EESC-USP, it is a widely used refrigerant in industry and research, and it is thermodynamically a similar fluid to C_4F_{10} . The boiling points of R245fa and C_4F_{10} at atmospheric pressure are 15.14°C and -2.09°C, respectively, but the rest of thermophysical properties are similar, as reported in Table 6.1. The greatest difference occurs for the vapour specific volume, which is greater for R245fa. This means that the vapour phase has a greater velocity compared to the liquid phase than for C_4F_{10} , motivating a more uniform liquid film in the tube wall perimeter (under stable boiling conditions) and lower variations of the heat transfer coefficients in the channel section. A

Table 6.1: Thermophysical properties of C₄F₁₀ and R245fa refrigerants at saturation temperatures of 15°C and 41°C.

T_{sat} [°C]	Property	R245fa		C ₄ F ₁₀	
		Liquid	Vapour	Liquid	Vapour
15	p_{sat} [kPa]	100.8		192.0	
	ρ [kg m ⁻³]	1365.3	5.9	1533.6	20.9
	ν [m ³ kg ⁻¹]	0.00073	0.169	0.00065	0.048
	μ [μ Pa s]	464.3	9.9	246.2	11.9
	c_p [J kg ⁻¹ K ⁻¹]	1301.5	918.5	1062.6	825.5
	α [W m ⁻¹ K ⁻¹]	0.091	0.012	0.459	0.013
41	p_{sat} [kPa]	258.8		435.6	
	ρ [kg m ⁻³]	1293.8	14.6	1433.0	46.8
	ν [m ³ kg ⁻¹]	0.00077	0.069	0.00070	0.021
	μ [μ Pa s]	333.8	10.8	178.6	13.0
	c_p [J kg ⁻¹ K ⁻¹]	1359.6	1015.4	1124.3	905.9
	α [W m ⁻¹ K ⁻¹]	0.083	0.014	0.042	0.015

consequence of the higher velocity of the vapour phase is the earlier suppression of nucleate boiling, with intensification of convective boiling effects. The higher liquid viscosity of R245fa results in thicker liquid films. However, since R245fa shows a higher liquid thermal conductivity than C₄F₁₀, it is not clear whether the thermal resistance across the liquid film is higher for R245fa. Last, the differences between thermophysical properties of the two fluids become smaller as the saturation temperature increases. Further data on the properties of the two saturated fluids at different temperatures can be found in appendix C.

6.2 Experimental apparatus

6.2.1 Test rig

A new experimental test rig, depicted in Fig. 6.1, was designed and built at the HTRG lab at EESC-USP and was installed in an already existing experimental facility described later in subsection 6.2.2. The test rig is conceived to fulfil the following requirements:

1. Have the boiling R245fa refrigerant reaching the polyimide channel inlet in the desired range of saturated conditions.
2. Monitor all the necessary parameters in order to obtain the mean heat transfer coefficient along the polyimide channel with minimal uncertainty.
3. Visualise the flow pattern at the outlet of the polyimide channel.

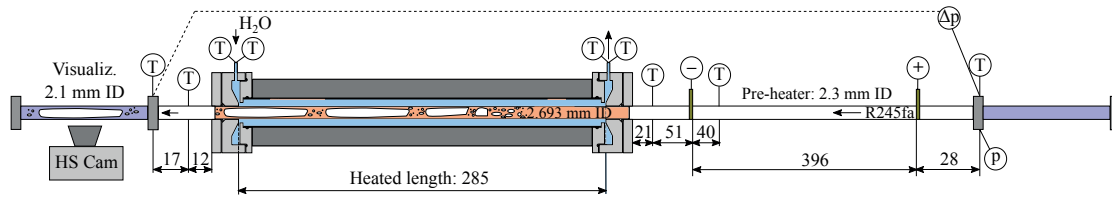


Figure 6.1: Schematic view of the test rig (not scaled). Dimensions expressed in mm. Flow is from right to left.

The elements of the test rig are described taking as a reference the path of the refrigerant, from right to left in Fig. 6.1. First, after being pumped, the liquid R245fa refrigerant mass flow rate is measured in a Coriolis-effect flow meter (see Fig. 6.6a). The fluid is then subcooled using a secondary glycol/water loop. The subcooled liquid R245fa refrigerant enters the first visualisation section, a 2.1 mm ID quartz tube. Afterwards, a thermocouple immersed in the flow at the flange and a 0-400 kPa pressure transducer provide temperature and absolute pressure experimental readings through which the enthalpy of the liquid is determined. The fluid is then heated at the pre-heater to the desired saturated condition at the polyimide channel entrance. A thermocouple placed at the stainless steel tube outer surface 51 mm away from the pre-heater's second electrode tracks the saturation temperature right before the entrance to the polyimide channel. The two-phase refrigerant enters the polyimide channel and is heated up by a counter-current water flow rate circulating in the annular gap between the channel and a larger glass tube in a concentric heat exchanger fashion.

Downstream of the polyimide channel, the refrigerant temperature is obtained with a thermocouple placed inside a hole in the insulated brass outlet flange, reaching 0.8 mm away from the internal wall. The refrigerant temperature is then again monitored using a thermocouple immersed in the flow, in the same way as in the test rig inlet. The differential pressure with respect to the inlet of the pre-heater is recorded too thanks to a 0-300 kPa differential pressure transducer. Finally, a second visualisation section made of quartz, identical to the one at the inlet of the test rig, is used to record the flow with a 4000 FPS high-speed camera, before the refrigerant leaves the test rig on its way to the condenser and back to the pressurised tank. By heating or cooling this vessel using a secondary water-glycol loop, the operating pressure of the system can be adjusted.

All temperatures are measured using 0.25 mm type K thermocouples. When measuring wall temperatures, the thermocouples are attached tightly to the surface with plastic tape. Thermal paste is applied at the wall-thermocouple contact surface to ensure good thermal contact.

The data acquisition, conditioning, and the system control are performed using instrumentation from National Instruments and the LabVIEW software. In particular, the uncertainty of the temperature readings must be very low to minimise the propagated error on the heat transfer coefficient. A fine calibration and measurement stability was achieved by using two SCXI-1112 thermocouple input modules. Each of these modules have 8 differential analog input channels, each with its own cold-junction sensor, allowing for high-accuracy temperature measurements. Further information is provided in

section 6.6 and in appendix D.

A picture of the test rig is displayed in Fig. 6.2a. The following elements are displayed, from right to left: the visualisation section at the inlet, the absolute pressure transducer, the differential pressure sensor connection, the insulated pre-heater, the insulated water-heated test section, with the water rotameter located in a vertical position in front of it, the LED light for the high-speed images, and the high-speed camera lens at the left. Fig. 6.2b shows the quartz visualisation section at the outlet of the test rig. The nylon flange connecting the polyimide channel outlet and the visualisation section houses the thermocouple immerse in the refrigerant and the outlet differential pressure sensor branch. The design and features of the main test rig elements are described in the following subsections.

Pre-heater

The mission of the pre-heater is to heat and partially evaporate the subcooled R245fa refrigerant so it reaches the polyimide channel in the desired saturated conditions. The pre-heater consists of a single, round 2.3 mm ID stainless steel tube. It is 496 mm long, of which 396 mm are heated by Joule effect using two copper electrodes welded to the tube and connected to a Lambda Genesys 750W DC (20 V-40 A) power supply. This configuration allows a large array of vapour qualities of the R245fa refrigerant at the polyimide tube entrance in the $100\text{-}500\text{ kg m}^{-2}\text{ s}^{-1}$ mass flux range. The pre-heater is well insulated with mineral wool and closed-cell insulation foam, as illustrated in Fig. 6.2a.

A thermal entry region is expected for the R245fa refrigerant at the pre-heater, as described in subsection 4.2.1. The heat transfer coefficient within the thermal development region is higher than for the fully developed flow [136]. In two-phase flow boiling, the length of the thermal entry region depends on multiple parameters, like bubble growth and collapse, flow pattern, and liquid entrainment, as well as the flow condition and hydrodynamic development at the entrance of the heated region. As a result, there is no exact way of expressing the thermal entry length for two-phase flows. Such

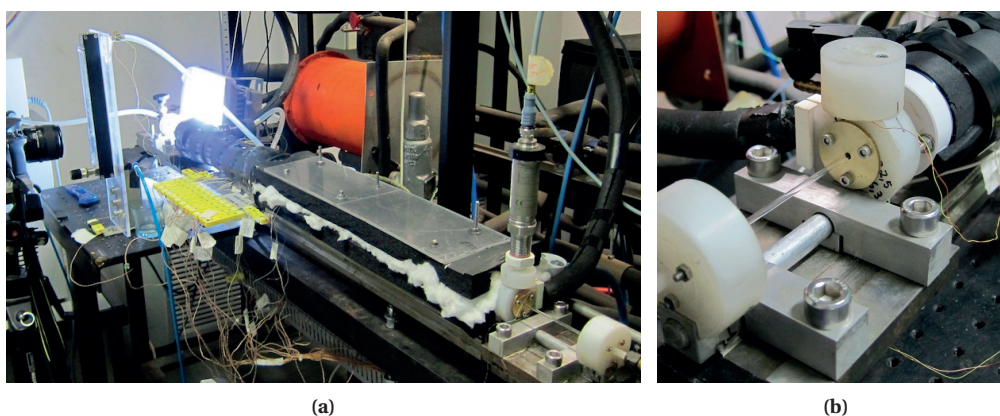


Figure 6.2: Experimental facilities: (a) a picture of the test rig assembled in the experimental facilities, (b) a detailed view of the outlet visualisation section.

calculation would probably need, additionally, from extra inputs like the flow pattern and the liquid entrainment, which are not always easy to determine accurately. Thus, the single-phase thermal entry length calculations reported below are used as a first approximation for two-phase flows.

For laminar single-phase flows at a constant, uniform heat flux in a round channel, the thermal entry length is defined as follows [136]:

$$\frac{L_{th,dev,lam}}{D_i} \approx 0.05 Re Pr \quad (6.1)$$

Single-phase turbulent flows display thermal entry lengths that are independent from the Prandtl number and similar to the hydrodynamic entry length. Thus, the thermal development length in turbulent flows in uniform heat flux conditions is defined as:

$$10 < \frac{L_{th,dev,turb}}{D_i} < 60 \quad (6.2)$$

$\frac{L_{th,dev,turb}}{D_i} < 60$ is assumed for the most conservative approach.

Fig. 6.3 displays the expected thermal entry length in the pre-heater versus the mass flux of R245fa refrigerant at 35°C. The circles represent the pre-heater R245fa mass fluxes used in the flow boiling heat transfer tests. Note that for a given mass flow rate, the mass flux in the pre-heater is higher than in the polyimide channel since the pre-heater cross section is smaller. Thermal development of the lowest mass flux occurs almost entirely in the pre-heater. However, the second lowest mass flux, corresponding to 200 kg m⁻² s⁻¹ in the polyimide channel, needs a longer length to thermally develop. The rest of the mass fluxes are in the transitional flow regime, where the thermal development length

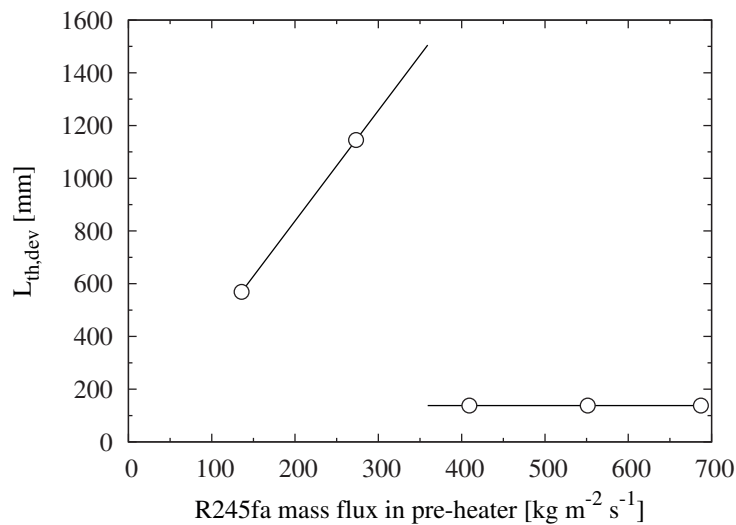


Figure 6.3: Single-phase thermal entry length for the R245fa refrigerant in the 2.3 mm ID pre-heater versus R245fa mass flux in the pre-heater. The circles show the tested mass fluxes.

is only 138 mm, and can be achieved well within the pre-heater. It should be emphasised that these calculations correspond to single-phase R245fa refrigerant, and thus serve only as an approximation in case of two-phase flows. Likewise, the changes in tubing diameter and the flow condition before the pre-heater may alter the thermal entry length predictions.

A thermocouple monitors the R245fa saturation temperature before entering the polyimide tube. This thermocouple is placed far enough from the copper electrode used to power the pre-heater, which, although it is well insulated, can act as a fin and cool down the end of the pre-heater tube. A 1-D conduction analysis was done to calculate the minimum distance from the thermocouple to the electrode that guarantees no thermal influence of the electrode, yielding 22 mm as a result. The thermocouple was positioned 51 mm away from the pre-heater's second electrode, as shown in Fig. 6.1.

Polyimide channel

The polyimide channel is the effective test section. It consists of a single, circular, 2.689 mm ID polyimide channel, 300 mm long, where 285 mm are heated. The tube wall thickness is $63\ \mu\text{m}$, resulting in a 2.816 mm OD. The channel diameters and tolerances are given by the manufacturer [66]. However, since these parameters are critical for the study, especially for the global uncertainty of the heat transfer coefficient, they were carefully verified by the author.

The polyimide tubes are manufactured by extrusion. This method guarantees a very uniform inner diameter of the tube, but the outer diameter, and subsequently the wall thickness, may vary slightly within a tube section longer than 1.5 m [158]. The manufacturer inspects the tubes after the extrusion process to verify the uniformity of the outer diameter and ensure there are no blimps or other defects on the outer surface. Although the 300 mm-long section used in this study is short enough to not experience significant variations of the outer diameter [158], two samples, one from each end of the same channel later used in the tests, were cut and their dimensions measured in a projection microscope. After considering the uncertainty of the coordinate table of the microscope, determined using a standard reference block, the dimensional tolerances of the channel are calculated from multiple measurements of the tube samples, following a similar methodology to the one indicated in appendix D, derived from [159]. Table 6.2 displays the channel dimensions as reported by the manufacturer and the values measured by the author. The last column concerns the tolerance of each dimension. Fig. 6.4a shows micropictures of one of the samples of the polyimide channel, illustrating the low thickness of the wall.

The surface roughness was not quantified in this study. Instead, the roughness values measured by Fiorenza *et al.* [25] for the polyimide microchannels cooling system initially proposed for the ITS Upgrade detector were adopted. These authors reported statistical average roughness values ranging from 12 to $35\ \mu\text{m}$ measured using Atomic Force Microscopy (AFM). The surface topology is reproduced in Fig. 6.4b. However, the optical micropictures of the tube samples displayed in Fig. 6.4a revealed the

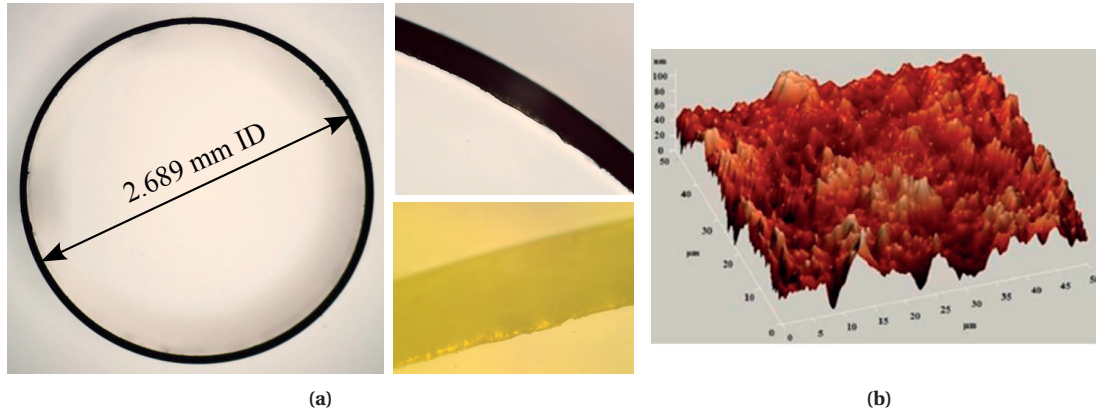


Figure 6.4: (a) Micropictures of a section of the polyimide tube used in the experimental studies; (b) reconstructed surface roughness, by Fiorenza *et al.* [25].

presence some longitudinal microgrooves at the channel inner surface. These features are possibly related to the extrusion manufacturing process of the channel, and may eventually act as potential nucleation sites for the vapour bubbles [113]. Additionally, a detailed qualitative examination of the tube surfaces, performed by the CERN EN-MME-MM group, is presented in section B.3. This study focused on the surface degradation of a polyimide tube after continuous, long-term water circulation, and included the examination of the inner surface of brand-new polyimide channels. Scanning Electron Microscopy (SEM) examination showed the sparse presence of surface defects of 3 to 5 μm in size (see Fig. B.6). Certainly, polyimide channels are smoother than stainless steel tubes in similar experimental heat transfer studies, but a more detailed roughness characterisation, accounting for the surface profile, waviness and peak size is recommended in future studies.

The test section length may have an effect on the flow boiling heat transfer, as reported in subsection 2.5.6. First, for a given heat load, shorter test sections display a higher heat flux. Because of the high wall superheating needed, nucleate boiling is intensified at higher heat fluxes. The presence of this heat transfer mechanism would be thus stronger in short test sections. Indeed, long test sections usually display heat transfer effects conventionally related to convective boiling, such as increasing heat transfer coefficients with increasing mass fluxes and vapour qualities, as reported by Karayiannis *et al.* [108]. The present 300 mm-long polyimide channel is heated in the central 285 mm, an average length compared to recent experimental flow boiling heat transfer tests [79]. The maximum heat flux

Table 6.2: Dimensions and tolerances of the polyimide channel.

Parameter	Manufacturer values [m]	Measured values [m]	Tolerance [m]
D_i	$2.667 \cdot 10^{-3}$	$2.689 \cdot 10^{-3}$	$2.50 \cdot 10^{-5}$
D_e	$2.795 \cdot 10^{-3}$	$2.816 \cdot 10^{-3}$	$5.25 \cdot 10^{-5}$
w	$6.40 \cdot 10^{-5}$	$6.33 \cdot 10^{-5}$	$1.05 \cdot 10^{-5}$

tested is 55 kW m^{-2} . Considering as well the low thermal conductivity of the tube, $0.12 \text{ W m}^{-1} \text{ K}^{-1}$ and its low wall thickness, convective boiling is initially expected to be the dominant heat transfer mechanism in the tested polyimide channel.

Another effect of the test section length regards flow patterns. In long channels, flow patterns will develop and change more along the channel than in shorter test sections. As only the mean heat transfer coefficient in the whole test section is measured in the present study, local heat transfer changes associated to changes in flow patterns will not be captured in the average heat transfer coefficient. However, in order to minimise the occurrence of changes in flow patterns in the test section, the chosen tests conditions display low vapour quality differences between the inlet and the outlet of the polyimide tube ($\Delta x_{in-out} < 0.35$).

Last, assuming a linear two-phase pressure drop in a long test section may lead to wrong heat transfer coefficient measurements [108]. This issue is considered in the present study by characterising the two-phase pressure drop in the test rig in two-phase flow adiabatic tests (see section 6.5.2).

Heating water loop

The heat flux for evaporating the R245fa refrigerant is provided by a counter-current water flow rate circulating in the annular space between the polyimide channel and a larger concentric glass tube. This configuration was chosen because plastic channels cannot be electrically heated through the Joule effect like metallic tubes.

A turbulent water flow minimises the convective thermal resistance with the polyimide tube outer wall, yielding less influence of this parameter in the mean flow boiling heat transfer coefficient. However, a high water flow rate results in a low water temperature change, an essential variable to calculate the heat flux. This derives in a high heat flux uncertainty, which ultimately propagates to the boiling heat transfer coefficient. A compromise between these two opposite effects was found through a detailed parametric analysis aimed to determine the water flow characteristics that minimise the mean heat transfer coefficient uncertainty for the whole range of flow boiling conditions. This study^a consisted on discretising the lengths of the polyimide tube and the water annular gap, and calculate the heat transfer between the water and the boiling R245fa fluid using the approach later described in section 6.3.2 (Eqs. 6.6 to 6.11). The boiling heat transfer coefficient was calculated in each discrete element using the Liu and Winterton correlation [121]. This particular correlation was chosen due to its simplicity and because the polyimide tube is similar in size to the minimum diameter in the correlation validity range. The heat transfer coefficient between the water flow and the polyimide tube is calculated using the correlations by Gnielinski for forced convection to the internal cylinder in a cylindrical annulus [160]. This analytical study was run for an array of flow boiling conditions (different mass fluxes, heat fluxes, saturation temperatures and vapour qualities at the polyimide tube

^a The methodology and results of this analytical study are not shown in depth in this dissertation for the sake of brevity.

entrance), with the condition of keeping a water Reynolds number higher than 3000 that would ensure low convective thermal resistance between the heating water and the polyimide tube outer surface. The external annulus diameter and the water flow rate and temperature were allowed to vary with the aim of achieving the minimum mean flow boiling heat transfer coefficient uncertainty. Below are the needed heating water parameters for accomplishing this target:

1. Reynolds numbers from 3000 to 5500, which yield low convective thermal resistance between the heating water and the polyimide tube outer wall.
2. Temperature differences from the water inlet to the outlet (ΔT_{water}) between 0.9 to 2.5 K, which provide acceptable heat flux uncertainty (13 to 39%, as reported in section 6.6), as ΔT_{water} is the parameter contributing the most to it.

To comply with these requirements, a 4.925 mm ID glass tube was chosen, resulting in an annular gap with the polyimide tube of 2.108 mm. Water flow rates of 0.7-0.8 L min⁻¹ and temperatures from 45 to 80°C guarantee the aforementioned conditions in the whole flow boiling experimental range. The glass tube is properly insulated with mineral wool and closed-cell insulation foam, as depicted in Fig. 6.2a (at the right, next to the LED light for flow visualisation), minimising heat loss to the ambient.

Fluid flows in the transitional regime are strongly influenced by the inlet conditions. The water inlet manifold (see Fig. 6.1) is designed in order to provide good mixing of the water flow and ensure turbulent conditions inside the annulus along the whole length of the polyimide channel. Thermal stratification of the water should be avoided so as to guarantee a uniform heat flux distribution in the polyimide channel periphery. The water flow and heat transfer in the annulus were simulated with CFD tools, assuming a constant boiling heat transfer coefficient in the refrigerant side as calculated for a specific flow boiling condition using the Liu and Winterton correlation [121]. Almost no thermal stratification of the water flow was observed in the test section length, with water temperatures differing by less than 0.1 K between the top and the bottom of the annular gap, as shown in Fig. 6.5b.

6.2.2 Experimental facility

The test rig is installed in an existing experimental facility at EESC-USP, the same used and described by Tibiriçá and Ribatski[103] with the sole addition of a specific loop for circulating distilled water to heat the polyimide channel. A schematic view of the experimental facility is depicted in Fig. 6.6a. The operating pressure of the R245fa refrigerant, and ultimately the saturation temperature of the fluid at the test section, is ruled by the saturation temperature of the fluid in the refrigerant tank. A water-glycol mixture is circulated in a serpentine inside the tank to change the temperature of the R245fa refrigerant. As liquid R245fa is circulated out of the vessel, it is cooled at the liquid subcooler 1. After passing through a filter and a visor (not shown in Fig. 6.6a), the subcooled liquid flows through a gear pump, which adjusts the mass flux by a closed loop control system. A Coriolis-effect mass flow meter is installed downstream of the pump. A second heat exchanger (subcooler 2) cools down the liquid before it enters the test rig through the 2.1 mm ID visualisation section. After being partially

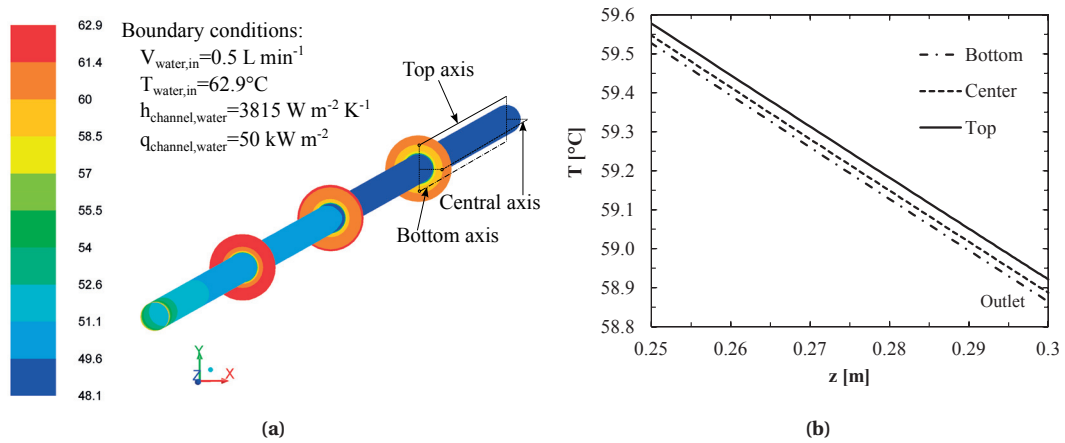


Figure 6.5: CFD simulation of the heating water flow thermal stratification: (a) water temperature [$^\circ\text{C}$] at 3 sections of the annulus and simulation boundary conditions; (b) temperature along three longitudinal axes: top, bottom and central part of the annulus, as indicated in (a).

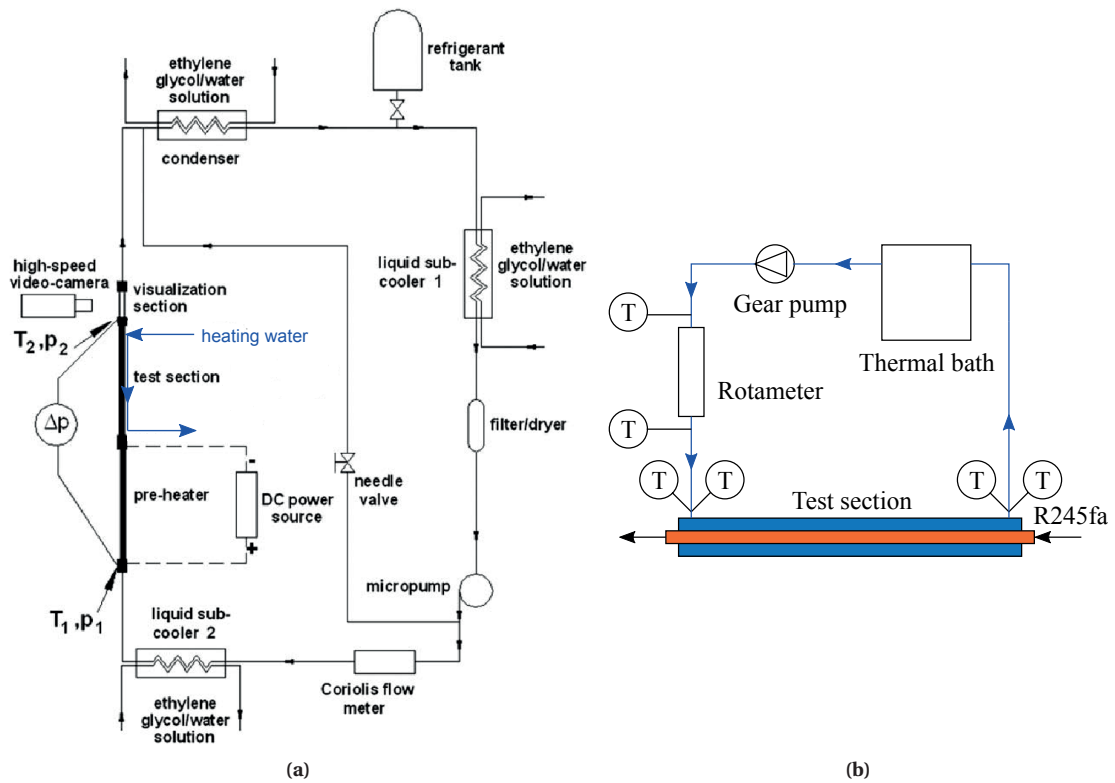


Figure 6.6: Schemes of the experimental facility: (a) two-phase loop (adapted from [103]), and (b) heating water circuit.

evaporated to the desired condition in the pre-heater, it flows through the polyimide tube, where the heating water counter-current flow provides the boiling heat flux. The two-phase R245fa refrigerant flow pattern is observed in the second visualisation section with the high-speed camera, before the fluid is condensed and returned to the tank. Further detail on the test section components can be

found in [125].

The distilled water loop is displayed in Fig. 6.6b. First, a thermal bath sets the water temperature. The water passes through a self-lubricating gear pump controlled with a variable-speed drive, and then through a rotameter. Since the measured volumetric flow rate here depends on the temperature of the fluid, the water temperature is tracked at the inlet and the outlet of the rotameter. The water enters the test section annulus space and decreases its temperature as it evaporates the boiling R245fa flow. Two thermocouples are installed at the water inlet, right before the water starts heating the polyimide channel, and another two are located at the outlet. The temperature readings are doubled in order to decrease the water temperature difference uncertainty. No deviation higher than the sensor uncertainty was registered in the readings of the two pairs of thermocouples.

A LabVIEW DAQ panel was specifically programmed for recording/controlling, among other parameters, the refrigerant flow rate, the pre-heater power, and the refrigerant tank temperature (setting the operation pressure of the system). Calibration functions can be introduced for the measured variables, which are monitored and recorded at rates up to 100 Hz. The physical properties of the fluids are provided in real time by the REFPROP software by NIST.

6.3 Experimental methodology

6.3.1 Heat flux

The mean heat flux in the polyimide channel heated length, L_{heated} , is calculated as:

$$q_{ts,m} = \frac{E_{net}}{\pi D_{i,ts} L_{heated}} \quad (6.3)$$

where $D_{i,ts}$ is the polyimide channel (test section) internal diameter, and E_{net} is the net heat transfer rate from the heating water to the boiling R245fa. It is expressed as follows:

$$E_{net} = E_{water} - E_{air} \quad (6.4)$$

E_{air} is the heat transfer rate to the ambient estimated by the free convection heat transfer correlation for a long horizontal cylinder by Churchill and Chu [161], considering the measured ambient temperature around the test section as the free stream temperature (see section A.2.1 for its implementation). Since the test section is well insulated, losses due to free convection constitute less than 5% of the total heat load. Radiative heat transfer losses are estimated to be even lower. E_{water} is computed as follows:

$$E_{water} = \dot{m}_{water} c_{p,water} \Delta T_{water} \quad (6.5)$$

where \dot{m}_{water} is the water mass flow rate and ΔT_{water} is the water temperature decrease.

Matkovic *et al.* [162] used water as the cooling agent in their experimental condensation studies, calculating local heat fluxes by fitting water temperature measurements of the water stream along the test section by a second order polynomial and applying an energy balance. Such strategy was considered in the present study, but was abandoned as it results in high uncertainty and complexity: it was estimated that 12 or more water temperature readings were needed along the annulus to provide acceptable, low error results. At the same time it was proven that, given the length of the heated channel and high water flow rates, little heat flux variation happens along the test section (see below). Hence, using the average heat flux was found to be the best approach.

The plot in Fig. 6.7 summarises two cases studied analytically, displaying these two ways of expressing the heat flux. The blue filled dots represent the heat flux calculated as constant in the test section, according to Eq. 6.3, including the propagated uncertainty for a generic two-phase flow boiling case. The white dots are the local, linear heat flux values calculated from deriving a second order polynomial fitting 12 temperature measurements in the water stream, as described by Matkovic *et al.* [162]. The higher uncertainty at the extremities of the test section is a consequence of propagating the temperature measurement errors in the fitting [163]. The uncertainties are always higher than if considering a constant heat flux. The little variation of the heat flux, coupled to the complexity of installing 12 thermocouples immersed in the water, guaranteeing their precise location in the water flow, motivated the simpler choice of averaging the heat flux instead, measuring the flow boiling heat transfer coefficient averaged along the polyimide channel.

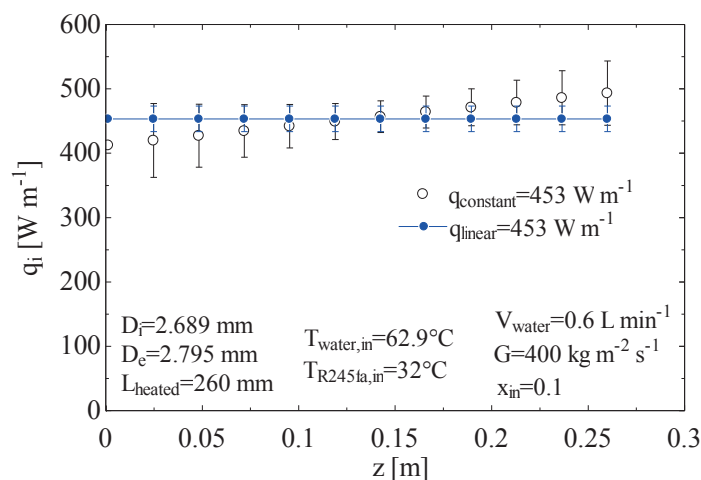


Figure 6.7: Different ways of calculating the linear heat flux on the polyimide channel [W m^{-1}]: as a constant (Eq. 6.3), or linear (deriving the water temperature profile fitted by a second order polynomial from 12 measurements in the water stream).

6.3.2 Heat transfer coefficient

The primary result in the present study is the boiling heat transfer coefficient averaged along the whole polyimide channel length. Most of the recent similar experimental works report local heat transfer coefficient values by measuring the tube wall temperature locally, but such measurements proved to be unreliable in the present polyimide channel setup. The sensors have to be physically separated from the heating water flow by encapsulating them, adding an extra thermal resistance in this operation which decreases the local heat flux. This, combined with the low conductive heat transfer rate in the channel wall due to the low thermal conductivity of polyimide, resulted in lower local wall temperatures than in naked sections of the channel. Likewise, good thermal contact between the thermocouples and the channel surface, lacking rigidity and adherence, was not guaranteed. These obstacles discouraged a local approach to the results.

The global resistance to heat flow from the heating water to the boiling R245fa may be expressed using average thermal resistances, as follows:

$$R_{global} = R_{conv,ann} + R_{cond,wall} + R_{conv,int} \quad (6.6)$$

The three thermal resistances above are calculated using the following equations:

$$R_{conv,ann} = \frac{T_{water,m} - T_{wall,ts,e}}{E_{net}} \quad (6.7)$$

$$R_{cond,wall} = \frac{T_{wall,ts,e} - T_{wall,ts,i}}{E_{net}} \quad (6.8)$$

$$R_{conv,int} = \frac{T_{wall,ts,i} - T_{R245fa,m}}{E_{net}} \quad (6.9)$$

All temperatures in Eqs. 6.7, 6.8 and 6.9 are referred to mean values. $T_{wall,ts,e}$ and $T_{wall,ts,i}$ are the polyimide channel external and internal mean temperatures, respectively. $T_{water,m}$ and $T_{R245fa,m}$ are the mean temperatures of the water flow and the R245fa refrigerant.

The thermal resistance of conduction across the polyimide tube wall ($R_{cond,wall}$) is determined as described in subsection 6.4.1. A validated, single-phase heat transfer correlation provides the convection thermal resistance from the heating water to the outer polyimide channel wall ($R_{conv,ann}$) following the procedure discussed more in detail in subsection 6.4.2. $R_{conv,int}$ is the sought convective thermal resistance between the polyimide tube inner wall and the boiling refrigerant. It can be calculated by

combining the equations above, resulting in the following expression:

$$R_{conv,int} = \frac{T_{water,m} - T_{R245fa,m}}{E_{net}} - R_{conv,ann} - R_{cond,wall} \quad (6.10)$$

Finally, the mean two-phase flow boiling heat transfer coefficient inside the polyimide channel, or test section (ts), $h_{ts,m}$, is calculated as:

$$h_{ts,m} = \frac{1}{R_{conv,int} (\pi L_{heated} D_{i,ts})} \quad (6.11)$$

6.3.3 Vapour quality

The vapour quality is expressed averaged along the polyimide channel (test section) considering the vapour qualities at its inlet and outlet ($x_{ts,in}$ and $x_{ts,out}$):

$$x_{ts,m} = \frac{x_{ts,in} + x_{ts,out}}{2} \quad (6.12)$$

Assuming that thermodynamic equilibrium is achieved in steady-state conditions, the thermodynamic vapour quality at the polyimide channel inlet, $x_{ts,in}$, can be calculated as follows:

$$x_{ts,in} = \frac{\left(\frac{E_{ph}}{G_{ph} A_{i,ph}} + i_{ph,in} \right) - i_{l,ts,in}}{i_{lv,ts,in}} \quad (6.13)$$

E_{ph} is the electric power supplied to the pre-heater; G_{ph} and $A_{i,ph}$ are the mass flux and the internal cross section in the pre-heater. $i_{l,ts,in}$ and $i_{lv,ts,in}$ are the liquid and vaporisation enthalpies at the polyimide channel entrance. These two parameters are calculated from the saturation pressure at the polyimide tube inlet, which is determined from the saturation pressure at the pre-heater outlet minus a singular pressure drop at the inlet (see subsection 6.5.2).

The vapour quality at the polyimide channel outlet is determined according to Eq. 6.14:

$$x_{ts,out} = \frac{\left(\frac{E_{ph}}{G_{ph} A_{i,ph}} + \frac{E_{net}}{G_{ts} A_{i,ts}} + i_{ph,in} \right) - i_{l,ts,out}}{i_{lv,ts,out}} \quad (6.14)$$

G_{ts} and $A_{i,ts}$ are the mass flux and the internal cross section in the polyimide channel. $i_{l,ts,out}$ and $i_{lv,ts,out}$ are the liquid and vaporisation enthalpies at the polyimide channel outlet, calculated from the measured outlet saturation pressure after accounting for the singular two-phase pressure drop in the outlet flange determined beforehand (see subsection 6.5.2).

6.4 Water-water tests

Tests with two streams of water in counter-current (i.e. in the annular space and inside the polyimide channel) were conducted with two goals: experimentally measure $R_{cond,wall}$, and validate the use of empirical correlations to determine $R_{conv,ann}$. These two thermal resistances are required to calculate $R_{conv,int}$ on Eq. 6.10 and, subsequently the mean heat transfer coefficient in the polyimide channel in Eq. 6.11 during the two-phase flow boiling tests.

6.4.1 Thermal resistance of conduction across the tube wall

A steady-state, 1-D thermal conduction analysis across the tube wall using cylindrical coordinates results, applying Fourier's law of thermal conduction, in a logarithmic temperature distribution [164]. The thermal resistance of conduction across the tube wall can be expressed as follows:

$$R_{cond,wall} = \frac{\ln\left(\frac{D_{e,ts}}{D_{i,ts}}\right)}{2\pi \alpha_{ts} L_{heated}} \quad (6.15)$$

where α_{ts} is the thermal conductivity of the channel wall. In practice, when considering the dimensional tolerances of $D_{e,ts}$ and $D_{i,ts}$ reported in Table 6.2, Eq. 6.15 yields high uncertainty. This is due to the low thermal conductivity of the polyimide channel: $0.12 \text{ W m}^{-1} \text{ K}^{-1}$ [66], or more than 130 times lower than stainless steel. Error propagation in Eq. 6.11 may result in heat transfer coefficient uncertainties often exceeding 100%.

A series of water-water tests were carried out with the aim of determining experimentally the thermal resistance across the polyimide tube wall in the channel later used in the flow boiling heat transfer tests, using neither the channel dimensions nor its thermal conductivity. The test strategy is the following:

1. Set a highly turbulent water flow rate inside the channel ($Re_{int} > 20000$) at a fixed temperature.
2. Set a counter-current water flow rate in the annulus to a fixed temperature, significantly higher than the internal flow.
3. Gradually increase the annulus water flow rate from $Re_{ann} = 3000$ to the maximum value possible.

The global thermal resistance between the two water flows can be expressed as in Eq. 6.6. Since the internal flow rate is fixed and turbulent, the convective thermal resistance ($R_{conv,int}$) can be accurately calculated through Eq. 6.11, after determining $h_{ts,m}$ using a single-phase, forced convection heat transfer coefficient correlation for the turbulent flow regime in circular channels. The correlation for turbulent flows in circular channels by Gnielinski [150] as described in chapter G1, section 4.1 of the VDI Atlas [147] was chosen (see appendix A, page 201). The convective thermal resistance between the water in the annulus and the polyimide channel outer wall ($R_{conv,ann}$) will depend on the

variable mass flow rate in the annulus. Considering an infinitely high water flow rate ($Re_{ann} \rightarrow \infty$), $R_{conv,ann}$ converges to zero. In such conditions, and taking into account $R_{cond,wall}$ is a constant, the global thermal resistance expressed in Eq. 6.6 remains as the sum of two constant thermal resistances, $R_{cond,wall}$ and $R_{conv,int}$. An expression of R_{global} fulfilling the conditions stated above is the following:

$$R_{global} = (R_{conv,int} + K_1) e^{\left(\frac{K_2}{Re_{ann}}\right)} \quad (6.16)$$

As R_{global} is calculated using the ε -NTU method for concentric, counter-current heat exchangers [165], and $R_{conv,int}$ is known, the experimental data can be fitted using the unweighted least squares method to match Eq. 6.16 by tuning the values of the K_1 and K_2 constants. K_1 is the ultimately sought $R_{cond,wall}$ value.

Fig. 6.8 shows the experimental thermal resistance values versus Re_{ann} for a case where the annulus water stream is at 50°C and the water inside the tube is at 20°C. R_{global} is fitted according to Eq. 6.16, with $R_{conv,int}=0.012 \text{ K W}^{-1}$ as calculated using the Gnielinski correlation [150, 147]. A value of $R_{cond,wall}=0.095 \text{ K W}^{-1}$ is obtained. The same procedure was repeated for different water flow and temperature conditions, resulting in an average $R_{cond,wall}$ value of $0.0924 \pm 0.0087 \text{ K W}^{-1}$ as reported in Table 6.3. It should be emphasised that the only reason behind the choice of a temperature difference between the two water flows of 30 K in all cases is that it is a large enough temperature difference that requires neither high or low temperatures in the two water flows, which could derive in significant heat exchange with the ambient and less accuracy in the calculation of $R_{cond,wall}$.

The sole heat transfer coefficient correlation used when calculating $R_{cond,wall}$ was the one to determine $h_{ts,m}$ and ultimately $R_{conv,int}$. Furthermore, for all tests performed, $R_{conv,int} < 0.1 R_{global}$, so the impact of $R_{conv,int}$ in the R_{global} fit, and subsequently in the sought $R_{cond,wall}$ parameter, is minimal.

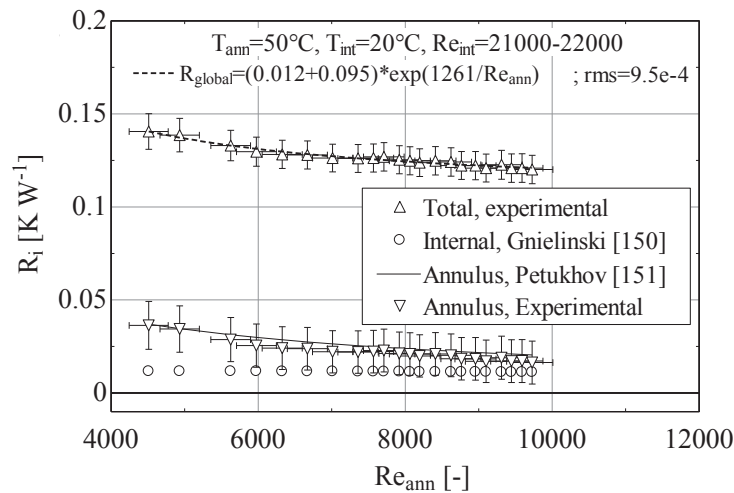


Figure 6.8: Water-water thermal resistances vs. annulus Reynolds number. The annulus water flow displays an inlet temperature of 50°C, and the internal water flow enters the polyimide tube at 20°C.

Table 6.3: Summary of the conditions in the water-water tests and the experimental results of the thermal resistance of conduction across the polyimide channel wall. The water flow inside the polyimide tube and in the annular space outside it are counter-current.

Case	T_{ann} [°C]	T_{int} [°C]	Re_{ann} [-]	Re_{int} [-]	$R_{cond,wall}$ [K W ⁻¹]	$U(R_{cond,wall})$ [K W ⁻¹]
1	50	20	4500-9760	~ 21500	0.0902	0.0082
2	60	30	5350-11400	~ 28000	0.0901	0.0089
3	40	10	2670-8070	~ 16700	0.0968	0.0090
Average					0.0924	0.0087

6.4.2 Validation of the heat transfer coefficient correlation in the annulus

Once $R_{cond,wall}$ is determined, the experimental value of $R_{conv,ann}$ may be obtained through Eq. 6.6 and compared to the values given by single-phase, forced convection heat transfer coefficient correlations in the annulus. The following forced convection correlations for circular channels were considered: Gnielinski [150], Petukhov [151], and Dittus and Boelter [123]. In these models, the characteristic dimension is the hydraulic diameter of the annulus. Specific correlations by Gnielinski for the cylindrical annulus geometry [160], described in chapter G2, sections 1 to 7 of the VDI Atlas, were used too. These correlations cover the transition region between laminar and turbulent flow [149], as well as the fully developed turbulent flow region [166]. Those are the heating water flow regimes in all the experiments in this chapter. All the correlations in this section are described in appendix A, pages 201 and 202.

The deviation between the values given by the correlations and the experimental thermal resistances is expressed using the mean relative error (mre) and the mean absolute error (mae), calculated according to Eqs. 6.17 and 6.18:

$$mre = \frac{1}{n} \sum_{i=1}^n \frac{X_{pred} - X_{exp}}{X_{exp}} \quad (6.17)$$

$$mae = \frac{1}{n} \sum_{i=1}^n \left| \frac{X_{pred} - X_{exp}}{X_{exp}} \right| \quad (6.18)$$

where X is, in this case, $R_{conv,ann}$.

Table 6.4 reports the mae for several water-water cases, as well as a water-single-phase R245fa case in the last row. It is observed that the correlation by Petukhov [151] and its version for low Reynolds numbers by Gnielinski [150] provide the minimum mae , being the Petukhov correlation the best overall fit. The use of this correlation for calculating $R_{conv,ann}$ in two-phase flow conditions is hence justified and will yield fairly accurate results.

Table 6.4: Mean absolute error (*mae*) of the heat transfer coefficient between the water and the polyimide tube outer wall in the annulus given by four heat transfer correlations with respect to the experimental values. The water flow inside the polyimide tube and in the annular space outside it are counter-current.

Case	T_{ann} [°C]	T_{int} [°C]	Mean absolute error (<i>mae</i>) [%]			
			Gnielinski [150]	Petukhov [151]	Gnielinski-VDI [160]	Dittus-Boelter [123]
0	50	20	22.6	6.4	11.7	31.6
1	50	20	30.7	12.2	20.3	39.8
2	60	30	48.3	29.2	33.5	58.2
3	40	10	19.4	3.1	18.9	25.7
4	Water	R245fa	14.8	16.6	-	-

6.5 Validation tests

6.5.1 Single-phase flow tests

A series of single-phase R245fa tests were performed with the aim of validating the experimental setup. First, single-phase adiabatic tests were conducted. In order to keep adiabatic conditions in the polyimide tube, a low water flow rate was established (laminar flow regime) and its temperature set equal to the average temperature of the single-phase R245fa refrigerant, so negligible water temperature changes were recorded. Measured single-phase R245fa pressure drop values in adiabatic conditions were compared to the frictional pressure drop correlations by Churchill [145] and Gnielinski [150], as illustrated in Fig. 6.9. An excellent match was observed, especially with the correlation by Churchill.

Diabatic single-phase tests were conducted with a dual purpose: performing energy balances, and assessing the effective uncertainty of the heat transfer coefficient inside the polyimide tube. Energy

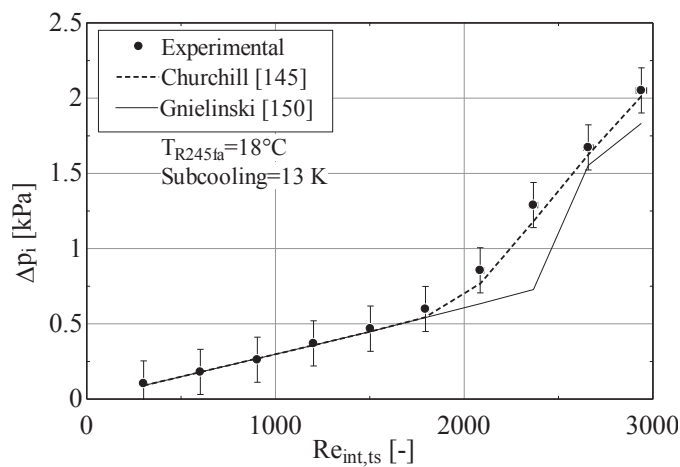


Figure 6.9: Comparison between the experimental single-phase R245fa pressure drop and the values obtained with correlations versus the Reynolds number inside the polyimide tube.

balances are of key importance to ensure accurate vapour quality estimates and quantify the effective heat transfer rate to the refrigerant. To do these tests, the pre-heater was powered, while the polyimide tube was kept in adiabatic conditions by applying the strategy described above. The energy balance in the pre-heater only, using the temperature difference between the test rig inlet and the value measured by the thermocouple before the polyimide channel ($\Delta T_{in-bef,ts}$), is calculated as follows:

$$\left[\frac{\Delta E}{E} \right]_{ph} = \frac{\dot{m}_{R245fa} c_{p,R245fa} \Delta T_{in-bef,ts} - E_{ph}}{E_{ph}} 100 [\%] \quad (6.19)$$

The energy balance in the pre-heater is plotted in Fig. 6.10a, showing deviations within $\pm 15\%$ for $Re_{ph} > 2000$. A second diabatic test was performed, keeping the pre-heater off and heating with water the single-phase R245fa at the polyimide channel only. In this case, the energy balance consists in comparing the net heat load provided by the heating water (E_{net}), computed according to Eqs. 6.4 and 6.5, and the total power received by the R245fa (E_{R245fa}), as follows:

$$\left[\frac{\Delta E}{E} \right]_{ts} = \frac{E_{net} - E_{R245fa}}{E_{R245fa}} 100 [\%] \quad (6.20)$$

where E_{R245fa} is calculated using the expression below:

$$E_{R245fa} = \dot{m}_{R245fa} c_{p,R245fa} \Delta T_{in-out} \quad (6.21)$$

where ΔT_{in-out} is the temperature difference between the test rig inlet and outlet, measured by the thermocouples immersed in the R245fa flow. Fig. 6.10b displays the energy balance in the polyimide channel. Deviations around -10% are reported at $Re_{ts} > 2000$. Given the accuracy expected in the experimental setup, these results are considered acceptable.

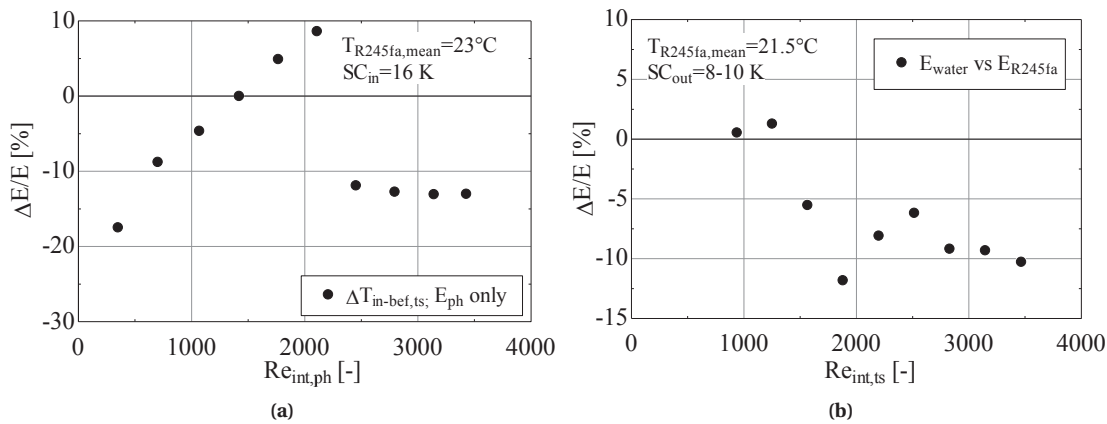


Figure 6.10: Single-phase energy balances at the: (a) pre-heater, keeping the polyimide tube in adiabatic conditions; (b) test section (polyimide tube), with no power applied to the pre-heater.

The single-phase heat transfer coefficient in the polyimide tube was assessed as an additional validation of the setup. The procedure consists in calculating, first, R_{global} according to the ε -NTU method for concentric, counter-current heat exchangers [165] with E_{R245fa} as input. By then introducing $R_{cond,wall}=0.0924 \text{ K W}^{-1}$ and determining $R_{conv,ann}$ through the validated correlation by Petukhov [151], $R_{conv,int}$, and subsequently the values of $h_{ts,m}$, are calculated, as described in Eqs. 6.10 and 6.11. The values of $h_{ts,m}$ obtained using the R245fa stream are very accurate, thanks to the low uncertainty of E_{R245fa} , and thus are considered in the scatter plot in Fig. 6.11 as the benchmark heat transfer coefficients (X -axis, h_{exp}). In the Y -axis, h_{pred} can be determined in two ways:

1. Experimentally as $h_{ts,m}$, using the heat load as calculated from the water stream by repeating the method above using E_{net} instead of E_{R245fa} , as it will be done in the two-phase flow boiling tests. This involves a higher error due to the higher uncertainties of the instrumentation in the heating water circuit.
2. Theoretically, from the correlations by Churchill [145] and Gnielinski [150].

Results are brought into comparison in Fig. 6.11. h_{pred} , calculated as by the two approaches above, fall well within a $\pm 30\%$ deviation range with respect to the reference heat transfer coefficients estimated from E_{R245fa} (h_{exp}), except at the bottom of the scale, where higher uncertainties were observed.

6.5.2 Singular two-phase flow pressure drop evaluation

Two-phase flow tests with R245fa refrigerant in adiabatic conditions at the polyimide channel provide a way to obtain the singular two-phase pressure drops. They were observed after comparing the

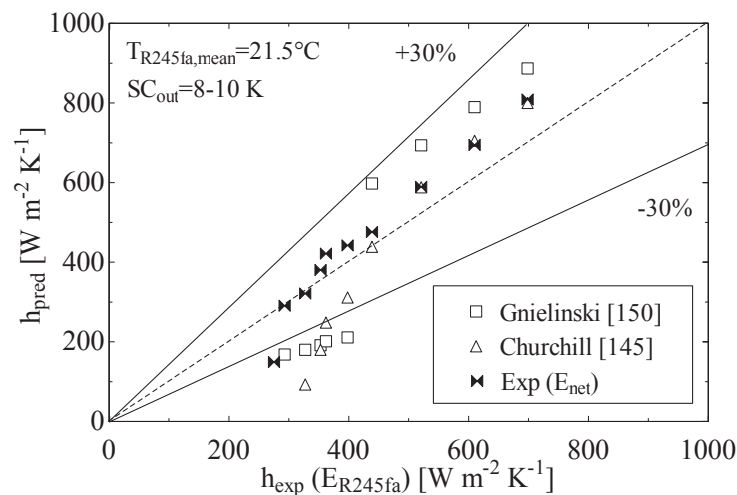


Figure 6.11: Single-phase heat transfer coefficient in the polyimide channel: comparison between predictions and experimental values calculated from the heat loads measured in the water (E_{net}) and the R245fa flows (E_{R245fa}).

experimental and the total theoretical pressure drop values, expressed as follows:

$$\Delta p_{total,theory} = \Delta p_{frict} + \Delta p_{mom} \quad (6.22)$$

where Δp_{frict} is the two-phase frictional pressure drop component. Multiple methods from literature, described in section 2.5.5, were considered for the calculation of this component: Müller-Steinhagen and Heck [93], Friedel [92], Da Silva and Ribatski [95], and Sempértegui-Tapia and Ribatski [96]. These correlations are detailed in appendix A, section A.1.2.

Δp_{mom} is the momentum pressure gradient. For separated and disperse flows in saturated conditions, in a circular channel of uniform diameter, it is calculated with the following equation, according to Collier and Thome [75]:

$$\Delta p_{mom} = G^2 \left\{ \left[\frac{(1-x)^2}{(1-\varepsilon)\rho_l} + \frac{x^2}{\varepsilon\rho_v} \right]_{out} - \left[\frac{(1-x)^2}{(1-\varepsilon)\rho_l} + \frac{x^2}{\varepsilon\rho_v} \right]_{in} \right\} \quad (6.23)$$

where ε is the void fraction, calculated in this case using Steiner's version [84] of the drift flux void fraction correlation by Rouhani and Axelsson [83] (see section A.3 for the model equations). No gravity component is included, as the system is horizontal. Fig. 6.12 reports the deviation between the experimental and the theoretical two-phase pressure drop using the Müller-Steinhagen and Heck correlation [93] for the frictional component. The difference between the two is attributed to the pressure drop in the singularities.

According to the local saturation temperature drops recorded by the thermocouples before and after the polyimide channel, singular pressure drops are localised at the connections with the pre-

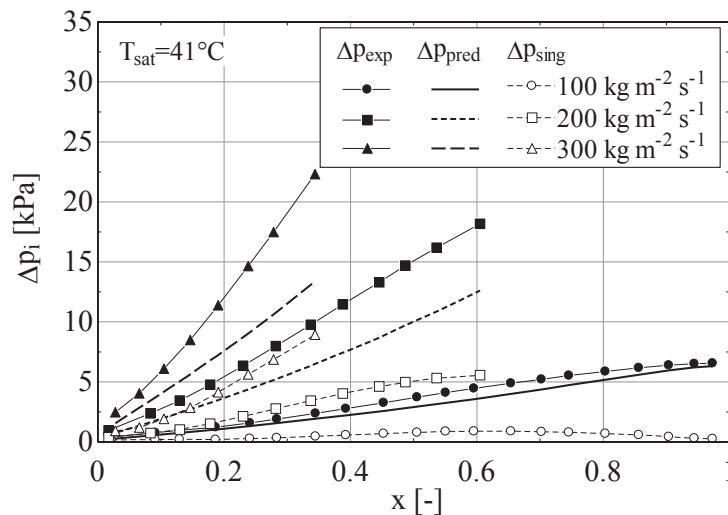


Figure 6.12: Experimental (Δp_{exp}), theoretical ($\Delta p_{pred} = \Delta p_{frict} + \Delta p_{mom}$), and singular (Δp_{sing}) two-phase adiabatic pressure drops for the R245fa refrigerant in the test rig versus mean vapour quality. The frictional component is calculated using the Müller-Steinhagen and Heck correlation [93].

heater and the outlet flange. Indeed, the diameter changes before the polyimide tube, from the 2.3 mm ID pre-heater tube to the 2.689 mm ID of the polyimide channel, and vice versa at the outlet. Assuming the difference between the theoretical and experimental two-phase pressure drops is entirely due to singularities, the following expression can be used:

$$\Delta p_{sing} = \Delta p_{exp} - \Delta p_{total,theory} \quad (6.24)$$

In order to determine Δp_{sing} , the use of a frictional pressure drop model should be validated to obtain $\Delta p_{total,theory}$. To do so, the procedure below was followed:

1. Run two-phase flow cases with adiabatic conditions in the polyimide channel for several mass fluxes and vapour qualities. For each run, calculate the Δp_{sing} values using different correlations for the frictional pressure drop component: Müller-Steinhagen and Heck [93], Friedel [92], Da Silva and Ribatski [95], and Sempértegui-Tapia and Ribatski [96], and Eqs. 6.22 to 6.24.
2. Run identical cases (i.e. identical vapour quality at the polyimide channel entrance), but heating the polyimide tube with the heating water. $\Delta p_{total,theory}$ can be determined by entering the values of Δp_{sing} calculated previously in the adiabatic cases for each two-phase frictional pressure drop model, as described above, plus the momentum pressure gradient values using Eq. 6.23.
3. Compare the experimental and the theoretical two-phase pressure drops calculated in steps 1 and 2, choosing the frictional two-phase pressure drop model providing the minimum deviation.

This validation method assumes that $\Delta p_{sing,in} = \Delta p_{sing,out}$, even though $x_{ts,out} > x_{ts,in}$ in the diabatic test runs. How the singular pressure drop is distributed between the inlet and the outlet of the polyimide channel is uncertain, as there are small plenums at the connections in both ends of the polyimide channel with the two-phase circuit. A sensitivity check was performed on the experimental two-phase diabatic test data recorded at step 2 above. It consists in altering the location of the singular pressure drop, placing it either entirely at the channel inlet or the outlet. After recalculating the mean vapour quality and the heat transfer coefficient, the observed changes are several times lower than the uncertainty of the two parameters. Thus, it can be assumed that the singular pressure drop localised at the two ends of the polyimide channel is equally distributed between the inlet and the outlet. Also, the small vapour quality increases experienced in the diabatic tests have little influence on the variations of Δp_{sing} .

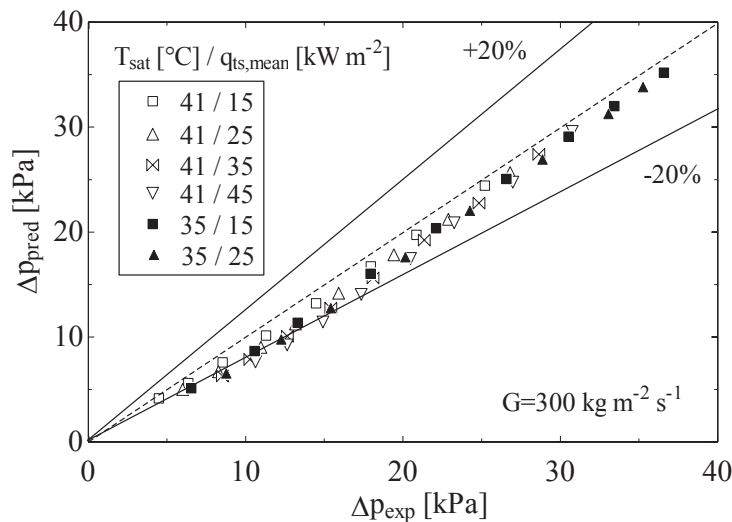
Table 6.5 summarises the *mre* and *mae*, as expressed in Eqs. 6.17 and 6.18, of the predicted two-phase pressure drop values ($\Delta p_{total,theory}$), calculated using each of the four two-phase frictional pressure drop correlations, versus the experimental pressure drop (Δp_{exp}), for the entire experimental database, nearly 300 points. The fraction of data predicted within the $\pm 20\%$ error band is also indicated ($\varphi_{20\%}$). It can be concluded that the two-phase frictional pressure drop correlations by

Table 6.5: Statistical analysis of the comparison between experimental and calculated two-phase pressure drops for the different methods used for evaluating the frictional component.

Author/method	$\varphi_{20\%}$ [%]	mre [%]	mae [%]
Müller-Steinhagen and Heck [93]	81.3	10.3	11.1
Friedel [92]	78.6	10.6	11.5
Da Silva and Ribatski [95]	75.9	12.4	12.7
Sempértegui-Tapia and Ribatski [96]	83.0	9.5	10.0

Müller-Steinhagen and Heck [93] and by Sempértegui-Tapia and Ribatski [96], provide the best accuracy in determining Δp_{sing} . The first was finally chosen, since the method by Sempértegui-Tapia and Ribatski yields higher propagated uncertainties in the current setup. A visual comparison between the theoretical and experimental total pressure drops can be found in Fig. 6.13.

Once $\Delta p_{sing,in}$ is determined for each of the two-phase flow boiling tests, the saturation temperature at the inlet of the polyimide channel can be accurately estimated. First, a 3-equation system is solved in the pre-heater section, involving the subcooled liquid energy balance, the liquid pressure drop (using the correlation by Gnielinski for calculating the friction factor [150]), and the equation of state relating T_{sat} and p_{sat} . The result is the saturation temperature in the pre-heater at $x=0$. Eq. 6.22 yields the pressure drop in the pre-heater saturated region. The saturation pressure at the polyimide channel inlet is determined by subtracting $\Delta p_{sing,in}$ from the saturation pressure at the pre-heater tube end.

**Figure 6.13:** Theoretical (frictional pressure drop correlation by Müller-Steinhagen and Heck correlation [93], plus the singular pressure drop, plus the momentum pressure gradient) versus the experimental pressure drop in several two-phase flow diabatic cases at $G=300 \text{ kg m}^{-2} \text{ s}^{-1}$.

6.6 Calibration, error analysis and stability of the experiments

All temperature measurements were recorded using 0.25 mm type K (chromel-alumel) thermocouples, calibrated here to the 23-79°C range following the method by Abernethy and Thompson [159], and their uncertainty determined as recommended by the NIST standards [167]. The water rotameter was calibrated at 40, 50, 60, 70 and 80°C, since the readings of the volumetric flow rate depend on the flow density and viscosity. Double linear interpolations were utilised for intermediate water temperature and flow rates. Further information on the calibration procedure is detailed in appendix D.

The uncertainties in derived parameters were propagated using the method by Kline and McClintock [168], shown in Eq. 4.26. Prior to data acquisition, the experimental system was always allowed to achieve steady-state conditions. For each experimental point, the standard deviations of all the steady-state measurements in time were calculated and verified that their values did not exceed 10% of the uncertainty of the instrument.

Table 6.6 indicates the uncertainties of the measured variables. The uncertainty of the calculated variables is reported in Table 6.7. For the mean heat transfer coefficient and vapour quality parameters, the propagated uncertainty depends on the experimental conditions. Generally, the uncertainty of the mean heat transfer coefficient ranges between 13 to 39%, with a global average value of 21%. Only heat transfer coefficient values with uncertainties below 35% are considered in this study. The average uncertainty of the mean vapour quality in the test section is 4%.

Table 6.6: Experimental uncertainty of the measured variables.

Polyimide channel ID	(2.689 ± 0.025) mm
Polyimide channel OD	(2.816 ± 0.053) mm
Polyimide channel heated length (L_{heated})	(285 ± 1) mm
Water enclosure ID	(4.925 ± 0.050) mm
Pre-heater electric power	$\pm 0.8\%$ W
Temperature (water)	± 0.10 K
Temperature (R245fa)	± 0.11 K
Temperature (tube walls)	± 0.11 K
Water flow rate	± 0.031 L min ⁻¹
R245fa mass flow rate	$\pm 0.1\%$ g s ⁻¹
Absolute pressure	± 4.50 kPa
Differential pressure	± 0.15 kPa

Table 6.7: Global uncertainties of the two-phase flow parameters at the experimental setup in EESC-USP.

Parameters	Global uncertainty (95% CI)
Polyimide channel mass flux (G)	$\pm 1.9\%$
Mean vapour quality in the polyimide channel ($x_{ts,m}$)	$\pm 2-17\%$
Mean flow boiling heat transfer coefficient ($h_{ts,m}$)	$\pm 13-39\%$

To ensure the experiments were performed at stable conditions, it was verified that in steady-state flow boiling, oscillations of the absolute pressure and the differential pressure measurements in time did not exceed the uncertainty of the instruments. This condition was also checked for all temperature measurements. Instabilities in the form of liquid fronts moving at higher speed than the two-phase flow were observed in the high-speed flow images under certain experimental conditions. Tibiriçá and Ribatski [103] and later Sempértegui-Tapia *et al.* [169] used the present experimental facilities for their studies, acknowledging instabilities of the same nature in some experimental cases. Such instabilities increase the liquid entrainment in the flow and may be related to unstable boiling conditions. In the present study they were almost completely mitigated by adjusting the needle valve upstream the experimental section, although there were certain conditions where it was not possible to eliminate them entirely. By checking with the high-speed camera that no liquid fronts related to boiling instabilities occur and verifying that no significant fluctuations of the measured variables are recorded, all the experimental results reported in this chapter are guaranteed to be taken under stable boiling conditions. Also, potential hysteresis effects related to increasing or decreasing heat flux [117] were minimised by changing each parameter (saturation temperature mass flux, heat flux, vapour quality, in this order) using the same sequence and letting the system stabilise for several minutes after each change.

Repeatability tests were performed to ensure the stability of the facilities over time. The plot in Fig. 6.14 shows the results of two test runs with identical conditions performed on different days, with no significant deviation observed in the mean heat transfer coefficient values.

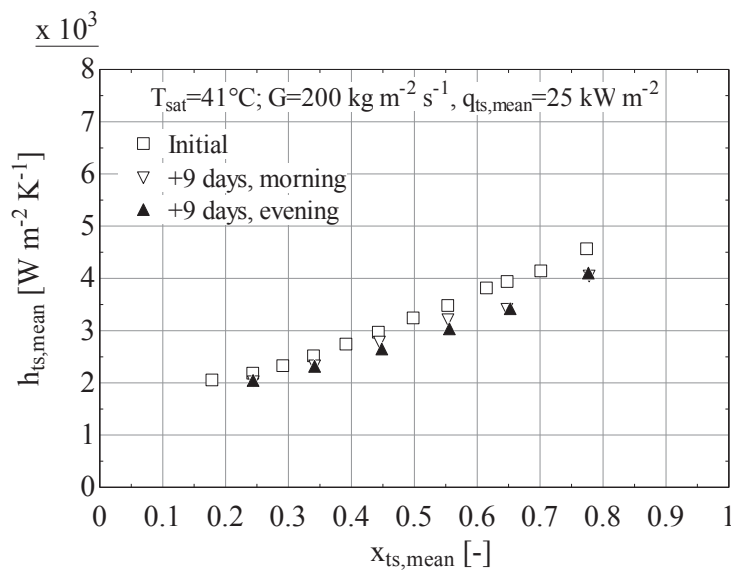


Figure 6.14: Repeatability of the diabatic two-phase flow boiling experimental tests.

6.7 Experimental results

Flow boiling tests were run for R245fa refrigerant at three mean saturation temperatures in the polyimide channel (35, 41 and 47°C) for mass fluxes ranging from 100 to 500 kg m⁻² s⁻¹, heat fluxes from 15 to 55 kW m⁻², and vapour qualities between 0.05 and 0.80. Results of the mean heat transfer coefficients in the polyimide channel, as indicated in Eq. 6.11, were analysed parametrically and their trends compared to those provided by prediction methods and similar experimental studies in the literature.

Stratification of the flow was observed at low vapour qualities, as shown in Fig. 6.15. As the flow visualisation was performed at the 2.1 mm ID quartz tube at the end of the test section, it can be deduced that, if flow stratification is observed here, such an effect occurs in the larger polyimide tube too. Indeed, the Confinement number (Co) is 0.37 in the polyimide channel at the lowest saturation temperature in the tests. Applying the macro- to microscale transition criterion by Kew and Cornwell [69], ($Co > 0.5$ for microchannels), the two-phase flow boiling in the polyimide channel falls in the macroscale region, where gravitational effects dominate over surface tension forces and flow stratification occurs. The transition criterion by Ong and Thome [170], mainly depending upon the uniformity of the liquid film thickness in the channel perimeter, establishes that Co values between 0.3 and 1 correspond to a transitional regime (mesoscale), changing from macroscale ($Co < 0.3$) to microscale regime ($Co > 1$) gradually. Thus, the two-phase flows in the polyimide channel most probably dwell in a transitional regime between macro- and microscale. Also, other studies using R245fa reported stratified flows for channels larger than 2 mm ID [171].

Dryout conditions were difficult to capture with the existing instrumentation and methodology, since only the mean heat transfer coefficients and vapour qualities were studied, and the tests involve low vapour quality increases in the polyimide channel. Fig. 6.16 shows a slight heat transfer coefficient drop at high vapour qualities for $G=100$ kg m⁻² s⁻¹, which suggests partial dryout conditions, while the high-speed images certainly confirm liquid film evaporation from the tube wall (see Fig. 6.16b).

6.7.1 Parametric analysis of the results

Influence of the mass flux

The flow boiling heat transfer coefficient increases with increasing mass velocity for fixed heat flux and saturation temperature conditions, as shown in Fig. 6.16a. This effect is stronger at higher vapour

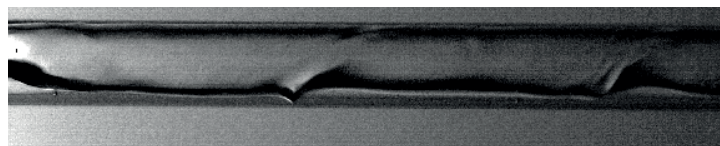


Figure 6.15: Two-phase flow stratification recorded at the 2.1 mm ID visualisation section, at $G=200$ kg m⁻² s⁻¹, $x=0.05$, $T_{sat}=35^\circ\text{C}$. Flow is from right to left.

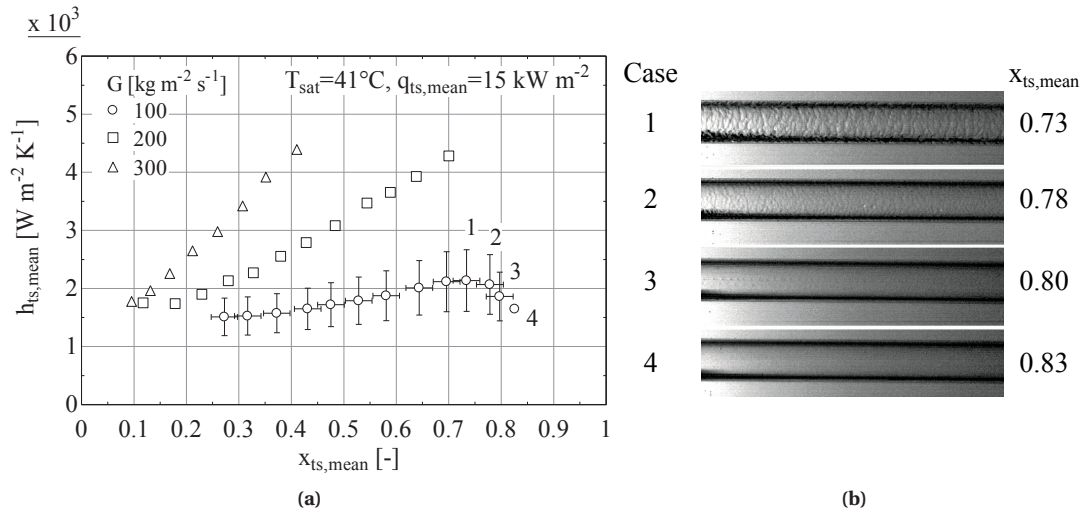


Figure 6.16: Influence of the mass flux on the heat transfer coefficient. High-speed flow images of the four points with highest vapour qualities (1-4) at the lowest mass velocity ($G=100 kg m^{-2} s^{-1}$) are displayed in (b), illustrating the captured partial dryout conditions.

qualities and mass flux values between 200 and $300 kg m^{-2} s^{-1}$. In general, similar convective boiling experimental studies and heat transfer coefficient correlations and models report this behaviour. The saturation temperature has also an impact on the magnitude of the influence of the mass flux: as reported in Fig. 6.17, the heat transfer coefficient increasing with increasing mass flux is mildly amplified at lower saturation temperatures. Last, by comparing Fig. 6.16a and Fig. 6.17b, it can be seen that the effect is more intense at lower heat fluxes. In any case, the heat transfer coefficient increases with increasing vapour qualities in a rather linear fashion, after a small plateau at low vapour qualities, only observed at low mass and heat fluxes.

It must be emphasised that, if keeping all parameters constant, increasing the mass flux will result in a lower vapour quality increase (Δx_{in-out}) within the polyimide tube. As a result, the influence of the mass flux on the mean flow boiling heat transfer coefficient cannot be studied in an isolated way in the present setup, as it implies a change on Δx_{in-out} . This is a known limitation of experimental heat transfer setups that track mean and not local parameters. Fig. 6.18 depicts the same results displayed in Fig. 6.17a, but plotting the mean heat transfer coefficient versus the vapour quality at the inlet and the outlet of the polyimide channel, and averaged along it. The inlet and outlet vapour qualities are represented as the left and right ends of the horizontal “error band”, whilst the mean vapour quality value is pictured by the symbol at its centre. It can be observed that, despite the fact that Δx_{in-out} changes as the mass flux is altered, there is indeed an increase of the mean heat transfer coefficient with mass flux. In the polyimide tube, $\Delta x_{in-out} \approx 0.3$ at $200 kg m^{-2} s^{-1}$, ≈ 0.225 at $300 kg m^{-2} s^{-1}$, and ≈ 0.15 at $400 kg m^{-2} s^{-1}$. It is easy to see that even shifting the curves by $\Delta x = 0.075$, the mean heat transfer coefficient will be higher for a higher mass flux. Last, if there was an influence of the different Δx_{in-out} (e.g. a shift of flow pattern and/or dominant heat transfer mechanisms), the linear

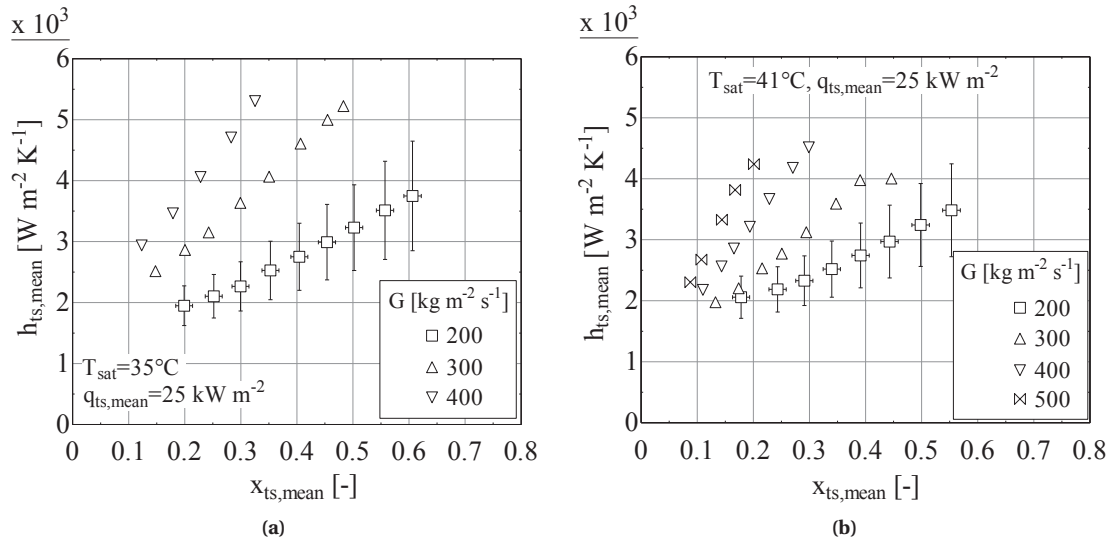


Figure 6.17: Influence of the mass flux on the mean heat transfer coefficient at two different saturation temperatures: (a) 35°C; (b) 41°C.

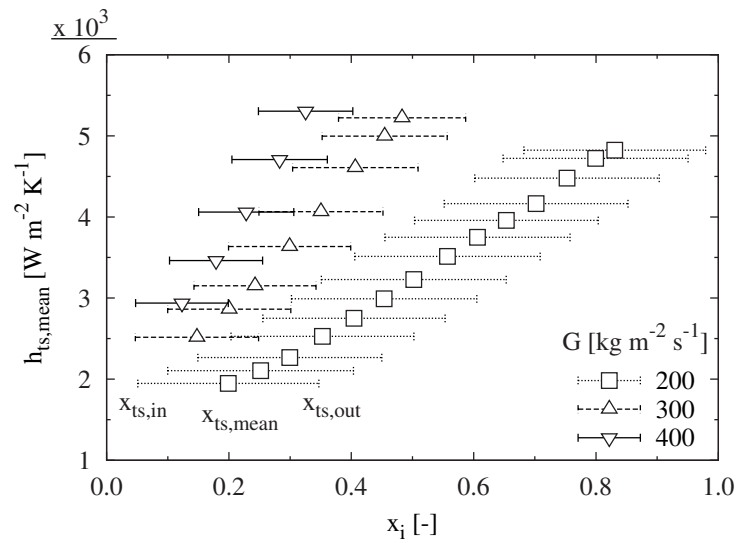


Figure 6.18: Influence of the mass flux on the mean heat transfer coefficient versus the inlet, outlet and mean vapour quality in the polyimide tube, at $q_{ts,m}=25 \text{ kW m}^{-2}$ and $T_{sat}=35^\circ\text{C}$. The inlet and vapour qualities are represented by the left and right ends, respectively, of the horizontal line for each experimental point. The symbol at the middle corresponds to the mean vapour quality.

heat transfer coefficient trends observed in the plots would probably be altered for each mass flux.

Influence of the heat flux

No relevant heat transfer coefficient dependence on the heat flux was observed. According to the plot in Fig. 6.19a, the heat transfer coefficient does not increase when shifting $q_{ts,m}$ from 15 to 25 kW m^{-2} . At heat fluxes from 5 to 15 kW m^{-2} , the heat transfer coefficient seems to increase slightly within the

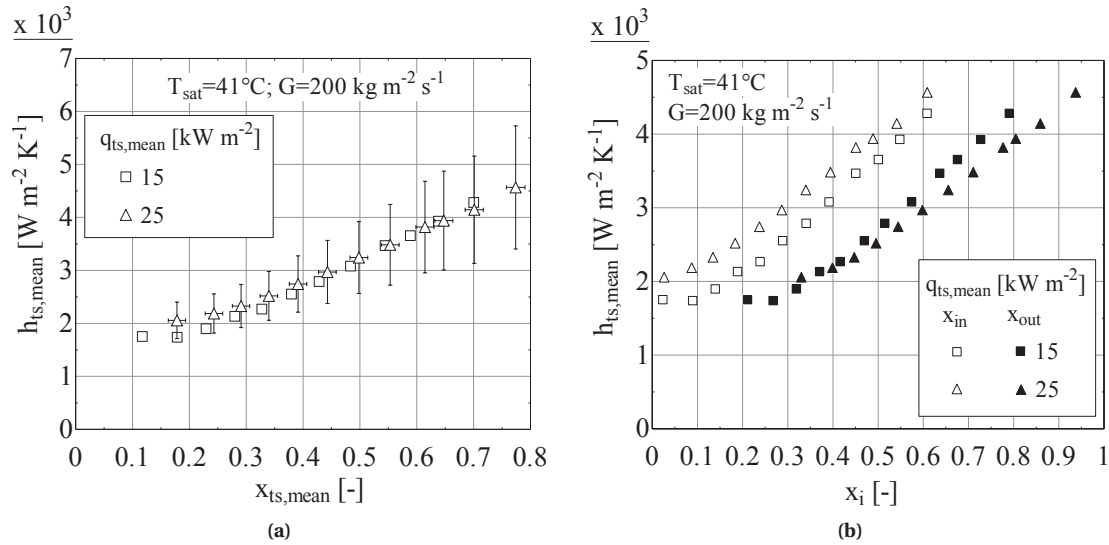


Figure 6.19: Effect of the heat flux on the mean heat transfer coefficient, plotted against: (a) mean vapour qualities in the polyimide channel; (b) inlet and outlet vapour qualities in the polyimide channel.

uncertainty range with increasing heat flux (not shown in Fig. 6.19, as the uncertainty at 5 kW m^{-2} was too high).

As illustrated when describing the influence of the mass flux, it is emphasised that, for a fixed mass flux and different heat fluxes, the vapour quality difference from the polyimide channel inlet to the outlet is higher at higher heat fluxes. Therefore, quantifying the influence of the heat flux on the average heat transfer coefficient values by directly comparing different cases might be misleading. For instance, in Fig. 6.19a, the vapour quality increase in the polyimide channel ($\Delta x_{\text{in-out}}$) is 0.18 at 15 kW m^{-2} and 0.30 at 25 kW m^{-2} . Thus, the two experimental conditions cannot be fairly compared directly. This effect is illustrated in Fig. 6.19b, where the mean heat transfer coefficient in the polyimide channel is plotted versus the inlet and outlet vapour qualities, instead of the mean values. However, it can be seen that, in the cases considered, the heat transfer coefficient does not significantly increase with the heat flux; otherwise, the 25 kW m^{-2} points would be shifted towards the top left of the plot in Fig. 6.19a.

If the heat transfer coefficient increasing effect with the heat flux is only slightly noticeable but not significant at low mass flux and low vapour qualities, it disappears at higher mass fluxes, as it can be observed by comparing Fig. 6.19a and Fig. 6.20b. In these plots, it can be seen that at low vapour qualities, the heat transfer coefficients tend to be slightly lower at the lower heat fluxes, whilst at 47°C (not displayed in Fig. 6.20) the same behaviours were observed.

Little or no influence of the heat flux on the heat transfer coefficient is generally interpreted as dominance of convective boiling [108]. Likewise, as the flow develops along the test section, which is not short, the leading heat transfer mechanism becomes convective boiling, according to the mean heat transfer coefficient experimental trends. Also, the observed flow patterns correspond mostly to

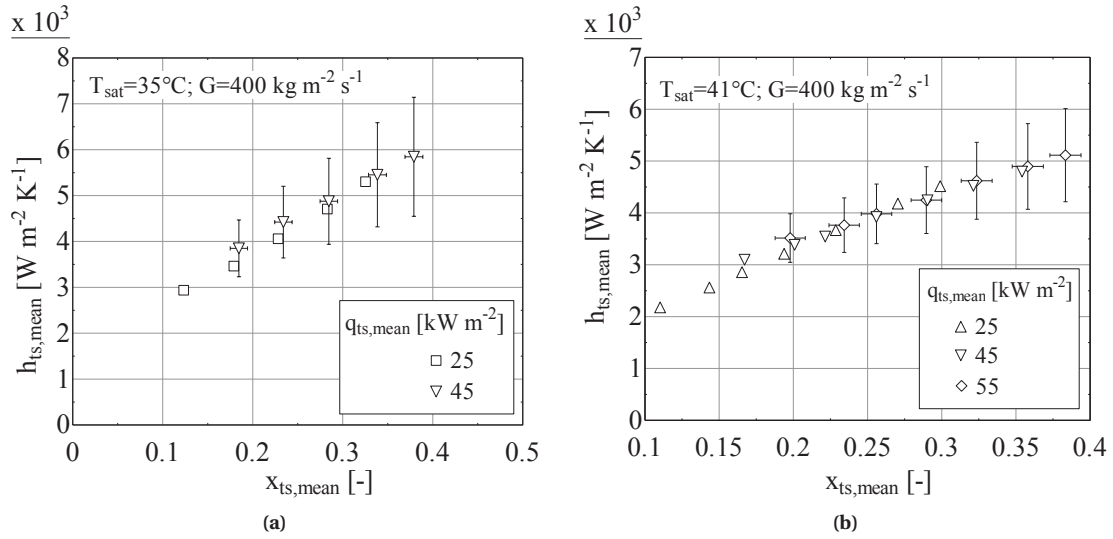


Figure 6.20: Effect of the heat flux on the mean heat transfer coefficient plotted against the mean vapour quality at $G=400 \text{ kg m}^{-2} \text{ s}^{-1}$ and (a), $T_{sat}=35^\circ\text{C}$; (b) $T_{sat}=41^\circ\text{C}$.

annular flows. Nucleate boiling may be an important mechanism at high heat fluxes and low vapor qualities. In the present studies, since the maximum heat flux is 55 kW m^{-2} and the minimum mean vapour quality is just over 0.1, nucleate boiling effects are not expected to dominate. Besides, should such heat transfer mechanism occur, its effects would be easily masked in the mean heat transfer coefficient by convective boiling dominating as vapour quality increases along the test section.

Another factor likely suppressing nucleate boiling is the smoothness polyimide tube surface, which displays a lack of cavities for potential nucleation sites. This effect is, nevertheless, uncertain, as some features on the polyimide channel inner surface were observed by the author using optical microscopy (see Fig. 6.4a). These surface characteristics, probably related to the extrusion process used for manufacturing the polyimide tubes, could act as nucleation sites. On the other hand, the polyimide tube wall thermal conductivity is extremely low ($0.12 \text{ W m}^{-1} \text{ K}^{-1}$, or 130 times lower than stainless steel), hindering reaching the required high wall superheating needed for nucleate boiling to occur continuously. Furthermore, the R245fa refrigerant displays a high specific volume of vapour. For a given mass flux, two-phase flow of fluids with high specific volume of vapour display high velocities of the vapour phase. This enhances forced convective effects between the liquid and vapour interfaces, suppressing nucleation of vapour bubbles next to the wall.

The results showing no dependence of the heat flux on the heat transfer coefficient are opposite to the flow boiling data obtained by Tibirić and Ribatski [103] at the same experimental apparatus with the same fluid (R245fa) in a stainless steel channel of similar inner diameter, 2.32 mm ID, but longer length, 464 mm. This indicates that the material and the surface characteristics of the channel may in fact influence the flow boiling heat transfer mechanisms.

Influence of the saturation temperature

The fluid pressure is the last of the parameters influencing the flow boiling heat transfer coefficient considered in this study. Since the R245fa refrigerant enters the polyimide channel in saturated conditions at all times, examining the influence of the mean saturation temperature of the fluid on the mean heat transfer coefficient is equivalent to using the mean pressure. Two trends were identified:

1. At low mass and heat fluxes, the mean heat transfer coefficient depends weakly on the saturation temperature, increasing slightly for higher temperatures, as reported in Fig. 6.21a.
2. At higher mass and heat fluxes, the mean heat transfer coefficient shows the opposite trend: it decreases when increasing the saturation temperature, as shown in Fig. 6.21b.

Trend 2 is most probably related to the decrease of the vapour specific volume at higher temperatures (see appendix C, R245fa refrigerant saturation temperatures of 35, 40 and 50°C), which reduces the intensity of convective effects, leading to a slight decrease of the heat transfer coefficient. The decrease of the liquid thermal conductivity might be contributing to the heat transfer coefficient drop too.

Tibirića and Ribatski [103] reported that the heat transfer coefficient increases with increasing saturation temperature in a 2.32 mm ID stainless steel channel, especially at low mass fluxes and low vapour qualities, the conditions where nucleate boiling typically dominates. Increasing the fluid pressure (or saturation temperature) caused a decrease of the surface tension and, subsequently, lower bubble departure diameters. The result is a higher density of nucleation sites and intensification of

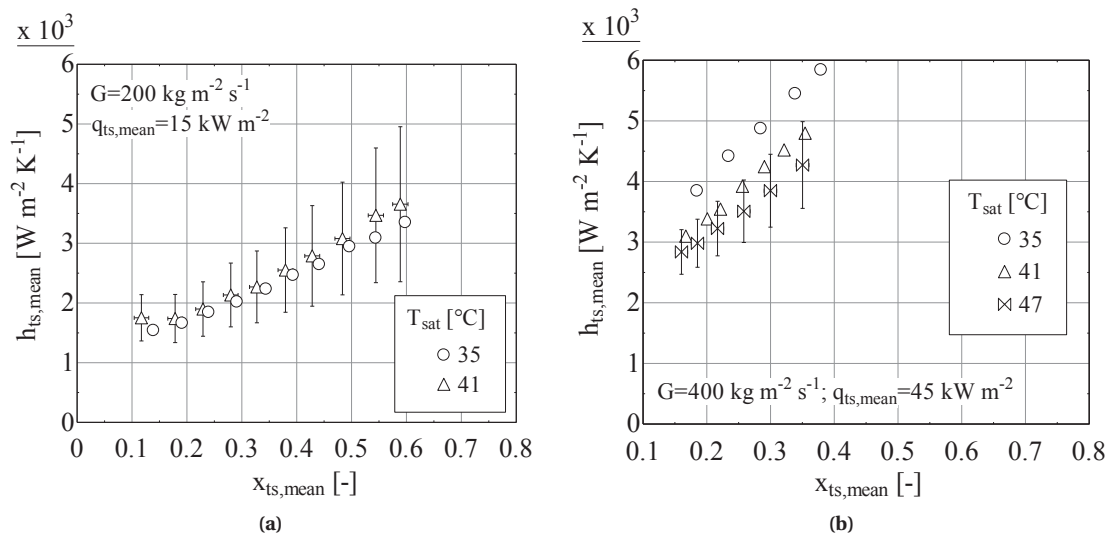


Figure 6.21: Effect of the saturation temperature on the mean heat transfer coefficient, plotted against the mean vapour quality in the test section, at: (a) $G=200 kg m^{-2} s^{-1}$ and $q_{ts,m}=15 kW m^{-2}$, and (b) $G=400 kg m^{-2} s^{-1}$ and $q_{ts,m}=45 kW m^{-2}$.

nucleate boiling. These effects were suppressed at high mass flux and vapour qualities, where convective boiling dominated. As no heat transfer intensification was observed in the present experimental tests upon increasing the fluid saturation temperature, it may be concluded that nucleate boiling does not become an important mechanism. It should be again noted that mean and not local heat transfer coefficients are measured, and thus any nucleate boiling effects occurring close to the polyimide channel inlet (where the refrigerant displays low vapour qualities) may be masked by convective boiling dominating in the rest of the test section.

6.7.2 Comparison with experimental results from similar studies

Fig. 6.22a presents experimental data obtained by Tibirićá and Ribatski [103] and Kanizawa *et al.* [125] in a 2.32 mm ID channel with R245fa refrigerant, compared to results from the present work. Also, the heat transfer coefficient dependence on the heat flux was studied by Kanizawa *et al.* [125], observing increasing values for increasing heat fluxes at low vapour qualities, whereas this effect disappears at higher qualities, as illustrated in Fig. 6.22b. The authors attributed this behaviour to nucleate boiling effects dominating at $x < 0.4$, with convective boiling taking over at higher qualities. Such effects were not observed in the present study, indicating again the dominance of convective boiling in the polyimide channel. The heat transfer coefficient trends with vapour quality were reproduced.

Studies in metallic channels have also reported heat transfer coefficient drops with increasing vapour quality at low vapour qualities and high heat fluxes, as displayed in Fig. 6.22b. This effect is related to nucleate boiling suppression effects [170] and bubble coalescence processes [125]. No heat

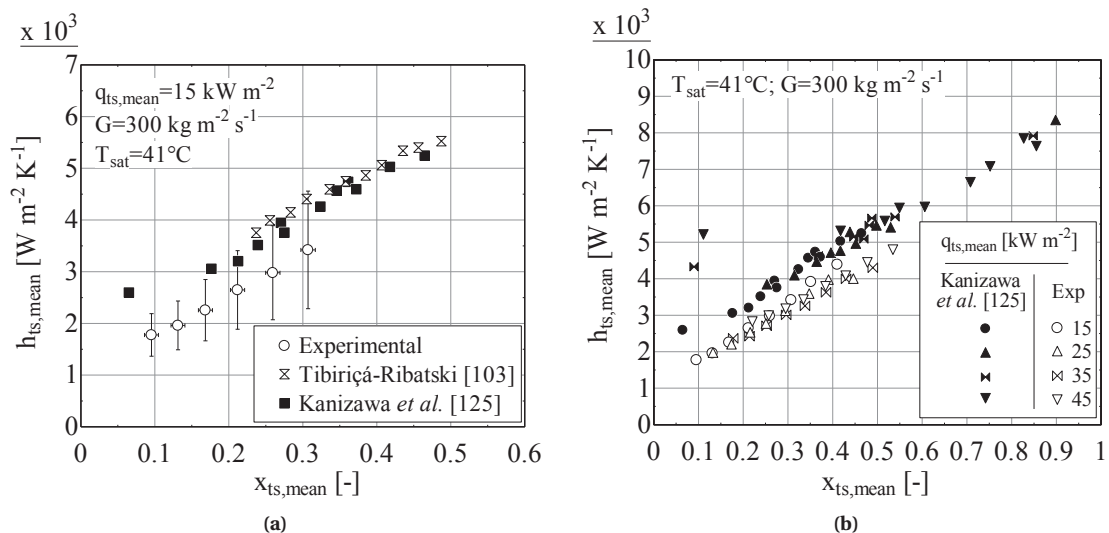


Figure 6.22: Comparison of the experimental data taken in the present work with similar experimental studies with R245fa in a 2.3 mm ID stainless steel channel: (a) data by Tibirićá and Ribatski [103] and Kanizawa *et al.* [125]; (b) influence of the heat flux as recorded by Kanizawa *et al.* [125].

transfer coefficient drops were observed in this study, since mean heat transfer coefficients and vapour qualities were reported along the test section, instead of local values. Besides, the weak nucleate boiling effects expected in the smooth, low thermal conductivity polyimide channel will not give rise to a heat transfer coefficient dependence on the heat flux.

6.7.3 Comparison with heat transfer prediction methods

A comparison between the experimental data and four flow boiling heat transfer prediction methods [121, 124, 130, 125] was conducted with the aim of evaluating their ability to predict the present flow boiling experimental data recorded in the polyimide channel. The heat transfer coefficient correlations are described in appendix A, section A.2.3. The prediction methods are implemented using the measured mean vapour quality in the polyimide tube ($x_{ts,m}$). The results yielded by the heat transfer coefficient methods are compared to the experimental data, using the mean absolute and relative error, (mae , mre), as defined in Eqs. 6.18 and 6.17, and the fraction of data predicted within the $\pm 30\%$ error band, $\varphi_{30\%}$. Table 6.8 summarises the statistical comparison of the methods with the present full experimental database (top rows) and with the experimental points displaying heat transfer coefficient uncertainties lower than $\pm 35\%$ (bottom rows).

The annular flow suite model by Cioncolini and Thome [130] is a purely convective approach, capturing the intensification of the convective effects in smooth tubes. According to Table 6.8, this method predicts more than 80% of the experimental results within a $\pm 30\%$ error band, if considering only the experimental data with uncertainty below $\pm 35\%$. Besides, it presents low mae and mre . The parametric effects of the mass flux, and especially the vapour quality, on the heat transfer coefficient, are well reproduced, as reported in Fig. 6.23. The method by Cioncolini and Thome is based upon an algebraic turbulence model for annular flows, the flow pattern in most of the two-phase experimental conditions tested in the present study, as recorded in the high-speed images, and it is the only one of the four methods evaluated here that does not take into consideration the influence of the heat flux

Table 6.8: Statistical analysis of the comparison between experimental and predicted mean two-phase flow boiling heat transfer coefficients in the polyimide channel.

Database	Parameter	Method			
		Liu-Winterton [121]	Kandlikar-Balasub. [124]	Cioncolini-Thome [130]	Kanizawa <i>et al.</i> [125]
Entire database	$\varphi_{30\%}$ [%]	50.7	26.9	73.5	22.4
	mae [%]	50.7	43.2	21.2	60.5
	mre [%]	35.7	-37.9	18.0	59.5
$U(h_{ts,m}) < 35\%$	$\varphi_{30\%}$ [%]	44.2	32.6	81.4	16.9
	mae [%]	44.2	39.2	18.0	65.8
	mre [%]	28.9	-32.8	15.0	65.6

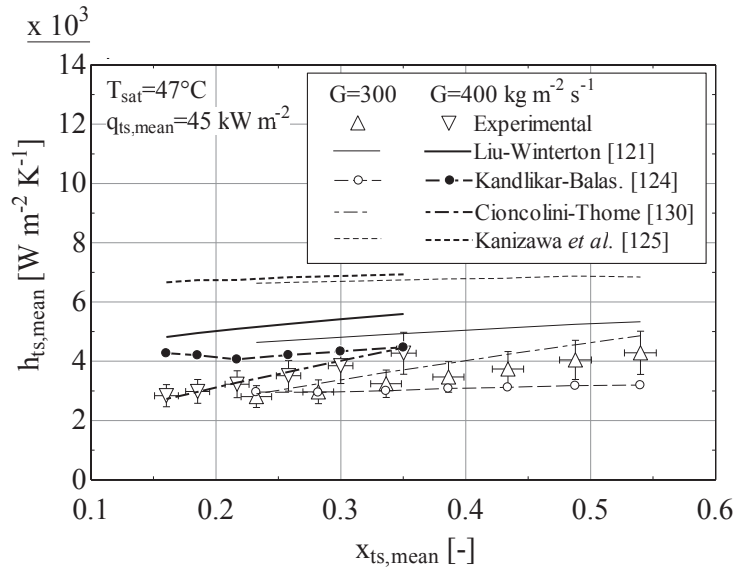


Figure 6.23: Influence of the mass flux on the heat transfer coefficient as computed by the methods from the literature, compared to the experimental data, at $q_{ts,m}=45 \text{ kW m}^{-2}$ and $T_{sat}=47^\circ\text{C}$.

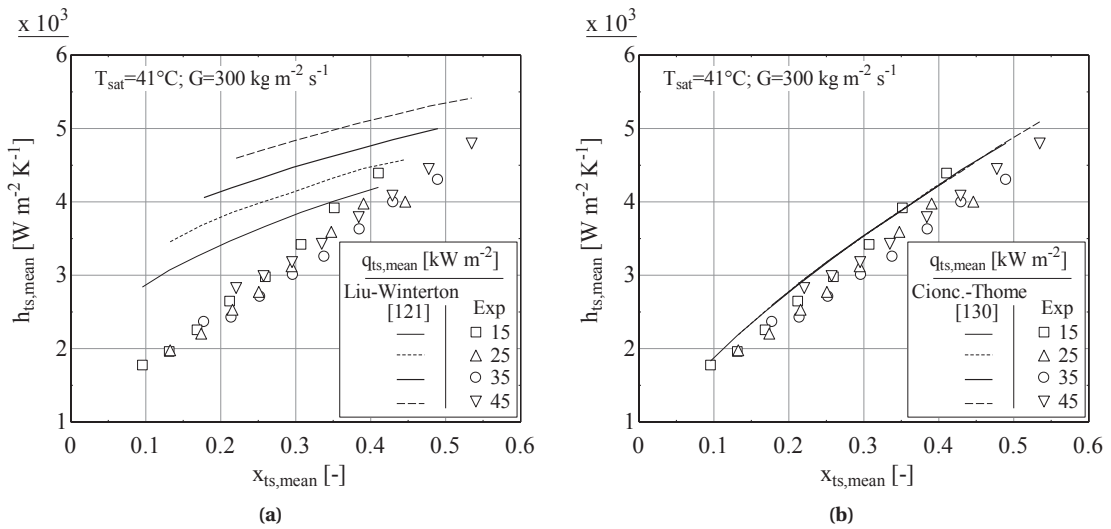


Figure 6.24: Influence of the heat flux on the heat transfer coefficient as computed by the methods by: (a) Liu and Winterton [121], and (b) Cioncolini and Thome [130]. Compared to the experimental data, at $G=400 \text{ kg m}^{-2} \text{ s}^{-1}$ and $T_{sat}=41^\circ\text{C}$.

(see Fig. 6.24b). This was precisely an effect observed in the entire experimental database. Also, the effect of the saturation temperature is qualitatively reproduced too, as displayed in and 6.25b.

The method by Liu and Winterton [121], originally developed for channels larger than 3 mm ID, is the second best from the four considered, although it barely predicts 50% of the entire experimental database with a $\pm 30\%$ error. The average errors with respect to the experimental database are also high. However, it provides acceptable qualitative predictions of the experimental mean heat transfer

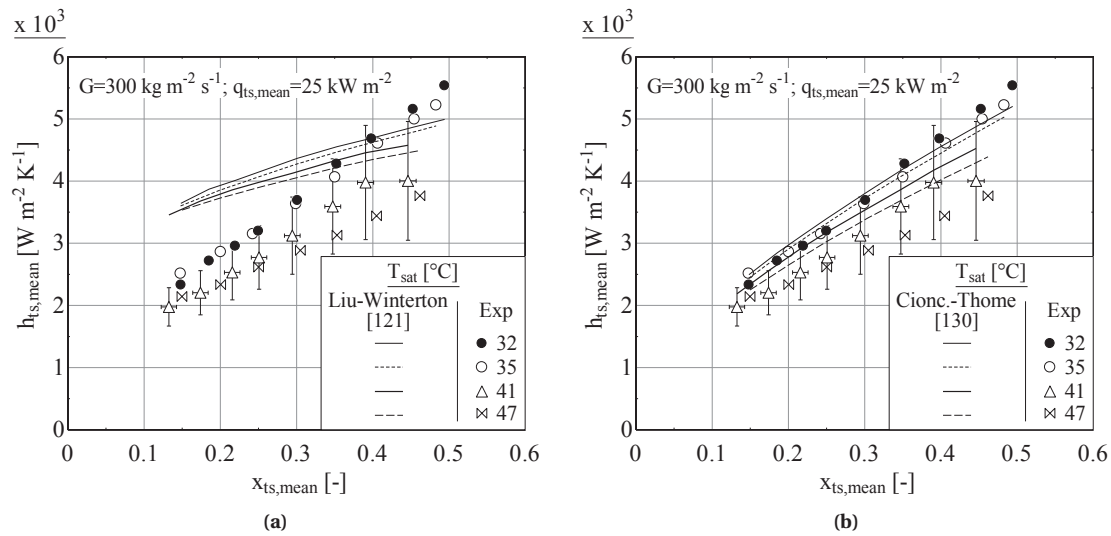


Figure 6.25: Influence of the saturation temperature on the heat transfer coefficient as computed by the methods by: (a) Liu and Winterton [121], and (b) Cioncolini and Thome [130]. Compared to the experimental data, at $G=300 \text{ kg m}^{-2} \text{ s}^{-1}$ and $q_{ts,m}=25 \text{ kW m}^{-2}$.

coefficient dependence on mass flux (Fig. 6.23) and saturation temperature (Fig. 6.25a). On the other hand, the method tends to overestimate heat transfer coefficients at low vapour qualities as it accounts for nucleate boiling effects. The method fails to predict the independence of the heat transfer coefficient with the heat flux, as observed in Fig. 6.24a.

Kandlikar and Balasubramanian [124] proposed a heat transfer coefficient correlation for flow boiling in the micro- and minichannel range. As reported in Table 6.8, the method only predicts 32.6% of the experimental data with a $\pm 30\%$ error span. They reported overestimation of the heat transfer coefficient at low vapour qualities due to increased heat transfer rate associated to the onset of nucleate boiling in the experimental database they used. At high vapour qualities, this method tends to underestimate the heat transfer coefficient, presenting it as nearly independent of the vapour quality. This is one of the reasons why the *mae* and *mre* are so high. The method qualitatively predicts the heat transfer coefficient trend with the mass flux, as displayed in Fig. 6.23, although it displays tendencies for the saturation temperature that are opposite to the ones observed experimentally. Lastly, the method predicts a positive influence of the heat flux on the heat transfer coefficient, especially at high mass fluxes, not found in the present data.

The heat transfer method for minichannels by Kanizawa *et al.* [125], based on the methodology proposed by Saitoh [119], predicts only 17% of the experimental database with less than $\pm 30\%$ error. Indeed, this method consistently overestimates the heat transfer coefficient values, especially at high mass and heat flux. It accounts for a positive influence of the mass flux on the heat transfer coefficient (see Fig. 6.23), but also a great dependence on the heat flux and on the saturation temperature, which are tendencies not observed for the present experimental database. It should be highlighted that the

roughness of the tubes evaluated by the authors varies from 100 to 400 nm, while polyimide films present roughness values of only between 12 and 35 nm [25].

Each of the methods was validated by verifying if they predict the trends observed in the experimental results, as described above. Fig. 6.26 provides a comparison of all the methods with several experimental cases, involving their dependence on the mean vapour quality. It is observed that the method by Cioncolini and Thome predicts the slope of the heat transfer coefficient with the mean vapour quality and matches the experimental data almost within the uncertainty of these, except for the case in Fig. 6.26a. In this case, all models fail to predict the heat transfer coefficient drop due to the

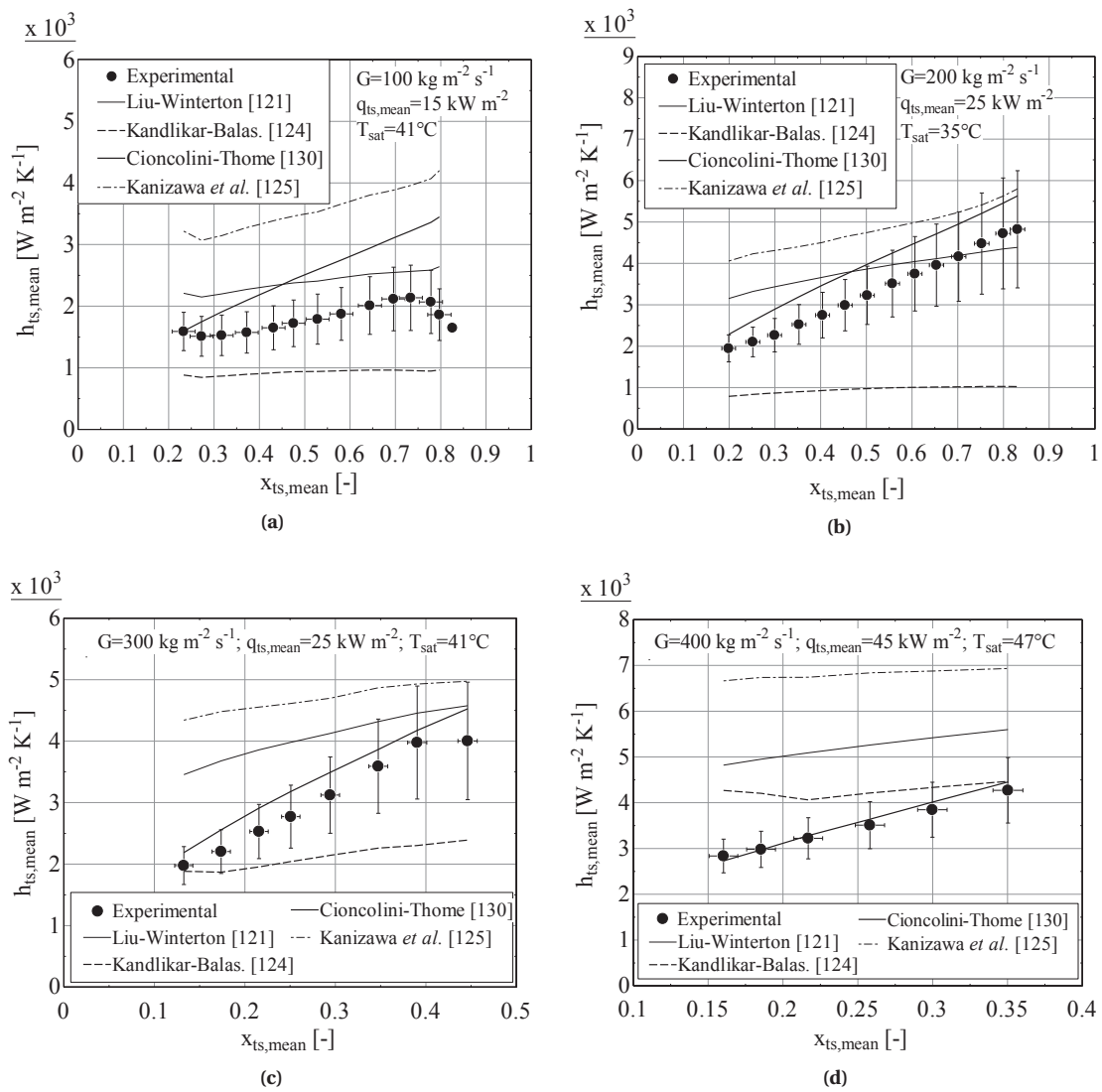


Figure 6.26: Comparison of the experimental data with four heat transfer coefficient prediction methods in the literature at different conditions: (a) $G=100 kg m^{-2} s^{-1}$, $q_{ts,m}=15 kW m^{-2}$, $T_{sat}=41^{\circ}C$; (b) $G=200 kg m^{-2} s^{-1}$, $q_{ts,m}=25 kW m^{-2}$, $T_{sat}=35^{\circ}C$; (c) $G=300 kg m^{-2} s^{-1}$, $q_{ts,m}=25 kW m^{-2}$, $T_{sat}=41^{\circ}C$; (d) $G=400 kg m^{-2} s^{-1}$, $q_{ts,m}=45 kW m^{-2}$, $T_{sat}=47^{\circ}C$.

onset of partial dryout conditions, which could be potentially captured by the flow regime-based model by Wojtan, Ursenbacher and Thome [76], but will not be done here. The method by Kandlikar and Balasubramanian exhibits low dependence on the vapour quality and underestimates the heat transfer coefficient at 35 and 41°C. The method by Liu and Winterton overestimates the heat transfer coefficient, like the correlation by Kanizawa *et al.*, which displays the worse fit of the whole experimental data.

6.8 Conclusion

The work described in this chapter showcases a new set of experimental results for average heat transfer coefficients of two-phase flow boiling R245fa in a 285 mm-long, 2.689 mm ID, water-heated, thin-walled polyimide channel, obtained at the Heat Transfer Research Group (HTRG) lab at the Escola de Engenharia de São Carlos, University of São Paulo (EESC-USP), Brazil, under the supervision of Prof. G. Ribatski. The following conclusions are reached:

- A complete experimental database provides an entirely new database for the mean flow boiling heat transfer coefficient in a polyimide channel with R245fa refrigerant, with mass fluxes ranging from 100 to 500 kg m⁻² s⁻¹, heat fluxes from 15 to 55 kW m⁻², vapour qualities between 0.05 and 0.80, and saturation temperatures of 35, 41 and 47°C.
- In general, mean heat transfer coefficients increase with increasing mass flux and vapour quality. No significant dependence on the heat flux was observed. These behaviours indicate the dominance of convective boiling as the main heat transfer mechanism. On the other hand, two trends are present regarding saturation temperature dependence: at low mass and heat fluxes, the mean heat transfer coefficient increases slightly for higher temperatures, while for higher mass and heat fluxes, the influence of the saturation temperature is stronger and shows the opposite trend.
- Results were compared to experimental data taken in the same experimental facility in smaller metallic channels. The heat transfer coefficient trends were qualitatively reproduced, although no local effects were observed, as the present work involves mean and not local heat transfer coefficients.
- Experimental results were compared against several leading heat transfer methods from the literature. The method by Cioncolini and Thome for convective boiling [130] provides the best results, with more than 80% of the experimental database predicted within a ± 30% error band, and reproduces the effects of the flow boiling parameters on the experimental heat transfer coefficients. This method is thus recommended for predicting flow boiling heat transfer coefficients in polyimide channels of less than 3 mm ID. The second best method is the one by Liu and Winterton [121], which however predicts a positive influence of the heat flux on the heat transfer coefficient, an effect not seen in the experimental results. The methods by Kandlikar and Balasubramanian [124], and by Kanizawa *et al.* [125] provided poor predictions in general.

Chapter 7

Conclusions and recommendations

This chapter covers the concluding remarks and recommendations on the work performed on the development of the ALICE ITS Upgrade cooling system at CERN, and the experimental flow boiling tests in a small polyimide channel. Appendix E focuses on the limitations of the aforementioned studies.

7.1 ALICE ITS Upgrade ultra-lightweight cooling system

Novel ultra-lightweight thermal concepts were proposed and studied here for the new cooling system of the ITS Upgrade detector. Solutions have been experimentally validated here that meet the material budget requirements, conform to material compatibility issues, and surpass the cooling requirements. Below, specific aspects are addressed.

- The Inner Barrel stave cooling system consists of a high-conductivity cooling plate made of CFRP with lightweight 1.024 mm ID polyimide channels on one side and the detector chips glued to the other side. The Outer Barrel half-staves have a similar design but are up to 5 times longer and 2 times wider, thus having 2.052 mm ID polyimide channels. The Inner and Outer Barrel stave baseline designs weigh 1.4 and 20.7 g and display estimated global material budgets of 0.28% and 0.77%, respectively, lower than the maximum admissible values of 0.30% and 1.00%.
- The baseline Inner Barrel stave provides a temperature difference between the heater and the coolant of less than 3 K for a power density of 0.15 W cm^{-2} and a water flow rate of 3 L h^{-1} . The detector can be cooled with the coolant hotter than the air dew point (maximum 12°C) keeping the chips below their maximum admissible temperature, 30°C . Good cooling performance was found at 0.30 and 0.50 W cm^{-2} . Cooling with two-phase C_4F_{10} refrigerant is possible with no changes to their structure, obtaining a similar cooling performance as with water. Using two-phase C_4F_{10} refrigerant results in an estimated 10.4% material budget reduction compared to liquid water, thanks to the presence of the vapour phase, 50 times less dense than the liquid.
- The two half-stave architectures proposed for the Outer Barrel provide a chip temperature

difference relative to the coolant of less than 8 K at 0.15 W cm^{-2} with water at 6 L h^{-1} . At 0.30 W cm^{-2} , the temperature difference is 15 K, the operational limit of the proposed Outer Barrel half staves. The staves also display similar cooling performance with two-phase C_4F_{10} refrigerant and water. Although larger cooling channels are required (2.667 mm ID), the estimated reduction of the stave global material budget with two-phase C_4F_{10} refrigerant as coolant is 3.8%.

- In general, the conduction thermal resistance in the stave dominates over the convective thermal resistance between the channel wall and the coolant. The staves are thus thermally robust. Using different coolants and operating conditions has low impact on the cooling performance.
- A set of nominal cooling conditions were identified. For water, they display pressure drops below 0.3 bar, ensuring on-stave sub-atmospheric coolant pressure. With two-phase C_4F_{10} as coolant, mass fluxes between 200 and $400 \text{ kg m}^{-2} \text{ s}^{-1}$ and mean vapour qualities in the stave around 0.4 are preferred. These conditions show good cooling performance, saturation temperature drops below 5 K, and high void fractions, yielding low coolant material budget peaks. Low temperature gradients on the heater (between 5 to 10 K) were seen upon examination of the infrared images.
- Single- and two-phase frictional pressure drops were predicted using methods for straight channels and singularities, validating the experimental setup.
- Coolant inventory experimental measurements with two-phase C_4F_{10} refrigerant were performed as a way of validating the use of void fraction prediction methods from the literature for the calculation of the material budget of the two-phase C_4F_{10} refrigerant. The void fraction method in the literature providing the best match with the experimental coolant inventory measurements after integrating it in the cooling channel length is the one by Niño *et al.* [85], followed by the methods by Zivi [81] and Steiner's version [84] of the void fraction method by Rouhani and Axelsson [83].

7.1.1 Recommendations

- It is recommended to subject fully-assembled staves (chips, FPC, and power bus) to cooling tests with the chosen coolant, once all services are developed. Water cooling tests for all the Inner Barrel staves in parallel and a single Outer Barrel layer, are foreseen in the ITS Upgrade agenda.
- Up to 30% of the total pressure drop is expected to occur at the Π -bend in the Inner Barrel staves (20% in the Outer Barrel half-staves). It can be minimised if using U-bends with smooth corners. 3D-printing allows fast manufacturing of the bends as one part each, provided that the polymers used comply with CERN regulations and tolerances of the ITS Upgrade detector are met.
- The experimental two-phase coolant inventories are compared to predictions over a wide range of vapour qualities, mass fluxes and heat fluxes. If further insight is required, it is recommended to determine the expected flow patterns by, at least, mass flux and vapour quality, and compare the data of each pattern with the most appropriate prediction methods from the literature.

7.2 Experimental flow boiling heat transfer in polyimide channels

- A new experimental flow boiling heat transfer database of nearly 300 points was recorded for a 2.689 mm ID water-heated, 285 mm-long polyimide channel with R245fa as operating refrigerant. The database comprises mass fluxes ranging from 100 to 500 kg m⁻² s⁻¹, heat fluxes from 15 to 55 kW m⁻², vapour qualities between 0.05 and 0.80, and three saturation temperatures: 35, 41 and 47°C. The average heat transfer coefficient uncertainty is 21% and ranges between 13 and 39%.
- The mean heat transfer coefficient increases with the mass flux and the vapour quality. No significant dependence on the heat flux was observed. As the tube is smoother than metallic channels used in similar studies, fewer nucleation points are available, resulting in an earlier suppression of nucleate boiling in favour of convective boiling. Two trends were observed regarding the dependence of the heat transfer coefficient on the saturation temperature: at low mass and heat fluxes, the mean heat transfer coefficient weakly increases for higher temperatures, while at higher mass and heat fluxes it decreases for increasing saturation temperatures.
- Results were compared to experimental data taken at the same experimental facility in 2.3 mm ID stainless steel channels. The heat transfer coefficient trends with mass flux and vapour quality were reproduced. No nucleate boiling effects were seen for different heat fluxes at low x and G .
- The experimental database was compared against several heat transfer methods from the literature. The method by Cioncolini and Thome [130] provides the best match, predicting more than 80% of the data within a $\pm 30\%$ error band, and reproduces well the effects of all the studied flow boiling parameters on the heat transfer coefficient. This method is thus recommended for predicting flow boiling heat transfer coefficients in polyimide channels of less than 3 mm ID.

7.2.1 Recommendations and suggestions on further research aspects

- Since the heating water inlet-outlet temperature difference is the parameter making up for most of the global heat transfer uncertainty, using a thermopile instead of the four thermocouples currently installed will significantly lower the uncertainty of the mean heat transfer coefficient.
- Direct flow visualisation on the test section is possible by removing locally the thermal insulation, since all tubes and fluids have good transparency. Flow pattern identification may be performed at saturation temperatures close to the ambient in two-phase adiabatic conditions.
- Other heat transfer studies on polyimide channels that may be done in the same facility are:
 - Influence of the refrigerant: repeat the flow boiling tests with other fluids (R134a, R1234ze).
 - Influence of the channel diameter: the test section can be adapted to a 2.052 mm ID channel, the same size used in the ITS Upgrade Outer Barrel half-staves. The 1.024 mm ID tube, used in the Inner Barrel staves, would require further alterations to the test rig.
 - Experimental condensation studies can be performed with no changes to the test section.

Appendix A

Correlations and methods

This appendix summarises the correlations and methods used in the present dissertation. The implementation of all the correlations was validated by the author using data from the source papers and books. Nevertheless, the reader is encouraged to refer to the original literature to better understand the range of validity and the use of each correlation.

A.1 Pressure drop

A.1.1 Single-phase pressure drop correlations

Straight channels

The single-phase pressure drop of a fluid of density ρ flowing with an average velocity u in a pipe of inner diameter D_i over a length L (assuming the pressure gradient is constant over that length), is defined by:

$$\Delta p = \zeta \frac{L}{D_i} \frac{\rho u^2}{2} \quad (\text{A.1})$$

where ζ is the Darcy friction factor. Churchill [145] proposed a friction factor correlation spanning all flow regimes, as follows:

$$\zeta = 8 \left[\left(\frac{8}{Re} \right)^{12} + \frac{1}{(A+B)^{1.5}} \right]^{(1/12)} \quad (\text{A.2})$$

where

$$A = \left\{ -2.457 \log \left[\left(\frac{7}{Re} \right)^{0.9} + 0.27 \left(\frac{Ra}{Di} \right) \right] \right\}^{16} \quad (\text{A.3})$$

$$B = \left(\frac{37530}{Re} \right)^{16} \quad (\text{A.4})$$

Singularities (bends)

Singularities are elements in internal flows that change the direction of the flow or the section available for it, resulting in additional pressure drops. Singular pressure drops are expressed as follows:

$$\Delta p_{sing} = \zeta_{sing} \frac{\rho u^2}{2} \quad (\text{A.5})$$

where ζ_{sing} is the friction factor due to the presence of a singularity. This parameter depends on the flow regime, the type of singularity and its geometry, but it is also sensitive to the presence of other singularities and the flow condition upstream and downstream. Predictive methods of ζ_{sing} are mostly empirical and account for a variety of pipe configurations and flow conditions. The author recommends the use of the methods by Idelchik [146] for approximately estimating the singular pressure drops in single-phase flows.

The singularity contributing more to the global pressure drop in the ALICE ITS Upgrade staves is the Π -bend element connecting the two polyimide tubes. Idelchik [146] proposes in his manual (section VI, Diagram 6-7) a correlation to calculate the singular pressure drop in sharp elbows with a 0° to 180° bend and rough walls, at any Reynolds number. The singular friction factor is defined as follows:

$$\zeta_{sing} = k_{\Delta} k_{Re} C_1 A \zeta_1 \quad (\text{A.6})$$

where k_{Δ} and k_{Re} are determined from a table. For $300 < Re < 40000$, $k_{\Delta} = 1.0$ and $k_{Re} = 45 \lambda_{Re}$. λ_{Re} is the Darcy friction factor for smooth pipes, and can be calculated using correlations such as the Churchill one [145], or Eqs. A.9, A.10, or A.54, depending on the flow regime.

$C_1 = 1$ for circular sections. Finally, $A = 1.20$ and $\zeta_1 = 3.00$ for a 180° bend. With the value of ζ_{sing} (Eq. A.6), the singular pressure drop is calculated using Eq. A.5. The expression can be multiplied by 1.2 if there is a recess in the bend (i.e. a dead-end volume at the outside of the curve).

For any different geometry or flow conditions than reported here, the reader is encouraged to review the methods in the handbook by Idelchik [146]. Also, the diameter variations at the stave inlet/outlet connections contribute to the singular pressure drops, but they are not abrupt and represent only a small fraction (less than 20%) of the dominant pressure drop across the Π -bend. For this

reason, although the singular pressure drops due to changes in the diameters were considered in the calculations in chapter 5, these methods are not described here for brevity. Besides, they require different inputs depending on the size of the channels and the geometries. The reader is referenced to the original bibliography [146] for further information.

A.1.2 Two-phase frictional pressure drop correlations

Straight channels

One of the most used correlations in literature to estimate the frictional pressure drop of a two-phase flows in straight vertical or horizontal channels is the correlation by Friedel [92]. This separated flow model uses a two-phase multiplier to define the two-phase frictional pressure drop, as follows:

$$\Delta p_{tp,frict} = \Delta p_{LO} \Phi_{LO}^2 \quad (\text{A.7})$$

where Δp_{LO} is the liquid-only pressure drop, as described in Eq. A.1. Rearranging it, the equation remains as expressed below:

$$\Delta p_{LO} = \frac{\zeta_{LO}}{2\rho_l} \frac{L}{D_i} \left(\frac{\dot{m}}{A_i} \right)^2 \quad (\text{A.8})$$

with the liquid-only Darcy friction factor ζ_{LO} calculated depending on the flow regime:

$$\zeta_{LO} = \frac{64}{Re_{LO}} \quad , \quad Re_{LO} < 2300 \quad (\text{A.9})$$

$$\zeta_{LO} = \frac{0.3164}{(Re_{LO})^{0.25}} \quad , \quad 2300 \leq Re_{LO} \leq 100000 \quad (\text{A.10})$$

For more accurate ζ_{LO} results in the transitional regime, the correlation by Churchill [145] can be used instead. Re_{LO} is the Reynolds number evaluated assuming the liquid-vapour mixture flows entirely as a liquid. It is defined below:

$$Re_{LO} = \frac{GD_i}{\mu_l} \quad (\text{A.11})$$

The vapour-only Darcy friction factor (ζ_{VO}) is calculated with Re_{VO} , in the same fashion.

Φ_{LO} is the two-phase multiplier:

$$\Phi_{LO} = E + \frac{3.23 F H}{Fr^{0.045} We^{0.035}} \quad (\text{A.12})$$

where the dimensionless variables are defined as follows:

$$E = (1 - x)^2 + x^2 \frac{\rho_l \zeta_{VO}}{\rho_v \zeta_{LO}} \quad (\text{A.13})$$

$$F = x^{0.78} (1 - x)^{0.224} \quad (\text{A.14})$$

$$H = \left(\frac{\rho_l}{\rho_v} \right)^{0.91} \left(\frac{\mu_v}{\mu_l} \right)^{0.19} \left(1 - \frac{\mu_v}{\mu_l} \right)^{0.70} \quad (\text{A.15})$$

The dimensionless Froude and Weber numbers:

$$Fr = \frac{G^2}{g D_i \rho_{Homog}^2} \quad (\text{A.16})$$

$$We = \frac{G^2 D_i}{\gamma \rho_{Homog}} \quad (\text{A.17})$$

where the homogeneous density is defined below:

$$\rho_{Homog} = \frac{\rho_l \rho_v}{x \rho_l + (1 - x) \rho_v} \quad (\text{A.18})$$

The Friedel correlation, based on a large experimental database, is applicable to a large number of fluids with fair accuracy. Several authors, though, restrict its use to cases and fluids displaying viscosity ratios (μ_l/μ_v) lower than 1000.

The method of Müller-Steinhagen and Heck [93] is often referenced in the literature due to its accuracy and its simplicity. The two-phase frictional pressure gradient along a channel is defined as follows:

$$\left(\frac{dp}{dz} \right)_{tp,frict} = H(1 - x)^{1/\gamma} + Bx^\gamma \quad (\text{A.19})$$

with

$$H = A + \omega(B - A)x \quad (\text{A.20})$$

$$A = \left(\frac{dp}{dz} \right)_{LO} \quad (\text{A.21})$$

$$B = \left(\frac{dp}{dz} \right)_{VO} \quad (\text{A.22})$$

where $\omega = 2$ and $\lambda = 3$. A and B are the frictional pressure gradients, calculated using Eqs. A.8 to A.11, considering the two-phase flow mixture as entirely liquid or vapour, respectively.

Since the original method by Müller-Steinhagen and Heck is based upon an experimental database made mainly of results for conventional channels, Da Silva and Ribatski [95] modified it to adapt it better to two-phase flow boiling results obtained in mini- and microchannels. The authors redefined the ω and λ parameters, with $\omega = 1.037$ and $\lambda = 1.026$ as the new values fitting best their experimental database. In the results in chapter 6 in this thesis, the original method by Müller-Steinhagen and Heck fitted better the experimental results in adiabatic conditions than the model by Da Silva and Ribatski, despite it was developed with the R245fa and R134a refrigerants in the same experimental facility described in chapter 6, but for stainless steel rigs of 1.1 and 2.3 mm ID.

Last, Sempértegui-Tapia and Ribatski [96] proposed another modification of the Müller-Steinhagen and Heck [93] method in order to account for different channel geometries. Their model is based upon experimental two-phase pressure drop data obtained in stainless steel minichannel rigs at the same experimental facility described in chapter 6. It consists of the same equations as the Müller-Steinhagen and Heck model [93] (Eqs. A.19 to A.22), but the parameters have different values. In particular, $\lambda = 2.313$, and ω now accounts for the influence of the vapour-only Reynolds number, as follows:

$$\omega = a \exp(b Re_{VO}) \quad (\text{A.23})$$

with $a = 3.01314$ and $b = -0.00000463745$. Re_{VO} is the Reynolds number for the liquid-vapour mixture flowing entirely as a vapour. It is defined as in Eq. A.11, but considering the vapour physical properties instead.

Singularities (bends)

The B-type equation presented in the correlation by Chisholm [101] is used to calculate the two-phase frictional pressure drop in a bend (90° to 180°) of a bending radius r :

$$\Delta p_{tp,frict} = \Delta p_l \Phi_l^2 \quad (\text{A.24})$$

where Δp_l is the liquid pressure drop:

$$\Delta p_l = \frac{\zeta}{2 \rho_l} \frac{z}{D_i} \left(\frac{\dot{m}}{A_i} \right)^2 \quad (\text{A.25})$$

z/D is the ratio between the equivalent length and the channel diameter, calculated using the relative radius of the bend, r/D , as the input in the plot in Fig. A.1 [172]. The liquid Darcy friction factor ζ is calculated using Eqs. A.9 or A.10, depending on the flow regime, although other implementations of the Darcy friction factor for the transitional/turbulent flow regimes are possible. The liquid Reynolds number (Re_l) is used instead of the liquid-only Reynolds number:

$$Re_l = \frac{G(1-x)D_i}{\mu_l} \quad (\text{A.26})$$

Assuming the friction factor is independent of the Reynolds number, the two-phase multiplier is calculated as follows:

$$\Phi_l^2 = 1 + \left(\frac{\rho_l}{\rho_v} - 1 \right) [Bx(1-x) + x^2] \quad (\text{A.27})$$

where, for bends from 90° to 180° , B is defined as follows:

$$B = 1 + \frac{2.2}{\zeta \frac{z_{90^\circ}}{D_i} \left(2 + \frac{r}{D_i} \right)} \frac{z_{90^\circ}}{z} \quad (\text{A.28})$$

For 90° bends, $z_{90^\circ} = 1$.

More information on this correlation, as well as its validation against experimental data, can be found in the VDI Atlas, chapter L2.2, section 3 [147].

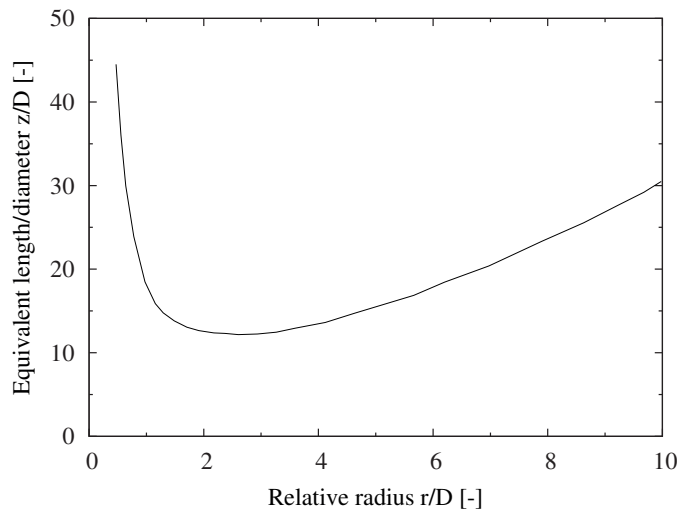


Figure A.1: Ratio of the equivalent length and the tube diameter with the same pressure drop as that of a 90° bend. Plot adapted from [172].

A.2 Heat transfer

The Nusselt number represents the ratio of the heat transfer occurring by convection between a solid surface and a fluid in contact with it, to the heat transfer by conduction (as if the fluid was stagnant):

$$Nu = \frac{hD_i}{\alpha} \quad (\text{A.29})$$

The heat transfer coefficient can be calculated from the equation above:

$$h = \frac{Nu\alpha}{D_i} \quad (\text{A.30})$$

Different correlations can be used to calculate the Nusselt number, depending on the physical state of the fluid, the flow conditions and the dominant heat transfer mechanism, among other parameters. The correlations used in this dissertation are shown below.

A.2.1 Free convection

Free convection problems usually consists in finding the relationship between Nu , Pr and the Rayleigh number, Ra . This number expresses the relationship between buoyancy and viscous forces accounting at the same time for the contribution of momentum and thermal diffusivities. It is defined in a simplified way as follows:

$$Ra = \frac{g\beta(T_{wall} - T_{\infty})L^3}{\nu\kappa} \quad (\text{A.31})$$

where L is the characteristic length, T_{∞} is the fluid temperature far from the surface, and β is the isobaric volume expansion coefficient, which for ideal gases can be approximated as $\beta = 1/T'$. κ is the thermal diffusivity, defined below:

$$\kappa = \frac{\alpha}{\rho c_p} \quad (\text{A.32})$$

The physical properties of the fluids are expressed at the film temperature $T_{film} = (T_{wall} - T_{\infty})/2$.

Several correlations are available in the literature to estimate the free convection heat transfer depending on the geometry and the Rayleigh number. A comprehensive explanation on the physics of each case can be found in [164].

Horizontal plate

In an horizontal plate of dimensions $a \times b$, the characteristic length L is defined as the area divided by two times the perimeter:

$$L = \frac{ab}{2(a+b)} \quad (\text{A.33})$$

Two free convection heat and mass transfer scenarios may take place in an horizontal exchanging heat with a surrounding fluid by free convection:

1. The top surface of the plate is warmer than the surrounding fluid, which is equivalent to the scenario of the bottom surface being cooler than the fluid.

2. The top surface is colder than the fluid (same as bottom surface being warmer than the fluid)

For the first scenario, the correlation by Stewartson [141] may be used:

$$Nu = 0.766 [Ra f_2(Pr)]^{1/5}, \quad \text{if } Ra f_2(Pr) \leq 7 \cdot 10^4 \quad (\text{laminar flow}) \quad (\text{A.34})$$

$$Nu = 0.15 [Ra f_2(Pr)]^{1/3}, \quad \text{if } Ra f_2(Pr) \geq 7 \cdot 10^4 \quad (\text{turbulent flow}) \quad (\text{A.35})$$

where $f_2(Pr)$ describes the effect of the Prandtl number in the $0 < Pr < \infty$ range:

$$f_2(Pr) = \left[1 + \left(\frac{0.322}{Pr} \right)^{11/20} \right]^{-20/11} \quad (\text{A.36})$$

In the second scenario (top surface colder than the fluid), the correlation by Churchill [142] is used for the laminar flow regime only ($1000 < Ra f_1(Pr) < 10^{10}$):

$$Nu = 0.6 [Ra f_1(Pr)]^{1/5} \quad (\text{A.37})$$

where $f_1(Pr)$ accounts for the effect of the Prandtl number in the $0.001 < Pr < \infty$, according to Churchill and Usagi [173]:

$$f_1(Pr) = \left[1 + \left(\frac{0.492}{Pr} \right)^{9/16} \right]^{-16/9} \quad (\text{A.38})$$

Vertical plate

The correlation by Churchill and Chu [140] quantifies the free convection heat transfer for vertical plates in the $0.1 \leq Ra \leq 10^{12}$ range, as follows:

$$Nu = \left\{ 0.825 + 0.387 [Ra f_1(Pr)]^{1/6} \right\}^2 \quad (\text{A.39})$$

with $f_1(Pr)$ defined in Eq. A.38. The characteristic dimension in vertical plates is the vertical dimension.

Inclined surfaces represent an intermediate case between horizontal and vertical (see [164]).

Long cylinder

The correlation by Churchill and Chu [161] is applied, considering the characteristic dimension as the cylinder diameter ($L = D$):

$$Nu_D = \left\{ 0.60 + \frac{0.387 Ra_D^{1/6}}{[1 + (0.559/Pr)^{9/16}]^{8/27}} \right\}^2, \quad Ra_D \lesssim 10^{12} \quad (\text{A.40})$$

A.2.2 Single-phase forced convection in internal flows

It is important to take into consideration the flow thermal and hydraulic development, as well as the heat transfer boundary conditions, to estimate the forced convection heat transfer in internal flows. For this reason, the reader is encouraged to review the available methods to find the most appropriate one for each particular case. Comprehensive reviews can be found in [147, 164].

The correlations used in this thesis are described below, including the conditions and ranges of applicability. The physical properties of the fluids are expressed at its mean temperature $T_m = (T_{in} - T_{out})/2$. For large fluid temperature differences, it is recommended to review the original bibliography and use appropriate correlations.

Laminar flow, constant heat flux: hydrodynamic and thermal development of the flow

The thermal entry length for laminar single-phase flows ($Re < 2300$) at a constant, uniform heat flux in a round channel is defined as follows [136]:

$$\frac{L_{th,dev,lam}}{D_i} \simeq 0.05 Re_{D_i} Pr \quad (\text{A.41})$$

while the hydrodynamic development length is independent of the Prandtl number:

$$\frac{L_{hydro,dev,lam}}{D_i} \simeq 0.05 Re_{D_i} \quad (\text{A.42})$$

Fully developed (thermally and hydrodynamically) laminar flows with a constant heat flux bound-

ary condition show a Nusselt number at a distance z from the pipe inlet of:

$$Nu_{z,1} = 4.354 \quad (\text{A.43})$$

For flows developed hydrodynamically but still developing thermally, the local Nusselt number is given by an asymptote:

$$Nu_{z,2} = 1.302 (Re Pr D_i / z)^{1/3} \quad (\text{A.44})$$

where z is the longitudinal (axial) coordinate of the pipe.

Gauler [174] developed an expression to calculate the local Nusselt number in the thermal and hydrodynamic entry region of the flow into a pipe:

$$Nu_{z,3} = 0.462 (Pr)^{(1/3)} (Re D_i / z)^{1/2} \quad , \quad Pr > 0.7 \quad (\text{A.45})$$

Finally, Spang [148] combined the expressions above to calculate in a numerical way the local Nusselt numbers for thermally and hydrodynamically developing flows in a pipe at a constant heat flux and at a distance z from the inlet:

$$Nu_z = [Nu_{z,1}^3 + (Nu_{z,2} - 1)^3 + Nu_{z,3}^3]^{1/3} \quad (\text{A.46})$$

If the flow is hydrodynamically developed but it is still developing thermally, then:

$$Nu_z = [Nu_{z,1}^3 + 1 + (Nu_{z,2} - 1)^3]^{1/3} \quad (\text{A.47})$$

These equations can be implemented by discretising the pipe flow in length, obtaining the local Nusselt numbers and heat transfer coefficients. More expressions regarding the mean Nusselt numbers in thermally/hydrodynamically developing laminar flows, as well as expressions regarding high temperature changes in the fluid can be found in the VDI Atlas, chapter G1, section 3 [147].

Transition between laminar and fully developed turbulent flow

In these conditions, the flow regime strongly depends on the entrance geometry and the upstream flow conditions, among other factors. Gnielinski [149] developed a correlation that interpolates between the laminar ($Re = 2300$) and the turbulent flow regimes ($Re = 10000$):

$$Nu = (1 - \eta) Nu_{m,lam,2300} + \eta Nu_{m,turb,10000} \quad (\text{A.48})$$

η is expressed below:

$$\eta = \frac{Re - 2300}{10000 - 2300}, \quad 0 \leq \eta \leq 1 \quad (\text{A.49})$$

$Nu_{m,lam,2300}$ is the average Nusselt number at $Re = 2300$. For a constant wall heat flux, it can be calculated from the mean Nusselt number expression put forward by Spang [148], as follows:

$$Nu_{m,lam,2300} = [83.326 + (Nu_{m,2,Re=2300} - 0.6)^3 + Nu_{m,3,Re=2300}^3]^{1/3} \quad (\text{A.50})$$

where

$$Nu_{m,2,Re=2300} = 1.953 (2300 Pr D_i/L)^{1/3} \quad (\text{A.51})$$

$$Nu_{m,3,Re=2300} = 0.924 (Pr)^{1/3} (2300 D_i/L)^{1/2} \quad (\text{A.52})$$

$Nu_{m,turb,10000}$ is the Nusselt number at $Re = 10000$. According to Eq. A.56, it is defined as follows:

$$Nu_{m,turb,10000} = \frac{(0.0308/8) 10000 Pr}{1 + 12.7 (0.0308/8)^{1/2} (Pr^{2/3} - 1)} \left[1 + \left(\frac{D_i}{L} \right)^{2/3} \right] \quad (\text{A.53})$$

Fully developed turbulent flow

Petukhov [151] put forward an expression of the friction factor in the $3000 \lesssim Re \lesssim 5 \cdot 10^6$ range:

$$\zeta = [1.82 \log_{10}(Re) - 1.64]^{-2} \quad (\text{A.54})$$

The Nusselt number can be calculated as follows in the $10000 \lesssim Re \lesssim 5 \cdot 10^6$; $0.5 \lesssim Pr \lesssim 2000$ range:

$$Nu = \frac{(\zeta/8) Re Pr}{1.07 + 12.7 (\zeta/8)^{1/2} (Pr^{2/3} - 1)} \quad (\text{A.55})$$

Gnielinski [150] advanced the expression by Petukhov to account for the relative size of the pipe:

$$Nu = \frac{(\zeta/8) Re Pr}{1 + 12.7 (\zeta/8)^{1/2} (Pr^{2/3} - 1)} \left[1 + \left(\frac{D_i}{L} \right)^{2/3} \right] \quad (\text{A.56})$$

with

$$\zeta = [1.8 \log_{10}(Re) - 1.5]^{-2} \quad (\text{A.57})$$

This correlation is intended for the $10000 \leq Re \leq 10^6$ and $0.1 \leq Pr \leq 1000$ ranges, with pipes displaying $D_i/L \leq 1$. For pipes displaying low D_i/L ratios (i.e. long, slender tubes), Gnielinski [150] proposed another expression of the Nusselt number, which is applicable to a wider range of conditions:

$$Nu = \frac{(\zeta/8)(Re - 1000)Pr}{1 + 12.7(\zeta/8)^{1/2}(Pr^{2/3} - 1)} \quad (\text{A.58})$$

with ζ calculated according to Eq. A.54. This expression is valid in the $3000 \lesssim Re \lesssim 5 \cdot 10^6$ and $0.5 \lesssim Pr \lesssim 2000$ ranges.

The correlation by Dittus and Boelter [123] typically yields a significantly worse match with experimental data than the correlations presented above, with deviations up to 25% [164]. However, it is used in a few two-phase heat transfer correlations. The Nusselt number is expressed below:

$$Nu = 0.023 Re^{4/5} Pr^n \quad (\text{A.59})$$

where $n=0.4$ when the fluid is being heated, and $n=0.33$ when it is being cooled. The Dittus-Boelter correlation is valid in these conditions: $Re \geq 10000$; $0.6 \leq Pr \leq 160$; and $L/D_i \geq 10$.

All the correlations in this subsection can be used for both constant heat flux or constant wall temperature boundary conditions, as they yield very similar results in fully developed turbulent flows.

Flow in a concentric annular duct

In the study described chapter 6, the heat flux to boil the R245fa refrigerant flowing inside a polyimide channel is provided with warm water flowing in the annular space between the polyimide channel and a larger glass tube, in a concentric heat exchanger fashion. Some correlations specifically developed for flows in cylindrical annular gaps are used for calculating the heat transfer coefficient between the water and the outer polyimide tube surface. They are described in the VDI Heat Atlas [147], chapter G2, sections 1 to 7.

The validity of these correlations for the particular experimental cases in 6 was assessed using experimental data from tests with two counter-current water flows (see section 6.4.2). It must be emphasised that these correlations are intended for a constant wall temperature boundary condition, which, for the turbulent flows established in the tests in chapter 6, is equivalent to the constant heat flux boundary condition. Therefore, only the correlations for the transitional and fully turbulent flow regimes are described in this subsection, because the water flow in the annulus in all tests shown in chapter 6 was always chosen in order to display $Re_{ann} > 3000$.

The hydraulic diameter of the annulus is defined as follows:

$$D_h = D_{ann} - D_e \quad (\text{A.60})$$

where D_{ann} is the inner diameter of the large tube in the annulus (the glass tube in the studies in chapter 6) and D_e is the external diameter of the annulus small tube (the polyimide channel). The diameter ratio is defined below:

$$a = D_e / D_{ann} \quad (\text{A.61})$$

The boundary condition consists in heat transfer occurring between the flow in the annulus and the small tube (polyimide channel) outer surface. The inner surface of the large tube (glass tube) is considered adiabatic, as there is very low heat transfer to the room air. The correlation for this boundary condition is described below for different flow regimes.

For fully developed turbulent flows with $10^4 \leq Re_{ann} \leq 10^6$; $0.6 \leq Pr \leq 1000$; and $0 \leq D_h / L \leq 1$, the heat transfer between the fluid in the annulus and the inner tube can be correlated by an equation proposed by Gnielinski [160], which is a modification of the Petukhov correlation:

$$Nu = \frac{(\zeta_{ann}/8) Re_{ann} Pr}{k_1 + 12.7 (\zeta_{ann}/8)^{1/2} (Pr^{2/3} - 1)} \left[1 + \left(\frac{D_h}{L} \right)^{2/3} \right] F_{ann} \quad (\text{A.62})$$

where:

$$k_1 = 1.07 + \frac{900}{Re_{ann}} - \frac{0.63}{(1 + 10 Pr)} \quad (\text{A.63})$$

The friction factor is calculated as follows [166]:

$$\zeta_{ann} = [1.8 \log_{10}(Re^*) - 1.5]^{-2} \quad (\text{A.64})$$

where:

$$Re^* = Re_{ann} \frac{(1 + a^2) \ln a + (1 - a^2)}{(1 - a^2) \ln a} \quad (\text{A.65})$$

F_{ann} is defined below for the heat transfer with the inner, small tube boundary condition:

$$F_{ann} = 0.75 a^{-0.17} \quad (\text{A.66})$$

In the transition region between laminar and fully developed turbulent flows ($2300 \leq Re_{ann} \leq 10000$), a similar approach as in page 200 is taken [149]. In particular, the Nusselt number is defined using the interpolation described in Eqs. A.48 and A.49. The Nusselt numbers at $Re_{ann} = 2300$ and 10000 are defined differently depending on the heat transfer boundary condition. With heat exchange between the fluid in the annulus and the inner (smaller) tube, the laminar component is calculated as

follows:

$$Nu_{lam, Re=2300} = (Nu_1^3 + Nu_{2, Re=2300}^3 + Nu_{3, Re=2300}^3)^{1/3} \quad (A.67)$$

where

$$Nu_1 = 3.66 + 1.2 a^{-0.8} \quad (A.68)$$

$$Nu_{2, Re=2300} = 1.615 (1 + 0.14 a^{(-1/2)}) (2300 Pr D_h / L)^{1/3} \quad (A.69)$$

$$Nu_{3, Re=2300} = \left(\frac{2}{1 + 22 Pr} \right)^{1/6} (2300 Pr D_h / L)^{1/2} \quad (A.70)$$

The turbulent Nusselt number component ($Nu_{turb, Re=10000}$) in Eq. A.48 is calculated using Eqs. A.62 to A.66, with $Re_{ann} = 10000$ as the input.

It is always recommended to resort the source bibliography in order to understand the limitations of these correlations, the possible boundary conditions, and their validity.

A.2.3 Two-phase flow boiling heat transfer in internal flows

Liu and Winterton correlation [121]

Liu and Winterton [121] developed an asymptotic heat transfer correlation ($n=2$) based on a large experimental database of subcooled and saturated flow boiling data in channels of 2.9 mm to 32 mm ID. For horizontal channels and $Fr_{LO} \geq 0.05$ the two-phase heat transfer coefficient is expressed as a combination of the convection, liquid heat transfer coefficient and the nucleate boiling heat transfer coefficient, as follows:

$$h_{tp} = \left[(Sh_{nb})^2 + (F h_{sp})^2 \right]^{\frac{1}{2}} \quad (A.71)$$

where:

$$F = \left[1 + x Pr_l \left(\frac{\rho_l}{\rho_v} - 1 \right) \right]^{0.35} \quad (A.72)$$

$$S = (1 + 0.055 F^{0.1} Re_{LO}^{0.16})^{-1} \quad (A.73)$$

h_{sp} is calculated using the Dittus-Boelter correlation [123], with the liquid-only Reynolds number (Re_{LO}) as input in Eq. A.59. The nucleate boiling heat transfer component h_{nb} is determined using the pool boiling correlation by Cooper [122]:

$$h_{nb} = 55 q^{2/3} p_r^{0.12-0.4343 \ln(R_a)} [-\log_{10}(p_r)]^{-0.55} M^{-0.5} \quad (\text{A.74})$$

where R_a is the superficial roughness of the tube, p_r is the fluid reduced pressure, and M is the molar mass, in g mol^{-1} .

Kandlikar and Balasubramanian correlation [124]

Kandlikar and Balasubramanian [124] proposed a heat transfer correlation for flow boiling in the mini- and microchannel range. The flow boiling heat transfer coefficient is the highest between the nucleate boiling and the convective boiling heat transfer coefficients:

$$h_{tp} = \max(h_{nb}, h_{cb}) \quad (\text{A.75})$$

The authors put forward the expressions to calculate h_{nb} and h_{cb} :

$$h_{nb} = 0.6683 C^{-0.2} (1-x)^{0.8} f_2(Fr_{LO}) h_{LO} + 1058.0 Bo^{0.7} (1-x)^{0.8} F_{Fl} h_{LO} \quad (\text{A.76})$$

$$h_{cb} = 1.136 C^{-0.9} (1-x)^{0.8} f_2(Fr_{LO}) h_{LO} + 667.2 Bo^{0.7} (1-x)^{0.8} F_{Fl} h_{LO} \quad (\text{A.77})$$

where F_{Fl} is the fluid-surface parameter, which is considered equal to 1 for all fluids in stainless steel channels. Since no polyimide channels are considered in the table at the source article, it is considered as 1 when implementing this correlation in chapter 6.

C is the convective number, and Bo is the boiling number:

$$C = \left(\frac{\rho_v}{\rho_l} \right)^{0.5} \left(\frac{1-x}{x} \right)^{0.8} \quad (\text{A.78})$$

$$Bo = \frac{q}{i_{lv} G} \quad (\text{A.79})$$

Depending on the value of the liquid-only Reynolds number (Re_{LO}), the remaining parameters in the equations are calculated differently. In the $Re_{LO} > 3000$ region, the channels are considered as large diameter tubes. Here, according to the article by Kandlikar and Steinke [175], $f_2(Fr_{LO})$ is simply the liquid-only Froude number in the present correlation. The single-phase, liquid-only heat transfer

coefficient, h_{LO} , is calculated using the correlation by Gnielinski [150], Eq. A.58, for $3000 \leq Re \leq 10000$, and the correlation by Petukhov [151], Eq. A.55, for $10000 \leq Re \leq 5 \cdot 10^6$.

In the $Re_{LO} < 1600$ region, the tubes are considered to be minichannels. Here, $f_2(Fr_{LO}) = 1$, and h_{LO} is calculated assuming $Nu_{LO} = 4.36$.

Finally, the $1600 < Re_{LO} < 3000$ range is the transition flow region. Again, $f_2(Fr_{LO}) = 1$. However, h_{LO} is calculated interpolating from the laminar and the turbulent values. Alternatively, the correlation by Churchill [145] can be used.

This correlation is valid down to very low Reynolds numbers, and therefore applicable to the smallest micro-channels. More information can be found in the original article [124].

Cioncolini and Thome correlation [130]

This semi-empirical heat transfer method [130] consists of an algebraic turbulence model for annular flows, as part of a unified annular flow modeling suite. It is built considering a two-phase flow database spanning channel diameters from 1.03 to 14.4 mm.

The cross-sectional void fraction (ε) is defined as follows [86]:

$$\varepsilon = \frac{h x^n}{1 + (h - 1) x^n} \quad (\text{A.80})$$

$$h = -2.129 + 3.129 (\rho_v / \rho_l)^{-0.2186} \quad (\text{A.81})$$

$$n = 0.3487 + 0.6513 (\rho_v / \rho_l)^{0.5150} \quad (\text{A.82})$$

The entrained liquid fraction (e) is calculated with a simple iteration [87], considering initially the density of the vapour (ρ_v):

$$We_{initial} = \frac{(xG)^2 D_i}{\gamma \rho_v} \quad (\text{A.83})$$

$$e_{initial} = [1 + 279.6 We_{initial}^{-0.8395}]^{-2.209} \quad (\text{A.84})$$

With the values above, one can determine the core density, as follows:

$$\rho_{core,initial} = \frac{x + e_{initial}(1 - x)}{\frac{x}{\rho_v} + \frac{e_{initial}(1 - x)}{\rho_l}} \quad (\text{A.85})$$

By recalculating Eqs. A.83 and A.84 with $\rho_{core,initial}$ instead of ρ_v , the final e value is obtained. ρ_{core} can be recalculated via Eq. A.85 using the final entrained liquid fraction.

The core flow diameter, velocity and Weber number are determined below:

$$D_{core} = D_i \left(\varepsilon \frac{x\rho_l + e(1-x)\rho_v}{x\rho_l} \right)^{1/2} \quad (\text{A.86})$$

$$u_{core} = \frac{xG}{\rho_v \varepsilon} \quad (\text{A.87})$$

$$We_{core} = \frac{\rho_{core} u_{core}^2 D_{core}}{\gamma} \quad (\text{A.88})$$

The value of the Fanning friction factor (ζ_f) depends of the Bond number (Bd):

$$\zeta_f = 0.172 (We_{core}^{-0.372}) \quad , \quad Bd > 4 \quad (\text{macroscale}) \quad (\text{A.89})$$

$$\zeta_f = 0.0196 (We_{core}^{-0.372}) (Re_{LF}^{0.318}) \quad , \quad Bd \leq 4 \quad (\text{microscale}) \quad (\text{A.90})$$

where the Bond number is defined below:

$$Bd = \frac{g(\rho_l - \rho_v) D_i^2}{\gamma} \quad (\text{A.91})$$

The liquid film Reynolds number is expressed as follows:

$$Re_{LF} = \frac{(1-e)(1-x)GD_i}{\mu_l} \quad (\text{A.92})$$

The wall shear stress (τ_{wall} , in Pa), and the frictional pressure gradient [98] are expressed as follows:

$$\tau_{wall} = 0.5 \zeta_f \rho_{core} u_{core}^2 \quad (\text{A.93})$$

$$\left(\frac{dp}{dz} \right)_{frict} = \frac{4\tau}{D_i} \quad (\text{A.94})$$

The dimensionless liquid film thickness (t^+) is determined as the maximum of two values:

$$t^+ = \max(\sqrt{0.5 Re_{LF}}, 0.0165 Re_{LF}) \quad (\text{A.95})$$

With the distance wall scale (Y^*), the liquid film thickness (t) can be calculated:

$$t = t^+ Y^* \quad (\text{A.96})$$

$$Y^* = \frac{\mu_l}{\sqrt{\rho_l \tau_{wall}}} \quad (\text{A.97})$$

Finally, the two-phase flow boiling Nusselt number and the heat transfer coefficient can be calculated:

$$Nu = 0.0776 (t^+)^{0.90} Pr_l^{0.52} \quad (\text{A.98})$$

$$h_{tp} = \frac{Nu \alpha_l}{t} \quad (\text{A.99})$$

An interactive implementation of the Cioncolini and Thome unified annular flow suite and the source code is available in <http://2phaseflow.org/active:annularmodels>.

Kanizawa *et al.* correlation [125]

The minichannels heat transfer correlation by Kanizawa *et al.* [125] consists in first discerning between the convective boiling region and the dryout inception. The first step is thus calculating x_{dryout} . The x_{dryout} is assumed to be the vapour quality at which the Critical Heat Flux (*CHF*) occurs. The authors suggest to determine it using the x_{crit} obtained applying the *CHF* method by Zhang *et al.* [126]. Then:

1. If $x < x_{dryout}$, the flow boiling heat transfer coefficient is calculated using a modification of the additive method by Saitoh *et al.* [119] (Eqs. A.102 to A.115 below).
2. If $x_{dryout} \leq x \leq 1$, a linear interpolation is performed between the heat transfer coefficient at $x = x_{dryout}$, calculated as in step 1, and the forced convection to vapour heat transfer coefficient value, as follows:

$$h = h_{tp} x_{dryout} \left(\frac{1-x}{1-x_{dryout}} \right) + h_{VO} \left(\frac{x-x_{dryout}}{1-x_{dryout}} \right) \quad (\text{A.100})$$

where h_{tp} is calculated via Eq. A.102, and h_{VO} is the vapour-only heat transfer coefficient following

the correlation by Dittus and Boelter [123]:

$$h_{VO} = 0.023 \frac{\alpha_v}{D} Re_{VO}^{4/5} Pr_v^{1/3} \quad (\text{A.101})$$

Re_{VO} is the Reynolds number calculated considering the liquid-vapour mixture flows as a vapour. Eq. A.11 is used for its calculation, introducing the vapour physical properties.

To calculate the convective boiling heat transfer coefficient for the $x < x_{dryout}$ case, the additive method of Saitoh [119] is used:

$$h_{tp} = S h_{nb} + F h_{cb} \quad (\text{A.102})$$

The nucleate boiling effects are calculated by the pool boiling correlation by Stephan and Abdelsalam [176] for halocarbons:

$$h_{nb} = 207 \frac{\alpha_l}{D} \left(\frac{q D_b}{\alpha_l T_{sat}} \right)^{0.745} \left(\frac{\rho_v}{\rho_l} \right)^{0.581} \left(\frac{\mu_l \rho_l c_{pl}}{\rho_l \alpha_l} \right)^{0.533} \quad (\text{A.103})$$

The characteristic length D_b is given by the bubble equilibrium break-off diameter in pool boiling [176]:

$$D_b = 0.51 \sqrt{\frac{2\gamma}{g(\rho_l - \rho_v)}} \quad (\text{A.104})$$

The convective heat transfer coefficient is calculated through the Dittus and Boelter correlation [123]:

$$h_{cb} = 0.023 \frac{\alpha_l}{D} Re_l^{4/5} Pr_l^{1/3} \quad (\text{A.105})$$

where Re_l is the liquid Reynolds number:

$$Re_l = \frac{G(1-x)D}{\mu_l} \quad (\text{A.106})$$

In Eq. A.102, F is the convective enhancement factor, defined by the authors as follows:

$$F = 1 + \frac{2.50 X^{-1.32}}{1 + We_{u_v}^{0.24}} \quad (\text{A.107})$$

where We_{u_v} :

$$We_{u_v} = \frac{\rho_v u_v^2 D}{\gamma} \quad (\text{A.108})$$

$$u_v = \frac{Gx}{\rho_v \varepsilon} \quad (\text{A.109})$$

The void fraction is calculated in this correlation using the method by Kanizawa and Ribatski [82]:

$$\varepsilon = \left[1 + 1.021 Fr_m^{-0.092} \left(\frac{\mu_l}{\mu_v} \right)^{-0.368} \left(\frac{\rho_v}{\rho_l} \right)^{1/3} \left(\frac{1-x}{x} \right)^{2/3} \right]^{-1} \quad (\text{A.110})$$

with

$$Fr_m = \frac{G^2}{gD(\rho_l - \rho_v)^2} \quad (\text{A.111})$$

X_{tt} is the Lockhart and Martinelli factor in Eq. A.107, and it is calculated assuming the liquid phase is turbulent [177]:

$$X_{tt} = \left(\frac{1-x}{x} \right)^{0.9} \left(\frac{\rho_v}{\rho_l} \right)^{0.5} \left(\frac{\mu_l}{\mu_v} \right)^{0.1}, \quad \text{if } Re_v > 1000 \quad (\text{A.112})$$

$$X_{tl} = \frac{1}{18.7} Re_v^{0.4} \left(\frac{1-x}{x} \right)^{0.9} \left(\frac{\rho_v}{\rho_l} \right)^{0.5} \left(\frac{\mu_l}{\mu_v} \right)^{0.1}, \quad \text{if } Re_v \leq 1000 \quad (\text{A.113})$$

where Re_v is the vapour Reynolds number, calculated using Eq. A.106 with the vapour properties as input.

The nucleate boiling suppression factor (S) is defined below:

$$S = \frac{1.06 Bd^{-8 \cdot 10^{-3}}}{1 + 0.12 \left(\frac{Re_{tp,mod}}{10000} \right)^{0.86}} \quad (\text{A.114})$$

where Bd is the Bond number, and $Re_{tp,mod}$ is the two-phase modified Reynolds number, expressed as follows:

$$Re_{tp,mod} = Re_{LO} F^{1.25} \quad (\text{A.115})$$

Re_{LO} is the liquid-only Reynolds number (see Eq. A.11).

The complete code to implement this correlation in MatLab, EES and similar calculation softwares can be found as additional material at the article website. The reader is encouraged to review the original article to find the equations for other fluids and data for validating the method.

A.3 Two-phase void fraction models

The homogeneous void fraction method considers the two phases traveling at the same velocity. Several definitions of the two-phase mixture density are available in literature. The one used in the studies in section 5.4 is the following:

$$\varepsilon = \left[1 + \left(\frac{1-x}{x} \right) \frac{\rho_v}{\rho_l} \right]^{-1} \quad (\text{A.116})$$

The analytical void fraction model by Zivi [81] is defined as follows:

$$\varepsilon = \left[1 + \left(\frac{1-x}{x} \right) \left(\frac{\rho_v}{\rho_l} \right)^{2/3} \right]^{-1} \quad (\text{A.117})$$

Zivi provided an annular flow void fraction model including liquid entrainment in the vapour core:

$$\varepsilon = \left\{ 1 + e \left(\frac{1-x}{x} \right) \left(\frac{\rho_v}{\rho_l} \right) + (1-e) \left(\frac{1-x}{x} \right) \left(\frac{\rho_v}{\rho_l} \right)^{2/3} \left[\frac{1 + e \left(\frac{1-x}{x} \right) \left(\frac{\rho_v}{\rho_l} \right)}{1 + e \left(\frac{1-x}{x} \right)} \right]^{1/3} \right\}^{-1} \quad (\text{A.118})$$

where e was chosen to be calculated using the method by Cioncolini and Thome [87] in this thesis, as expressed in Eq. A.84, and following the methodology in page 206.

Rouhani and Axelsson [83] developed an empirical drift-flux (considering different velocities of the liquid and vapour phase) void fraction method for annular flow in vertical channels. The model was adapted for horizontal channels by Steiner [84], as follows:

$$\varepsilon = \frac{x}{\rho_v} \left[(1 + 0.12(1-x)) \left(\frac{x}{\rho_v} + \frac{1-x}{\rho_l} \right) + \frac{1.18(1-x)(g\gamma(\rho_l - \rho_v))^{0.25}}{G\rho_l^{0.5}} \right]^{-1} \quad (\text{A.119})$$

The void fraction correlation by Niño *et. al* [85] for annular flow in small channels is defined below:

$$\varepsilon = \left[1 + \left(X_{tt} + \frac{1}{We^{1.3}} \right) \left(\frac{\rho_l}{\rho_v} \right)^{0.9} \right]^{-0.06} \quad (\text{A.120})$$

with We calculated as in Eq. A.83 and X_{tt} as follows:

$$X_{tt} = \left(\frac{1-x}{x} \right)^{0.875} \left(\frac{\rho_v}{\rho_l} \right)^{0.5} \left(\frac{\mu_l}{\mu_v} \right)^{0.125} \quad (\text{A.121})$$

The void fraction model by Cioncolini and Thome [86] was described in page 206, Eq. A.80. Likewise, the void fraction correlation by Kanizawa and Ribatski [82] was detailed in the flow boiling heat transfer correlation, page 210, Eqs. from A.110 to A.113.

Appendix B

Polyimide tubing characterisation

B.1 Introduction

This appendix addresses specific issues of the polyimide tubing used in the cooling system for the ALICE ITS Upgrade detector at CERN, and the recommendations to overcome potential problems. An analytical study on the stability of the tube circular section with coolants displaying positive and negative gauge pressures is first presented, followed by experimental tests on the long-term compliance of polyimide channels with water as circulating coolant.

B.2 Sectional stability of polyimide channels

B.2.1 Introduction

The ITS Upgrade detector staves and half-staves have embedded cooling channels made of polyimide, as introduced in chapters 3 and 4, with the aim of decreasing the global material inventory of the detector and preserve its local momentum resolution. Cooling is possible with water in leak-less mode (i.e. with sub-atmospheric pressures in the stave), or with a two-phase coolant, specifically C_4F_{10} refrigerant, involving absolute pressures between 1.8 and 2.7 bar. Besides, during the experimental flow boiling heat transfer tests with R245fa refrigerant, presented in chapter 6, pressures up to 3.2 bar are set inside the tube.

Since the tubes are thin-walled and far less rigid than metallic ones, it must be analysed whether its section would swell under positive gauge pressures of the coolant (two-phase cooling or single-phase dielectric coolants), or if it would collapse if sub-atmospheric pressure conditions are established

inside the channel (water cooling, vacuum). This question is tackled analytically in the present section. It must be emphasised that the tubes in the staves are covered by carbon fleece plies and a TPG foil, in full, firm contact with the tube outer surface, ensured by the fleece resin, conferring robustness to the polyimide channel section. Thus, no channel deformation or collapse is expected, and indeed no evidence of this phenomena was observed during the experimental tests.

B.2.2 Dimensions and physical properties of the polyimide channels

The baseline stave and half-stave designs proposed in this dissertation were presented in chapter 5. The Inner Barrel baseline staves have 1.024 mm ID channels made of pure polyimide with a wall thickness of 25 μm , as reported in Table 5.1, while the Outer Barrel baseline half-staves for water cooling, named OB1 and OB2 (see Table 5.6), display 2.052 mm ID polyimide channels with walls 32 μm thick. A third half-stave proposal, OB3 (see Table 5.8), was conceived for two-phase cooling with C_4F_{10} refrigerant as coolant, and has channels of 2.667 mm ID and 64 μm -thick walls. The dimensions of the polyimide channels and their geometrical parameters are summarised in Table B.1.

Polyimide, described in detail in section 2.4.4, is a thermoset plastic available in different grades with excellent mechanical properties. However, the thin walls considered in the ITS Upgrade stave tubing could make them fragile in certain conditions. The mechanical properties of the polyimide channels used at the ITS Upgrade are reported in Table B.2.

Table B.1: Dimensions of the polyimide channels used in the ITS Upgrade staves.

Stave	Inner Barrel		Outer Barrel	
	IB1	OB1, OB2	OB3	
$D_i \pm U(D_i)$ [mm]	1.024 ± 0.013	2.052 ± 0.025	2.667 ± 0.025	
w [mm]	0.025	0.032	0.064	
w/r_i^a [-]	0.05	0.03	0.05	
D_e/w [-]	43	66	44	
L [mm]	290	1504	1504	

Table B.2: Mechanical properties of the polyimide channels.

Property	Value	Reference
Minimum hoop stress limit [MPa]	76	[178]
Ultimate tensile strength (rupture) [MPa]	306	[66]
Elastic modulus (E_y) ^b [MPa]	2300	[66, 179]
Poisson ratio (ν_p) [-]	0.34	[179]

^a If equal or lower than 0.05, the assumption of thin-walled cylinder is valid.

^b Yield strength giving a 5% deformation.

B.2.3 Hoop stress elongation

When an internal pressure is set inside a tube, three mutually perpendicular stresses are set up in the tube wall. These are the hoop stress or circumferential stress (tangential in the circular wall thickness), the longitudinal stress (parallel to the tube axis), and the radial stress (in the radial direction, perpendicular to the tube axis). The channel wall can be considered thin if the wall thickness to inner diameter of the tube ratio is equal or less than 0.05, a condition fulfilled by the three channel sizes considered in the ITS Upgrade cooling system (see Table B.1). Under the thin-walled tube assumption, it can be stated that the hoop and longitudinal stresses are uniform across the thickness of the wall, and that the radial stress is negligible compared to the aforementioned components. Besides, since the channel ends are open, the longitudinal stress can be neglected. The hoop stress can be expressed as follows:

$$\sigma_1 = \frac{pr_i}{w} \quad (\text{B.1})$$

A graphic representation of the hoop stresses of an internal positive gauge pressure inside a thin tube is depicted for the top half of the tube cross section in Fig. B.1a.

The strain (λ) resulting from hoop stresses caused by internal pressures higher than atmospheric values may be calculated as follows:

$$\lambda = \frac{\sigma}{E_y} \quad (\text{B.2})$$

Finally, the increase of the inner diameter is expressed below:

$$\Delta D_i = D_i \lambda \quad (\text{B.3})$$

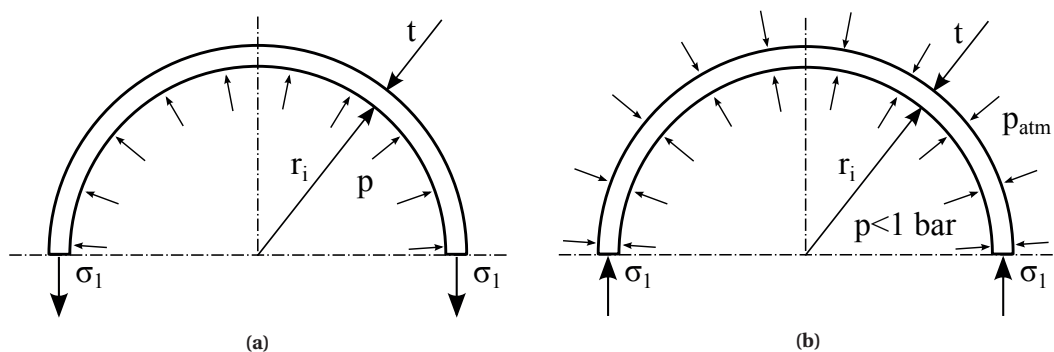


Figure B.1: Schematic view of the hoop stress in a thin-walled tube for: (a) internal positive gauge pressures; (b) internal negative gauge pressures (sub-atmospheric).

Table B.3 reports the inner diameter increases of the considered polyimide channels at the maximum expected gauge pressure, applying a factor of safety of 1.5. The gauge pressures in Table B.3 result in inner diameter increases lower than the dimensional tolerances of the tubes, and can be thus considered negligible. The case in the last column regards a case with a factor of safety of 3.5, involving a gauge pressure of 10.5 bar. The inner diameter increase in those conditions would be 0.025 mm, the same as the tube inner diameter tolerance, as specified by the manufacturer. Thus, in the experimental conditions reported in this dissertation, no significant expansion of the polyimide channel sections is expected.

If the internal pressure increases dramatically, permanent plastic deformation or even channel burst may occur. Here, different estimates were evaluated. First, the manufacturer MicroLumen reports the minimum hoop stress that would make the channel burst [178], and recommends the following equation to calculate the critical pressure above which such effect would occur:

$$p_{burst, MicroLumen} = \frac{\sigma_1 w}{D_e} \quad (B.4)$$

As small channels will surely withstand hoop stresses higher than the minimum claimed by MicroLumen (usually reported for their biggest tubes), assuming this burst pressure is conservative.

An alternative burst pressure method is the one involving the Barlow's formula for tubes and pressure vessels:

$$p_{burst, Barlow} = \frac{2 S}{D_e} \quad (B.5)$$

where S is the allowable stress. If this parameter is defined as the polyimide channel Young modulus as reported in Table B.1, Eq. B.5 yields the internal pressure resulting in a deformation of 5%. If using the ultimate tensile strength, the burst pressure is obtained.

Last, destructive burst pressure tests were performed at CERN using stave and half-stave prototypes. Each specimen was connected to a water pumping loop with the outlet channel closed. The

Table B.3: Hoop stresses and predicted increases of the inner diameter for all the polyimide channels used in the ITS Upgrade under positive gauge pressures.

Location	Inner Barrel		Outer Barrel	
	$D_i \pm U(D_i)$ [mm]	1.024 ± 0.013	2.052 ± 0.025	2.667 ± 0.025
w [mm]	0.025	0.032	0.064	
p_{gauge} [bar]	6	6	6	10.5
σ_1 [MPa]	12.3	19.2	12.5	21.9
λ [-]	$5.34 \cdot 10^{-3}$	$8.36 \cdot 10^{-3}$	$5.44 \cdot 10^{-3}$	$9.51 \cdot 10^{-3}$
ΔD_i [mm]	0.006	0.017	0.015	0.025

water pressure was increased little by little until bursting. All bursting failures occurred at the polyimide channels (not at the glued interfaces with the inlet/outlet connector or the Π -bend), and always manifested as longitudinal cracks, as displayed in Fig. B.2. This evidences the channels do burst due to excessive hoop stresses. As displayed in the pictures, the CFRP stave structure is affected by the channel burst, with local delamination of the carbon fleece and the TPG foil.

All the described burst pressure values are reported in Table B.4, in addition to the nominal values claimed by the manufacturer. The expected pressures in the experimental tests, not exceeding 4 bar, are too low to cause significant inner diameter increases in the considered polyimide channels. The most pessimistic estimates predict a minimum burst pressure, of 11.5 bar for the Outer Barrel 2.052 mm ID channels, which is well above the maximum operating pressure.

B.2.4 Channel collapse

In case there is a negative internal gauge pressure inside the channels, i.e. a pressure lower than the atmospheric one, the section of the polyimide tubes might get squeezed locally, to the point of collapsing completely. In this case, the circular section is not entirely recovered after setting atmospheric conditions inside the channel again, as plastic deformation might have occurred. This was seen during vacuum tests with spare channel specimens not embedded in staves. On the other hand, the tubes in

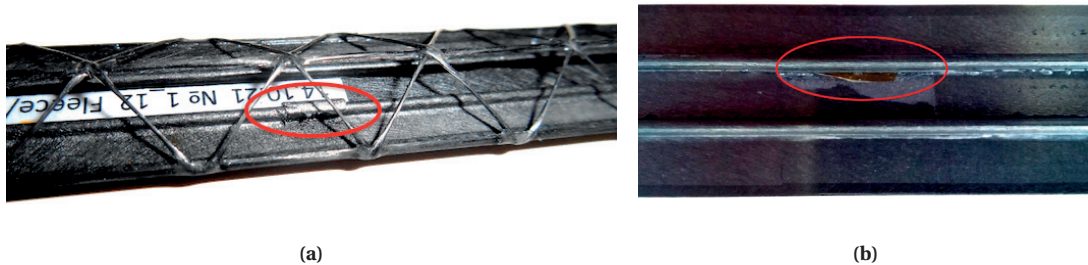


Figure B.2: Experimental burst failures: (a) Inner Barrel stave, after 51 bar; (b) Outer barrel half-stave, after 26 bar. Images courtesy of the ITS Upgrade collaboration.

Table B.4: Analytical, nominal, and measured burst pressures in the polyimide channels used in the ITS Upgrade.

Location	Inner Barrel	Outer Barrel	
	$D_i \pm U(D_i)$ [mm]	1.024 ± 0.013	2.052 ± 0.025
w [mm]	0.025	0.032	0.064
Burst MicroLumen [178] [bar]	17.7	11.5	17.4
5% deformation (Barlow) [bar]	32.1	20.9	31.6
Burst pressure (Barlow) [bar]	71.2	46.3	70.0
Manufacturer specification [bar]	40	25	38
Experimental burst pressure [bar]	51	26	-

the ITS Upgrade staves are embedded in a CFRP layered structure, with confers rigidity to the whole assembly and it is firmly in contact and adhered to the channel outer surface. Experimental cooling tests were performed in an Outer Barrel stave^a before and after setting the channels in medium vacuum for days at a time. No differences were observed either in pressure drop values or in cooling performance. The same kind of tests were conducted after sequentially alternating vacuum with atmospheric conditions, equally resulting in no pressure drop increase or cooling performance deterioration.

Many theoretical and empirical methods exist in the literature predicting the critical pressure causing channel collapse. However, they are mostly applied to stainless steel tubing or deep-well casing, which regard subterranean or submarine applications where a high external pressure actuates on the tube external surface. As a result, the applicability of these method to thin-walled, small polyimide channels is uncertain, Nevertheless, some estimates are presented in this subsection with the aim of defining an approximate critical pressure threshold and provide recommendations.

Let us define $\Delta p_{collapse}$ as the collapse pressure difference for a specific tube, calculated by one of the methods presented below. $\Delta p_{collapse}$ can be expressed as the difference between the absolute pressure in the external tube wall (atmospheric, $p_e = 1$ bar) and the absolute pressure inside the polyimide channel (p_i):

$$\Delta p_{collapse} = p_e - p_i = 1 - p_i \quad (\text{B.6})$$

Eq. B.6 is interpreted as follows:

- If $\Delta p_{collapse} < 1$ bar, the polyimide channel will collapse for an internal absolute pressure of $p_i = 1 - \Delta p_{collapse}$ bar.
- If $\Delta p_{collapse} > 1$ bar, collapse will not occur, even with vacuum inside the channel.
- $\Delta p_{collapse} = 1$ bar would correspond to an unstable condition where the tube would collapse where there is weak area on its surface or where it is not perfectly circular.

Thus, values of $\Delta p_{collapse}$ higher than 1 bar are desired, in order to ensure the channel will not collapse under any circumstance.

Clinedinst *et al.* [180] proposed a rational expression to calculate the critical pressure above which plastic shrinkage of a tube occurs. It can be expressed as follows:

$$\Delta p_{collapse} = \frac{2 E_y}{(1 - \nu P^2)} \frac{1}{\frac{D_e}{w} \left(\frac{D_e}{w} - 1 \right)^2} \quad (\text{B.7})$$

Holmquist and Nadai [181] put forward a theoretical formula to determine the elastic collapse for

^a Thin-walled, large channels are more prone to collapse than smaller ones with similar wall thickness.

deep-well casing:

$$\Delta p_{collapse} = \frac{2 E_y}{(1 - \nu_p^2)} \left(\frac{w}{D_e - w} \right)^3 \quad (\text{B.8})$$

Beyond this pressure difference threshold, the tube would present plastic deformation, ruled by the reduced elastic modulus. They also provided calculations for a tube section presenting ovality (previously deformed), stating that the pressure causing an elastic collapse will be lower in that case.

In his Ph.D thesis, Sturm [182], proposed an expression for the collapsing pressures in thin-walled cylinders with pressure applied to the sides of the tubes only and the edges simply supported^a:

$$\Delta p_{collapse} = K E_y \left(\frac{w}{D_e} \right)^3 \quad (\text{B.9})$$

where K is a constant to be graphically determined in a diagram, depending on the values of w/D_e and L/r_e .

Last, Kennedy and Venard [183] performed an experimental study on the collapse of stainless steel tubes by external pressure. Although the mechanical properties of steel differ from those of polyimide, the authors crafted master curves and expressions depending on the elastic modulus, Poisson ratio, and the tube dimensions. In particular, the collapse pressure difference of a tube can be expressed as follows:

$$\Delta p_{collapse} = \frac{\phi E_y w}{(1 - \nu_p^2) r_m} \quad (\text{B.10})$$

where ϕ is a constant graphically determined in a diagram with L/r_m and r_m/w as inputs.

Table B.5 summarises the pressure differences between the external and internal tube surfaces that would cause collapse as reported by the different methods above.

Table B.5: Pressure difference between the external and internal tube surfaces ($\Delta p_{collapse}$) resulting in collapse of the polyimide channels of the ITS Upgrade staves (see Table B.1), predicted by theoretical and analytical methods. Atmospheric pressure conditions are considered outside the channel.

Location	Inner Barrel	Outer Barrel	
D_i [mm]	1.024	2.052	2.667
w [mm]	0.025	0.032	0.064
Clinedinst <i>et al.</i> [180] [bar]	0.69	0.19	0.65
Holmquist and Nadai [181] [bar]	0.66	0.18	0.62
Sturm [182] [bar]	0.67	0.18	0.64
Kennedy and Venard [183] [bar]	0.74	0.24	0.73

^a If some length of the outer tube wall is glued to another cylindrical surface, the collapse pressure will be higher than if considering simply supported edges. Therefore, this assumption is conservative.

The results by all the considered methods match well. In general, with water cooling, a leak-less system is chosen to prevent water spills on the electronics in case of failures. This implies absolute water pressures inside the polyimide channels ranging from 0.6 to 0.9 bar, since the cooling system is designed to display a maximum 0.3 bar pressure drop in the stave. In view of the results by the method by Holmquist and Nadai [181], yielding the most pessimistic approach, the 2.052 mm ID “free” channel^a would collapse if the absolute pressure inside the channel is 0.18 bar below the atmospheric pressure outside. In other words, collapsing occurs for water pressures below 0.82 bar, according to Eq. B.6. The 1.024 mm ID and the 2.667 mm ID channels would withstand pressures as low as 0.34 and 0.38 bar before collapsing, respectively. In vacuum conditions inside the tubes, all “free” channels will collapse. An immediate solution to prevent this problem from occurring involves increasing the channel wall thicknesses.

B.2.5 Recommended polyimide channel thicknesses

In order to prevent the channel from collapsing under any circumstance, polyimide tubing with thicker walls are recommended, in particular 30 μm thick for the 1.024 mm ID channel (instead of 25 μm), 60 μm for the 2.052 mm ID one (instead of 32 μm) and 78 μm in the 2.667 mm ID tube (rather than 64 μm). Repeating the same analysis as in the previous subsection, the pressure differences between the external and internal tube surfaces that would cause collapse of the channels are reported in Table B.6 for the analytical methods described in subsection B.2.4.

The thicker walls result in predicted values of $\Delta p_{collapse}$ higher than 1 bar, meaning that the channels will not collapse even if vacuum is set inside them. If considering that the stave CFRP provides robustness to the channel section, it is ensured the thicker channels will remain circular for the entire pressure range in the cooling operational conditions.

However, thicker channel walls negatively affect the global stave material budget. Fig. B.3 displays the material budget of the OB1 half-stave (see Table 5.6) if the original 2.052 mm ID polyimide channels

Table B.6: Pressure difference between the external and internal tube surfaces ($\Delta p_{collapse}$) resulting in collapse of the recommended polyimide channels with thicker walls, predicted by theoretical and analytical methods. Atmospheric pressure conditions are considered outside the channel.

Location	Inner Barrel	Outer Barrel	
D_i [mm]	1.024	2.052	2.667
w suggested [mm]	0.030	0.060	0.078
Clinedinst <i>et al.</i> [180] [bar]	1.17	1.16	1.16
Holmquist and Nadai [181] [bar]	1.10	1.10	1.10
Sturm [182] [bar]	1.12	1.12	1.12
Kennedy and Venard [183] [bar]	1.18	1.18	1.18

^a A polyimide channel not embedded in the stave CFRP structure.

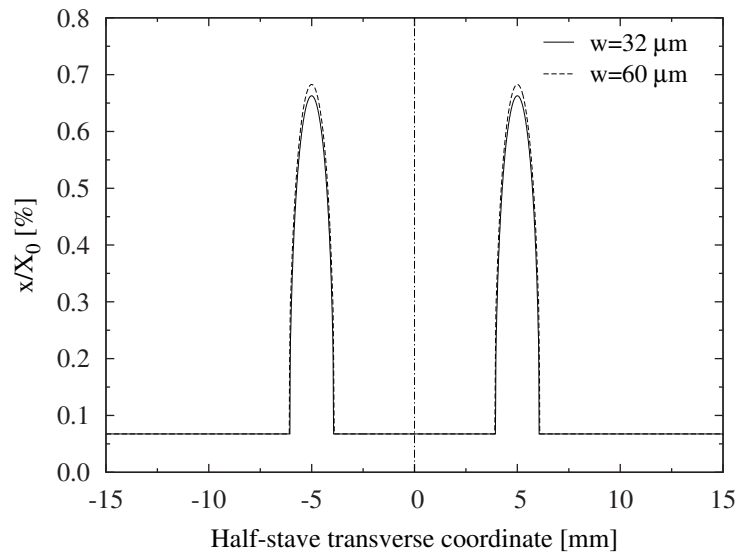


Figure B.3: Material budget of the OB1 (see Table 5.6) stave with 2.052 mm ID channels with wall thicknesses of 32 μm and 60 μm , and water as coolant.

with walls 32 μm thick are substituted by 60 μm -thick ones, with water as coolant. The peaks due to the thicker tube wall reach slightly higher values, but their influence on the global stave material budget is very little, as reported in Table B.7, with global values still below the 0.30% and 1.00% per layer limits for the Inner and Outer Barrel, respectively.

In conclusion, it is recommended to use polyimide channels with the wall thicknesses reported above in order to avoid channel deformation or collapse during the long-term ITS Upgrade operation. The presence of thicker walls does not affect significantly the global material budget of the staves.

Table B.7: ITS Upgrade stave material budget if increasing the wall thicknesses of the the polyimide channels to the recommended values guaranteeing no channel collapse.

Stave (coolant)	D_i [mm]	Original channel			Thick-walled channel		
		w [mm]	$[x/X_0]_{stave}^a$ [%]	$[x/X_0]_{full}^b$ [%]	w [mm]	$[x/X_0]_{stave}^a$ [%]	$[x/X_0]_{full}^b$ [%]
IB1 (water)	1.024	0.025	0.079	0.277	0.030	0.080	0.278
OB1 (water)	2.052	0.032	0.134	0.770	0.060	0.138	0.774
OB3 (2-Ph. $\text{C}_4\text{F}_{10}^c$)	2.667	0.064	0.105	0.741	0.078	0.108	0.744

^a Includes: plate assembly, channels and coolant inside the channels. No spaceframe included.

^b For a fully-equipped stave: half-stave, water as coolant, pixel chips, and Flex Printed Circuit (FPC) (and power bus in the Middle and Outer Barrel staves). The overlap with neighbouring staves is considered too.

^c Considered $\epsilon=0.85$. The calculation procedure is described in subsection 2.5.4.

B.3 Water-polyimide channels long-term compatibility test

This section aims to provide an overview on the possible long-term effects of water flowing inside polyimide channels, especially in radioactive environments. Experimental water circulation tests on several polyimide tube specimens were run and are here described, together with the examination techniques of the tube samples in search for surface damage.

B.3.1 Introduction

The use of polyimide channels for liquid and evaporative cooling proposed in this dissertation for the ALICE ITS Upgrade detector constitutes an innovation. The low wall thicknesses and lightness of the tubes strongly contribute to a material budget reduction in comparison with metal piping. However, little knowledge exists about the degradation of the pipes after long periods of service. The cooling channels may deteriorate because of mechanical reasons (e.g. erosion due to fluid friction with the tube walls, solids in suspension, etc.), chemical reactions and/or thermal degradation.

Erosive wear can be described as a short sliding motion on the channel inner surface. It might be caused by the impact of solid or liquid particles against the surface. The impacts could gradually remove material from the surface through repeated deformations and cutting actions. Several types of erosive wear that can affect the polyimide channels in this study are identified:

- **Solid particle erosion:** the presence of solid particles in the flow collide into the tube wall, causing abrasion by shear stress, with or without material removal.
- **Cavitation-erosion:** possibly one of the biggest problems in leak-less water cooling systems. If small leaks are present, air bubbles get entrained in the liquid flow, and could cause erosion in the cooling lines, especially at the bends, pipe connections, and expansions. The erosive effect is caused by the impact of high velocity liquid wavefronts from collapsing bubbles onto the solid surfaces.
- **Liquid droplet erosion:** could occur in two-phase mist flows, but only if velocities are very high.

The rate of erosive wear is dependent upon a number of factors. The characteristics of the particles, such as their shape, hardness, impact velocity and impingement angle are the primary factors along with the properties of the surface being eroded. The impingement angle is one of the most important factors [184]. For ductile materials the maximum wear rate is found when the impingement angle is approximately 30° , whilst for non ductile materials the maximum wear rate occurs when the impingement angle is normal to the surface.

Erosion in the ALICE ITS Upgrade polyimide tubes is expected to be generally small or negligible: polyimide shows low creep and high wear resistance, and low nominal coolant velocities are expected (see chapter 5). Besides, the flow will not carry solid particles, and, in case a two-phase coolant is

chosen, mist flow patterns and high mass fluxes are out of the array of nominal conditions. However, the presence of blimps, narrow passages or section changes can have negative impact on local erosive wear rates.

Polyimide has excellent thermal stability, radiation resistance, and low ageing rate. It is also corrosion-resistant to acids and neutral chemicals. However, even though polyimide is chemically stable, it is prone to be attacked by alkalis and concentrated acids. Very strong bases, hydroxides, and generally strong oxidising and reducing agents could also attack polyimide and are advised against. Polyimide is compatible with all the materials and the coolants in the ITS Upgrade detector, and the detector cooling facilities are planned to have equipment guaranteeing no impurities and stable chemical conditions of the coolant (see subsection B.3.2). Still, radiation could cause the apparition of hazardous agents attacking locally the polyimide channels.

In order to evaluate the effects of long-term water circulation inside polyimide channels, a dedicated facility was commissioned at the ALICE cavern. A fraction of the deionised water used to cool the present ITS SDD and SSD detectors is continuously circulated inside several polyimide tube specimens. The water flow rate, pressure, and temperature are controlled and set to similar values to those expected in the ITS Upgrade detector. Periodical removal and examination of the specimens allows to determine if erosive wear or chemical degradation occurs.

B.3.2 Experimental setup

The dedicated experimental facility consists of a multiport device where several pipes can be simultaneously attached. The facility is equipped with a visual flow meter, a pressure regulator and a manometer. Two manual valves, set before and after the multiport, allow to isolate the facility from the loop. This is useful when removing tube specimens for analysis or installing new ones. Once all the test tubes are installed, a desired flow rate, distributed in parallel between all the specimens, is established and kept continuously in time. Fig. B.4 displays an overview of the facility.

The multiport is connected to a spare loop available at the SSD/SDD water cooling plant [24] at

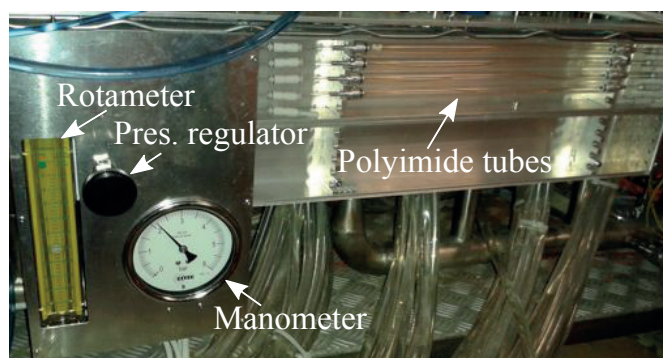


Figure B.4: Overview of the long-term water circulation experimental facility.

the ALICE underground cavern, so the same water used to cool the detectors during their operation is circulated in the multiport. This means that, after the restart of LHC and the detectors in early 2015 after the Long Shutdown 1 (LS1), the facility would operate with water circulating in a radioactive environment. Results of the erosion tests during this period would be therefore of great importance and representative of real operational conditions the polyimide tubes would have to comply with in the ITS Upgrade detector.

The SDD/SDD water loop includes the following equipment to guarantee stable physical properties of the cooling water:

1. **Mechanical filter:** a fine grid capturing solids of an specific size. It is replaced every 6 months. Potential solids in suspension in the loop might be, for instance, particles of PTFE thread seal tape.
2. **Demineralisation filter:** its target is to reduce the presence of minerals in the water that may change its conductivity. A mixed-bed deioniser holding two nuclear-grade ion exchange resin components is used in the SDD/SSD cooling plant [24]. This device is able to remove anionic and cationic particles. A conductivity transmitter measures the purity of the water that is sent to cool the detectors.
3. **Micro-porous hydrophobic membrane contactors:** can remove dissolved O_2 and CO_2 down to a 100 ppb order of magnitude. Dissolved O_2 is measured with a polarographic probe within the 0.1 ppb-20 ppm range.
4. **Sterilising UV lamp:** to remove all bacteria and algae that can grow in the water. These organisms can clog or decompose certain components in the loop.

B.3.3 Specimens and test conditions

Six polyimide channel specimens of around 1 mm ID, five straight and one shaped as displayed in Fig. 2.10b, were assembled in the multiport test facility. Prior to be installed, they are inspected for defects (blimps, pinched sections) and then subjected to a thermal cycle of 2 hours at $120^\circ C$, to simulate the curing process the ITS Upgrade staves, made of CFRP materials, will undergo to polymerise the carbon structure. The test conditions are the following:

- **Water flow rate:** the total flow rate through the multiport is measured, but not through every single pipe. Considering all the test specimens have the same internal cross section, and assuming the connections to the multiport are all identical, the flow will be equally distributed between them^a. The specimens are the same size as the polyimide channels in the ITS Upgrade Inner

^a The shaped tube will display a slightly higher pressure drop than the straight channels, but according to the dimensions of the bend, it is estimated that its value is not significantly higher. Thus, it is assumed the water flow rate inside it is the same as for the other 5 samples.

Barrel staves. Hence, a water flow rate higher than the nominal 3 L h^{-1} must be ensured so the test is representative of the real operational conditions. This corresponds to a Reynolds number of 1000, so the flow is laminar. In order to accelerate potential erosion effects, a total flow rate was adjusted so each individual specimen would experience to 5 to 6 times the nominal flow rate value, i.e. $15\text{-}18 \text{ L h}^{-1}$. The Reynolds number in this case is over 5000, well into the transitional regime, where the shear stresses should accelerate erosive wear. This constitutes a conservative approach to the tests.

- **Water inlet absolute pressure:** 3.5 bar.
- **Water temperature:** kept around 20°C (room temperature at the ALICE cavern).
- **Test duration:** the operational life of the detector is foreseen to be 6 to 10 years. The erosion tests cannot extend for such a period of time as the ITS Upgrade will be commissioned in 2019. This is the reason why the water flow rate in the long-term erosion tests is set 5 to 6 times higher than the nominal conditions. Periodical removal of a specimen for inspection (placing another one of the same dimensions in the multiport) allows to detect incipient failures.

Table B.8 summarises the characteristics of each sample and the number of days of continuous water circulation at an estimated $15\text{-}18 \text{ L h}^{-1}$. It was verified periodically that the flow conditions remain stable and that there was no failure in the pipes by visual inspection.

B.3.4 Inspection methodology

The most direct consequence of erosive wear on the polyimide channels is the loss of material and hence a decrease in weight of the specimens. Since polyimide has a high surface hardness and the nominal water flow rates are laminar, it is expected that the effects of abrasive erosion will be very weak. Considering also the channel dimensional tolerances, the uncertainty of the density of the material, and the non-negligible water absorption rate of 0.841% of the mass of the tube in 24 h, it was deemed impossible to measure representative changes in the mass of each tube. Thus, the inspection of the samples is performed in an entire qualitative way, using SEM and Optical Microscopy (OM).

The preparation of the samples for inspection from one specimen consists of the following steps:

Table B.8: Test specimens, current status and total time of water circulation.

Specimen	1	2	3	4	5	6
D_i [mm]	1.024	1.024	1.024	1.024	0.993	Shaped, 0.993
Status ^a	Stop	Stop	Ongoing	Ongoing	Ongoing	Ongoing
Nr. days of water circulation ^a	58	594	964	802	802	726

^a As of 20th January 2016.

1. After stopping the water flow, the tube specimen is removed and flushed with nitrogen, then letting it dry in a environment with controlled humidity.
2. The specimens are cut in half longitudinally, in order to expose the inner surface.
3. Each specimen is chopped in several parts, named samples, to be analysed (i.e. tube inlet, centre, outlet).

The inspection was carried out by the CERN EN-MME-MM section, using the following instrumentation:

- **SEM:** Scanning Electron Microscope, field emission gun FEG Sigma (ZEISS) with InLens (Secondary Electron), Evan-Thornley Secondary Electron (SE2), and back-scattered electron (AsB) detectors (imaging).
- **OM:** digital microscope KEYENCE VHX 1000.

A comparison between the results with SEM and with OM is performed for a single specimen, to determine if the same features are observed with the two inspection technologies. The inspection of the available samples is then performed with the most adequate instrument. The results shown below are credited to CERN EN-MME-MM section and can be found in an extended version in [185].

B.3.5 Results

At the time this document is written, three of the specimens described in Table B.8 were inspected:

1. A brand new specimen (not subjected to water circulation), after curing it for 2 hours at 120°C. This is named *Specimen 0*.
2. *Specimen 1*, after 58 days of continuous water circulation.
3. *Specimen 2*, after 594 days of continuous water circulation.

The specimens were cut in several samples as indicated above, corresponding to the inlet, central and outlet regions. Specimens 1 and 2 were cured at 120°C before being flushed with water.

SEM versus OM

SEM is a very powerful tool, but needs from a conductive surface for topographic inspection, so the samples must be coated beforehand with a thin metallic layer, in this case made of gold a few nanometers thick. Thus, if this technology is used, it should be ensured that the gold deposition will not mask surface defects. A way to verify it is by inspecting a tube surface with OM and SEM.

Fig. B.5 shows a comparison of the micro-images of the same specimen at the same location, taken with OM and with SEM. The image taken with OM shows the surface as it is, as no gold deposition



Figure B.5: Comparison of OM and SEM images at the same location in one sample. Surface features observed with the two technologies are highlighted in red. Images adapted from [185].

is needed for this inspection technique. Then, prior to SEM scanning, the sample was deposited with a thin gold layer. It is observed that the defects highlighted in red are visible with both technologies, so OM and SEM can be used for inspection. SEM provides a better depth perception and allows to observe smaller features, while OM displays a more natural view of the surface, though is prone to reflections and it is not recommended for detailed imaging beyond 1 kx.

SEM results

Various surface irregularities are observed in the surfaces of both specimens 0 (new tube) and 2 (water circulation for 594 days), as displayed in Fig. B.6. The surface defects are in the order of the tenths of micrometers. Also, in specimen 2, local smoother areas were observed using SEM at 5kx, as depicted in Fig. B.7. This indicates that the water flow might have locally smoothed out the surface. However, the magnitude of the smoothed area and its depth is significantly smaller than the defects naturally present in the polyimide tubes.

OM results

OM inspection revealed the presence of surface defects (i.e. grooves, cavities), sometimes showing patterns, in samples of all specimens tested, including the brand new tube. This would indicate that they are features related to the manufacturing process of the tubes (extrusion). Fig B.8 displays the inner surfaces of two samples from specimens 1 and 2. OM did not show smooth local areas, as SEM did. This is related to the fact that OM is not precise enough over 1 kx, for which SEM is recommended.

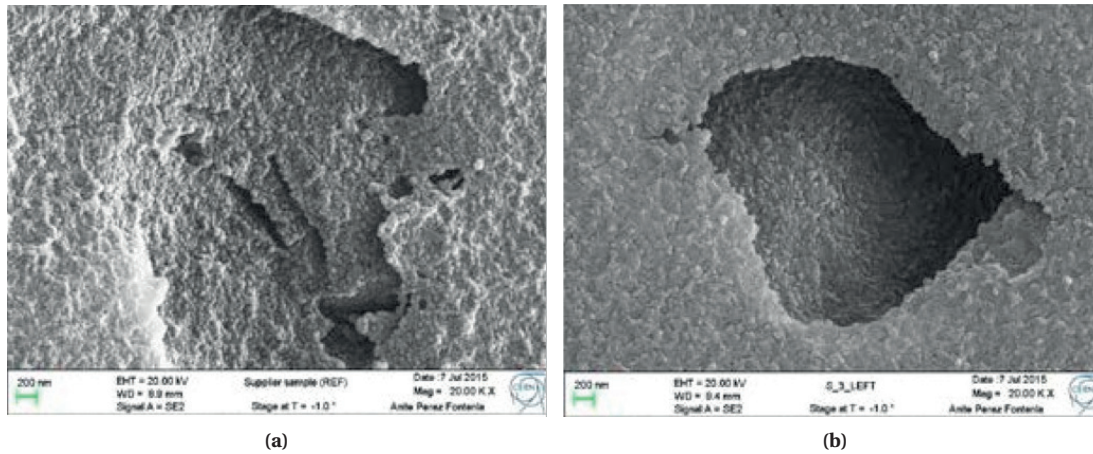


Figure B.6: SEM images at 20 kx of two samples from specimens 0 (new pipe) and 2 (water flow for 594 days). Images adapted from [185].

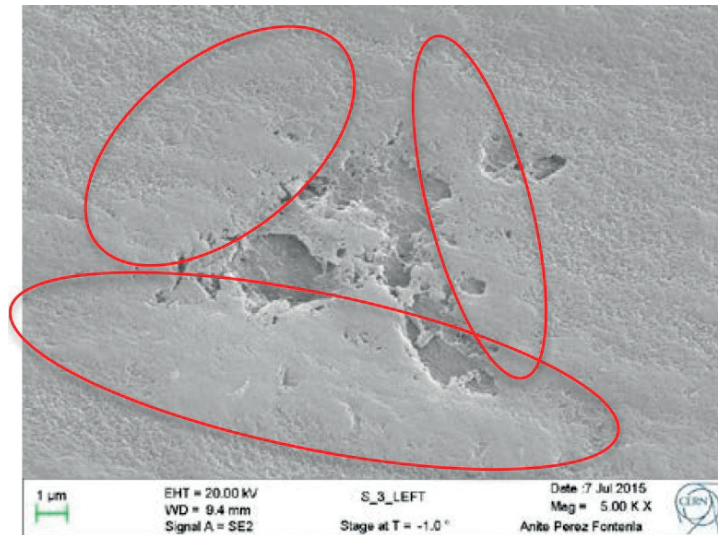


Figure B.7: SEM images of the inner surface local smoothing in specimen 2 (flushed with water for 594 days). Image adapted from [185].

B.3.6 Conclusions

The main conclusions so far on the ongoing long-term water-polyimide channel compatibility tests are the following:

- A dedicated facility was commissioned to continuously circulate water in several polyimide tube specimens, with one of them currently installed since 2 years and 8 months.
- No failures (leaks, increase of pressure drop) were so far observed in any specimen, even after sustaining each a water flow rate 5 to 6 times the nominal expected in the ITS Upgrade Inner Barrel staves, where the flow is laminar. Furthermore, no failures are acknowledged after nearly

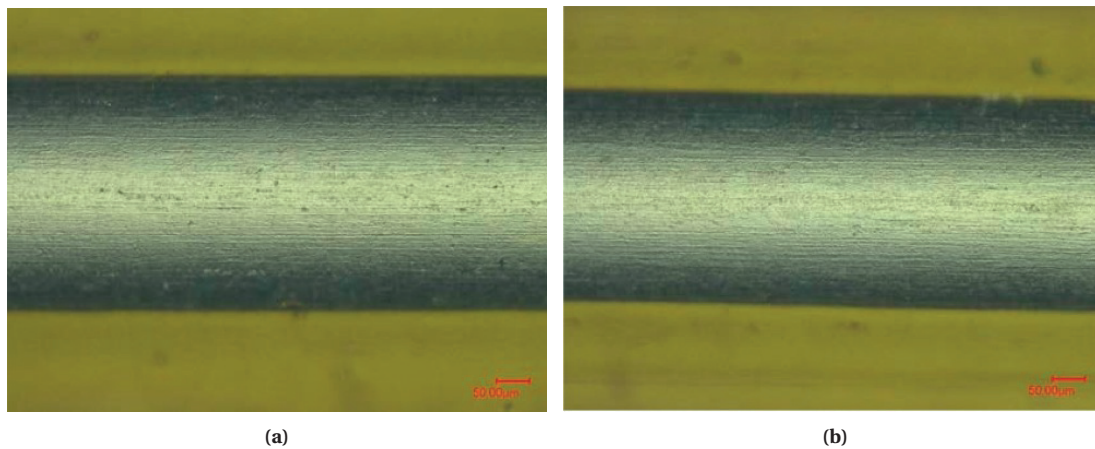


Figure B.8: OM images of the inner surface of the two central samples from specimens 1 and 2 (flushed with water for 58 and 594 days respectively). Images adapted from [185].

12 months of circulating water inside the specimens in a radioactive environment.

- Samples from three polyimide tube specimens were examined using SEM and OM technologies: one brand new tube, and two circulated with water for 58 and 594 days, respectively.
- Both OM and SEM inspection revealed the presence of surface defects in both the new specimen and the one tested for 594 days. These features are related to the tubes' manufacturing process. The gold layer deposited for SEM examination did not mask the surface features.
- SEM revealed locally smoother areas nearby the surface defects in the specimen which was flushed with water for 594 days. This suggests that the water flow slightly eroded the surface relief, although the magnitude of this smoothing is many times smaller than the size of the surface defects.
- OM inspection of the samples subjected to water flow for 58 and 594 days displayed no significant differences between them.
- In general, it can be concluded that the water cooling flow will not cause major damage to the polyimide piping.

B.3.7 Further studies

At the time this dissertation was written, the erosion study is still running, with only two pipe specimens removed so far. The next step is to examine specimens flushed for long time with water in radioactive conditions. This operation should gradually start in mid-2016.

A full Inner Barrel stave was connected to the test facility in January 2015, before the restart of the LHC experiments, and subjected to a sustained water flow rate at a pressure of 3.5 bar. The goal of

this test is to verify there are no failures in the stave after long-term water circulation in radioactive conditions. Special attention is devoted to the central part of the Π -bend, where the water flow impinges perpendicularly, and to the glued joints between the polyimide channels and the carbon fibre-reinforced PEEK connectors. The specimen was removed in January 2016, with no noticeable damage after visual inspection, and installed again in the facility to resume the test.

Other recommended studies involve measuring the surface roughness with Atomic Force Microscopy (AFM), an ongoing process at the INFN Bari, Italy, and the analysis of the particles captured in the mechanical filters at the experimental facility. Should failure occur in one sample, chemical analysis of the water is recommended to verify whether the polyimide was chemically attacked.

Appendix C

Thermophysical properties of the C_4F_{10} and the R245fa fluids

The thermophysical properties of the C_4F_{10} and R245fa refrigerants are described in Tables C.1 and C.2, respectively. The main differences are summarised below:

- The vapour specific volume is significantly higher for R245fa. Thus, the vapour phase for this fluid would accelerate more than for C_4F_{10} in equivalent flow conditions.
- The higher liquid viscosity of R245fa results in thicker liquid films.
- R245fa displays a higher liquid thermal conductivity than C_4F_{10} , so it generally is a better coolant.

Table C.1: Thermophysical properties of the C₄F₁₀ refrigerant.

T_{sat} [°C]	p_{sat} [kPa]	ρ_l [kg m ⁻³]	v_l [m ³ kg ⁻¹]	v_v [m ³ kg ⁻¹]	$i_{l,v}$ [J kg ⁻¹]	α_l [W m ⁻¹ K ⁻¹]	μ_l [μPa s]	Pr_l [-]	γ [N m ⁻¹]
-15	58.41	1631.8	6.721	0.1488	101.1	0.0504	365.7	7.31	0.0113
-10	72.86	1616.4	8.279	0.1208	99.5	0.0496	341.1	6.98	0.0108
-5	89.99	1600.7	10.109	0.0989	97.9	0.0488	318.7	6.69	0.0103
0	110.12	1584.6	12.244	0.0817	96.3	0.0481	298.3	6.41	0.0097
5	133.59	1568.0	14.719	0.0679	94.6	0.0473	279.5	6.16	0.0092
10	160.76	1551.1	17.575	0.0569	92.8	0.0466	262.2	5.92	0.0087
15	192.00	1533.6	20.855	0.0479	91.0	0.0459	246.2	5.70	0.0082
20	227.69	1515.6	24.607	0.0406	89.2	0.0452	231.3	5.50	0.0077
25	268.25	1497.1	28.885	0.0346	87.3	0.0445	217.5	5.30	0.0072
30	314.07	1477.9	33.748	0.0296	85.3	0.0438	204.5	5.12	0.0067
35	365.59	1458.0	39.266	0.0255	83.3	0.0431	192.3	4.94	0.0062
40	423.26	1437.3	45.516	0.0220	81.1	0.0425	180.8	4.78	0.0057
45	487.53	1415.7	52.591	0.0190	78.9	0.0418	169.9	4.62	0.0053
50	558.89	1393.2	60.597	0.0165	76.6	0.0412	159.6	4.47	0.0048

Table C.2: Thermophysical properties of the R245fa refrigerant.

T_{sat} [°C]	p_{sat} [kPa]	ρ_l [kg m ⁻³]	v_l [m ³ kg ⁻¹]	v_v [m ³ kg ⁻¹]	$i_{l,v}$ [J kg ⁻¹]	α_l [W m ⁻¹ K ⁻¹]	μ_l [μPa s]	Pr_l [-]	γ [N m ⁻¹]
-15	25.35	1441.4	1.617	0.6184	212.5	0.1005	725.2	9.01	0.0192
-10	32.77	1429.0	2.058	0.4859	209.8	0.0990	668.3	8.49	0.0185
-5	41.87	1416.6	2.592	0.3859	207.2	0.0974	618.0	8.03	0.0179
0	52.92	1404.0	3.231	0.3096	204.5	0.0959	573.2	7.61	0.0172
5	66.21	1391.2	3.989	0.2507	201.7	0.0943	533.1	7.25	0.0166
10	82.05	1378.3	4.884	0.2048	199.0	0.0928	497.0	6.92	0.0160
15	100.76	1365.3	5.930	0.1686	196.1	0.0912	464.3	6.62	0.0153
20	122.70	1352.0	7.147	0.1399	193.3	0.0897	434.5	6.35	0.0147
25	148.25	1338.5	8.553	0.1169	190.3	0.0881	407.3	6.11	0.0140
30	177.79	1324.9	10.169	0.0983	187.3	0.0865	382.3	5.89	0.0134
35	211.72	1310.9	12.018	0.0832	184.3	0.0849	359.2	5.69	0.0128
40	250.46	1296.7	14.124	0.0708	181.1	0.0834	337.9	5.50	0.0121
45	294.46	1282.2	16.513	0.0606	177.9	0.0818	318.1	5.33	0.0115
50	344.17	1267.4	19.213	0.0520	174.6	0.0802	299.7	5.17	0.0109

Appendix D

Calibration procedure

D.1 Introduction

In the experimental flow boiling heat transfer study described in chapter 6, guaranteeing low heat flux uncertainty is essential for low error propagation to the mean heat transfer coefficient. According to Eqs. 6.3 to 6.5, it is necessary to minimise the uncertainty of the water temperature measurements and the water flow rate. An accurate calibration of the instrumentation will ensure low uncertainty of these measurements. This appendix is dedicated to the description of the calibration methodology applied to the DAQ channels for the temperature measurements, and the water rotameter.

D.2 Calibration of the temperature measurements

All the type K thermocouples are submerged in water in a Thermo Scientific HAAKE™ A25B thermal bath, carefully placed in a plastic support that prevents short circuits and interferences. Next to the thermocouples and equally submerged in the thermal bath, a high-precision, NIST-calibrated glass thermometer, with a resolution of 0.1°C and a type B error of 0.05°C, is placed. This instrument provides the “true” temperature value, namely the reference temperature (T_{ref}) during the calibration.

The calibration is performed for temperatures ranging from 23 to 79°C in increments of 8°C, so there are $m=8$ target temperatures. For each temperature, steady-state conditions were ensured before saving the measurements. The temperature readings were recorded for at least 20 seconds. Then, the standard deviation of the measurements in time was calculated, and verified it does not exceed 0.05 K, half the target uncertainty (0.1 K).

The calibration procedure follows the methodology described by Abernethy and Thompson [159],

which consists of the following steps:

1. **Record N calibration curves:** each curve is constituted by the readings of each channel of the DAQ system for reference temperatures, measured with the glass thermometer, in increments of 8°C from 23 to 79°C and then back to 23°C . This is to ensure no hysteresis effects are present in the system. A total of $N=5$ curves were recorded in this way, in order to decrease the global uncertainty of the calibration.
2. **Curve fitting:** since the voltage provided by the type K thermocouples in the 23 - 79°C range varies in an almost linear fashion, the temperature data in each curve is fitted by the least square method to a linear function, defined as follows:

$$T_{meas} = a T_{ref} + b \quad (\text{D.1})$$

where a is the slope of the fitted curve and b the intercept constant. T_{ref} is the reference temperature measured by the precision glass thermometer. Note that T_{ref} and T_{meas} may differ from the target temperature set at the thermal bath (T_{target}).

3. **Calibration uncertainty:** referred as the *expanded uncertainty* (U , defined in a similar way as in section 4.3.6), it is determined as recommended by NIST [167]:

$$U = \pm (errB + kP) \quad (\text{D.2})$$

where $errB$ is the type B uncertainty of the calibration instrument, namely its systematic error ($errB=0.05$ K); and P is the calibration precision coefficient:

$$P = \pm \sqrt{\sum_{i=1}^m s_i^2} \quad (\text{D.3})$$

where s_i , the uncertainty of each thermocouple for each of the m target temperatures (T_{target}) in each calibration curve, is defined as follows:

$$s_i = \pm \sqrt{\frac{1}{N-1} \sum_{j=1}^N (T_{meas_{i,j}} - \bar{T})^2} \quad (\text{D.4})$$

N is the number of calibration curves (5); $T_{meas_{i,j}}$ are the temperature values calculated with Eq. D.1 for each of the m target temperatures (T_{target}) in each of the N calibration curves; and \bar{T} is the average of the aforementioned $T_{meas_{i,j}}$ values for each T_{target} .

In Eq. D.2, k is the coverage factor for a desired confidence interval of the calibration uncertainty. To calculate it, it is necessary to define which statistical distribution follows the recorded data, a confidence interval, and the degrees of freedom of the distribution. For databases with few data points, such as the present calibration, a t -distribution of the data can be assumed, so $k = t$. The

degrees of freedom (df) are calculated as follows:

$$df = \frac{\left(\sum_{i=1}^m s_i^2 \right)^2}{\sum_{i=1}^m \frac{s_i^4}{N-1}} \quad (\text{D.5})$$

A confidence interval of 95% is defined, so $t=t_{95}$. To calculate t_{95} , one can use t -distribution tables with df and $\alpha = 1 - 0.95 = 0.05^a$ as inputs. Any software with statistical capabilities, like MS Excel, has built-in functions that calculate $t=t_{95}$ iteratively. As the degrees of freedom were typically high, t_{95} displayed values typically between 2 and 2.3.

4. **Final curve fitting:** a linear fit of T_{meas} versus T_{ref} is performed for all the data spanning the N calibration curves:

$$T_{meas} = a' T_{ref} + b' \quad (\text{D.6})$$

Therefore, the equation yielding the true temperature measurement is the following:

$$T_{true} = \frac{1}{a'} T_{meas} + \frac{b'}{a'} \quad (\text{D.7})$$

In the LabVIEW panel, the temperature measured at each channel is multiplied by $1/a'$ and the b'/a' constant is subtracted in order to obtain the true temperature measurement. Table D.1 displays all the calibration uncertainty parameters and the fitting constants for the channels measuring the temperatures of the heating water at the test section annulus inlet and outlet, the water flow at the rotameter, the R245fa flow at the test rig inlet and outlet, and the metallic tube walls before and after the test section (see Fig. 6.1). Other temperature measurements, such as the ambient air and at the pre-heater surface were calibrated too, but the results are not shown here for simplicity.

In order to increase the accuracy of the calibration and guarantee it during the experimental tests, the following practices were followed:

- The ambient temperature was controlled during the calibration and the experimental tests and set to a stable value around 21°C. Small fluctuations from thermal loads from other facilities in the lab were seldom observed; in those cases, the tests were postponed until optimal ambient conditions were achieved again.
- Two SCXI-1112 thermocouple input modules from National Instruments were used for the temperature measurements. Each of the 8 analog input channels in each of the modules has its own independent cold-junction sensor. Their temperatures were constantly monitored, ensuring

^a The tail probability is $\alpha/2$. α is the probability of the two tails of the t -distribution.

Table D.1: Calibration uncertainty parameters and correction constants for the temperature measurements.

Location	Heating water				Rotameter		R245fa		Tube wall	
Channel	T_{in_1}	T_{in_2}	T_{out_1}	T_{out_2}	T_{in}	T_{out}	T_{bef-ts}	$T_{after-ts}$	T_{in}	T_{out}
P [K]	0.024	0.023	0.018	0.033	0.033	0.042	0.026	0.023	0.027	0.029
df [-]	10.17	16.44	17.39	18.23	8.03	17.50	10.92	7.81	17.58	18.71
$errB$ [K]	0.05	0.05	0.05	0.05	0.05	0.05	0.05	0.05	0.05	0.05
t_{95} [-]	2.23	2.12	2.11	2.10	2.31	2.11	2.23	2.36	2.11	2.10
U [K]	0.10	0.10	0.09	0.12	0.13	0.14	0.11	0.10	0.11	0.11
a' [-]	1.004	1.004	1.004	1.004	1.004	1.004	1.003	1.004	1.004	1.004
b' [K]	1.438	1.323	1.427	1.360	1.702	1.390	1.535	1.367	1.511	1.383
$1/a'$ [-]	0.996	0.996	0.996	0.996	0.996	0.996	0.997	0.996	0.996	0.996
b'/a' [K]	1.432	1.317	1.421	1.354	1.696	1.384	1.530	1.361	1.505	1.377

stability during the tests at values close to the ones recorded during the calibration campaign.

This allowed to achieve the low temperature measurement uncertainties reported in Table D.1.

- The data acquisition system was left permanently on, in order to ensure it is in thermal equilibrium with the ambient.

D.3 Calibration of the water flow rate measurements

The volumetric flow rate readings provided by the water rotameter depend on the flow density and viscosity. These two physical properties change with temperature, especially the second one. Thus, a calibration of the water rotameter was performed in order to ensure accurate heat flux calculations.

The rotameter is calibrated at flow temperatures of 40, 50, 60, 70 and 80°C using an adaptation of the methodology described above. First, five target flow rates were selected, spanning the whole graded scale of the rotameter. Each calibration curve was built for those five flow rate targets, both increasing and decreasing the flow rate. Five calibration curves were recorded for each reference temperature. To measure the reference flow rate, a stopwatch, a scale and a graduated cylinder were used, quantifying beforehand the systematic error of this kind of measurements.

Finally, the uncertainty of the measured flow rate was quantified for each reference temperature. An average uncertainty value of $\pm 0.031 \text{ L min}^{-1}$ was found. During the data processing, double linear interpolations were used for intermediate water temperatures and flow rates between the values obtained in the calibration. A second rotameter, used in the water-water validation tests in section 6.4, was also calibrated in the corresponding water temperatures. The water flow rate in the two-phase diabatic tests is read at the top of the rotameter scale, minimising the error of the instrument.

The differential pressure transducer calibration was verified using a Mensor CPG 2500 Digital Pressure Gauge as the reference instrument. The previous calibration was found to be valid, with an uncertainty of the measurements of 0.15 kPa, as reported in Table 6.6.

Appendix E

Limitations of the present studies

This appendix describes the limitations acknowledged in the presented work regarding the ALICE ITS Upgrade cooling tests, reported in chapters from 3 to 5, and the experimental flow boiling heat transfer studies in a small polyimide channel, described in chapter 6.

E.1 ALICE ITS Upgrade experimental cooling studies

- For the staves and half-stave prototypes, a uniform heat flux on the polyimide channels' walls was assumed. This hypothesis is not validated, because, although in most of the tested prototypes there is a TPG foil on top of the cooling channels to enhance the thermal contact with the cooling plate below, the heat is most likely transferred through the contact surface of the channels with the cooling plate. Furthermore, the low thermal conductivity of polyimide and the thin wall thickness promote the presence of a localised heat flux. Thus, where made, the assumptions of uniform heat flux in the cooling channel are not verified. This is likely to be one of the reasons behind the mismatch between predicted and experimental two-phase heat transfer coefficients in the staves cooling tests performed at CERN, as reported in subsection 5.3.4.
- Material and coolant compatibility in radioactive conditions were taken into account when designing the staves. However, long-term compatibility of water and polyimide in a radioactive environment is being experimentally verified (see appendix B). In principle, no problems are expected for the flow rates, temperatures and radiation doses foreseen in the ITS Upgrade detector.

E.2 Experimental flow boiling heat transfer studies in a small polyimide channel

- No complete surface characterisation of the polyimide channel was performed in the present work. Thorough examination of the surface finish, discerning between the profile, waviness and roughness, as well as the size of the peaks on the inner surface of the channel is recommended in future studies, as it would provide more information on the importance of the different heat transfer mechanisms and would allow further comparison with similar works in the literature.
- Since it was not possible to accurately measure local wall temperatures on the polyimide channel, the results refer to heat transfer coefficients averaged along the heated 285 mm of the channel. Thus, no insight on local effects was obtained. Phenomena such as nucleate boiling and dryout onset were not captured, although the last was indeed observed in the high-speed images. This must be taken into account when making direct comparisons with local heat transfer results from other similar experimental studies.
- The polyimide channel was assembled inside the glass tube where the heating water flows, with some traction pre-load provided at the extremities by O-rings. After close examination of the assembly, it could be seen that the polyimide tube, which is not as rigid as a metallic channel, was not perfectly centered in the whole test section length. This could lead to a non-uniform water flow distribution in the annular space between the polyimide channel and the glass tube, and potential local heat flux non-uniformities. However, it is expected they are averaged out when calculating the mean heat transfer coefficient.
- Assessing the influence of the heat flux on the mean heat transfer coefficient is misleading in cases where the rest of flow parameters remain constant, as they display different vapour quality differences between the polyimide channel inlet and outlet (Δx_{in-out}). When comparing cases with big differences between their corresponding Δx_{in-out} , a visual overview on the influence of the heat flux on the mean heat transfer coefficient is provided by plotting it versus the inlet and outlet vapour qualities, such as in Fig. 6.19.
- Two-phase flow instabilities were occasionally observed. They were suppressed by closing the needle valves upstream and downstream the test section, but in some cases could not be mitigated. Such experimental cases were not included in the experimental database.

Bibliography

- [1] The ALICE Collaboration. The ALICE experiment at the CERN LHC. *Journal of Instrumentation*, 3(08):S08002, 2008. URL <http://stacks.iop.org/1748-0221/3/i=08/a=S08002>.
- [2] L Rossi. LHC Upgrade Plans: Options and Strategy. (CERN-ATS-2011-257):6 p, Dec 2011.
- [3] The CMS Collaboration. Technical proposal for the upgrade of the CMS detector through 2020. Technical Report CERN-LHCC-2011-006. LHCC-P-004, CERN, Geneva, Jun 2011.
- [4] The ALICE Collaboration. Conceptual Design Report for the Upgrade of the ALICE Inner tracking System. Technical Report CERN-LHCC-2012-005. LHCC-G-159, CERN, Geneva, Mar 2012.
- [5] The ALICE Collaboration. Technical Design Report for the Upgrade of the ALICE Inner Tracking System. Technical Report CERN-LHCC-2013-024. ALICE-TDR-017, CERN, Geneva, Nov 2013.
- [6] M. S. Tyagi. *Introduction to Semiconductor Materials and Devices*. John Wiley and Sons, 1991. ISBN 0-471-60560-3.
- [7] C.A. Heusch, A.G. Holodenko, and H.G. Moser. Measurements of Silicon Detector Thermal Runaway. 1999.
- [8] R. L. Clough. High-energy radiation and polymers: A review of commercial processes and emerging applications. *Nuclear Instruments and Method in Physics Research Section B*, 185 (1-4): 8–33, 2001.
- [9] B. G. Kumar, R. P. Singh, and T. Nakamura. Degradation of carbon fiber-reinforced epoxy composites by ultraviolet radiation and condensation. 36(24):2713–2733, 2002. doi: 10.1177/002199802761675511.
- [10] F. Guarino, C. Hauviller, and M. Tavlet. *Compilation of radiation damage test data, part IV: adhesives*. CERN, Geneva, 2001. URL <http://cds.cern.ch/record/531818>.

- [11] S. Ilie and M. Tavlet. Qualification of coolants and cooling pipes for future high-energy-particle detectors. *Nuclear Instruments and Methods in Physics Research B*, 185:318–322, December 2001. doi: 10.1016/S0168-583X(01)00806-0.
- [12] H. Schönbacher and A. Stolarz-Izycka. *Compilation of radiation damage test data, part I: cable insulating materials*. CERN, Geneva, 1979. URL <http://cds.cern.ch/record/133188>.
- [13] M. Tavlet and H. Schönbacher. *Compilation of radiation damage test data, part I, 2nd edition: Halogen-free cable-insulating materials*. CERN, Geneva, 1989. URL <http://cds.cern.ch/record/205520>.
- [14] H. Schönbacher and A. Stolarz-Izycka. *Compilation of radiation damage test data, part II: thermosetting and thermoplastic resins*. CERN, Geneva, 1979. URL <http://cds.cern.ch/record/120566>.
- [15] M. Tavlet, A. Fontaine, and H. Schönbacher. *Compilation of radiation damage test data, part II, 2nd edition: thermoset and thermoplastic resins, composite materials*. CERN, Geneva, 1998. URL <http://cds.cern.ch/record/357576>.
- [16] P. Beynel, P. Maier, and H. Schönbacher. *Compilation of radiation damage test data, part III: materials used around high-energy accelerators*. CERN, Geneva, 1982. URL <http://cds.cern.ch/record/141784>.
- [17] M. Battistin, S. Ilie, R. Setnescu, and B. Teissandier. Chemical and radiolytical characterization of some perfluorocarbon fluids used as coolants for LHC experiments: Chemical characterization. Technical report, CERN, Geneva.
- [18] S. Ilie, R. Setnescu, and B. Teissandier. Chemical and radiolytical characterization of perfluorocarbon fluids used as coolants for LHC experiments: radiolysis effects in perfluorohexane fluids. Technical report, CERN, Geneva.
- [19] Materials and Cables Working Group. The Use of Plastics and other Non-Metallic Materials at CERN with respect to Fire Safety and Radiation Resistance. Technical Report IS-41, rev. 1. EDMS: 335806, TIS Commission, Geneva, 2005.
- [20] R. J. Tapper. Diamond detectors in particle physics. *Reports on Progress in Physics*, 63(8):1273, 2000. URL <http://stacks.iop.org/0034-4885/63/i=8/a=203>.
- [21] H. H. Wieman, E. Anderssen, L. Greiner, H. S. Matis, H. G. Ritter, X. Sun, and M. Szelezniak. STAR PIXEL detector mechanical design. *Journal of Instrumentation*, 4(05):P05015, 2009. URL <http://stacks.iop.org/1748-0221/4/i=05/a=P05015>.
- [22] P. Kuijer. The ALICE silicon strip detector system. *Nucl. Instrum. Meth.*, A447:251–256, 2000. doi: 10.1016/S0168-9002(00)00196-0.

- [23] S. Beole et al. The ALICE silicon drift detectors: Production and assembly. *Nucl. Instrum. Meth.*, A582:733–738, 2007. doi: 10.1016/j.nima.2007.07.087.
- [24] M. A. Pimenta Dos Santos. ALICE SSD and SDD cooling system. Technical Report 490537, Ago 2004. URL <https://edms5.cern.ch/document/490537/1>.
- [25] G. Fiorenza, V. Manzari, C. Pastore, I. Sgura, M. Torresi, and C. Gargiulo. An innovative polyimide microchannels cooling system for the pixel sensor of the upgraded ALICE Inner Tracker. In *Proceedings, 5th IEEE International Workshop on Advances in Sensors and Interfaces (IWASI 2013)*, pages 81–85, 2013. doi: 10.1109/IWASI.2013.6576065.
- [26] The ATLAS Collaboration. ATLAS: Detector and physics performance technical design report. Volume 2. 1999.
- [27] A. Mapelli, A. Catinaccio, J. Daguin, H. van Lintel, G. Nuessle, P. Petagna, and P. Renaud. Low material budget microfabricated cooling devices for particle detectors and front-end electronics. *Nucl. Phys. Proc. Suppl.*, 215:349–352, 2011. doi: 10.1016/j.nuclphysbps.2011.04.050.
- [28] P. Bonneau. Compatibility of PF5060 / FC72 (C6F14) with materials. Technical report, CERN, Geneva.
- [29] A. Pepato et al. The mechanics and cooling system of the ALICE silicon pixel detector. *Nuclear Instruments and Methods in Physics Research Section A: Accelerators, Spectrometers, Detectors and Associated Equipment*, 565(1):6 – 12, 2006. ISSN 0168-9002. doi: <http://dx.doi.org/10.1016/j.nima.2006.04.093>. Proceedings of the International Workshop on Semiconductor Pixel Detectors for Particles and Imaging.
- [30] B. Agostini, M. Fabbri, J. E. Park, L. Wojtan, J. R. Thome, and B. Michel. State of the art of high heat flux cooling technologies. *Heat Transfer Engineering*, 28(4):258–281, 2007. doi: 10.1080/01457630601117799.
- [31] D. Attree et al. The evaporative cooling system for the ATLAS Inner Detector. *Journal of Instrumentation*, 3(07):P07003, 2008. URL <http://stacks.iop.org/1748-0221/3/i=07/a=P07003>.
- [32] B. Verlaat and A. P. Colijn. CO₂ cooling developments for HEP detectors. *PoS, VERTEX2009:031*, 2009.
- [33] M. Capeans et al. ATLAS Insertable B-Layer Technical Design Report. Technical Report CERN-LHCC-2010-013. ATLAS-TDR-19, CERN, Geneva, Sep 2010. URL <http://cds.cern.ch/record/1291633>.
- [34] G. Alberti et al. Development of a Thermal Control System with Mechanically Pumped CO₂ Two-Phase Loops for the AMS-02 Tracker on the ISS. Technical Report arXiv:1302.4294, Feb 2013. URL <https://cds.cern.ch/record/1517395>.

- [35] A. Nomerotski et al. Evaporative CO₂ cooling using microchannels etched in silicon for the future LHCb vertex detector. *JINST*, 8:P04004, 2013. doi: 10.1088/1748-0221/8/04/P04004.
- [36] L. Feld, W. Karpinski, J. Merz, and M. Wlochal. CO₂ cooling for the CMS tracker at SLHC. *Journal of Instrumentation*, 6(01):C01091, 2011. URL <http://stacks.iop.org/1748-0221/6/i=01/a=C01091>.
- [37] *T300 Technical Data Sheet (CFA-001)*. Torayca Carbon Fibers America Inc., 2013. URL <http://www.toraycfa.com/pdfs/T300DataSheet.pdf>.
- [38] *M55J Technical Data Sheet (CFA-017)*. Torayca Carbon Fibers America Inc., 2013. URL <http://www.toraycfa.com/pdfs/M55JDataSheet.pdf>.
- [39] *M60J Technical Data Sheet (CFA-018)*. Torayca Carbon Fibers America Inc., 2013. URL <http://www.toraycfa.com/pdfs/M60JDataSheet.pdf>.
- [40] W. E. Cooper. Low-Mass Materials and Vertex Detector Systems. *PoS, Vertex2013*:036, 2013.
- [41] *K13C2U Technical Data Sheet*. Mitsubishi Chemical Holdings America. URL <http://www.mitsubishichemical.com/DataSheets/CarbonFiber/PD%20K13c2U.pdf>.
- [42] *K13D2U Technical Data Sheet*. Mitsubishi Chemical Holdings America. URL <http://www.mitsubishichemical.com/DataSheets/CarbonFiber/PD%20K13D2U.%pdf>.
- [43] S. Robitaille, G. Patz, and S. Johnson. Advanced Composite Stable Structures, Appropriate Materials for High Precision Detectors. 1994. URL <https://cds.cern.ch/record/399361>.
- [44] I. Bonad. *Thermo-mechanical characterisation of low density carbon foams and composite materials for the ATLAS upgrade*. PhD thesis, University of Glasgow, 2012.
- [45] C. Gargiulo. Studies on the mechanics and cooling of the ALICE ITS Upgrade based on carbon fibre structures. In *Forum on Tracking Detectors Mechanics, DESY, Hamburg, Germany*, 2014. URL <https://indico.cern.ch/event/287285/contribution/10>.
- [46] M. Smalc, G. Shives, G. Chen, S. Guggari, J. Norley, and R. A. Reynolds. Thermal performance of natural graphite heat spreaders. In *ASME 2005 Pacific Rim Technical Conference and Exhibition on Integration and Packaging of MEMS, NEMS, and Electronic Systems collocated with the ASME 2005 Heat Transfer Summer Conference*, pages 79–89. American Society of Mechanical Engineers, 2005.
- [47] Y. Xiong, M. Smalc, J. Norley, J. Chang, H. Mayer, P. Skandakumaran, and B. Reis. Thermal tests and analysis of thin graphite heat spreader for hot spot reduction in handheld devices. In *Thermal and Thermomechanical Phenomena in Electronic Systems, 2008. IThERM 2008. 11th Intersociety Conference on. IEEE, 2008*, pages 583–90, 2008.

- [48] F. Sarvar, D. C. Whalley, and P. P. Conway. Thermal interface materials-a review of the state of the art. In *Electronics Systemintegration Technology Conference, 2006. 1st*, volume 2, pages 1292–1302. IEEE, 2006.
- [49] *Thermograph FGS003 Technical Data Sheet*. AMEC THERMASOL. URL <http://www.amecthermasol.co.uk/datasheets/>.
- [50] C. A. Heusch, H. G. Moser, and A. Kholodenko. Direct measurements of the thermal conductivity of various pyrolytic graphite samples (PG, TPG) used as thermal dissipation agents in detector applications. *Nucl. Instrum. Meth.*, A480:463–469, 2002. doi: 10.1016/S0168-9002(01)01208-6.
- [51] A. A. Balandin, S. Ghosh, W. Bao, I. Calizo, D. Teweldebrhan, F. Miao, and C. N. Lau. Superior thermal conductivity of single-layer graphene. *Nano letters*, 8(3):902–907, 2008.
- [52] W. Cai, A. L. Moore, Y. Zhu, X. Li, S. Chen, L. Shi, and R. S. Ruoff. Thermal transport in suspended and supported monolayer graphene grown by chemical vapor deposition. *Nano Letters*, 10(5): 1645–1651, 2010. doi: 10.1021/nl9041966. URL <http://dx.doi.org/10.1021/nl9041966>. PMID: 20405895.
- [53] R. Prasher. Graphene spreads the heat. *Science*, 328(5975):185–186, 2010.
- [54] J. H. Seol, I. Jo, A. L. Moore, L. Lindsay, Z. H. Aitken, M. T. Pettes, X. Li, Z. Yao, R. Huang, D. Broido, N. Mingo, R. S. Ruoff, and L. Shi. Two-dimensional phonon transport in supported graphene. *Science*, 328(5975):213–216, 2010. doi: 10.1126/science.1184014. URL <http://www.sciencemag.org/content/328/5975/213.abstract>.
- [55] D. Gaies and K. T. Faber. Thermal properties of pitch-derived graphite foam. *Carbon*, 40(7): 1137–1140, 2002.
- [56] S. B. White, N. C. Gallego, D. D. Johnson, K. Pipe, A. J. Shih, and E. Jih. Graphite foam for cooling of automotive power electronics. In *Power Electronics in Transportation, 2004*, pages 61–65. IEEE, 2004.
- [57] J. W. Klett and M. Trammell. Parametric investigation of a graphite foam evaporator in a thermosyphon with fluorinert and a silicon cmos chip. *Device and Materials Reliability, IEEE Transactions on*, 4(4):626–637, 2004.
- [58] *EX1515 DS 120810 Technical Data Sheet*. TenCate, 2013.
- [59] *RS-3 DS 062612 Technical Data Sheet*. TenCate, 2013.
- [60] *Hysol EA9396 Technical Data Sheet*. Henkel Corp., 2013.
- [61] *EPO-TEK® H20E Technical Data Sheet*. Epoxy Technology Inc., 2013.

- [62] P. Riedler et al. Production and Integration of the ALICE Silicon Pixel Detector. *Nuclear Instruments and Methods in Physics Research Section A: Accelerators, Spectrometers, Detectors and Associated Equipment*, 572(1):128 – 131, 2007. ISSN 0168-9002. doi: <http://dx.doi.org/10.1016/j.nima.2006.10.178>.
- [63] S. Coelli. R&D for the local support and cooling channel for the ATLAS Pixel Insertable B-Layer (IBL). Technical report, ATL-COM-INDET-2010-091, 2010.
- [64] W. W. Wright and M. Hallden-Abberton. Polyimides. *Ullmann's Encyclopedia of Industrial Chemistry*, 2002.
- [65] S. Bachmann, I. Bagaturia, H. Deppe, F. Eisele, T. Haas, L. Hajduk, U. Langenegger, J. Michalowski, A. Nawrot, G. Polok, et al. The straw tube technology for the LHCb outer tracking system. *Nuclear Instruments and Methods in Physics Research Section A: Accelerators, Spectrometers, Detectors and Associated Equipment*, 535(1):171–174, 2004.
- [66] *Mikro-Polyimid Kapillarschlauch Data Sheet*. Detakta, 2013.
- [67] *Polyimide Liners for Cardiovascular Catheter Tubing Technology Sheet*. Putnam Plastics Inc., 2013.
- [68] S. G. Kandlikar and W. J. Grande. Evolution of microchannel flow passages—thermohydraulic performance and fabrication technology. *Heat transfer engineering*, 24(1):3–17, 2003.
- [69] P. A. Kew and K. Cornwell. Correlations for the prediction of boiling heat transfer in small-diameter channels. *Applied Thermal Engineering*, 17(8):705–715, 1997.
- [70] C. L. Ong and J. R. Thome. Macro-to-microchannel transition in two-phase flow: Part 1—two-phase flow patterns and film thickness measurements. *Experimental Thermal and Fluid Science*, 35(1):37–47, 2011.
- [71] S. G. Kandlikar. Scale effects on flow boiling heat transfer in microchannels: A fundamental perspective. *International Journal of Thermal Sciences*, 49(7):1073–1085, 2010.
- [72] S. S. Bertsch, E. A. Groll, and S. V. Garimella. Review and comparative analysis of studies on saturated flow boiling in small channels. *Nanoscale and Microscale Thermophysical Engineering*, 12(3):187–227, 2008.
- [73] L. Cheng, G. Ribatski, and J. R. Thome. Two-phase flow patterns and flow-pattern maps: fundamentals and applications. *Applied Mechanics Reviews*, 61(5):050802, 2008.
- [74] S. S. Mehendale, A. M. Jacobi, and R. K. Shah. Fluid flow and heat transfer at micro-and meso-scales with application to heat exchanger design. *Applied Mechanics Reviews*, 53(7):175–193, 2000.

- [75] J. G. Collier and J. R. Thome. Convective Boiling and Condensation. Oxford University Press, 1996.
- [76] L. Wojtan, T. Ursenbacher, and J. R. Thome. Investigation of flow boiling in horizontal tubes: Part I - A new diabatic two-phase flow pattern map. *International Journal of Heat and Mass Transfer*, 48(14):2955–2969, 2005.
- [77] R. Revellin, V. Dupont, T. Ursenbacher, J. R. Thome, and I. Zun. Characterization of Two-Phase Flows in Microchannels: Optical Measurement Technique and Flow Parameter Results for R-134a in a 0.5 mm Channel. *Int. J. Multiphase Flow*, 32:755–774, 2006.
- [78] R. Revellin and J. R. Thome. A new type of diabatic flow pattern map for boiling heat transfer in microchannels. *Journal of Micromechanics and Microengineering*, 17(4):788, 2007.
- [79] C. B. Tibirica and G. Ribatski. Flow boiling in micro-scale channels—synthesized literature review. *International Journal of Refrigeration*, 36(2):301–324, 2013.
- [80] J. E. Park and J. R. Thome. Critical heat flux in multi-microchannel copper elements with low pressure refrigerants. *International Journal of Heat and Mass Transfer*, 53(1):110–122, 2010.
- [81] S. M. Zivi. Estimation of steady-state steam void-fraction by means of the principle of minimum entropy production. *Journal of Heat Transfer*, 86(2):247–251, 1964.
- [82] F. T. Kanizawa and G. Ribatski. Void fraction predictive method based on the minimum kinetic energy. *Journal of the Brazilian Society of Mechanical Sciences and Engineering*, pages 1–17, 2015. ISSN 1678-5878. doi: 10.1007/s40430-015-0446-x. URL <http://dx.doi.org/10.1007/s40430-015-0446-x>.
- [83] S. Z. Rouhani and E. Axelsson. Calculation of void volume fraction in the subcooled and quality boiling regions. *International Journal of Heat and Mass Transfer*, 13(2):383–393, 1970.
- [84] D. Steiner. H3.1 Flow Patterns in Evaporator Tubes. Verein Deutscher Ingenieure. VDI Heat Atlas: Second Edition, 2010.
- [85] V. G. Niño, P. S. Hrnjak, and T. A. Newell. Characterization of two-phase flow in microchannels. Technical report, Air Conditioning and Refrigeration Center. College of Engineering. University of Illinois at Urbana-Champaign, 2002.
- [86] A. Cioncolini and J. R. Thome. Void fraction prediction in annular two-phase flow. *International Journal of Multiphase Flow*, 43:72–84, 2012.
- [87] A. Cioncolini and J. R. Thome. Entrained liquid fraction prediction in adiabatic and evaporating annular two-phase flow. *Nuclear Engineering and Design*, 243:200–213, 2012.

- [88] D. A. Yashar. Experimental investigation of void fraction during horizontal flow in smaller diameter refrigeration applications. Technical report, Air Conditioning and Refrigeration Center. College of Engineering. University of Illinois at Urbana-Champaign, 1998.
- [89] M. R. Hoehne and P. S. Hrnjak. Charge minimization in systems and components using hydrocarbons as a refrigerant. Technical report, Air Conditioning and Refrigeration Center. College of Engineering. University of Illinois at Urbana-Champaign, 2004.
- [90] L. Consolini. *Convective boiling heat transfer in a single micro-channel*. PhD thesis, EPFL, 2008.
- [91] R. W. Lockhart and R. C. Martinelli. Proposed correlation of data for isothermal two-phase, two-component flow in pipes.
- [92] L. Friedel. Pressure-drop during gas-vapor-liquid flow in pipes. *Chemie Ingenieur Technik*, 50(3): 167–180, 1978.
- [93] H. Müller-Steinhagen and K. Heck. A simple friction pressure drop correlation for two-phase flow in pipes. *Chemical Engineering and Processing: Process Intensification*, 20(6):297–308, 1986.
- [94] R. Revellin and J. R. Thome. Adiabatic two-phase frictional pressure drops in microchannels. *Experimental Thermal and Fluid Science*, 31(7):673–685, 2007.
- [95] J. D. Da Silva and G. Ribatski. Two-phase frictional pressure drop of halocarbon refrigerants inside small diameter tubes: data analyses and the proposition of a new frictional pressure drop correlation. In *Proceedings, 8th International Conference on Multiphase Flow (ICMF 2013), Jeju, Korea*, 2013.
- [96] D. F. Sempértegui-Tapia and G. Ribatski. Two-phase frictional pressure drop in horizontal micro-scale channels: Experimental data analysis and prediction method development. *International Journal of Multiphase Flow* (In Review), 2016.
- [97] J. M. Quibén. *Experimental and analytical study of two-phase pressure drops during evaporation in horizontal tubes*. PhD thesis, Dynamique des Fluides et des Transferts, Université Pierre et Marie Curie, Paris, France, 2005.
- [98] A. Cioncolini, J. R. Thome, and C. Lombardi. Unified macro-to-microscale method to predict two-phase frictional pressure drops of annular flows. *International Journal of Multiphase Flow*, 35(12):1138 – 1148, 2009. doi: <http://dx.doi.org/10.1016/j.ijmultiphaseflow.2009.07.005>.
- [99] E. Costa-Patry, J. Olivier, B. Michel, and J. R. Thome. Two-phase flow of refrigerants in 85 μ m-wide multi-microchannels: Part ii–heat transfer with 35 local heaters. *International Journal of Heat and Fluid Flow*, 32(2):464–476, 2011.

- [100] R. J. Da Silva Lima and J. R. Thome. Two-phase frictional pressure drops in U-bends and contiguous straight tubes for different refrigerants, orientations, tube, and bend diameters: Part 2. New models (RP-1444). *HVAC&R Research*, 18(6):1072–1097, 2012. doi: 10.1080/10789669.2012.672363. URL <http://www.tandfonline.com/doi/abs/10.1080/10789669.2012.672363>.
- [101] D. Chisholm. Two-phase flow in bends. *International Journal of Multiphase Flow*, 6(4):363–367, 1980.
- [102] M. Padilla, R. Revellin, and J. Bonjour. Two-phase flow visualization and pressure drop measurements of HFO-1234yf and R-134a refrigerants in horizontal return bends. *Experimental Thermal and Fluid Science*, 39:98–111, 2012.
- [103] C. B. Tibiriçá and G. Ribatski. Flow Boiling Heat Transfer of R134a and R245fa in a 2.3 mm Tube. *International Journal of Heat and Mass Transfer*, 53(11):2459–2468, 2010.
- [104] S. G. Kandlikar. High flux heat removal with microchannels -a roadmap of challenges and opportunities. *Heat Transfer Engineering*, 26(8):5–14, 2005.
- [105] S. Szczukiewicz, N. Borhani, and J. R. Thome. Two-phase heat transfer and high-speed visualization of refrigerant flows in $100 \times 100 \mu\text{m}^2$ silicon multi-microchannels. *International Journal of Refrigeration*, 36(2):402–413, 2013.
- [106] R. Revellin and J. R. Thome. Experimental investigation of R-134a and R-245fa two-phase flow in microchannels for different flow conditions. *International Journal of Heat and Fluid Flow*, 28(1):63–71, 2007.
- [107] W. Qu and I. Mudawar. Flow boiling heat transfer in two-phase micro-channel heat sinks—-II. Annular two-phase flow model. *International Journal of Heat and Mass Transfer*, 46(15):2773–2784, 2003.
- [108] T. G. Karayiannis, M. M. Mahmoud, and D. B. R. Kenning. A study of discrepancies in flow boiling results in small to microdiameter metallic tubes. *Experimental Thermal and Fluid Science*, 36:126–142, 2012.
- [109] R. Charnay, R. Revellin, and J. Bonjour. Flow boiling heat transfer in minichannels at high saturation temperatures: Part I—Experimental investigation and analysis of the heat transfer mechanisms. *International Journal of Heat and Mass Transfer*, 87:636–652, 2015.
- [110] G. Ribatski, L. Wojtan, and J. R. Thome. An analysis of experimental data and prediction methods for two-phase frictional pressure drop and flow boiling heat transfer in micro-scale channels. *Experimental Thermal and Fluid Science*, 31(1):1–19, 2006.
- [111] L. Consolini and J. R. Thome. Micro-channel flow boiling heat transfer of R-134a, R-236fa, and R-245fa. *Microfluidics and nanofluidics*, 6(6):731–746, 2009.

- [112] B. J. Jones and S. V. Garimella. Surface roughness effects on flow boiling in microchannels. *Journal of Thermal Science and Engineering Applications*, 1(4):041007, 2009.
- [113] S. G. Kandlikar and P. H. Spiesman. Effect of surface characteristics on flow boiling heat transfer. In *Engineering Foundation Conference on Convective and Pool Boiling, May*, pages 18–25, 1997.
- [114] E. A. Pike-Wilson and T. G. Karayiannis. Flow boiling of R245fa in 1.1 mm diameter stainless steel, brass and copper tubes. *Experimental Thermal and Fluid Science*, 59:166–183, 2014.
- [115] G. P. Celata, M. Cumo, V. Marconi, S. J. McPhail, and G. Zummo. Microtube liquid single-phase heat transfer in laminar flow. *International Journal of Heat and Mass Transfer*, 49(19):3538–3546, 2006.
- [116] T. Y. Lin and S. G. Kandlikar. A theoretical model for axial heat conduction effects during single-phase flow in microchannels. *Journal of Heat Transfer*, 134(2):020902, 2012.
- [117] M. M. Mahmoud and T. G. Karayiannis. Flow pattern transition models and correlations for flow boiling in mini-tubes. *Experimental Thermal and Fluid Science*, 70:270–282, 2016.
- [118] J. C. Chen. Correlation for boiling heat transfer to saturated fluids in convective flow. *Industrial & Engineering Chemistry Process Design and Development*, 5(3):322–329, 1966.
- [119] S. Saitoh, H. Daiguji, and E. Hihara. Correlation for boiling heat transfer of R-134a in horizontal tubes including effect of tube diameter. *International Journal of Heat and Mass Transfer*, 50(25):5215–5225, 2007.
- [120] D. Steiner and J. Taborek. Flow boiling heat transfer in vertical tubes correlated by an asymptotic model. *Heat transfer engineering*, 13(2):43–69, 1992.
- [121] Z. Liu and R. H. S. Winterton. A general correlation for saturated and subcooled flow boiling in tubes and annuli, based on a nucleate pool boiling equation. *International journal of heat and mass transfer*, 34(11):2759–2766, 1991.
- [122] M. G. Cooper. Heat flow rates in saturated nucleate pool boiling -a wide ranging examination using reduced properties. *Advances in heat transfer*, 16:157–239, 1984.
- [123] F. W. Dittus and Boelter L. M. K. Heat transfer in automobile radiators of the tubular type. *Publications in engineering. University of California*, 2:443–461, 1930.
- [124] S. G. Kandlikar and P. Balasubramanian. An extension of the flow boiling correlation to transition, laminar, and deep laminar flows in minichannels and microchannels. *Heat Transfer Engineering*, 25(3):86–93, 2004.
- [125] F. T. Kanizawa, C. B. Tibiriçá, and G. Ribatski. Heat transfer during convective boiling inside microchannels. *International Journal of Heat and Mass Transfer*, 93:566–583, 2016.

- [126] W. Zhang, T. Hibiki, K. Mishima, and Y. Mi. Correlation of critical heat flux for flow boiling of water in mini-channels. *International Journal of Heat and Mass Transfer*, 49(5):1058–1072, 2006.
- [127] N. Kattan, J. R. Thome, and D. Favrat. Flow boiling in horizontal tubes: part 3-development of a new heat transfer model based on flow pattern. *Journal of Heat Transfer*, 120(1):156–165, 1998.
- [128] L. Wojtan, T. Ursenbacher, and J. R. Thome. Investigation of flow boiling in horizontal tubes: Part II-Development of a new heat transfer model for stratified-wavy, dryout and mist flow regimes. *International Journal of Heat and Mass Transfer*, 48(14):2970–2985, 2005.
- [129] L. Cheng, G. Ribatski, and J. R. Thome. New prediction methods for CO₂ evaporation inside tubes: Part II-An updated general flow boiling heat transfer model based on flow patterns. *International Journal of Heat and Mass Transfer*, 51(1):125–135, 2008.
- [130] A. Cioncolini and J. R. Thome. Algebraic turbulence modeling in adiabatic and evaporating annular two-phase flow. *International Journal of Heat and Fluid Flow*, 32(4):805–817, 2011.
- [131] A. Francescon, G. Romagnoli, A. Mapelli, P. Petagna, C. Gargiulo, L. Musa, J. R. Thome, and D. Del Col. Development of interconnected silicon micro-evaporators for the on-detector electronics cooling of the future ITS detector in the ALICE experiment at LHC. *Applied Thermal Engineering*, 93:1367 – 1376, 2016. doi: <http://dx.doi.org/10.1016/j.applthermaleng.2015.09.013>.
- [132] H. Martin. Heat and mass transfer between impinging gas jets and solid surfaces. In *In: Advances in heat transfer. Volume 13. New York, Academic Press, Inc., 1977, p. 1-60.*, volume 13, pages 1–60, 1977.
- [133] M. Gómez Marzoa et al. Thermal studies of an ultra-low-mass cooling system for the ALICE ITS Upgrade project at CERN. In *Proceedings, 8th World Conference on Experimental Heat Transfer Fluid Mechanics and Thermodynamics, Lisbon, Portugal (ExHFT-8 2013)*, 2013. ISBN 978-972-8620-23-3.
- [134] S. Fujita, Y. Kamei, and K. Tanaka. Effect of water absorption in polyimide on electrical properties. In *Solid Dielectrics, 2001. ICSD'01. Proceedings of the 2001 IEEE 7th International Conference on*, pages 183–186. IEEE, 2001.
- [135] M. Atac, B. Gobbi, L. Cremaldi, and J. Hoffman. Radiation hardness studies of cooling fluids epoxies and capacitors for CMS pixel system. *Nuclear Instruments and Methods in Physics Research Section A: Accelerators, Spectrometers, Detectors and Associated Equipment*, 476(3): 676–679, 2002.
- [136] W. M. Kays and M. E. Crawford. *Convective heat and mass transfer*. McGraw-Hill, 1993.

- [137] A. Francescon, G. Aglieri Rinella, V. Altini, M. Battistin, S. Berry, C. Bianchin, C. Bortolin, J. B. Direito, C. Cavicchioli, C. Di Giglio, et al. Performance of the ALICE SPD cooling system. In *Journal of Physics: Conference Series*, volume 395, page 012063. IOP Publishing, 2012.
- [138] H. Boterenbrood and B. I. Hallgren. The development of embedded local monitor board (ELMB). Technical report, ATL-COM-DAQ-2003-070, 2003.
- [139] *REFPROP, standard reference fluid thermodynamic and transport properties database, version 9.0*. National Institute of Standards and Technology (NIST), 2013.
- [140] S. W. Churchill and H. H. S. Chu. Correlating equations for laminar and turbulent free convection from a vertical plate. *International journal of heat and mass transfer*, 18(11):1323–1329, 1975.
- [141] K. Stewartson. On the free convection from a horizontal plate. *Zeitschrift für angewandte Mathematik und Physik ZAMP*, 9(3):276–282, 1958.
- [142] S. W. Churchill. Free convection around immersed bodies. *Heat Exchanger Design Handbook*, 2 (14). Hemisphere Publishing, New York, Sec, 1983.
- [143] C. F. Colebrook and C. M. White. Experiments with fluid friction in roughened pipes. *Proceedings of the Royal Society of London. Series A, Mathematical and Physical sciences*, pages 367–381, 1937.
- [144] H. Blasius. *Das Ähnlichkeitsgesetz bei Reibungsvorgängen in Flüssigkeiten*. Springer, 1913.
- [145] S. W. Churchill. Friction-factor equation spans all fluid-flow regimes. *Chemical engineering*, 84 (24):91–92, 1977.
- [146] I. E. Idelchik and E. Fried. *Handbook of hydraulic resistance*. U.S. Atomic Energy Commission, 1966.
- [147] VDI-Gesellschaft Verfahrenstechnik und Chemieingenieurwesen (GCV). *VDI Heat Atlas*. Springer Science & Business Media, 2010.
- [148] B. Spang. Einfluß der thermischen Randbedingung auf den laminaren Wärmeübergang im Kreisrohr bei hydrodynamischer Einlaufströmung. *Heat and mass transfer*, 31(4):199–204, 1996.
- [149] V. Gnielinski. Ein neues Berechnungsverfahren für die Wärmeübertragung im Übergangsbereich zwischen laminarer und turbulenter Rohrströmung. *Forschung im Ingenieurwesen*, 61(9):240–248, 1995.
- [150] V. Gnielinski. New equations for heat and mass-transfer in turbulent pipe and channel flow. *International chemical engineering*, 16(2):359–368, 1976.
- [151] B. S. Petukhov. Heat transfer and friction in turbulent pipe flow with variable physical properties. *Advances in heat transfer*, 6(503):i565, 1970.

- [152] BIPM, IEC and IFCC, ISO and IUPAC, IUPAP. OIML (1995) Guide to the expression of uncertainty in measurement (GUM). *ISO, Geneva*, 1995.
- [153] M. Christians. *Heat transfer and visualization of falling film evaporation on a tube bundle*. PhD thesis, École Polytechnique Fédérale de Lausanne, 2010.
- [154] M. Gómez Marzoa and C. Gargiulo. Thermal performance of lightweight cooling systems for the ALICE ITS Upgrade. In *Forum on Tracking Detectors Mechanics, DESY, Hamburg, Germany*, 2014. URL <https://indico.cern.ch/event/287285/contribution/11>.
- [155] ASHRAE Handbook Fundamentals. Chapter 22: pipe sizing. *Atlanta*, 2009.
- [156] Carrier. *Piping design, in System design manual*. Carrier Air Conditioning Company, Syracuse, NY, 1960.
- [157] V. Dupont, J. R. Thome, and A. M. Jacobi. Heat transfer model for evaporation in microchannels. part ii: comparison with the database. *International Journal of Heat and Mass Transfer*, 47(14): 3387–3401, 2004.
- [158] M. Gomez Marzoa. *Personnal communication with Caroline Liberti, Applications Engineer at Microlumen Inc.*, 2013.
- [159] R. B. Abernethy. *Measurement uncertainty handbook*, volume 73. Instrumentation Systems &, 1980.
- [160] V. Gnielinski. Heat transfer coefficients for turbulent flow in concentric annular ducts. *Heat transfer engineering*, 30(6):431–436, 2009.
- [161] S. W. Churchill and H. H. S. Chu. Correlating equations for laminar and turbulent free convection from a horizontal cylinder. *International Journal of Heat and Mass Transfer*, 18(9):1049–1053, 1975.
- [162] M. Matkovic, A. Cavallini, D. Del Col, and L. Rossetto. Experimental study on condensation heat transfer inside a single circular minichannel. *International Journal of Heat and Mass Transfer*, 52(9):2311–2323, 2009.
- [163] W. H. Press, B. P. Flannery, S. A. Teukolsky, and W. T. Vetterling. *Numerical recipes: the art of scientific programming*. 2007.
- [164] T. L. Bergman, F. P. Incropera, and A. S. Lavine. *Fundamentals of heat and mass transfer*. John Wiley & Sons, 2011.
- [165] W. M. Kays and A. L. London. *Compact heat exchangers*. 1984.

- [166] V. Gnielinski. Berechnung des druckverlustes in glatten konzentrischen ringspalten bei ausgebildeter laminarer und turbulenter isothermer strömung. *Chemie Ingenieur Technik*, 79(1-2): 91–95, 2007.
- [167] B. N. Taylor and C. E. Kuyatt. Guidelines for Evaluating and Expressing the Uncertainty of NIST Measurement Results. Technical Report NIST Technical Note 25, NIST, 1994.
- [168] S. J. Kline and F. A. McClintock. Describing uncertainties in single-sample experiments. *Mechanical engineering*, 75(1):3–8, 1953.
- [169] D. Sempértegui-Tapia, J. De Oliveira Alves, and G. Ribatski. Two-phase flow characteristics during convective boiling of halocarbon refrigerants inside horizontal small-diameter tubes. *Heat Transfer Engineering*, 34(13):1073–1087, 2013.
- [170] C. L. Ong and J. R. Thome. Macro-to-microchannel transition in two-phase flow: Part 2—flow boiling heat transfer and critical heat flux. *Experimental Thermal and Fluid Science*, 35(6): 873–886, 2011.
- [171] L. Wojtan, R. Revellin, and J. R. Thome. Investigation of saturated critical heat flux in a single, uniformly heated microchannel. *Experimental Thermal and Fluid Science*, 30(8):765–774, 2006.
- [172] D. Chisholm. *Two-phase flow in pipelines and heat exchangers*. George Godwin London, 1983.
- [173] S. W. Churchill and R. Usagi. A general expression for the correlation of rates of transfer and other phenomena. *AIChE Journal*, 18(6):1121–1128, 1972.
- [174] K. Gauler. Wärme- und Stoffübertragung an eine mitbewegte Grenzfläche bei Grenzschichtströmung. *Diss. Univ. Karlsruhe (TH)*, 1972.
- [175] S. G. Kandlikar and M. E. Steinke. Flow boiling heat transfer coefficient in minichannels—correlation and trends. In *Proceedings of the Twelfth International Heat Transfer Conference*, volume 3, pages 785–790, 2002.
- [176] K. Stephan and M. Abdelsalam. Heat-transfer correlations for natural convection boiling. *International Journal of Heat and Mass Transfer*, 23(1):73–87, 1980.
- [177] E. Da Riva, D. Del Col, S. V. Garimella, and A. Cavallini. The importance of turbulence during condensation in a horizontal circular minichannel. *International Journal of Heat and Mass Transfer*, 55(13):3470–3481, 2012.
- [178] *MicroLumen High Performance Polyimide tubing Data Sheet*. MicroLumen Inc., 2012.
- [179] *Summary of Properties for Kapton[®] Polyimide Films*. DuPont Corp., 2014.
- [180] W. O. Clinedinst et al. A rational expression for the critical collapsing pressure of pipe under external pressure. In *Drilling and Production Practice*. American Petroleum Institute, 1939.

-
- [181] J. L. Holmquist, A. Nadai, et al. A theoretical and experimental approach to the problem of collapse of deep-well casing. In *Drilling and Production Practice*. American Petroleum Institute, 1939.
- [182] R. G. Sturm. A study of the collapsing pressure of thin-walled cylinders. *University of Illinois bulletin v. 39, no. 12*, 1941.
- [183] C. R. Kennedy and J. T. Venard. Collapse of tubes by external pressure. Technical report, Oak Ridge National Lab., Tenn., 1962.
- [184] T. Sınmazçelik and İ. Taşkıran. Erosive wear behaviour of polyphenylenesulphide (PPS) composites. *Materials & design*, 28(9):2471–2477, 2007.
- [185] A. T. Pérez Fontenla. Microscope observation of polyimide pipes. EDMS 502857. Technical report, CERN, 2015.

Curriculum Vitae

Personal information

Name	Manuel GÓMEZ MARZOA
Date of Birth	9 th September 1987
Nationality	Spanish

Education

2012-2016	Doctoral Student and Assistant, Laboratory of Heat and Mass Transfer (LTCM), Swiss Federal Institute of Technology Lausanne (EPFL), Switzerland
2011	M.Sc. Industrial Engineering. University of Vigo, Spain.

Professional experience

Mar 2012 - Nov 2015	Doctoral Student. Cooling and Ventilation group, CERN, Switzerland. Collaboration on the development of the ALICE ITS Upgrade cooling system and main responsible for thermal testing. Collaboration in CFD projects, supervising students as CFD-Team technical coordinator (Mar-Sep 2014).
Oct 2014 - Jul 2015	Swiss National Science Foundation (SNSF) Doctoral Mobility fellow. Developed an experimental heat transfer project at University of São Paulo, Brazil.
Ago 2010 - Sep 2011	Technical Student. Cooling and Ventilation group, CERN, Switzerland. Master Thesis on CFD and collaboration in CFD projects at the CFD-Team.
Jul - Sep 2009	Student researcher. Laser Processing Group. CSIC Optics Institute, Spain. Conducted experimental tests in thermo-optical switches. Laboratory assistance.

Journal Articles

1. M. Gómez Marzoa, G. Ribatski and J. R. Thome. Experimental flow boiling heat transfer in a small polyimide channel. *Applied Thermal Engineering*, 2016 (revised manuscript submitted).
2. CAST Collaboration (incl. M. Gómez Marzoa). Search for Solar Axions by the CERN Axion Solar Telescope with ^3He Buffer Gas: Closing the Hot Dark Matter Gap. *Phys.Rev.Lett.*, 112(9):091302, 2014
3. M. Jiménez de Castro, R. Serna, M. Gómez Marzoa, A. Castelo, C. N. Afonso, and E. Haro-Poniatowski. Thermo-optical response of layered Bi nanostructures produced by pulsed laser deposition. *Applied Surface Science*, 257(12):5172-5174, 2011.

Technical Reports

1. ALICE Collaboration (incl. M. Gómez Marzoa). Upgrade of the ALICE Inner Tracking System. Technical Report CERN-LHCC-2013-024. ALICE-TDR-017, CERN, Geneva, Nov 2013.
2. ALICE Collaboration (incl. M. Gómez Marzoa). Conceptual Design Report for the Upgrade of the ALICE ITS. Technical Report CERN-LHCC-2012-013. LHCC-P-005, CERN, Geneva, Aug 2012.

Conference Proceedings

1. M. Gómez Marzoa *et al.* Thermal Studies of an Ultra-Low-Mass Cooling System for the ALICE ITS Upgrade Project at CERN. In *Proceedings of the 8th World Conference on Experimental Heat Transfer, Fluid Mechanics and Thermodynamics*, Instituto Superior Técnico, Lisbon, June 2013.

Unpublished Work

1. A journal article on the experimental thermo-hydraulic characterisation of the cooling proposals for the ALICE ITS Upgrade detector at CERN.

